Kriterien für Wälzlagerstähle für das Induktionshärten

Vom Fachbereich Produktionstechnik

der

UNIVERSITÄT BREMEN

zur Erlangung des Grades

Doktor-Ingenieur

genehmigte

Dissertation

von

Dipl.-Ing. Michael Wendel

Gutachter: Prof. Dr.-Ing. habil. Franz Hoffmann

Prof. Dr.-Ing. habil. Olaf Keßler (Universität Rostock)

Tag der mündlichen Prüfung: 04.02.2020

Acknowledgements

The work present in this thesis was made possible by the financial support and supervision of the SKF Group and the former foundation institute of material science (today: IWT – Leibniz - Institut für werkstofforientierte Technologien) in Bremen. Thank you for the opportunity to pursue my degree and the close collaboration between SKF and IWT.

I would like to thank my academic supervisor Professor Franz Hoffmann and also Professor Hans-Werner Zoch for their supervision, guidance, advice, and the fruitful discussions. I sincerely thank Professor Olaf Keßler for taking the role as second assessor, as well as the board of examiners: Professor Brigitte Clausen, Professor Udo Fritsching, Heike Sonnenberg und Maryam Sasani. In addition, I acknowledge the colleagues from IWT for their support, open discussions and great laboratory work. Especially to mention the support from the metallographic analysis, the physical analysis and the heat treatment department. Thank you.

I thank Dr. Ulf Lindstedt, Ulf Sjöblom and Dr. Patrik Dahlman from SKF for the sponsorship and openness to conduct this work. Special thanks to Mr. Walter Datchary for the industrial supervision. Also I would like to thank the whole SKF heat treatment development department for their patience, good discussions and openness, that is to mention: Isabella Flodström, Augusta Sahlin, Malin Johnsson, Andreas Hultkrantz, Staffan Larsson, Rolando Velazquez, Robert Brandt.

Additional thanks go to the University of Cambridge, to Professor Harry Bhadeshia and to Dr. Peter Walker for the possibility to use their facilities and fatigue testing equipment and for arranging my stay in Cambridge.

A special thanks goes to Dr. Marco Burtchen, Dr. Martin Hunkel and Dr. Holger Surm for putting me in contact with the SKF Group as a student which led to my diploma work and the present work and thesis.

Finally I would like to thank my family, Maike and Jasper Emil, for their patience, understanding, encouragement, and great support.

German abstract

Randschichthärten, Durchhärten und Anlassen von Wälzlagerkomponenten mittels induktiver Erwärmung sind etablierte Produktionsprozesse, welche im Bereich der Forschung und Entwicklung weiterentwickelt werden. Sie bieten neben einem vergleichsweise niedrigen Einsatz von elektrischer Energie und damit verbundener Emissionen, die Möglichkeit der Einstellung hervorragender Produkteigenschaften. Vor allem im Vergleich zum Einsatzhärten können sich bezüglich des Prozesses und der verwendeten Stähle erhebliche Vorteile beim Ressourceneinsatz ergeben. Die Technologie des Erwärmens mittels Induktion in der Wärmebehandlung wird auf Grund des immer größer werdenden Umweltbewusstseins und der zukünftigen Verfügbarkeit bestimmter Legierungselemente (z.B. Nickel) weiter an Bedeutung gewinnen.

Neben vielen Faktoren hat die Werkstoffauswahl einen maßgeblichen Einfluss auf das Wärmebehandlungsergebnis und ist von zentraler Bedeutung. In der vorliegenden Arbeit wird eine Auswahl üblicher, sowie für das Induktionshärten potentiell interessanter Wälzlagerstähle bezüglich ihres Verhaltens beim induktiven Härten bewertet. Ziel der Arbeit ist, einen für das Induktionshärten geeigneten Wälzlagerstahl zu identifizieren.

Im ersten Teil der Arbeit wurden Stähle mittlerer bis hoher Kohlenstoffgehalte mit unterschiedlichen Legierungsstrategien für die Untersuchung ausgewählt. In Abhängigkeit der verschiedenen Stähle, sowie verschiedener Gefügezustände vor dem Härten, wurde die Stabilität des Härteergebnisses erörtert. Dabei wurde mit Hilfe einer Dilatometerstudie die Veränderung der Martensitstarttemperatur, der Härte, der ehemaligen Austenitkorngröße, und der nicht martensitischen Umwandlungsbestandteile des Gefüges für veränderte Austenitisierungsbedingungen verglichen.

Der Gefügezustand vor dem Härten zeigte sich als wichtige Einflussgröße für das Härteergebnis. Das Legieren mit Silizium und Mangan führte zu einer Reduzierung der nicht martensitischen Umwandlungsbestandteile des Gefüges nach dem Härten. Allgemein führten höhere Gehalte an Legierungselementen zu größeren Veränderungen der Martensitstarttemperatur mit veränderten Austenitisierungsbedingungen. Mit zunehmendem Legierungsgehalt wurde zudem eine geringere erreichbare Härte gemessen.

Als zentrales Ergebnis konnte in der Dilatometerstudie gezeigt werden, dass der Stahl 50CrMo4 ein geeigneter Wälzlagerstahl mit sehr robusten Wärmebehandlungsergebnis ist.

Im zweiten Teil der Arbeit wurden die Ergebnisse der Dilatometerstudie auf randschichtgehärtete Wellen übertragen. Es zeigte sich eine gute Korrelation der verschiedenen Einhärtetiefen (SHD) der Wellen mit den gemessenen Umwandlungstemperaturen A_{c3} im Dilatometer. Ebenfalls konnten die Härtegradienten in der Übergangszone (Übergang weicher Kern zur harten Randschicht) mit der Differenz der gemessenen Umwandlungstemperaturen der Ferrit-Austenit Umwandlung $A_{c3}–A_{c1}$ korreliert werden. Der radiale Härteabfall der Wellen entsprach der ermittelten, mittleren Härteänderung mit veränderten Austenitisierungstemperaturen der Dilatometerproben.

Im letzten Teil der Arbeit wurde die Ermüdung der Stähle bei Überrollung bewertet. Zur Bewertung wurden die sich veränderte Härte im überrollten Materialvolumen, die Änderung der Eigenspannungen, die Änderung der Halbwertsbreite, die Änderung des Gehalts an Restaustenit, sowie metallografische Untersuchungen herangezogen. In den metallografischen Untersuchungen wurden die Anzahl an Schädigungsbeobachtungen, die Anzahl an Schädigungsbeobachtungen mit weiß anätzenden Materialbereichen, die Anzahl an Rissen und die Länge von Rissen ausgewertet.

Die Härte nach der Wärmebehandlung wurde als entscheidende Eigenschaft für die klassische Ermüdungsschädigung identifiziert. Mit steigender Härte zeigte sich eine geringere Mikroplastizität, eine geringere Änderung der Eigenspannungen und Halbwertsbreite, sowie eine geringere Änderung des Gehalts an Restaustenit.

In den metallografischen Untersuchungen wurden zum Teil erhebliche Schädigungen im Gefüge festgestellt, wie etwa lange (etwa 250 µm) und zahlreiche Risse bis direkt unter die Laufbahn. Im Gegensatz zum Ergebnis der klassischen Werkstoffermüdung, zeigten vor allem Stähle mit vergleichsweisen hohe Kohlenstoffgehalten und einer hohe Härte nach der Wärmebehandlung viele und lange Risse. Zudem führte ein besserer metallografische Reinheitsgrad und kleinere ehemalige Austenitkorngrößen zu weniger und kürzeren Rissen. Das Ergebnis wurde vor dem Hintergrund der Werkstoffzähigkeit diskutiert.

Unter den gegebenen Testbedingungen mit hohen Kontaktspannungen (5,6 GPa) wurden hohe Kohlenstoffgehalte und eine hohe Härte nach der Wärmebehandlung auf Grund der Risserscheinungen als eher nachteilig bewertet. Ob die Rissempfindlichkeit für Stähle hoher Kohlenstoffgehalte und hoher Härten unter reduzierten, anwendungsnäheren Flächenpressungen ähnlich ausgeprägt ist, kann bezweifelt werden.

Eine Reduzierung von weiß anätzenden Materialbereichen wurde für höhere Druckeigenspannungen, höhere Siliziumgehalte, sowie geringere Chrom und Molybdängehalte gezeigt und diskutiert.

In der gesamten Bewertung der Überrollungsprüfung ergab sich eine vergleichsweise gutes Abschneiden des Stahls 67SiCr5.

Insgesamt, in Betracht der Dilatometerstudie und der Überrollungsprüfung, wurde der Stahl 67SiCr5 als geeigneter Stahl für das Induktionshärten identifiziert. Grund dafür ist die Kombination aus robusten Wärmebehandlungsergebnis und guter Überrollungsleistung unter den gewählten Überrollungsbedingungen.

Contents

Nomenclature

Symbol/ abbreviation	Description	Unit
wt.-%	Weight percent	Weight-%
Vol.-%	Volume percent	Volume-%
RA	Retained austenite	
NMTP	Non martensitic transformation products	
PAGS	Prior austenite grain size	
M_S	Martensite start	
M_F	Martensite finish	
Ac_1	Temperature for beginning of ferrite to austenite transformation upon heating	°C
Ac_3	Temperature for end of ferrite to austenite transformation upon heating	°C
RS	Residual stress	MPa
FWHM	Full width half maximum	°
RCF	Rolling contact fatigue	
V_{RA}	Volume fraction retained austenite	
$V_{Mart.}$	Volume fraction martensite	
HV	Hardness in Vickers	HV
HRC	Hardness in Rockwell	HRC
T_C	Curie Temperature	°C
C	Carbon	
Si	Silicon	
Mn	Manganese	
Cr	Chromium	
Ni	Nickel	
Mo	Molybdenum	
Cu	Copper	
V	Vanadium	
W	Tungsten	
N	Nitrogen	
B	Magnetic Induction	$T = V\ s\ m^{-2}$
H	Magnetic field strength	$A\ m^{-1}$
μ	Magnetic permeability	$V\ s\ m^{-1}\ A^{-1}$
μ_r	Relative magnetic permeability	
I	Electric current	A
I_1	Electric current coil	A
I_K	Induced electric current	A
δ	Current penetration depth	m
$\rho_{el.}$	Electric resistivity	$\Omega\ m = kg\ m^3\ A^{-2}\ s^{-3}$
r	Radius	m
f	Frequency	$Hz = s^{-1}$
TTA	Time Temperature Austenitisation Diagram	

A	Austenite	
C	Carbide	
F	Ferrite	
P	Perlite	
M	Martensite	
B	Bainite	
SA	Soft annealed	
QT	Quench and tempered	
p	Contact pressure	MPa = 10^6 kg m^{-1} s^{-2}
p_0	Maximum contact pressure	MPa = 10^6 kg m^{-1} s^{-2}
a, b	Semi axis contact ellipse	m
P	Contact load	N = kg m s^{-2}
$R_{1,2}$	Bodies radii	m
$E_{1,2}$	Bodies E-moduli	MPa = 10^6 kg m^{-1} s^{-2}
$\nu_{1,2}$	Bodies Poisson`s ratios	
$\sigma_{x,y,z}$	Mechanical stresses in x,y,z direction	MPa = 10^6 kg m^{-1} s^{-2}
τ_1	Principal shear stress	MPa = 10^6 kg m^{-1} s^{-2}
λ	Specific lubricant film thickness	
h_{min}	Minimum lubricant film thickness	m
$h_{central}$	Central contact position lubricant film thickness	m
R_a	Arithmetic average roughness	m
RMS	Root-mean-square roughness	m
η_0	Atmospheric dynamic viscosity	Pa s = kg m^{-1} s^{-1}
$P_{iv,as}$	Asymptotic isoviscous pressure	MPa = 10^6 kg m^{-1} s^{-2}
α	Pressure-viscosity exponent	MPa^{-1} = 10^{-6} kg^{-1} m s^2
HNO_3	Nitric acid	
WEA	White etching area	
WEC	White etching constituent	
DEA	Dark etching area	
DEC	Dark etching constituent	
WEB	White etching band	
WSF	White structure flaking	
LAB	Low angle bands	
HAB	High angle bands	
L_{10}	Life which statistically 90 % of bearings reach	
SEM	Scanning electron microscope	
TEM	Transmission electron microscope	
MnS	Manganese sulfide inclusion	
AL_2O_3	Aluminum oxide inclusion	
TiN/ TiC	Titanium nitride / carbide inclusion	
CaO	Calcium oxide inclusion	
AlN	Aluminum nitride precipitation	
MgO	Magnesium oxide inclusion	
SiO_2	Silicon oxide inclusion	
N	Number of load cycles	

rev/ min, rpm	Revolution per minute	min^{-1}
{hkl}	Crystallographic plane	
<uvw>	Crystallographic direction	
Q_{eff}	Activation energy	$J = kg\ m^2\ s^{-2}$
T_T	Tempering temperature	°C
T_A	Austenitisation temperature	°C
T_C	Curie temperature	°C
t	Time	s
t_{8-5}	Time between 800 °C and 500 °C during quenching	s
$Ø_O$	Outer diameter	m
$Ø_I$	Inner diameter	m
L	Volume diffusion distance	m
D	Diffusion coefficient	$m^2\ s^{-1}$
n.a.	Not available	
e.g.	Exempli gratia	
SHD	Surface hardening depth	m
S	Standard error of regression	
R^2 / R-sq	Coefficient of determination	
R-sq (adj.)	Adjusted coefficient of determination for comparison of models with different numbers of predictors	
R-sq (pred.)	Predicted coefficient of determination for detection of too complicated models with too many coefficients	
SE Coef.	Standard error of coefficient for determination of the precision of an coefficient	
T-Value	Ratio between coefficient and standard error	
P-Value	Probability that measures evidence against null hypothesis	
VIF	Variance inflation factor for detection of correlation between predictors	
EHD	Elastohydrodynamic lubrication conditions	
u	Surface velocity	$m\ s^{-1}$

1 Introduction and objective

The increasing awareness of environmental aspects as well as the pressure from globalisation in terms of productivity, cost competitiveness and product performance in the European market requires new or innovative manufacturing techniques and materials in many industrial sectors.

The German and European initiative to reduce CO_2 emissions by 40 % until the year 2020 (as compared to 1990) and even by 80-95 % until 2050 is just one ambitious example for the increasing environmental awareness [bmu18]. Considering that around 20 % of the German energy consumption is used for industrial heating processes (year 2016: 1713 Petajoule [uba18, bwe18]) shows the potential and need to reduce energy consumption and emissions with new or innovative technologies.

Globalisation and reduced cost for transportation puts pressure on the European industry which sees itself in competition to the so called “low cost countries”. To strengthen the European position, it is decisive to develop existing and new manufacturing techniques to increase productivity, reduce manufacturing cost and improve product performance.

Within the field of bearing manufacturing and the connected heat treatment, the above mentioned challenges can be faced by new heat treatment technologies or by the application of known heat treatment technologies to a wider product range. Induction heating or hardening can be a solution to reduce energy consumption and connected emissions, with a competitive cost and competitive product properties. When comparing case carburizing with induction hardening, as an example, detrimental effects can be reached for certain bearing components by changing the heat treatment to induction hardening. In some cases, like bearings for the wind industry, the heat treatment time can be reduced from one week to 15 minutes with a substantial reduction in consumed energy and connected emissions. Further advantages can be an increased material utilization connected to lower component distortion and post machining as well as savings due to the use of low alloyed induction hardening steels. A typical case carburizing bearing steel, such as 18NiCrMo14-6, contains up to 3.5 weight-% nickel. Considering a nickel price of 9.40 €/ kg (11.2018), an additional cost saving potential of around 330 € per heat-treated ton can be derived. Recent trends in the industry towards electric vehicles and the connected need for increased energy storing capacity and battery production might make nickel even more scarce and strategic in the future. Similar cost effects can be expected for decreased contents of chromium or molybdenum for some induction hardening steel grades.

The change of heat treatment to induction hardening leads to the question of the to be used components steel grade. Important factors to be considered for the choice of material are adequate process windows for a robust hardening process, the required product properties related to the intended application, the induction machine design with possible limitations and the connected induction hardening process. Likewise, the already used steel grades for induction hardening should be revised for the case of changed product requirements. An example is the trend of component downsizing and thereby an increase in energy density which in some cases requires a modification of the used steel chemistry.

The number of used steel grades which are conceived as suitable grades for induction hardening are limited in the bearing industry. The objective of this investigation is to benchmark potential and existing bearing steels in terms of their induction hardening response and their suitability for induction hardening.

Introduction and objective

Based on a literature study on alloying element effects, on the availability of steels and on the today's most commonly used steel grades for induction hardened bearing components, six potential and existing bearing steels are selected for this investigation.

In the following section, the robustness regarding the heat treatment result of the selected steels and their conditions prior to induction hardening shall be pointed out with the help of a dilatometer study. Here, the sensitivity of martensite start temperature (M_s), hardness after quenching, prior austenite grain size, and appearance of non-martensitic transformation products, depending on different austenitisation parameters are compared. Small changes of the mentioned properties with changed austenitisation conditions, as well as higher local hardenability or smaller amounts of non-martensitic transformation products after quenching are considered as favourable from a process stability point of view. Good process stability does not only result in less variation of, for example, the hardness or the M_s temperature of an induction hardened component. It also indicates smaller gradients of those properties within a component, taking into account the typical temperature gradients when applying induction heating. As one main result of the dilatometer study, the selected steels are benchmarked and a recommendation for a robust steel for induction hardening is made.

Following the dilatometer study, cylindrical rod-type samples are surface induction hardened and investigated in terms of hardness, microstructure and residual stresses. The purpose is to transfer the gained information and derived conclusions from the dilatometer study on the hardening result of surface induction hardened components. Here, the focus is put on the achieved surface hardening depth, the hardness gradients within the samples and the level of compressive residual stress.

Furthermore, the resistance towards rolling contact fatigue is investigated, as one major and important characteristic of a bearing steel. The effect of chemical composition and single alloying elements as well as other characteristics such as hardness, residual stresses, prior austenite grain size or cleanliness level are investigated. As one main result, the selected steels are benchmarked and a recommendation for a steel with good rolling contact fatigue performance shall be made. The comparison of rolling contact fatigue performance is made on induction through hardened rod-type samples to exclude the dependency of surface hardening depth on the fatigue performance.

Eventually, a suitable bearing steel shall be identified, providing a robust induction heat treatment response in combination with a comparable good resistance to rolling contact fatigue.

A summary of the above mentioned approach is schematically shown in Figure 1.

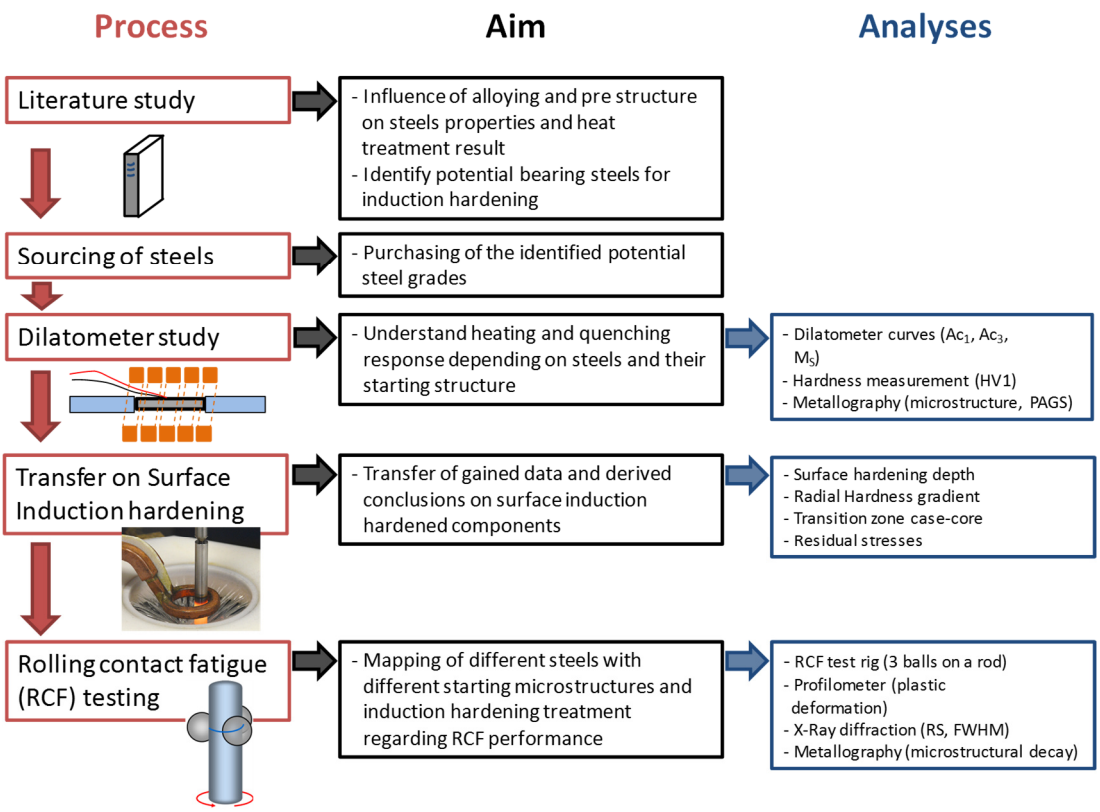

Figure 1: *Approach for identifying suitable bearing steel grades for induction hardening*

2 Literature review

2.1 Bearings

Bearings are transmitting forces, moments and movements between machine components with low friction, while providing accurate location. They can be divided by different criteria [Muh07]:

- Type of movement: plain bearings, rolling contact bearings, magnetic bearings
- Main direction of forces: radial bearings, axial bearings
- Function: fixed bearings, floating bearings
- Design: e.g. flange bearings, bearing units, hybrid bearings
- Assembly: non-split bearings, split bearings, demountable bearings.

Figure 2 shows an example of a simple radial and axial rolling contact bearing design. Rolling elements are running on dedicated raceways on the inner and outer ring or washer. This enables a relative rotational movement between the two rings or washers. The rolling elements conduct a combined movement of rolling and sliding. Cages enable a precise location of the rolling elements. Other important components of bearings are generally seals and lubrication (e.g. oil, grease).

Bearings are produced in a wide variety of types and sizes. Figure 2 shows the geometries of the most commonly used types of rolling elements, which are used to name and differentiate different bearing types.

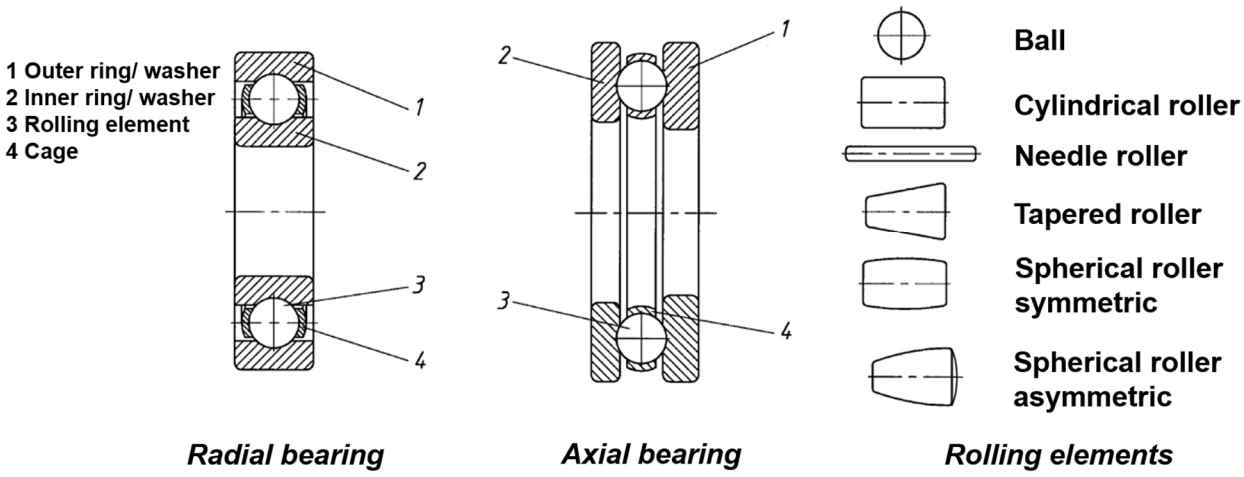

Figure 2: Bearing types and main parts of a bearing [Muh07]

2.2 Steel and heat treatment of bearings

The manufacturing chain of bearing components generally include forming and machining operations. Those operations require components with microstructures which are soft and provide good formability or machinability. At the end of the manufacturing chain, the same components need to provide hard and wear resistant microstructures to bear operational loads. In order to set those microstructures and related component properties, different, manufacturing related or operational related, heat treatment processes are applied. Bearing steel grade, applied heat treatment and achieved properties are always interconnected and should not be evaluated separately.

Bearing rings or washers and rolling elements need to bear high static and dynamic loads during operation. An appropriate steel and steel quality as well as a suitable heat treatment ensures that loads can be withstand and secures the bearings functionality. The basic bearing material requirements can be derived from the technical requirements for a bearing [Hen02, Zoc92]:

- High Hertzian contact stresses -> high hardness (min. 58 HRC)
- High number of load cycles -> rolling contact strength
- Sliding -> wear resistance
- Dimensional stability -> no microstructural changes
- Component strength -> sufficient toughness.

Additionally, in case of surface hardening heat treatment processes, a sufficient hardening depth is required to match the achieved strength profile to the loading dependent stress profile. Other requirements can be, for example, corrosions resistance or the ability to maintain sufficient strength at elevated temperatures. An appropriate combination of steel grade and applied heat treatment assures that bearing requirements are met.

Steels for bearings are listed in different standards, as DIN 17230 or ISO 683-17. Some examples can be found in Table 1:

Table 1: List of typical steel grades for bearings

Steel		Average chemical composition / wt.-%							
Designation	**Material number**	**C**	**Si**	**Mn**	**Cr**	**Ni**	**Mo**	**Cu**	**V / W / N**
Through hardening steels (ISO 683-17:2014)									
100Cr6	**1.3505**	0.99	0.25	0.35	1.48	-	max 0.1	max. 0.30	-
100CrMnSi6-4	**1.3520**	0.99	0.60	1.10	1.53	-	max 0.1	max. 0.30	-
100CrMo7-3	**1.3536**	0.99	0.30	0.70	1.80	-	0.28	max. 0.30	-
100CrMo7	**1.3537**	0.99	0.30	0.35	1.80	-	0.23	max. 0.30	-
100CrMnMoSi8-4-6	**1.3539**	0.99	0.50	0.95	1.93	-	0.55	max. 0.30	-
Case hardening steels (ISO 683-17:2014)									
17MnCr5	**1.3521**	0.17	max. 0.40	1.15	0.95	-	-	max. 0.30	-
19MnCr5	**1.3523**	0.19	max. 0.40	1.25	1.15	-	-	max. 0.30	-
18CrNiMo7-6	**1.6587**	0.18	max. 0.40	0.70	1.65	1.55	0.30	max. 0.30	-
18NiCrMo14-6	**1.3533**	0.18	max. 0.40	0.55	1.45	3.50	0.20	max. 0.30	-
Steels for quenching and tempering/ Induction- and flamehardening (ISO 683-17:2014)									
C56E2	**1.1219**	0.56	max. 0.40	0.75	-	-	-	max. 0.30	-
70Mn4	**1.1244**	0.70	max. 0.40	0.95	-	-	-	max. 0.30	-
43CrMo4	**1.3563**	0.43	max. 0.40	0.75	1.05	-	0.23	max. 0.30	-
Stainless steels (ISO 683-17:2014)									
X47Cr14	**1.3541**	0.47	max. 1.00	max. 1.00	13.50	-	-	-	
X65Cr14	**1.3542**	0.65	max. 1.00	max. 1.00	13.50	-	max. 0.75	-	
X108CrMo17	**1.3543**	1.08	max. 1.00	max. 1.00	17.00	-	0.60	-	
X40CrMoVN16-2	**1.4123**	0.41	max. 0.60	max. 0.60	15.75	max. 0.30	1.70	-	0.21 N, 0.30 V

High-temperature steels (ISO 683-17:2014)									
80MoCrV42-16	**similar AISI M50**	0.81	max. 0.40	0.25	4.10	-	4.25	max. 0.30	1.00 V, max. 0.25 W
X75WCrV18-4-1	**Similar AISI T1**	0.75	max. 0.40	max. 0.40	4.10	-	max. 0.60	max. 0.30	1.13 V, 18.25 W
13MoCrNi42-16-14	**Similar M50 NiL**	0.13	0.18	0.25	4.10	3.40	4.25	max. 0.10	1.15 V, max. 0.15 W

The listed steels are generally connected to certain heat treatments and bearing requirements. The most common heat treatment processes for bearings are shown in Figure 3 [Zoc92]. They include martensitic and bainitic through hardening, as well as thermochemical heat treatment processes, such as casehardening (including case carburising and carbonitriding) and nitriding. The schematic residual stress profiles show compressive residual stresses at the components surfaces or raceways for the majority of heat treatment processes. Compressive residual stresses in highly loaded material volumes were shown to be beneficial for the performance of components as bearings or gears [Lan96, Zwi80, Kra96, Hay75, Tot02]. Larger magnitudes of compressive residual stresses are of interest, since they can be superimposed to tensile stresses from mounting or operation, reducing the tensile stresses or material stressing in general [Zwi80]. Zwirlein shows in a computational study that an optimal level of compressive residual stress is existing. Larger or smaller levels of compressive residual stress lead to a reduction of their positive effect or become even a disadvantage as compared to residual stress free components [Zwi80].

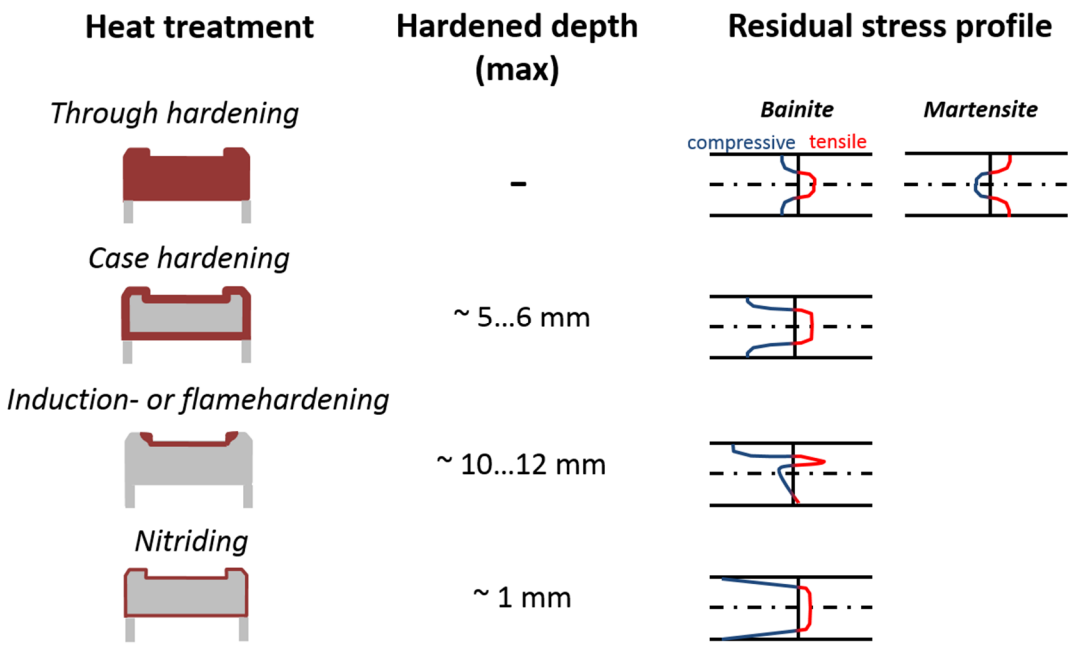

Figure 3: Common heat treatment processes for bearings, maximum achievable hardening depths and residual stress profiles (schematic) [Zoc92]

Most of the mentioned hardening heat treatments are followed by a tempering heat treatment. The main aim of tempering is to reduce the brittleness and increase the toughness of whole components or defined component volumes, especially for martensitic hardened ones. Furthermore, the residual stresses are relieved and the hardness is decreased. Commonly used tempering temperatures for hardened bearings steels can range from 150 °C to 240 °C and are held for several hours. In case of induction tempering, higher tempering temperatures and shorter heating and soaking times are used. The choice of the applied

tempering heat treatment not only depends on the achieved hardness and toughness, but also on the bearings` expected temperatures during operation.

The majority of bearings is made of 100Cr6 steel and higher alloyed derivations. The mentioned, through hardening bearing steels exhibit a comparably high hardenability, high achievable hardness, good formability and machinability, remaining carbides after hardening, as well as a comparably good availability. They are mainly used in combination with martensitic and bainitic through hardening.

2.3 Induction hardening of bearing components

Besides heating for forming, joining, assembly or melting, induction heating can be used for surface hardening, through hardening or tempering of hardened steel components. Induction heating can provide advantages over other conventional heating technologies like [Baa10]:

- Heat generation directly within the workpiece
- Fast heating due to high energy density
- High temperatures if required
- Demanded temperature distributions within the workpiece/ localized heating
- Comparatively low specific energy consumption and environmental impact (clean heating, lower CO_2 emissions)
- Reproducibility
- Good integration in the production line (in line equipment)
- On/ off equipment (low standby costs)
- High level of flexibility and automation.

For the bearing industry induction surface hardening, induction through hardening, and induction tempering of components like rolling elements or rings are established in production and are further developed in research and development. Among others, steel grade selection for induction hardening is one subject that needs to be considered. Figure 4 shows main factors impacting the result of an induction hardening process. The steels chemistry, its prior structure (alloying element distribution prior to hardening) and prior processing play important roles apart from the hardening process parameters and the induction machine design.

Induction heating or hardening processes are mostly characterized by shorter processing times and higher temperatures compared to conventional heating methods. The limited time at elevated temperature results in lower degrees of alloying element homogenization compared to furnace heating, especially for substitutional dissolved alloying elements with short diffusion distances. The steels chemistry as well as its prior structure play important roles and affect the austenitisation process and hence the degree of alloying element dissolution and homogenization in austenite during and after hardening.

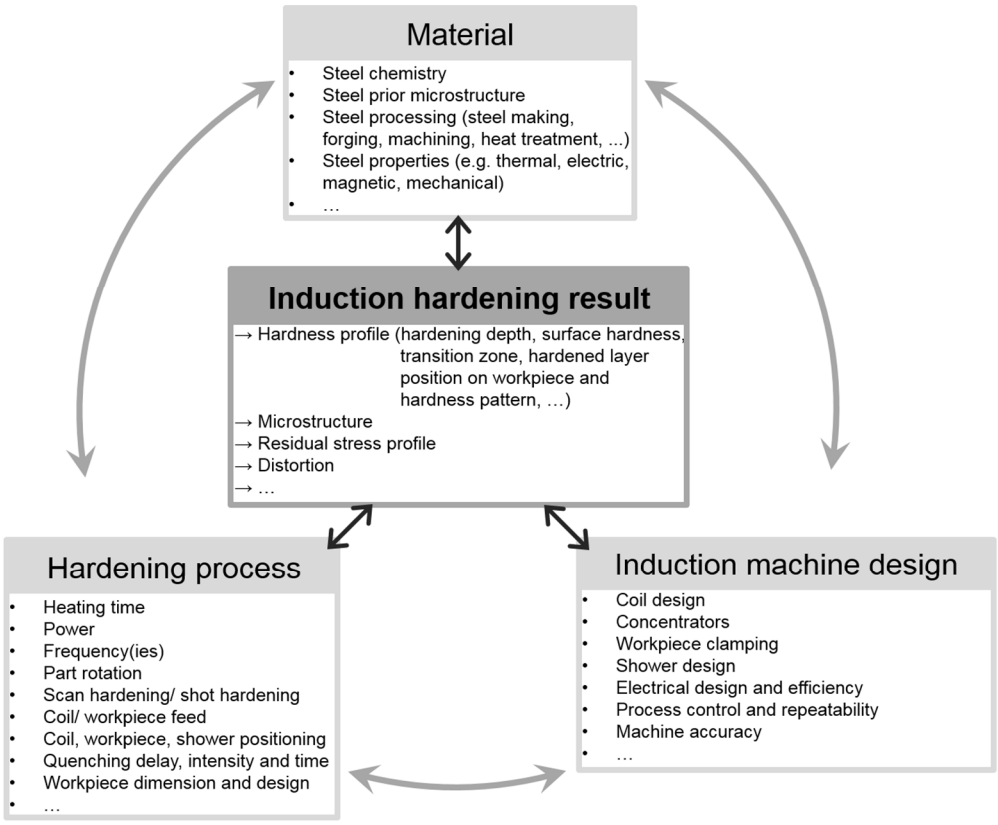

Figure 4 Major factors impacting Induction Hardening result

Typical induction hardened bearing components are truck or car hub unit rings, linear guides, slewing bearing rings or main shaft bearing rings for wind turbines.

2.3.1 Basics of induction heating

Electromagnetic induction was discovered 1831 by the English physicist Michael Faraday. He demonstrated the principle of induction with two coils, wrapped around iron cores. A change of the magnetic field in the first coil led to a voltage in the second coil. The missing contact between the coils resulted in the expression induction or induced voltage. The second coils` current, which is connected to the induced voltage, leads to an increase in temperature of the coil or the electrical conductive wire or component. This is the principal of induction heating.

Inductive heating is caused by two different mechanisms of energy dissipation. The first mechanism is joule heating. Electric energy is converted to heat by the interaction or collision of charged particles, as electrons and metal ions. High currents as well as high electric resistivity of materials lead to high joule losses or more effective heating. Joule heating is the only active, energy dissipating mechanism when heating non-magnetic materials (e.g. aluminium, steel $T > T_C$ Curie temperature) and the major for ferromagnetic materials.

The second, in general smaller, energy dissipating mechanism of inductive heating is caused by hysteresis losses in ferromagnetic materials when the applied magnetic field changes. Energy is converted into heat by the changing orientation of the Weiss domains in ferromagnetic materials [Zin88], see Figure 5.

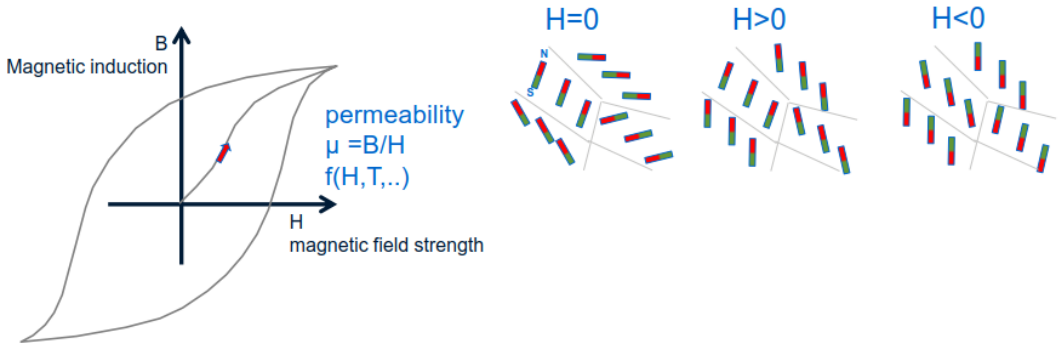

Figure 5: *Hysteresis losses in ferromagnetic materials*

In order to build up a sufficiently large alternating magnetic field strength in the proximity of a workpiece to be heated, high electric alternating currents (I_1) are used carried by good electric conductors (typically water cooled copper profiles). A coil design with a number of windings helps to increase the inductance or magnetic field. The induced voltage or current (I_K) into the workpiece is of opposite direction as well as the magnetic field caused by the induced current (see Figure 6).

Coil current and the resulting magnetic field as well as the induced current ("sleeve current") are shown schematically in Figure 7. The induced current shows a shift in phase by 90° and reaches its maximum at the maximal change of the magnetic field or the inflection points of coil current and magnetic field.

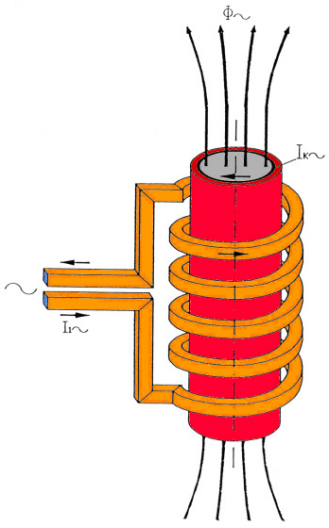

Figure 6: Directions of coil current I_I, induced current I_K and magnetic flux Φ [Hwg09]

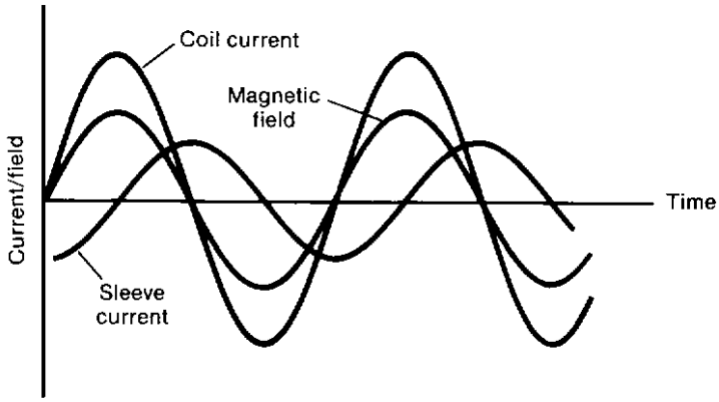

Figure 7: Coil current, magnetic field and induced current over time [Zin88]

Electric conductors carrying alternating current show a current distribution as shown in Figure 8. The so called skin effect describes a current distribution with its maximum at the surface and an exponentially decreasing current towards the centre of the conductor.

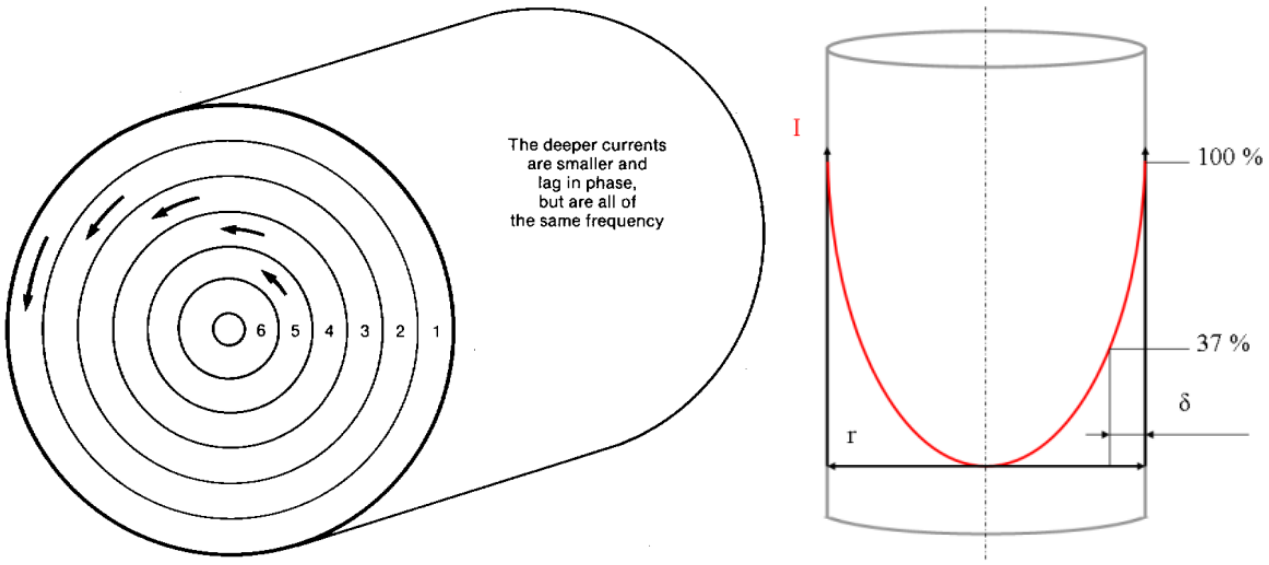

Figure 8: Distribution of induced current, skin effect [Zin88, Tud60]

One commonly used characteristic describing the skin effect is the currents penetration depth δ, which is defined as [Sem86]:

$$\delta = 503 \cdot \sqrt{\frac{\rho_{el.}}{f \cdot \mu_r}}. \tag{1}$$

where δ is the currents penetration depth in m, $\rho_{el.}$ is the electric resistivity of the conductor in Ω·m, f is the frequency of alternating current in 1/s and μ_r is the relative magnetic permeability. The current reaches ~ 37 % of its maximum at the depth of δ. The power density is decreased to ~14 % of its maximum at the depth of δ. By definition (see equation 1) δ is influenced by the material properties ($\rho_{el.}$, μ_r) as well as the applied frequency of alternating current. It is worth noting that $\rho_{el.}$ generally changes with the materials temperature and μ_r changes with temperature as well as magnetic field strength. δ generally increases with increasing conductor material temperature and increases rapidly after passing the Curie temperature of a ferro magnetic material.

Typical current penetration depths are shown in Figure 9.

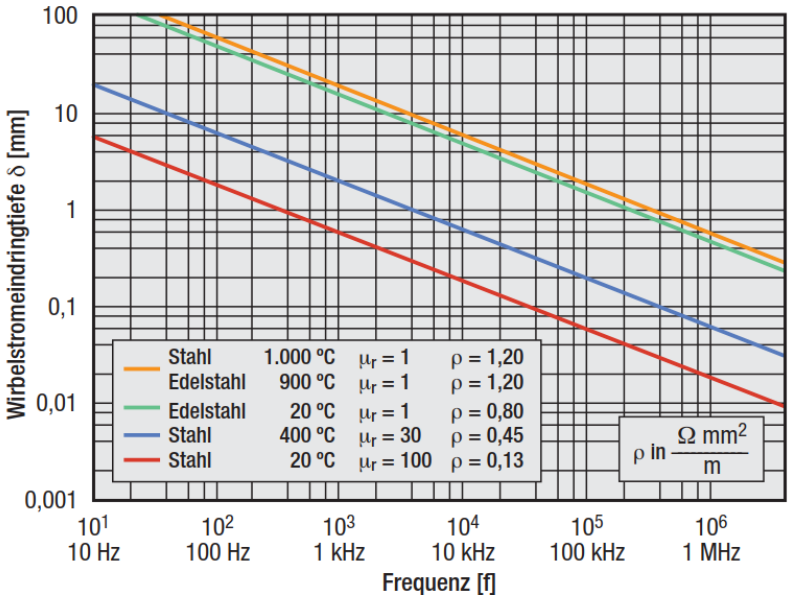

Figure 9: Typical penetration depths δ for different materials, temperatures and frequencies [Lie09]

In case of induction heating, the induction coil and the to be heated workpiece show the described skin effect. The current distribution in a conductor is further affected by neighbouring conductors carrying alternating current. Figure 10 shows the so called electromagnetic proximity effect. The proximity effect leads to a redistribution of magnetic fields and thereby a redistribution of the carried current. In case of opposite directions of current (see Figure 10), the maximum current will be present at the conductor surfaces facing each other, vice versa for identical current directions. The proximity effect leads to an increased current density for small distances (small coupling) between coil and workpiece (see Figure 10, right), an thereby a more pronounced induction heating. Centric rotation of the workpiece during induction heating facilitates a homogeneous heating along the cross-section in case of inhomogeneous coupling.

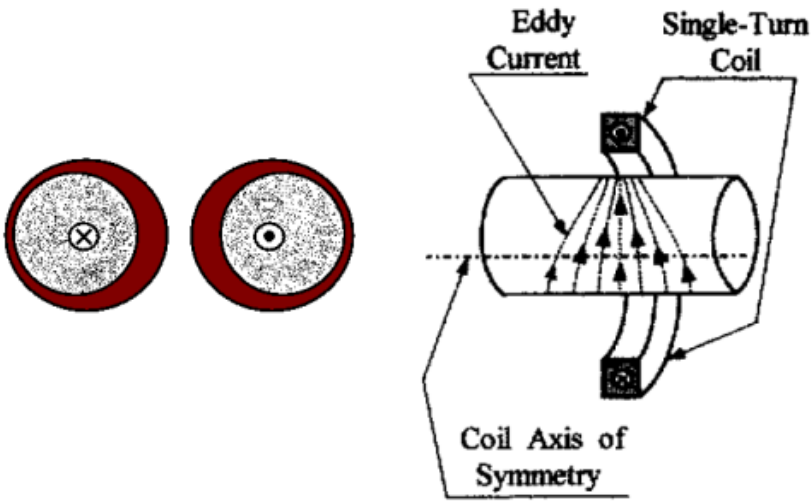

Figure 10: Proximity effect of two conductors with opposite direction of current (left) and its impact on inductive heating (right) [Rud03]

If the current carrying conductor has the shape of a ring or coil, the distribution of current changes as shown in Figure 11. The skin effect, the proximity effect and the ring effect leads to a comparably efficient induction heating of a workpiece located at the inside of a coil. The efficiency decreases if the workpiece is located at

the outside of the coil (bore heating) since ring effect and proximity effect are pushing the current in opposite directions.

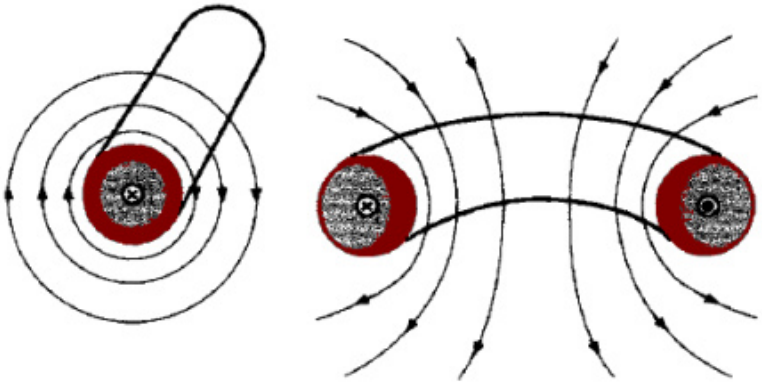

Figure 11: Ring effect of ring shaped conductor [Rud03]

The used frequencies for induction heating can be categorized as follows [Hwg09]:

- Low frequency range: 50 Hz – 500 Hz
- Medium frequency range: 500 Hz – 50 kHz
- High frequency range: 50 kHz – 3 MHz.

2.3.2 Basics of induction hardening

The above described induction heating leads to phase transformations within a heat treatable steel. The transformation kinetics can be followed with the help of time-temperature-austenitisation diagrams (TTA), as shown in Figure 12. The most relevant high temperature phase, the austenitic phase γ, and its chemical composition as well as its grain size determines to a great extend the properties of the hardened steel. The diffusion controlled processes during heating and soaking are strongly depended on time and temperature, which are:

- Phase transformations (Ferrite, Pearlite -> Austenite)
- Carbide dissolution
- Homogenisation of alloying elements
- Grain growth.

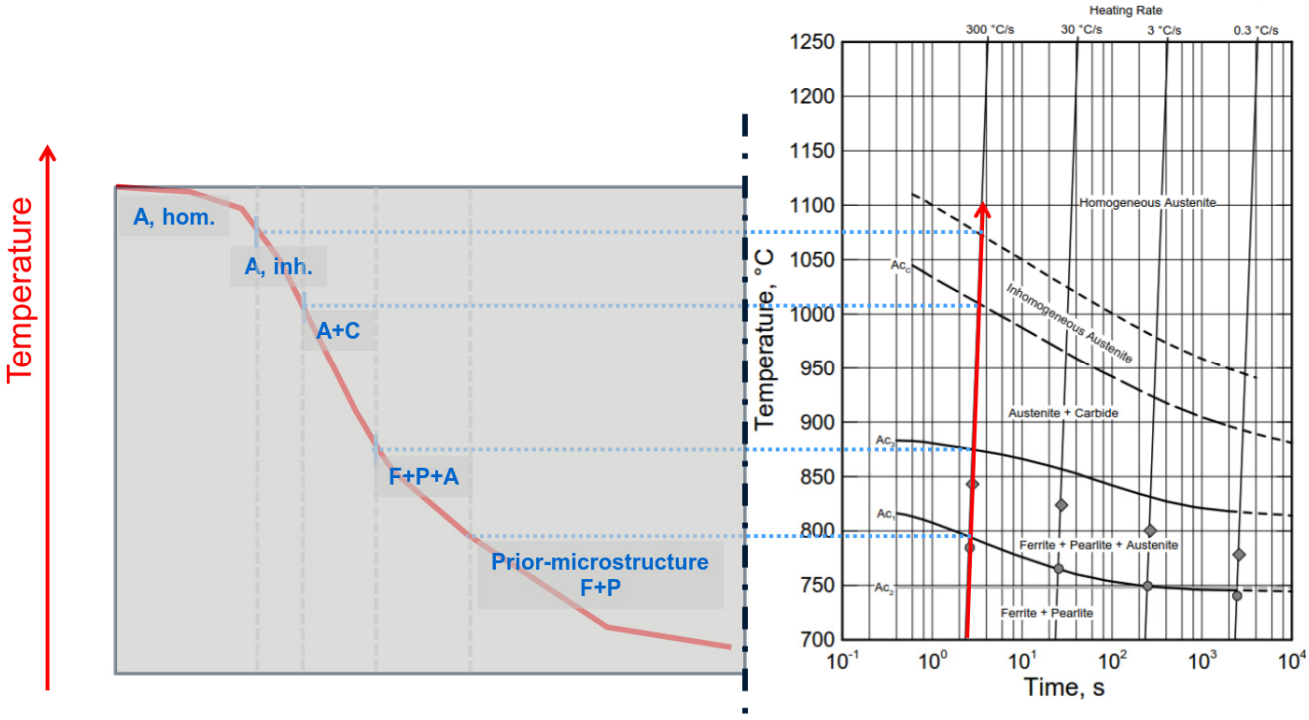

Figure 12: Typical radial temperature profile after induction heating (surface heating) and resulting phase distribution according to a TTA diagram; TTA from [Cla08]

Induction heating is followed by quenching of the heated component. Depending on the quenching intensity, the used steel grade as well as the history of heating (austenitisation conditions), the austenitic phase will transform into either martensite, bainite, pearlite, ferrite or will remain metastable after quenching. In case of severe quenching and no diffusion of alloying elements, austenite will transform mainly into the high strength phase martensite (see also Figure 13). In case of induction hardening, the presence of lower strengths, non-martensitic transformation products is generally unwanted, especially in areas of a component, which are highly loaded in operation.

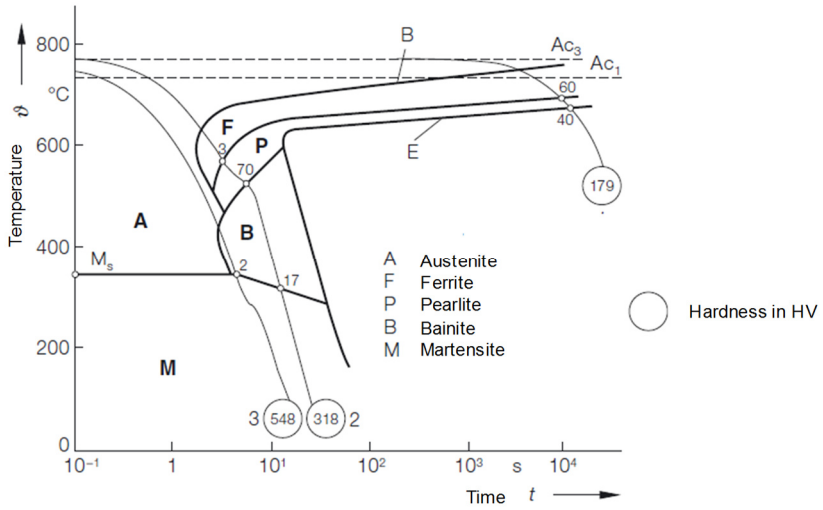

Figure 13: Continuous TTT diagram for a low alloyed steel with ~ 0,45 wt.-% carbon [Bar06]

Assuming a complete transformation of austenite into martensite during quenching, the below distribution of strengths or hardness and phase constituents will follow for the case of surface induction hardening (see Figure 14).

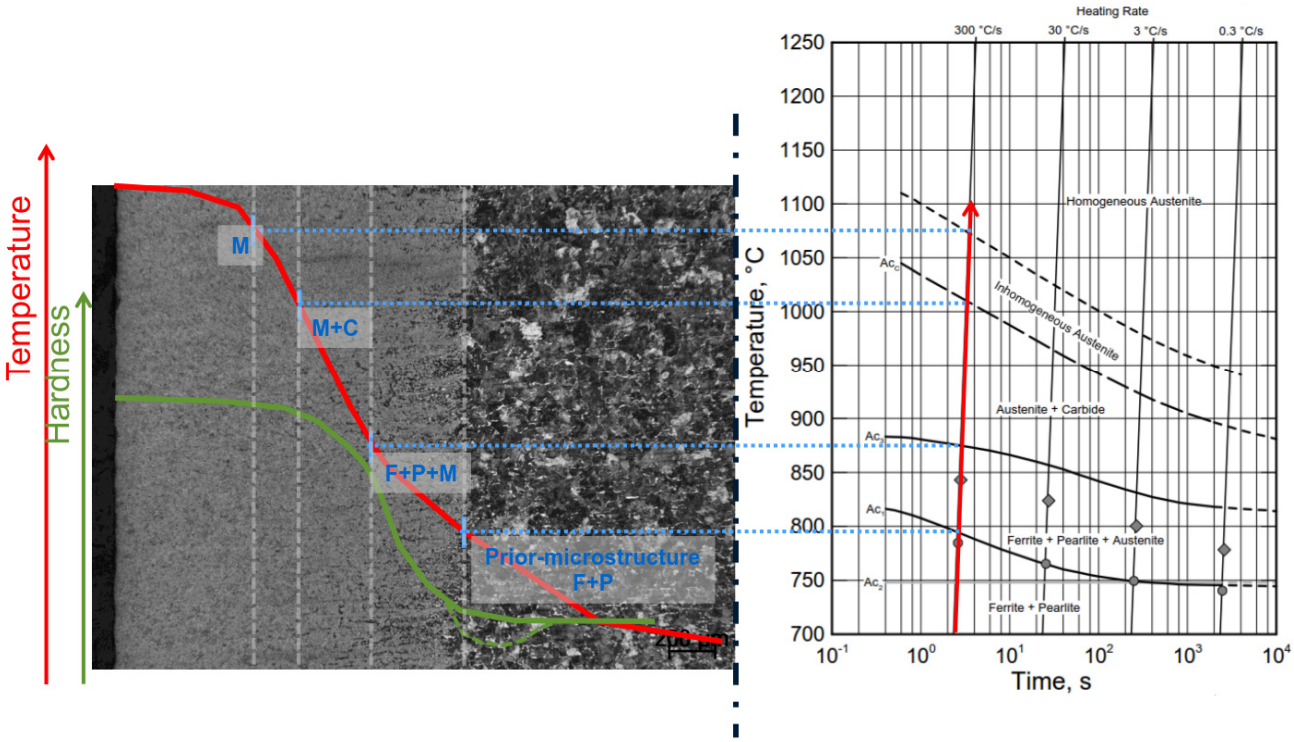

Figure 14: *Typical radial temperature profile and hardness profile after induction hardening (surface hardening) and resulting phase distribution according to a TTA diagram and assuming martensitic transformation of austenite; TTA from [Cla08]*

The diffusionless transformation of austenite into martensite is accompanied with a tetragonal distortion of the martensitic crystallographic lattice (distorted body centred cubic). Increased dissolved carbon contents in austenite lead to more severe lattice distortion and an increased specific volume. The severe distortion leads to plasticity, increased dislocation and twinning density and an increased hardness or strengths (see Figure 15 and Figure 16).

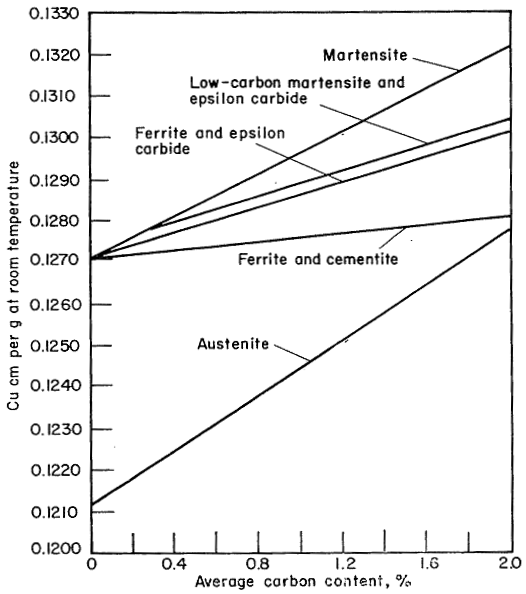

Figure 15: *Specific volume of different phases depending on carbon content [Lem59]*

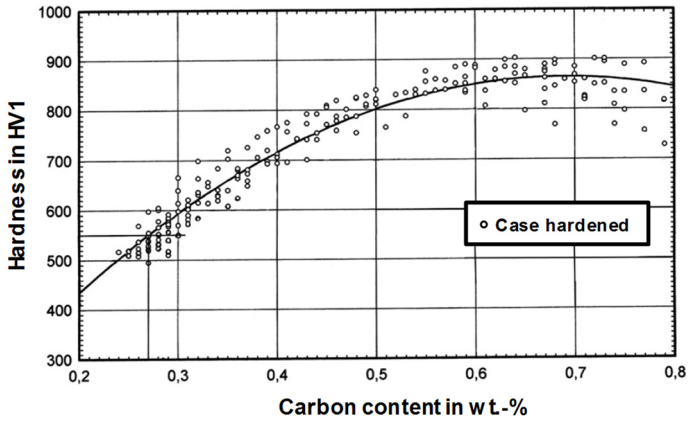

Figure 16: Martensite hardness depending on dissolved carbon content of case hardened samples [Kel01]

Martensitic transformation is often characterized by two distinct temperatures, the onset (martensite start temperature, M_S) and completion (martensite finish temperature, M_f) of martensitic transformation. Both temperatures are mainly affected by the dissolved alloy content and are generally lowered with increased alloy content (exceptions exist). A compilation of formulas for M_s calculation is given in [Kra03, Bes93]. The below example shows the strong effect of the dissolved carbon and manganese content, followed by nickel, chromium and molybdenum [And65]:

$$M_s\ (°C) = 539 - 423\ C - 30.4\ Mn - 12.1\ Cr - 17.7\ Ni - 7.5\ Mo. \quad (2)$$

Yang and Garcia-Junceda compiled earlier studies on the effect of prior austenite grains size on the M_S temperature [Yan09, Gar08]. They show that M_S can be lowered by a decrease in prior austenite grain size, see Figure 17. The effect is explained by different potential approaches including individual grain strengths and an increased resistance towards martensite formation and the accompanied plasticity or an impact of grain size on the nucleation density for martensite transformation. A discussion of the potential effects can be found in [Yan09] and [Gar08].

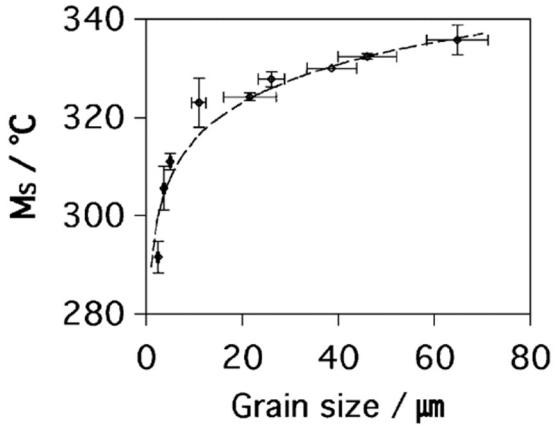

Figure 17: *Effect of prior austenite grain size on martensite start temperature M_s [Yan09]*

The steels carbon content also affects the martensite morphology and thereby the mechanical properties, see Figure 18. Lath martensite consists of fine units aligned in a parallel way. With increased carbon content the share of so called plate martensite will increase. Plate martensite has the tendency to form microcracks, especially for larger plates formed in larger prior austenite grains having different orientations in a non-parallel way. The material toughness decreases towards increased shares of brittle plate martensite [Kra09].

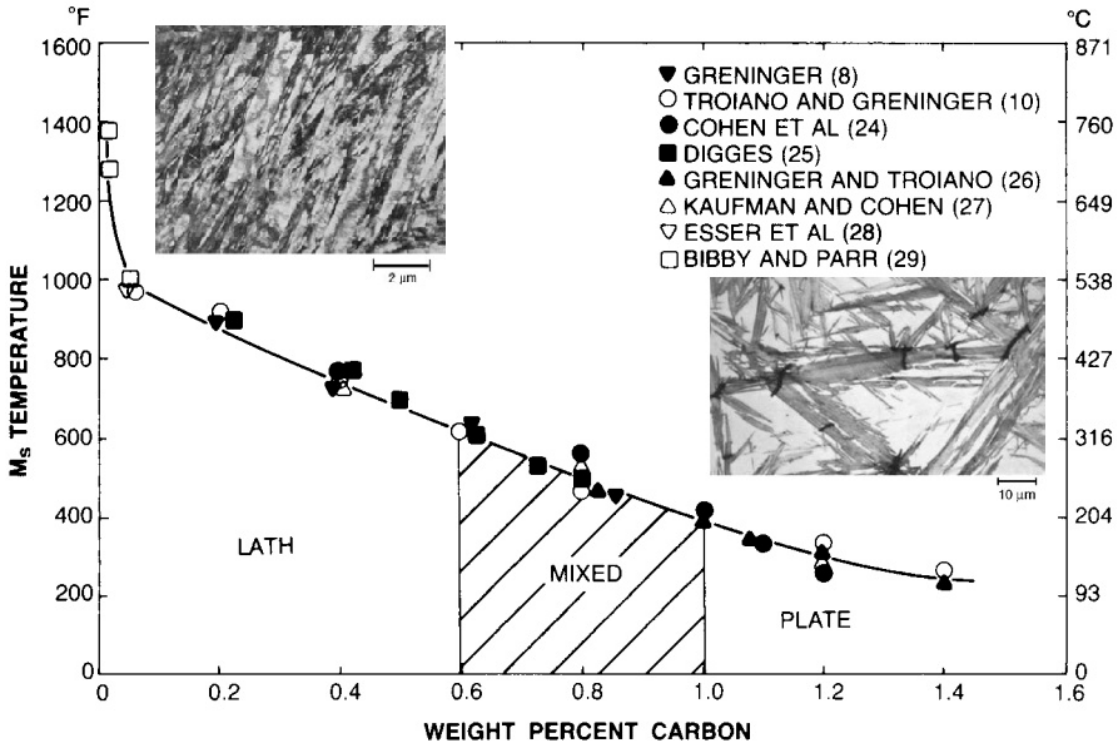

Figure 18: *Martensite morphology and martensite start temperature M_s as a function of carbon content [Kra03]*

If a component is quenched to temperatures above M_f temperature, metastable austenite remains (retained austenite). Subsequent heating to temperatures of 160 °C and above (by either tempering or temperatures in operation) or mechanical stresses can lead to a later decomposition of retained austenite. Such decomposition of retained austenite during operation can lead to unwanted dimensional changes and presence of brittle, non-tempered martensite. That is why the retained austenite content for bearing components is limited to a maximum level or retained austenite is mechanically, chemically or by its morphology stabilised to avoid transformation.

The effect of dissolved carbon on martensite hardness and on the presence of retained austenite (low strength) after quenching leads to maximum as quenched hardness at about 0.65 to 0.75 wt.-% carbon for most bearing steels.

2.3.3 Influence of alloying on induction hardening response

Induction heating or hardening processes are mostly characterized by shorter processing times and higher temperatures compared to conventional heating methods. The limited time at elevated temperature results in lower degrees of homogenization compared to furnace heating, especially for slower diffusing, substitutional dissolved alloying elements. The alloying itself as well as the distribution of alloying elements within the microstructure prior to induction heating play therefore an important role for the hardening result. The solubility and diffusivity of carbon or other alloying elements are decreased by the presence of alloying elements like chromium, hindering a fast austenitisation [Sch68, Smi00, Gar81, Pax67, Bes87]. Therefore, the use of steels alloyed with high amounts of, for example, chromium, molybdenum, or vanadium is questionable from a heating response perspective. They diffuse slowly, dissolve preferably to a large extend within stable carbides increasing their stability and slow down the diffusion of, for example, carbon. However, elements like chromium or molybdenum increase hardenability and stable carbides provide grain growth control.

The steels chemistry, as well as its prior microstructure, affects the phase transformation from ferrite to austenite during austenitisation. The effect of alloying elements on the onset and completion of the transformation to austenite are described in literature [Rud03, And65] (carbon content C < 0.6 wt.-% for A_{c3}):

$$A_{c1}\,(°C) = 723 - 10.7\,Mn - 16.9\,Ni + 29.1\,Si + 16.9\,Cr + 290\,As + 6.38\,W \quad (3)$$

$$A_{c3}\,(°C) = 910 - 203\,\sqrt{(C)} - 15.2\,Ni + 44.7\,Si + 104\,V + 31.5\,Mo + 13.1\,W. \quad (4)$$

A low temperature for the completion of ferrite to austenite formation at A_{c3} is seen as advantageous for induction hardening due to:

- Lower peak temperatures or shorter soaking/ heating times needed
- Less energy needed
- Less grain growth and surface oxidation/ degradation
- Less distortion
- Longer times for dissolution and homogenization in the austenitic regime
- Easier increase in surface hardening depth if heating time or heating power constraint present.

Thermocalc (TCFE8 database) was used to calculate the general effect on A_{c3} temperature for the steels used in this investigation. 100Cr6 steel is shown as a representative example below (see Figure 19). Silicon, chromium as well as manganese, nickel and carbon were identified as the most influential elements.

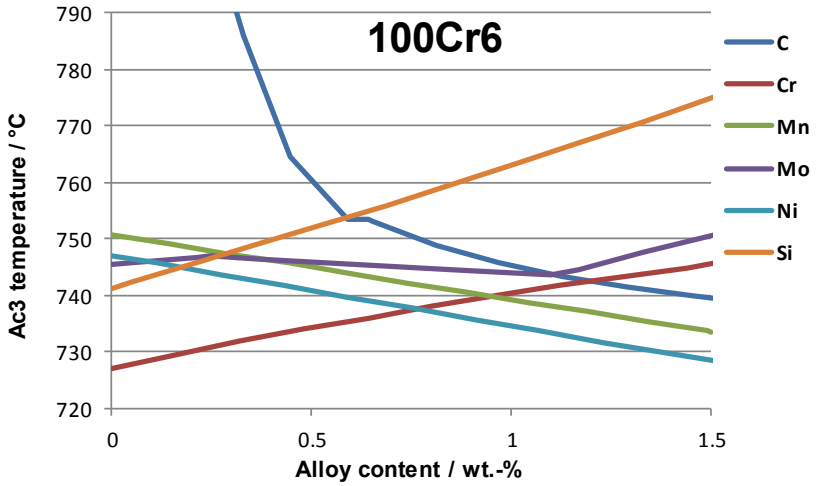

Figure 19: Effect of alloy content on A_{c3} temperature (thermodynamic equilibrium) of 100Cr6; calculated by thermocalc

The focus for the present investigation was put on the alloying elements carbon, silicon and manganese due to before mentioned and the following reasons:

Table 2: Motivation for the alloying strategy

Alloying element	Motivation
C > 0.5 wt.-%	➔ Sufficient hardness/ strengths ➔ Fast austenite transformation kinetics for higher C contents as shown in [Eck69, Sch59] ➔ Residual carbides for grain size control and stable heat treatment process window [Bes87]
Si	➔ Cost effective alloying element, low probability of future scarcity [Wou09, Die09] ➔ Dissolves in ferrite matrix providing “fast” hardenability and solid solution hardening ➔ Does not have a large influence on lowering M_s temperature (minor impact on retained austenite level and minor impact on cracking probability during quenching) ➔ Provides tempering resistance, retaining hardness after tempering and reducing hardness drop at transition zone (hardened surface – soft core) ➔ Increased rolling contact fatigue performance of Si alloyed bearing steels [Kim12, Cla14, And12, Nak08] ➔ Provides retained austenite stability [Kim12, Sid15] without promoting it
Mn	➔ Cost effective alloying element ➔ Dissolves to a large extend in ferrite matrix, depending on prior heat treatment, providing “fast” hardenability (e. g. share of 66 % dissolved in ferrite for a soft annealed 100Cr6 [And93]) ➔ Lowers A_{c1} and A_{c3} temperature, accelerates austenitisation [Bai39, Eck69]

Medium and high carbon (bearing) steels with modified silicon and manganese contents were selected for the present investigation.

2.3.4 Influence of prior microstructure on induction hardening response

Beside the steel's chemical composition, its prior structure before induction hardening plays an important role for the kinetics during heating and austenitisation and the subsequent quenching process. In general, it can be stated that coarse microstructures with big grains and long diffusion or carbide/cementite distances like soft annealed structures (SA) are unfavourable from an induction hardening point of view. They require longer diffusion distances and lead in general to higher transformation temperatures or longer times until transformation is completed and a homogenized austenite is formed [Cla08, Smi00, Sch74]. High temperatures and long times for austenitisation might lead to undesired hardening results including grain growth, coarse martensite, large transition zones, surface damaging like decarburization and distortion [Rud03].

Microstructures with small grain sizes and fine distributions of carbides and cementite, such as quench and tempered (QT) or bainitised structures, show advantageous hardening response. They assure a fast heating response and allow a reduction of temperature or time resulting in less energy consumption, less grain growth, surface damaging and distortion, possibly higher hardness and a deeper hardened case. Surface hardened components with QT prior microstructures also show narrow transition zones, high core hardness but less core toughness as compared to soft annealed (SA) prior microstructures [Rud03].

However, it is not only the heat treatment deciding the proper starting structure. Earlier steps in the manufacturing chain like cold forming (e.g. rolling) or machining (e.g. turning/ drilling) request a microstructure which provides good formability and/ or machinability such as a soft annealed structure in general does. A balance between heating response and related properties on the one hand (case and core) and costs for the prior microstructure and its machining and/ or forming in earlier production steps (e.g. soft machining, rolling) on the other hand needs to be considered. As a good compromise, quench and tough tempered starting structures (approximately 280 HV - 400 HV) are common practise.

Chemistry, prior microstructure and prior processing also affect the steels magnetic and electrical properties which in turn impact the induction hardening result [Rud03, Boz93]. Those aspects will not be given attention here.

2.4 Rolling contact fatigue testing of bearing steels

Among other factors, bearing life is governed by its materials rolling contact fatigue resistance. High contact pressures and numerous load cycles in the range of several millions lead to accumulation of damage at the surface or in a subsurface region, where the mechanical stresses reach a critical value. The accumulated damage can eventually lead to crack initiation, crack growth, loss of material and failure of the bearing. The presence of stress raisers can accelerate and trigger the fatigue process. Stress raisers can be present in the material (steel making, non-metallic inclusions, pores, carbides), can originate from the bearings environment and tribological conditions (wrong lubricant type, lubricant contaminations), from earlier manufacturing steps (machining, scratches, rough surfaces, induced residual tensile stresses), from the bearing design (wrong/ no crowning of raceway), or from wrong bearing mounting and operation, see also Figure 20. A materials weakening due to, for example, high operating temperatures, corrosion or hydrogen pickup can as well lead to accelerated fatigue.

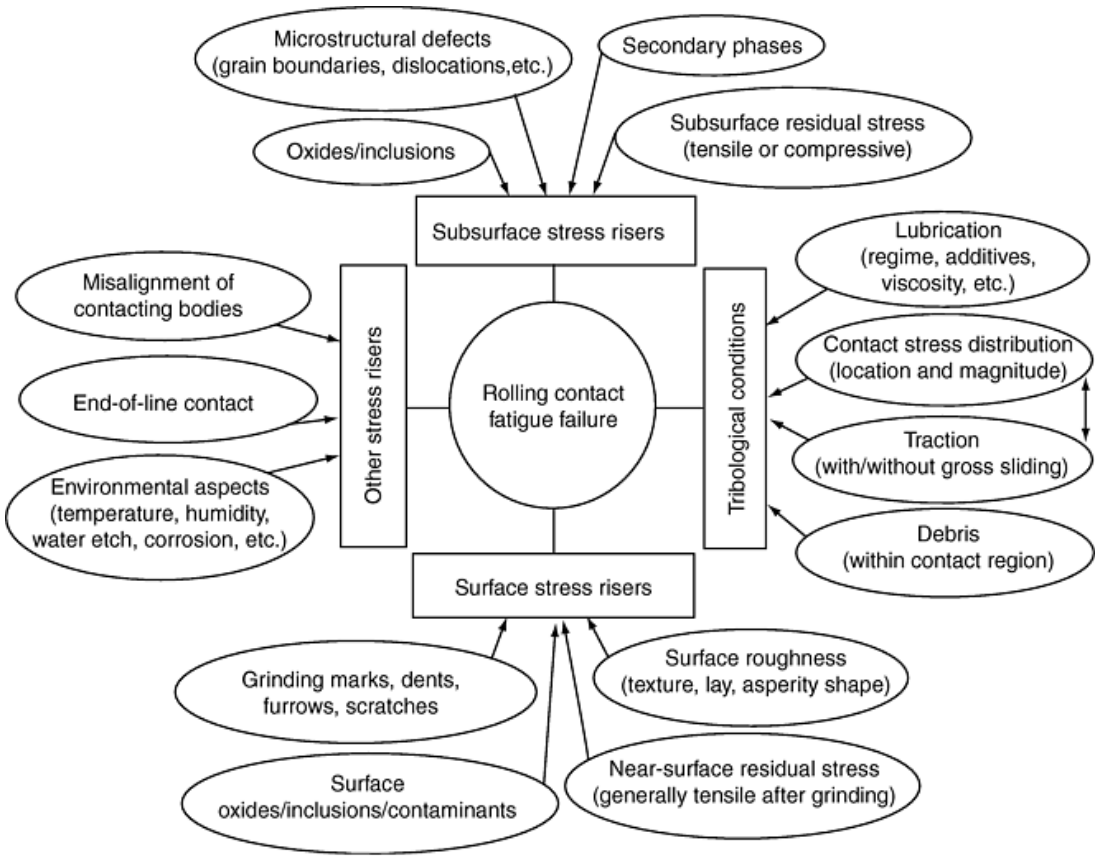

Figure 20: Influencing factors on rolling contact fatigue life [Ahm02]

2.4.1 Hertz contact

The stress state in case of a rolling contact can be approximated using Hertz theory [Her81]. Hertz described the deformation and resulting stress distribution in the contact area of two elastic solids, considering a small, generally elliptical contact area in regard to the bodies in contact, and the absence of friction. Assuming a contact ellipse with two semi axes a and b (see also Figure 21) and the maximum contact pressure p_0, the contact pressure is given by Johnson in [Joh03]:

$$p(x,y) = p_0\sqrt{1-(x/a)^2-(y/b)^2}. \tag{5}$$

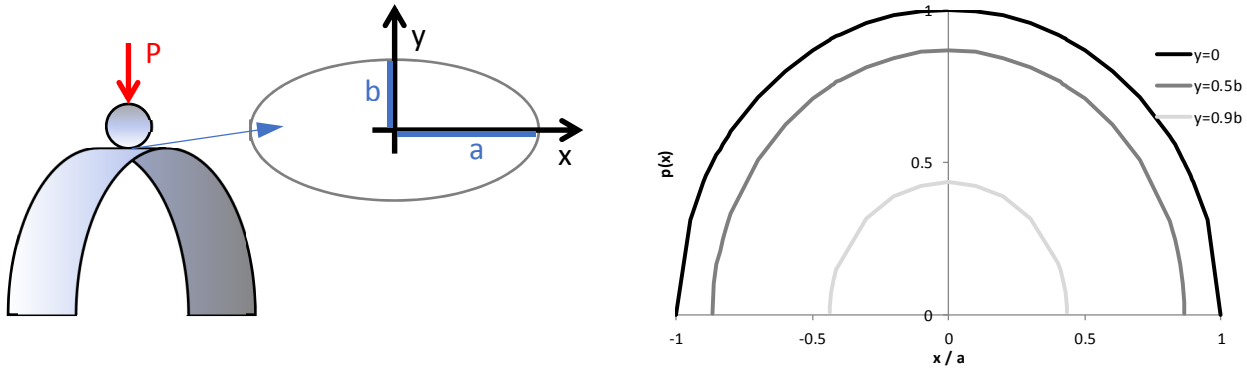

Figure 21: Two curved bodies in contact with an applied contact load P resulting in an contact ellipse with two semi axis a and b (left) and a contact pressure distribution p(x,y) of ellipsoidal shape (right)

For the simpler case of the contact of two cylindrical bodies with their axis lying parallel being sufficiently long (b >> a, see also Figure 22), the problem becomes two-dimensional and the distribution of the contact pressure is given by:

$$p(x) = p_0\sqrt{1-(x/a)^2}. \tag{6}$$

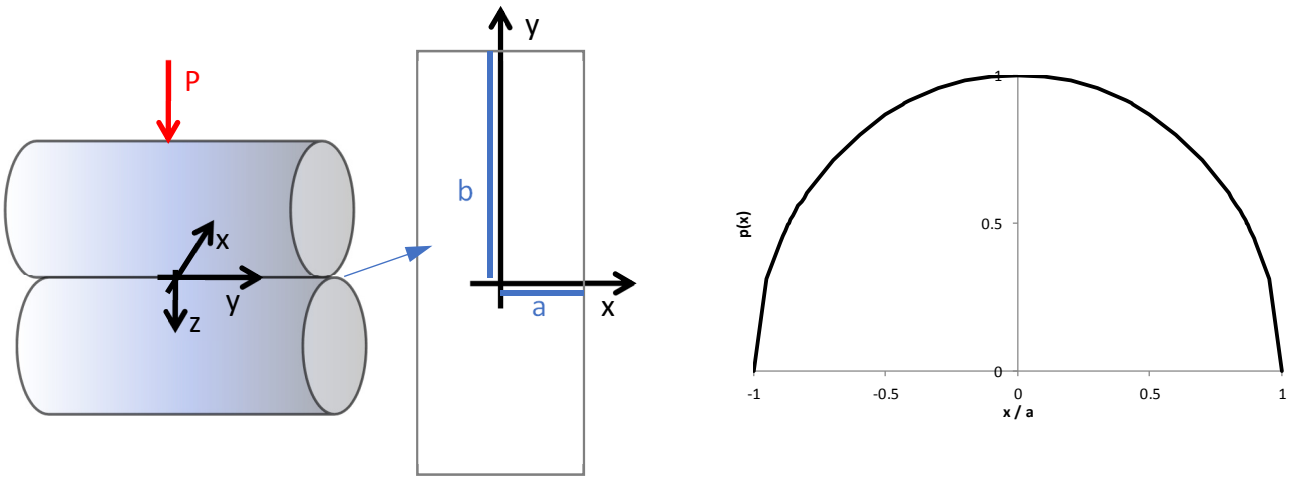

Figure 22: Two cylindrical bodies in contact with an applied contact load P resulting in a contact pressure distribution p(x) of ellipsoidal shape (right)

The maximum contact pressure p_0 can be calculated using the contact load P, as well as the cylinders radii R_1 and R_2, the cylinders E- moduli E_1 and E_2 and their Poisson's ratios ν_1 and ν_2:

$$p_0 = \sqrt{PE^*/\pi R^*} \tag{7}$$

where

$$E^* = [((1-\nu_1^2)/E_1) + ((1-\nu_2^2)/E_2)]^{-1} \tag{8}$$

and

$$R^* = (1/R_1 + 1/R_2)^{-1}. \tag{9}$$

For the centre point of the cylinders` contact area, the point of highest maximal contact stresses, the stresses in x-, y- and z-direction are principal stresses and are given in [Joh03]:

$$\sigma_x = -{p_0}/{a}\left[\frac{a^2+2z^2}{\sqrt{a^2+z^2}} - 2z\right], \tag{10}$$

$$\sigma_z = -{p_0}/{a}\left[\frac{1}{\sqrt{a^2+z^2}}\right], \tag{11}$$

$$\sigma_y = \nu(\sigma_x + \sigma_z). \tag{12}$$

For the principal shear stress τ_1 follows:

$$\tau_1 = \frac{1}{2}(\sigma_x - \sigma_z) = -{p_o}/{a}\left[z - \frac{z^2}{\sqrt{a^2+z^2}}\right]. \tag{13}$$

The development of the principal stresses perpendicular to the contact area (z-direction) in the centre point is shown in Figure 23. The highest principal shear stress $\tau_{1,\,max}$ = 0.3 p_0 develops at a depth of z=0.78 a.

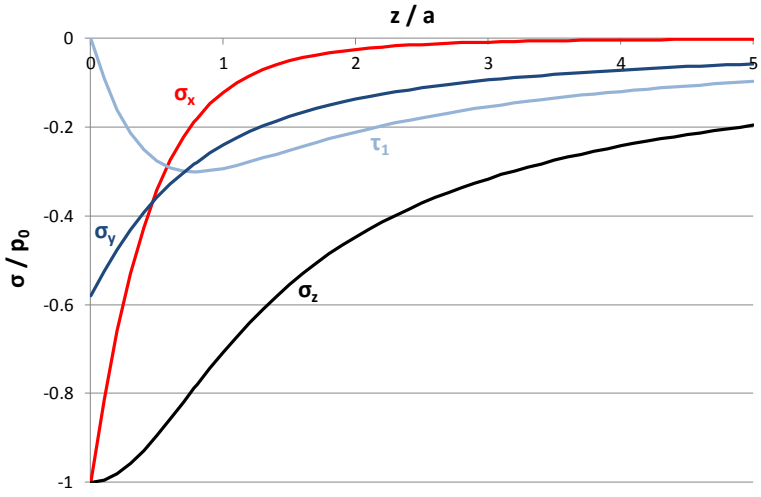

Figure 23: Principal stresses for contact of two cylindrical bodies with parallel axis

The calculation of general elliptical point contacts can be found in the work of Johnson [Joh03] with the help of elliptic integrals. Depending on the ratio of the ellipse semi axes a and b, the depth and magnitude of $\tau_{1,\,max}$ varies.

2.4.2 Tribological conditions

The above described, idealised stress state within bodies exposed to rolling contact is affected and changed by a number of factors. The tribological system plays a major role and affects the systems friction, its wear, and alters the bodies stress state. A good shape and roughness of rings and rolling elements, no or limited slip in the contact area, appropriate lubricants, appropriate running conditions (rpm, forces, temperature) are just a few examples of favourable tribological conditions.

In the bearing industry, the use of the specific lubrication film thickness λ is widely used to describe the friction conditions. The definition of λ is inconsistent and can be given as:

$$\lambda = \frac{h_{min}}{1/2(R_{a1}+R_{a2})} \text{ [Muh07] or } \lambda = \frac{h_{min}}{\sqrt{RMS_1^2+RMS_2^2}} \text{ [Hyd96],} \tag{14}$$

where h_{min} is the minimum lubricant film thickness in contact, R_{a1} and R_{a2} are the average roughness of the surfaces in contact and RMS_1 and RMS_2 the respective root-mean-square roughness. The minimum lubricant film thickness for fully flooded conditions and point contacts was described by Hamrock and Dowson [Ham76]:

$$h_{min} = R` \left[3.63 \left(\frac{\eta_0 u}{E`R`}\right)^{0.68} \left(\frac{E`}{p_{iv,as}}\right)^{0.49} \left(\frac{F}{E`R`^2}\right)^{-0.073} \left(1 - e^{-0.68\frac{a}{b}}\right)\right], \tag{15}$$

where

R` = effective radius of bodies 1 and 2 with radii R_1 and R_2 = $\frac{R_1 R_2}{R_1+R_2}$, (16)

η_0 = atmospheric viscosity,

u = surface velocity,

E` = $2\left[\left(\frac{1-\nu_1^2}{E_1}\right) + \left(\frac{1-\nu_2^2}{E_2}\right)\right]^{-1}$ with ν and E being Poisson's ratio and E-modulus of bodies 1 and 2, (17)

$p_{iv, as}$ = asymptotic isoviscous pressure = 1/α, α being the pressure-viscosity exponent,

F = normal load,

a, b = major (a) and minor (b) axis of contact ellipse.

Depending on the value of the specific lubrication film thickness λ, different amounts of friction, wear and wear mechanisms are present. It is obvious that for lower values of λ more and more solid-to-solid contacts will be present and the amount of friction and surface distress will be bigger. The contact fatigue life will decrease with decreasing λ [Hyd96]. Most authors state that a full separation between the two bodies in contact will be present from λ ≥ 3 [Czi08, Muh07]. Dowson recommends in [Dow95] a value of λ > 1.5..2 for major improvements in life for roller bearings.

In most bearing applications elastohydrodynamic (EHD) lubrication conditions are favoured, where rolling surfaces are separated by the lubrication film. Figure 24 shows the stress distribution of EHD contact conditions. Calculations and measurements showed that the stress distribution undergoes a second maximum close to the lubricant outlet of the contact, followed by a sharp drop. The stress development

causes the surface in contact to deform at the outlet, where the smallest lubrication film thickness h_{min} (~ 80 % of $h_{central}$) is to be expected [Dow95].

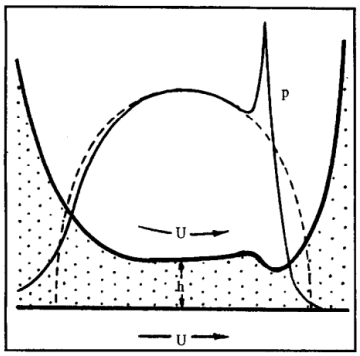

Figure 24: Hertzian pressure and pressure distribution in an EHD contact [Dow95]

2.4.3 Material reaction towards rolling contact fatigue

"The change in the structure, which is caused by the repeated stresses developed in the contacts between the rolling elements and the raceways, is described as fatigue" [ISO15243]. It can be distinguished between surface initiated and subsurface initiated fatigue.

Surface initiated fatigue (surface distress) is caused by excessive mechanical stresses at the over-rolled surface and can lead to asperity microcracks, asperity microspalls and microspalled areas. Reasons can be various, such as high sliding ratios, improper lubrication conditions, indentations by foreign particles, and others [ISO15243].

Subsurface fatigue is driven by Hertzian stresses which reach their maximum below the contact surface. The initiation of microcracks and cracks, as well as microstructural changes are observed and microcracks can grow and propagate towards the surface causing material loss (flaking, spalling, pitting, etc.). In the following the focus will be on subsurface fatigue.

The repetitive material loading during rolling contact leads to accumulation of microplasticity in the material. Different changes are observed as a response to the cyclic loading:

- Changes in etching response
- Changes in X-ray diffraction response (residual stresses, FWHM, retained austenite)
- Changes in hardness
- Changes in microstructural texture
- Grooving, plasticity
- Changes in carbide morphology.

The mentioned changes do not occur at the same time and do not develop in a linear way. Voskamp defines three stages of material behaviour during rolling contact fatigue, considering microplasticity, work hardening, residual stresses, decay of retained austenite, martensite and cementite, component growth and texture

development [Vos92, Vos97]. The occurrence of the three stages depends on the number of exposed load cycles and on the contact pressure (see also Figure 25). The shakedown stage, discussed in detail by Merwin et al. in [Mer63], is characterized by an initial change of the mentioned. Especially the occurrence of microplasticity, retained austenite decay, work hardening, and build-up of residual stresses were measured until the shakedown limit is reached and no alterations are observed during the second stage (steady-state). However, small changes on an atomic scale and accumulation of energy as a consequence of the cyclic loading and hysteresis, leading to short distance carbon diffusion, are suspected to take place [Vos92]. Stage 3 (instability) is characterized by a continuous change of the mentioned until failure. A further energy accumulation by the loaded microstructure is not possible and leads to a decay [Vos92]. From the authors observations, a correlation between material decay and component life or failure probability can be derived. Generally it can be concluded that the rolling contact fatigue life is governed by the microstructural stability of the matrix.

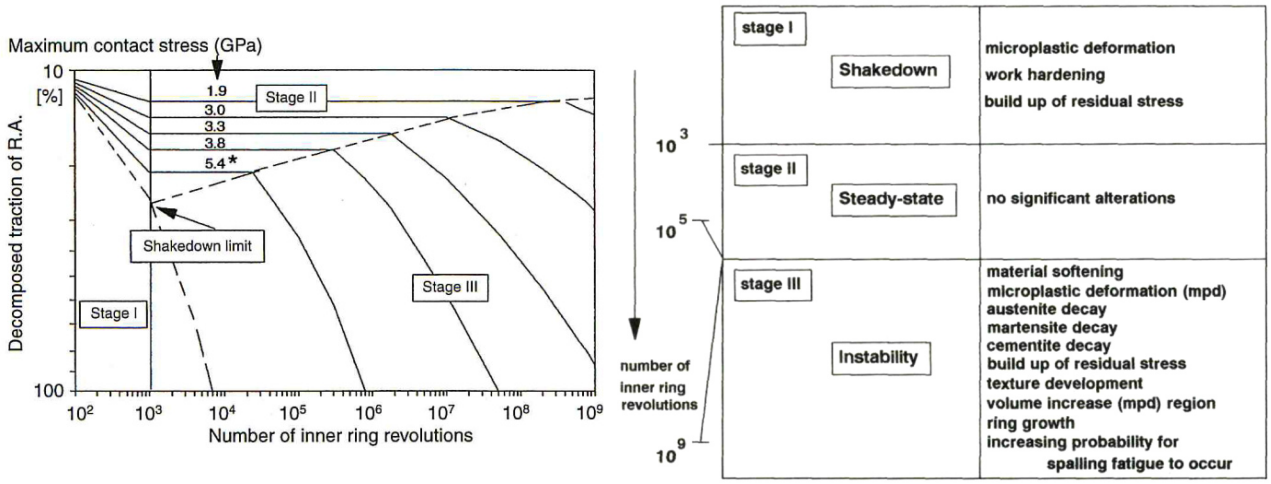

Figure 25: Schematic presentation of the three stages in material response pertaining to the subsurface volume at 0.2 mm below the ball track in a 6309 type deep groove ball bearing inner ring, indicating the alterations occurring in these three stages [Vos69]

In order to carry out RCF testing in a time and cost-efficient way and avoid full scale bearing testing, different RCF testing rigs have been developed. The use of high contact pressures, fast rotation, and elevated temperatures shall lead to accelerated fatigue response.

2.4.3.1 Etching response

Bearing steels react with several microstructural changes when exposed to cyclic rolling contact. These changes can be made visible when the stressed material volumes are etched with standard etching agents (e.g. diluted nitric acid HNO_3). Non- or lighter-etching constituents, such as white etching areas (WEA), butterflies, white etching bands (WEB), and dark etching areas (DEA) in bearings were observed in literature [e.g. Swa76, Fur96, Vos96, Gen65, Lit66].

The mentioned features appear at different times in components fatigue life and their appearance is stress depended, see Figure 26 and Figure 27 [Swa76, Fur96]. The first feature to observe are in general butterflies, followed by dark etching areas, 30° white etching bands and 80° white etching bands. In connection with early failed bearings in wind mill gear boxes so called white etching cracks (WEC) and white structure flaking (WSF) were reported as well. These appearances were observed at very early stages of the fatigue life (e.g. 1-10 % of L_{10} life, L_{10} = life at which statistically 90 % of bearings survive) and will not be given attention here [Eva12].

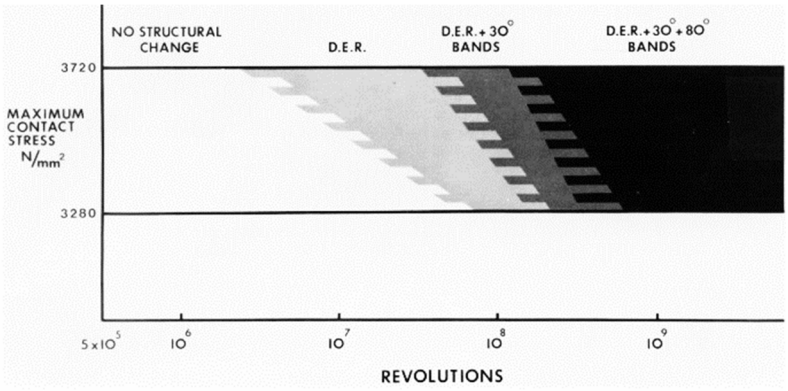

Figure 26: *Structural changes obtained as a function of stress level and increasing number of cycles; not all changes do necessarily appear [Swa76]*

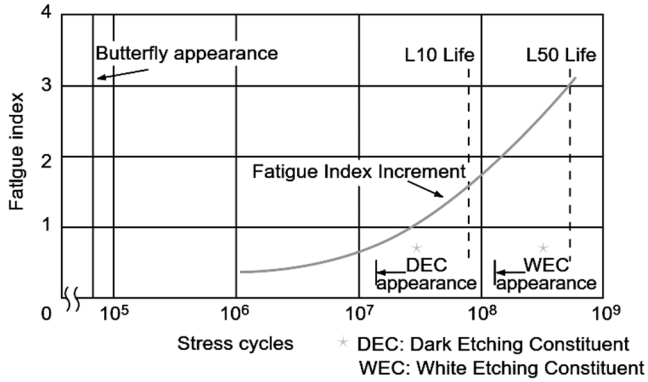

Figure 27: *Schematic diagram of microstructural alteration in rolling contact fatigue (3.4 GPa, deep groove ball bearing) [Fur96]*

White etching features, white etching matter or white etching areas (WEA) have been reported as a response to rolling contact fatigue by numerous authors (see following references). White etching describes the light or non-etching response to etching agents such as Nital (diluted nitric acid HNO_3), so that those material volumes appear as white regions in the light optical microscope. Depending on the appearance and features, the nomenclature can be different.

Butterflies were named after their appearance which resemble the shape of butterflies. They generally consist of two, wing shaped white etching areas (butterfly wings) with a non-metallic inclusion or pore in their middle (butterfly body), see Figure 28.

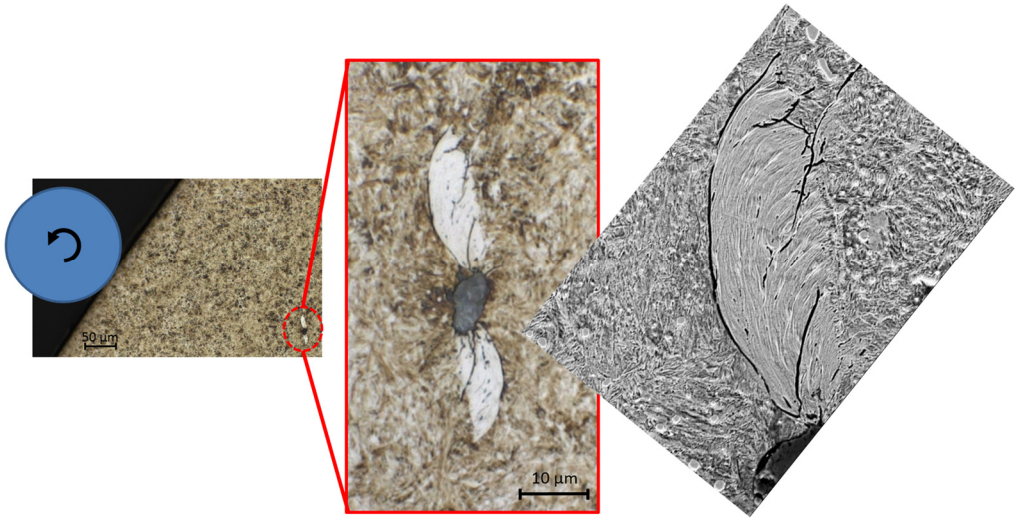

Figure 28: Butterfly after 1.5 million load cycles with 5.5 GPa contact pressure in a 100Cr6 steel; etched with 1.5% Nital 25 seconds

Sub-surface butterflies were found in components, loaded with high hydrostatic pressure and shear stresses, such as rolling contact stresses. The main characteristics are:

- The white etching areas in bearing steels were found to be carbide depleted or carbide free [Gra10b, Bri66, Swa76, Sug70, Öst82, Bri88] and exhibit a higher hardness than the surrounding matrix [Gra10b, Loy73, Ost82, Bea57, Sto63, Mar66, Sch68, Bor69, Mur70, Man70, Bec81, Lun10]. A recent work on bainitic 1C-1.5Cr wt.-% steel has revealed the existence of soft white etching matter and lower carbon content as compared to the matrix [Alv16]
- Butterflies often show an inclination angle of 40° - 45° in respect to the rolling contact surface [Sug70, Gra10b, Gra10a, Gra07, Mar66, Sch68, Bec81, Öst82]; the wing orientation is also connected to the rolling direction [Man70, Bec81]
- Microcracks are found, ranging from the non-metallic inclusion/ pore to the tip of the wing; the wings have a smooth side with a clear boundary to the adjacent matrix and a feathery side; the wing facing towards the raceway has its smooth side on top/ towards the raceway [Bec81, Sug70]
- The majority of butterflies were found to be located near the depth of highest shear stresses (z_0 depth) [Gen65, Sto63, Mar66, Veg10, Geg11, Sch68] but also considerably deeper [Bec81]
- The number and area of butterflies and their white etching matter increases with an increasing number of load cycles [Sug70, Sch68, Man70, Lit66, Lun10] and depends on the stress conditions [Lit66, Mar66, Sch68, Lun69, Fur96, Lun10, Öst82]; they are known to be able to appear at < 10^5 load cycles [Bha15, Fur96] and can be seen as first signs of fatigue damage; the presence of hydrogen promotes early butterfly/ white etching matter and crack initiation, like in e.g. [Veg10]
- Stress raisers such as non-metallic inclusions facilitate the generation of butterflies. Depending on the type and connected mechanical properties, its geometry as well as its bonding to the matrix, the probability for butterfly initiation is different [Lit66, Öst82]; the existence of a microcrack is seen to be a prerequisite for butterfly formation for some authors [Geg11, Sug70], others assume a cooperative crack growth and butterfly wing formation [Gra10a, Bec81]

- Diffraction patterns of white etching matter have revealed a crystalline structure, consisting of nano-sized grains of ferrite [Bri66, Mar66, Man70, Gra07, Bec81, Öst82]; the segregation of silicon and carbon within a WEA formed along a crack has been shown [Kan13].

Butterfly generation mechanisms are discussed controversially. They can appear early in component life (Figure 27) and initiate at different types of non-metallic inclusions (see Table 3), whereas alumina and mixed alumina-sulfide inclusions are often seen as most harmful for their initiation [Sug70, Bec81, Mar66, Lun10], see Figure 29, Figure 30 and Table 3. Grabulov observed in a SEM and TEM study on 52100 steel with artificially introduced, fully debonded Al_2O_3 particles three different stages of butterfly formation and growth [Gra10b, Gra10a] and proposes the following sequence:

1) Steel matrix adjacent to the inclusion locally acquires accumulated micro-plastic damage during interaction with the inclusion (cyclic, small scale rubbing movement) and atomistic scale material transfer from the matrix to the inclusion can take place; deposited material volume contains numerous crystal defects and stores high energy far from equilibrium
2) Dynamic recrystallization of deposited, high energy material volume and continuing material transfer from matrix to inclusion; recrystallized material volume consists of nanometer sized ferrite; porosity in recrystallized seam may result from condensation of vacancies; the gap between inclusion and steel matrix moves towards the interface between the deposited and recrystallized material volume on the inclusion and the undamaged steel matrix
3) Ongoing material transfer and recrystallization leads to migration of the interface further into the matrix by repeated diffusion bonding/ debonding (growth of crack like feature); the recrystallized material grows accordingly in a cooperative manner and builds an early butterfly wing.

According to the author, the butterfly formation or initiation takes place during the majority of fatigue life until the crack reaches a critical size and it can be described by standard crack growth models. One important detail is the hypothesis, that the matrix plastic damage is governed by creep-like micro-plasticity. The creep mechanism is characterized by dislocation climb and controlled by the density of mobile free vacancies and Iron self-diffusion. The creep mechanism would make the process kinetically controlled and be influenced by, e.g. temperature, time and matrix alloying.

Earlier studies from Österlund [Öst82] already proposed a dynamic recrystallization mechanism due to stress concentration and increased dislocation densities at inclusion/ matrix interfaces. Grain growth of the recrystallized grains as well as work hardening would proceed. Österlund believes that the hard and brittle butterfly wings won´t be able to yield upon further stressing and could be preferred nucleation sites for cracks. In that case, a microcrack would follow the butterfly wing and would not form simultaneously.

Other authors, such as Schlicht in [Sch73], assume that the white etching matter in butterflies is generated by local and fast heating/ austenitisation due to severe plastic deformation. Existing carbides dissolve in the plastically deformed austenite and a martensitic microstructure is creating after quenching due to heat diffusion.

Table 3: List of inclusion type and occurrence associated with butterfly formation [Sug70, ASM96]

Type of nonmetallic inclusion	Appearance of nonmetallic inclusion	Frequency of Butterflies
MnS	Elongated (< 3 µm)	Rare
	Elongated (> 3 µm)	Few
	Very thin and long	None
Al_2O_3	Finely dispersed stringers	**Many**
TiN		None
MnS + Al_2O_3		**Many**

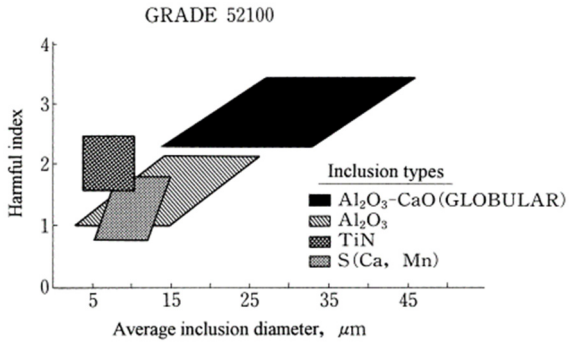

Figure 29: Harmful index of various inclusions (the ordinate scale unit is a decrease in fatigue strength of 125 MPa at N = 10^8) [Mur02, Mon88]

Lund examined butterflies and microcracks in tested spherical roller bearings (loaded with 5 GPa) as well as failed bearings from the field. He found that the majority of butterflies were generated at complex oxy-sulfide inclusion, where the oxides were mostly encapsulated by the sulfide inclusions being locally still in contact with the matrix [Lun10], see Figure 30.

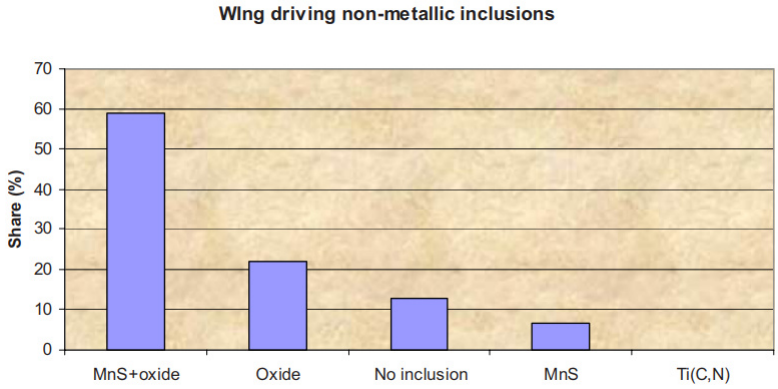

Figure 30: Statistical evaluation of microcrack and butterfly initiating non-metallic inclusions of run bearings from field [Lun10]

Dark etching regions or areas (DER, DEA) can generally appear after the formation of butterflies and before white etching bands form [Swa76, Fur96]. They were first mentioned by Jones in 1946 [Jon46]. The appearance of DEAs is stress and load cycle depended [Swa76, Vas72, Lun69], as well as operating temperature and heat treatment depended [Vos96, Bus61, Mar66, Mur70] and its area increases with contact pressure and number of load cycles [Sug70, Vos96, Zwi80, Sch68, Lun69, Gen65, Bus62]. DEAs do not extend until the contact surface and the shape in a circumferential section of a ran bearing ring (see Figure 31) resembles the shape of a typical subsurface stress field due to rolling contact [Vos96, Tal67]. The depth of the first appearance was found to coincide with the depth of highest induced shear stresses [Vos96, Swa76, Gen65, Sug70].

DEAs were observed to consist of heavily deformed ferrite and martensite [Vos96, Swa76], whereas ferrite is reported to originate from a stress-induced phase transformation. Swahn and Österlund observe the ferrite phase in groups of parallel discs, supersaturated in carbon and separated by martensite [Swa76, Öst80]. Voskamp found bands, which were grouped as lamella, oriented in a triangular way and of sub-micron

thickness [Vos96]. Schlicht, Styri and King [Sch70, Sch68, Sty51, Kin66] find heavily deformed martensite in the region of DEAs as well as fine, tempering like, carbides precipitations [Sch68].

King and Schlicht exclude the possible influence of local heating to form DEAs. Swahn proposes stress induced carbon diffusion from the martensite lattice towards dislocations or other defects. The martensite decay results in a ferritic phase, supersaturated with carbon [Swa76].

The reasons for the stronger etching response of the DEAs are discussed controversially in literature. Swahn proposes that a preferential etching of the closely spaced phase boundaries of the parent martensite and decomposed martensite/ ferritic phase or different etching rates of those phases cause the darker etching [Swa76].

Schlicht gives several possible reasons. The plastic deformation and connected an increase in dislocation density might result in poorer corrosions resistance [Sch68]. A possible formation of small grooves during etching and a resulting surface relief might also lead to less light reflection from the surface. A reduced corrosion resistance due to a more severe tempered martensite seems less likely [Sch70].

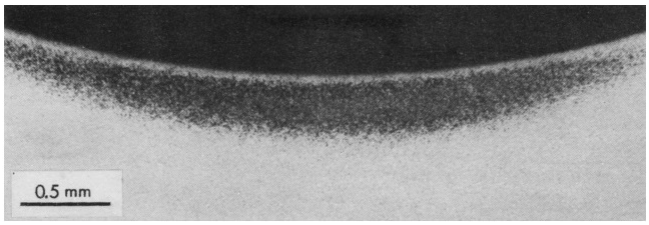

Figure 31: DER in the cross section of a tested deep groove ball bearing inner ring (3.3 GPa, N = 10^8, rpm=6000, 70 °C) [Vos96]

Lund reports in [Lun69] the absence of DERs in 6309 bearing inner rings for the case that the rings were tempered down to 57 HRC as compared to 64 HRC, where DER were found under identical running conditions. A similar observation was reported in [Mar66].

Gentile compared different steel melting techniques and resulting steels cleanliness levels in terms of DEA formation [Gen65]. Bearing rings made of cleaner steel variants showed a later initiation and slower formation of DEAs. The author concludes that the DEA formation is a result of induced stresses and their concentration by non-metallic inclusions.

Rollmann shows [Rol99] a delay of DER appearance with increased carbon dissolution and thereby increased retained austenite level for 100Cr6 rollers.

White etching bands (WEBs) can appear with an angle of approximately 30° (LABs, Low Angle Bands) and 80° (HABs, High Angle Bands) with regard to the stressed surface. They appear later in the fatigue life, see Figure 26. WEBs were found to be disc shaped, having an inclination angle of 30° and 80° towards the raceway with an inclination direction related to the rolling direction, see Figure 32, Figure 33, Figure 34 [Swa76, Lun69, Mar66].

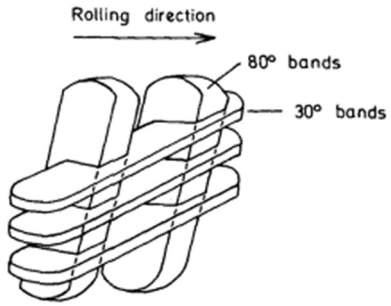

Figure 32: Schematic outline of the 30 and 80° bands [Swa76]

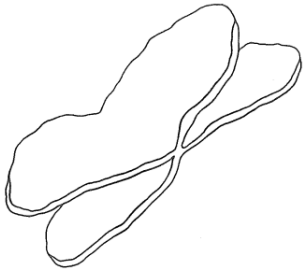

Figure 33: "Idealized" three-dimensional view of WEBs [Lun69]

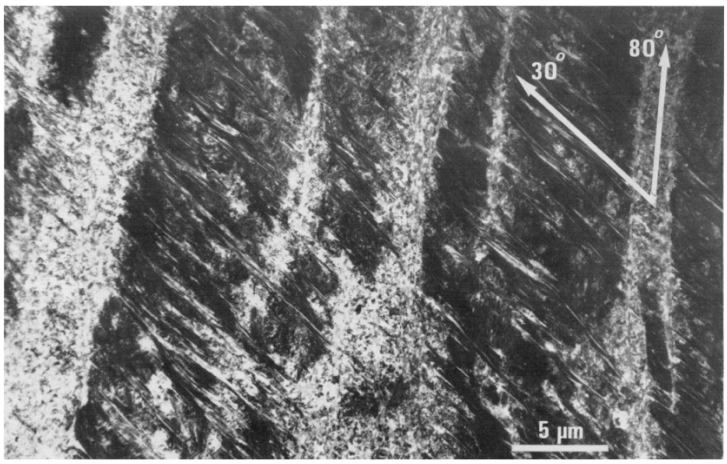

Figure 34: TEM image of 80° bands and 30° bands [Swa76]

Swahn found ***LAB*** lengths of 5 – 30 µm, thicknesses of 0.1 – 0.5 µm (~ 1 µm [Vos97]) and distances of 0.5 – 10 µm between them [Swa76]. The inclination angles can vary between ~ 32 - 40° closer to the raceway and ~ 20 - 28° in greater depths [Vos97, Zwi80]. They are reported to grow for increasing number of load cycles [Zwi80, Mar66]. A TEM study revealed LABs being "long ribbons of ferrite", partly sandwiched between carbide rich regions [Vos97]. Different authors show that LABs can pass and fragment carbides [Vos97, Swa76], whereas Voskamp claims that carbide obstacles obstruct and slow down LAB growth. Österlund shows the absence of carbides within LABs in a TEM study [Öst80].

Swahn explains the formation of LABs starting from the decayed martensite of a DER, being ferritic and supersaturated with carbon ("DER-ferrite"). The DER-ferrite, assuming to have lower strengths, will locally flow and dislocations will escape their carbon decorations and glide along defined directions, given by the asymmetric stress tensor (e.g. 30°). Carbon atoms which are forced into solution increase the corresponding energy and carbon will diffuse towards the matrix interface where carbides or carbide discs (agglomerate of small carbide particles) will be formed. The DER-ferrite turns into ferrite in thermodynamically equilibrium, having a lower strength.

Zwirlein explains the formation of WEBs with enhanced carbon diffusion and martensite decay by increased dislocation densities, caused by repeated microplasticity. He assumes that the generation of heat by the plastic deformation additionally might lead to increased carbon diffusion and martensite decay. The author shows in his calculations, taking into account the measured residual stress profile and friction conditions, that the inclination angle of LABs coincides with the direction of the biggest compressive stress/ smallest principal stress. The calculated, radial change in stress direction agrees with the observed, small changes of the LABs inclination angle [Zwi80].

Voskamp shows in [Vos96] that the orientation of LABs can be mirrored by a reversed over-rolling direction.

Martin found in [Mar66] a congruent distribution of LABs and unidirectional shear stress and assumes the formation of LABs being connected to the mentioned stress component. An increasing share and size of LABs with cycling was reported. Martin showed a cellular structure of LABs in a TEM study where the cellular structure consisted of dislocation clusters surrounding areas of lower dislocation density. The selected area electron-diffraction pattern revealed a ferritic structure with randomly oriented crystals and being of smaller grain size as compared to the parent matrix. The absence of temper carbides was observed.

Tallian shows an 23° angle of LABs in a deep groove ball bearing. A TEM study reveals the LABs to consist of small circular cells with dislocation tangle walls. Temper carbides are shown to be absent within the LABs [Tal67].

At a later stage of components life ***HABs*** can develop. Lengths up to 100 µm [Swa76], thicknesses of 5 - 20 µm [Vos97, Swa76] and distances of 5 – 50 µm in between [Swa76] have been reported. HABs are reported to consist of heavily deformed ferrite with a cell size of ~ 0.2 µm without carbides present [Swa76] or equiaxed ferrite regions with small fractions of tiny cementite particles [Vos97]. An X-ray microprobe analyses of HABs revealed very low amounts of carbon (0.06 wt.-%) [Bes75].

Swahn reports about an unknown nucleation mechanism of HABs, which preferably form in regions with high LABs densities [Swa76, Zwi80]. The reason for the direction of inclination remains unclear. Swahn suspects LABs being fast diffusion paths for carbon necessary for the formation of carbon free ferrite and the observed redistribution or dissolution and precipitation of carbides. This supports his observation of longer HABs and larger quantities of HABs in volumes of high LABs densities.

Voskamp found a dependency of HAB inclination angles on inner ring velocities of tested bearing rings. HABs inclined at ~ 30° were found in an inner ring tested with 9000 rpm, while being inclined at ~ 80° when tested with 6000 rpm [Vos97].

Lund reports a constant angle between LABs (inclined 20° - 25°) and HABs (inclined 65°- 70°) of 45° [Lun69].

Zwirlein shows in his calculations, taking into account the measured residual stress profile and friction conditions, that the inclination angle of HABs coincides with the direction of the biggest shear stress/ principal shear stress. The calculated, radial change in stress direction agrees with the observed, small changes of the HABs inclination angle [Zwi80]. The authors explain the formation of HABs by the decrease of martensite volumes in between LABs with increasing LAB density, which leads to instability of those volumes and a shear stress driven break up or decay.

Schlicht suspects in [Sch08] similar mechanisms for HABs and adiabatic shear bands formation. He suggests that a two-dimensional stress state is necessary for HAB formation (as for adiabatic shear bands) which is present at a later stage of the fatigue process. The proceeding plastic deformation and build-up of compressive residual stresses leads to a shift of the volume exposed to maximal stresses towards the contact surface. Due to the pressure distribution in an EHD contact (see Figure 24) and the rapid drop of pressure after the second maximum, he sees the material being exposed to a shock load or implosion at the outlet of the contact area. The two-dimensional stress state requires less energy for plastic deformation and the shear induced by the implosion would form WEBs (similar to the conditions under which adiabatic shear bands form). The author also sees sufficient amount of slip as a requirement for HABs formation, as is normally the case for curved raceways.

2.4.3.2 X-Ray diffraction

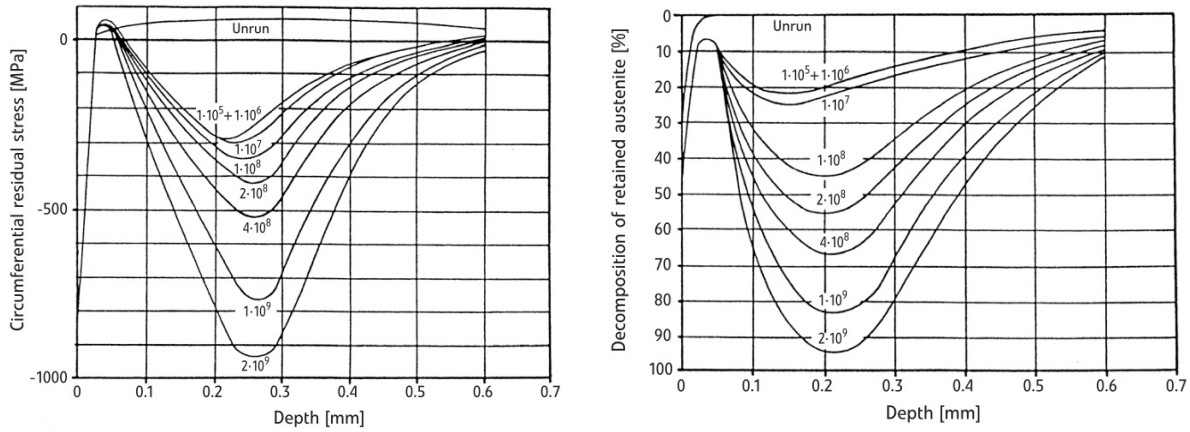

Figure 35: Radial profiles of the measured residual stresses (left) and retained austenite decomposition (right) for fatigue tested deep groove ball bearing rings [Vos97]

The change of the residual stress state [Vos97, Zwi80, Mur70, Mur73 Sch70, Roll99, Sch74, Swa75, Gen65, Bus62, Zar69] and change in retained austenite content [Vos97, Vos80, Roll99, Swa75, Man70] after rolling contact has been investigated by many authors. The change of residual stresses towards compressive stresses and the decrease of the X-ray diffraction peak widths, with a distinct minimum below the surface, are common observations, see Figure 35. A reduction in retained austenite content was reported, with a minimum in retained austenite content below the surface. All observations were more pronounced for increasing numbers of load cycles and higher loads. Voskamp however measured a stress relaxation for higher loads [Vos97]. Solely Zaretsky could not measure any clear effect of running time on the induced compressive residual stress [Zar69].

Schlicht reports identical depths for the minimum in diffraction peak width (FWHM) and the depth of strongest/ darkest etching response of the observed DEA. Since he sees plastic deformation as the driver for DEA formation, he concludes that the measured FWHM gives quantitative information about the degree of plasticity. The FWHM minimum coincides with the depth of the maximum principal shear stress. The generation of compressive residual stresses is explained with an increase in specific volume of the plasticised material volumes, connected to an increase in the density of dislocations and free vacancies [Sch70].

Voskamp describes the residual stress change as a consequence of micro-yielding of small volumes beneath the contact surface. After a passage of a rolling element and unloading of a previously plasticised small volume, the internal stress field of surrounding volumes will change due to the remaining plastic deformation of the plasticised volume upon unloading. A new loading cycle might lead to a possible plastic deformation in the neighbouring, previously elastically deformed volumes due to the changed internal stress field. During continued cycling loading the described process will continue, more elements will be plasticised in larger volumes and residual stress will accumulate. According to the author, a steady state will be reached after a certain number of load cycles and certain amount of plastic deformation, from which the material volumes under residual and external applied stress will deform elastically. Furthermore, the occurring phase transformations and the difference in specific volumes of the involved phases are affecting the internal stress field. While the decomposition of retained austenite generally leads to increased specific volume and compressive residual stress, the decomposition of martensite has the opposite effect. The commonly measured decrease in hardness after a sufficient number of load cycles [Lun69, Zwi80, Swa76] in the loaded

subsurface area leads to a decrease in yield stress. According to Voskamp the decreased yield stress can affect the residual stress field in opposite ways. An increase of compressive stress can be expected, since the micro-yield can spread to larger volumes. On the other hand, a decreased yield stress can lead to relaxation of residual stresses. The minimum of the measured radial residual stress profile coincides with the depth of highest unidirectional shear stress, as in [Bus62].

Apart from the axial and tangential residual stress components, which were presented to be compressive, radial stress components on sectioned rings were measured by Voskamp. The radial residual stress components turned out to be tensile, which might be crucial for the growth of surface parallel, sub-surface cracks. An explanation is given with the help of Figure 36. The highly stressed sub-surface volume (a) will plastically deform and expand mainly in axial and circumferential directions (b). The constraint of free expansion will result in compressive residual stresses in axial and circumferential directions. A contraction in radial direction must occur which will in result in tensile stresses (d) [Vos97].

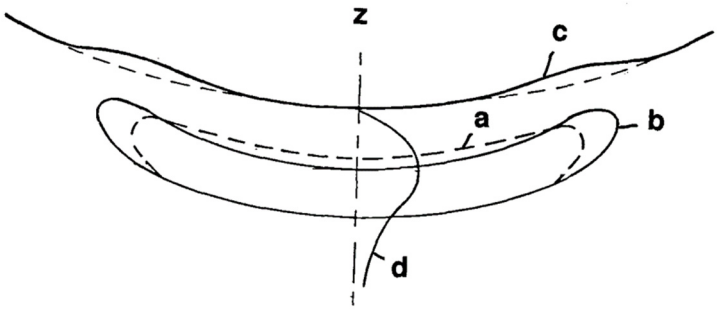

Figure 36: Microplastic flow in the sub-surface region; a = volume stresses above yield limit; b = changed shape due to plastic flow; c = elevation of surface; d = radial stress profile being tensile; a = reversed plastic flow [Vos97]

Swahn sees the measured increase in compressive residual stress as a direct consequence of the stress-induced retained austenite transformation and connected volume increase [Swa75]. The authors find the residual stress minimum as well as the minimum in X-ray peak line width (similar to FWHM) in the depth of maximum principal shear stress. Strong residual stress gradients and residual stress differences in axial and tangential directions are seen as possible sources for crack nucleation and failure.

Zwirlein shows in [Zwi80] a stress calculation for the case of constant residual stresses and a line contact. Compressive residual stresses on a moderate level lead to a decrease in the calculated van Mises stresses. After reaching a minimum, an increase in compressive residual stresses leads to increased van Mises stresses. Furthermore, the depth and contact plane position of maximum stresses, as well as the angle of the principal stress system are shifted for different levels of residual stresses (similar to the effect of increased friction). Increased compressive residual stresses lead to a shift of the stress maximum towards the surface. The calculated van Mises stress maximum coincided with the measured compressive residual stress maximum below the surface. The calculated van Mises stress profile helps to describe the position of the observed DEA.

Muro measures a considerable compressive residual stress build up after a single load cycle with sufficient contact pressure [Mur70]. He sees plastic deformation as the cause for residual stress change. Fatigue tests and residual stress measurements for different hardness levels of the tested steels showed the tendency for higher compressive stress peaks with higher initial hardness. The result remains difficult to understand with the authors opinion that plastic deformation is causing compressive residual stresses. The measured compressive residual stress peaks coincide with the depth of maximum principal shear stress [Mur70,

Mur73]. The author showed furthermore that shock loads as well as high rotational speeds (high strain rates) can lead to higher compressive residual stresses [Mur73].

2.4.3.3 Hardness

The change in hardness after rolling contact has been studied by different authors [Swa75, Swa76, Mur70, Zwi80, Lun69, Gen65, Sug70, Bea57, Bus62].

Swahn measured a hardness increase for tested rolls ran at high contact pressures ≥ 4 GPa running for $1.5x10^4$ – $6.5x10^5$ load cycles [Swa75]. The hardness maximum coincided approximately with the compressive residual stress maximum beneath the contact surface (depth of max. principal shear stress). Swahn assumes plastic deformation being responsible for work hardening, hardness increase and compressive residual stress formation. Additional 6309 bearing testing (contact pressure: 3.3 – 3.7 GPa) confirmed an initial work hardening and hardness increase from 875 HV to 900 HV after 10^6 load cycles. A softening occurred after 10^7 load cycles, after which hardness decreased to 850 HV. During further cycling softening proceeded and a well-defined hardness minimum was measured beneath the surface (e.g. ~680 HV after 10^9 cycles), see Figure 37. The decrease in hardness is thought to be connected to the observed microstructural decay (DER, WEBs) and coincides roughly with the depth of maximal principal shear stress [Swa76, Sug70].

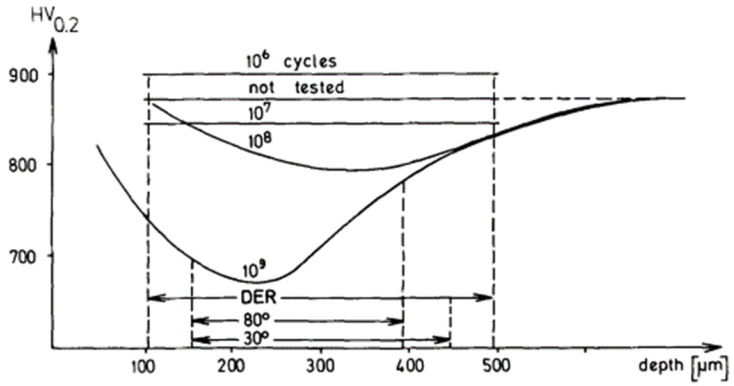

Figure 37: Radial microhardness profile of 6309 tested inner rings (SAE 52100) before and after rolling contact fatigue testing for different load cycles and a contact pressure of 3.3 – 3.7 GPa; depth of dark etching areas (DEA) and white etching bands (WEBs, 30° and 80°) [Swa76]

Muro finds a threshold contact stress of 3.5 – 4.5 GPa in order to measure a hardness increase after 10^6 load cycles. The authors tested cylinders with different hardness levels (62, 58 and 54 HRC) and different, mainly high carbon steels. Generally, a local hardness decrease was measured when structural changes occurred [Mur70]. A repetitive push test (ball on flat surface) without a rolling motion resulted in a stress field where the orthogonal shear stress components are absent. In such a test, compressive residual stresses formed of comparable magnitude as for the over-rolled specimen. A change in hardness, however, did not occur until > 10 million load cycles. The author concludes that the hardness increase is caused by the orthogonal shear stress component (over-rolling) and the residual stress change by the main shear stress (over-rolling and repetitive push test) [Mur70]. This was confirmed by a shallower peak of the hardness profile as compared to the residual stress profile.

Zwick measures a material softening for deep groove ball bearing inner rings, loaded with 2.9 GPa, see Figure 38. The softening occurs in the depth of microstructural changes. The first decrease in hardness was

measured at 900 hours, after the first occurrence of DEAs (~ 100 hours) and LABs (~ 500 hours) and before the first occurrence of HABs (~ 2500 hours). Increased running times lead to lower local hardness and a shift of hardness minimum towards the surface. The shift in hardness minimum might be due to the discussed shift in van Mises stress maximum towards the surface in case of increased friction and increased amounts of compressive residual stresses [Zwi80].

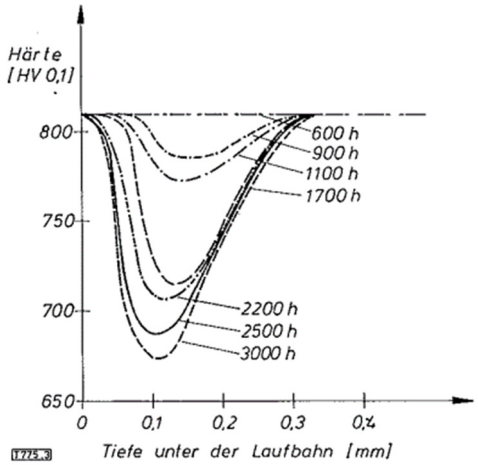

Figure 38: *Radial microhardness profiles of deep groove ball bearing inner rings for different testing times and a contact pressure of 2.9 GPa [Zwi80]*

Lund measures material softening of decayed material volumes of tested 6309 bearing inner rings, see Figure 39. The author reports a "direct dependence of the severity of phase transformation on the minimum hardness" [Lund69].

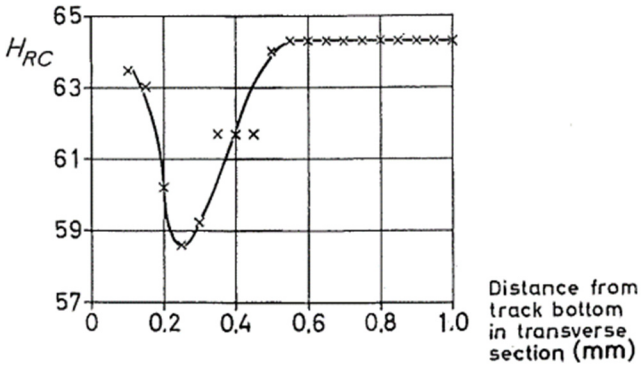

Figure 39: *Radial hardness profile of a 6309 bearing inner ring (SAE 52100) after testing at 3.3 GPa and decayed microstructure (DER, WEBs) [Lun69]*

Sugino compares the microhardness evolution of SAE 52100 steel (radial type RCF test on discs at 5 GPa) for different levels of retained austenite. In case of higher retained austenite levels (12 Vol.-%) the author measures an increase in hardness until 1.5×10^6 load cycles under the contact surface and a decrease for higher numbers of load cycles. No hardness change was measured for the case of low retained austenite (3 Vol.-%). The appearance of a DEA is shown to be connected to the hardness decrease [Sug70].

2.4.3.4 Texture

Voskamp used X-ray diffraction techniques to analyse the texture of the ferrite phase within a DER in fatigued 6309 bearing inner rings made of SAE 52100 [Vos97]. The author measured a strong, local texture (crystallographic preferred orientation) of the ferrite matrix as {100}<110> and {111}<211> beneath the contact surface. Crystallographic planes {hkl} and crystallographic directions <uvw> are preferably parallel with the contact surface and in direction of over-rolling. The applied load and testing temperature turned out to be decisive for the type of texture. Absence of any texture and DER was shown for the combination of high contact loads (3.3 GPa) and low testing temperatures (≤ 45 °C). Increased testing temperatures (55 – 90 °C) and contact loads (2.8 – 3.8 GPa) lead to the development of either strong {100}<110> texture (high contact pressures, lower testing temperatures), strong {111}<211> texture (high contact pressures, higher testing temperatures) or concurrent and less strong appearance of both. The author also reports that WEBs only appear in conjunction with the appearance of {111}<211> texture.

The texture formation is attributed to the localized plastic deformation and possible dynamic recrystallization. The local plasticity might lead to localized bursts of dissipated energy and temperature peaks, which in turn might make recrystallization possible.

2.4.3.5 Plasticity

Subsurface micro-plastic damage or micro-plasticity of fatigued samples has been measured in terms of surface geometry change, such as grooving or groove depth [Veg12, And12, Joh82] and radius change [Roll99, Sch06]. By measuring the plasticity after defined numbers of load cycles, the evolving fatigue damage and microstructural changes can be measured. The isolated investigation of the material performance, rather than the performance of the multiple component “bearing” system in case of full bearing tests is seen as an advantage [Veg12].

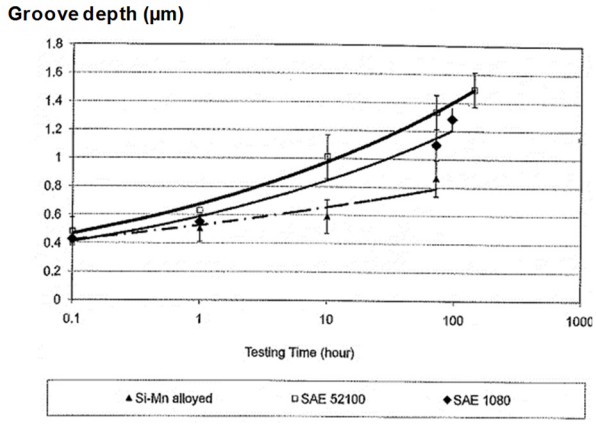

Figure 40: Grooving of shafts made of different bearing steels, 4 GPa contact pressure, 100 °C testing temperature [And12]

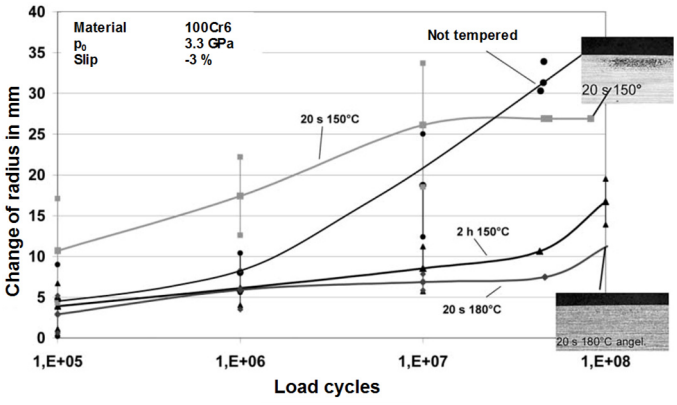

Figure 41: Changes in profile radius for 100Cr6 rollers and different tempering conditions [Sch06]

Andersson measured reduced grooving for a silicon and manganese alloyed bearing steel as well as for a variant with reduced chromium as compared to a SAE 52100, see Figure 40. He suspects that silicon acts as a matrix stabiliser, supresses carbide precipitation and supresses softening during cyclic stressing. Carbide forming elements, such as chromium, might act in opposite direction since they promote carbide formation and matrix carbon depletion.

Vegter proposes a material model for the groove formation, which describes the total grooving as the sum of the initial grooving during the first load cycles (plastic shakedown) and the continuous, load cycle dependent groove development. The initial grooving is suspected to be mainly hardness dependent and stabilizes due to rapid work hardening. The second, continuous contribution to the total grooving is believed to be temperature and time dependent. An activation energy Q_{eff} is used to describe the continuous grooving and is proposed to be understood as the materials rolling contact fatigue resistance (low for soft, less fatigue resistant steels). A thermally activated creep-like material damage mechanism and dislocation climb is mentioned governing the plasticity [Veg12].

Rollmann shows in [Rol99] that the change in the profile radius of tested rollers reflects the different stages of rolling contact fatigue (shakedown -> steady state -> instability). Following Rollmanns findings, Scheerer used the change in profile radius to rate the degree of rolling contact fatigue (see Figure 41).

2.4.3.6 Carbide morphology

The dissolution, deformation and re-precipitation of carbides are the most commonly accepted transitions. Swahn reports [Swa76b] a gradual break up and dissolution of primary cementite particles (incoherent, spherical, $(Fe,Cr)_3C$ type, median diameter 1 µm) and temper ε-carbides in fatigued (3.3 - 3.7 GPa, 50 - 55 °C, 6000 rev/min), martensitic and bainitic SAE 52100 bearing inner rings. The changes were reported to appear within white etching bands. Swahn proposes that the cyclic stresses and plasticity causes increased dislocation densities providing increased diffusion ability. Furthermore, an increase in vacancy concentration would lead to increased carbon solubility in ferrite. The resulting ferrite phase must be thermodynamically strongly supersaturated in carbon, with carbon being located along dislocations and in finely dispersed, continuously forming and dissolving precipitates [Swa76b]. Dissolution of carbides in fatigued material volumes is further reported [Sug70, Sco66, Gra07, Bri66, Buc68], where O`Brien and Scott report carbide dissolution or break up within white etching areas. Dissolution, elongation of carbides as well as lenticular carbides connected to butterfly wings were shown by Sugino [Sug70]. Distorted or elongated carbides were further reported in [Bus62, Sco66, Swa76, Mar66, Öst80, Bes75, Buc68, Gra07].

Buchwald proposes that carbides dissolve and carbon migrates from plasticized to undeformed regions due to its decreased solubility in highly deformed areas. He observed precipitation of lenticular carbides in between the matrix and the white etching area. He assumes that high hydrostatic pressures in highly deformed areas as well as higher dislocation densities would cause the dissolution of carbides and carbon migration [Buc68].

Martin reports that lenticular carbides form during cycling around LABs with the same angle in respect to the over-rolled surface. The author suspects and gives examples that lenticular carbide boundaries are weak links in the matrix and preferred crack propagation planes. The mechanisms of lenticular carbide formation and

growth was not clear, however, it was speculated if a diffusion controlled mechanism led to dissolution of temper carbides and precipitation of lenticular carbides [Mar66].

Österlund finds “protruding carbide ridges” or “carbide discs” between LABs [Öst80]. He also found that initial, disc shaped carbide precipitates were broken up and redistributed as fine precipitates in butterfly wings [Öst82]. Scott finds stringer type, elongated carbides at the edges and to a smaller extend within white etching areas, which may be formed by deformation or distortion of coarse carbides [Sco66]. The author also reports about a microprobe analyses of white etching matter, which revealed higher chromium and manganese contents as compared to the matrix. He concludes that primary or temper carbides must have been dissolved.

3 Experimental

3.1 Selection of steel grades

Table 4 shows the commercially available steel grades which were chosen as potential steel grades for induction hardening. Silicon and manganese alloyed steel grades and steels with carbon concentrations larger than 0.5 wt.-% are preferred grades. The selection of steel grades was made based on the findings in chapter 2.3.

*Table 4: List of used steel grades; alloying contents in weight-% from melt; M_S temperatures (*for reference heat treatment with dilatometer of as delivered prior structures T_A 860 °C, t_s 10 min, t_{8-5} 10 s ** for full dissolution of alloying elements, formulas from [Bes93, Kra05])*

Steel	Supplier	C	Si	Mn	P	S	Cr	Ni	Mo	Cu	Al	M_S*/ °C	M_S**/ °C
100Cr6	DEW	0.97	0.21	0.44	0.011	0.007	1.51	0.11	0.05	0.1100	0.0060	227 ± 5	127 ± 26
Ovako 832	Ovako	0.88	0.69	1.57	0.020	0.007	1.46	0.13	0.08	0.2040	0.0290	189 ± 5	116 ± 21
50CrMo4	Sidenor	0.51	0.24	0.70	0.008	0.006	1.05	0.08	0.17	0.2270	0.0160	262 ± 5	288 ± 17
67SiCr5	BGH	0.70	0.88	0.58	0.007	0.013	0.64	0.06	0.02	0.0377	0.0082	250 ± 5	234 ± 18
70Mn4	DEW	0.67	0.23	0.97	0.007	0.012	0.12	0.08	0.04	0.0760	0.0120	212 ± 5	248 ± 17
Ovako 677	Ovako	0.68	1.43	1.48	0.014	0.007	1.00	0.11	0.25	0.1570	0.0380	236 ± 5	194 ± 16

As a reference **100Cr6** was included as the most frequently used bearing steel. It is known as a steel grade, which can be suitable for induction hardening. Schlicht showed that induction heat treatment of rings made of 100Cr6 can lead to comparable properties in terms of hardness and strengths compared to conventional isothermal austenitisation, if soaking time was in the range of a few minutes [Sch68].

Ovako 832 is a derivation of 100Cr6 and contents higher amounts of silicon and manganese, expecting increased hardenability. The lower carbon content could lead to a lower fraction of carbides in the material and in total less alloying elements like chromium and manganese bound to them. The share of alloying elements dissolved in the matrix or in carbides however generally strongly depends on the prior treatment (e.g. soft annealing). Ovako 832 is in use as a bearing steel grade.

50CrMo4 is used as a bearing steel and contains the lowest amount of carbon. It contents a moderate amount of chromium and comparably high amount of molybdenum. Due to the low amount of carbon and low amount of alloying elements lowering M_S, the steel is assumed to be least critical regarding overheating. Moderate amounts of retained austenite after hardening (highest theoretical M_S temperature for full dissolution among investigated steels) can be expected.

67SiCr5 is a spring steel alloyed with silicon, chromium and some manganese. Due to the limited amounts of carbon and alloying elements lowering M_S (e.g. Cr, Mn, Mo), the steel is expected to be less sensitive to overheating. Moderate amounts of retained austenite after hardening are likely to be present. At the same time, a somewhat higher hardenability compared to plain carbon steels like C70 can be assumed. Please note that the chemical composition of the used 67SiCr5 steel shows a lower silicon (0.88 %) and a higher chromium (0.64 %) content as compared to the specification according to “Stahl-Eisen-Liste” (Si: 1.2 % - 1.4 %, Cr: 0.4 % - 0.6 %).

70Mn4 is used as a bearing steel. Apart from manganese and carbon, alloying is kept to a comparatively low level expecting fast transformation kinetics and less risk of overheating in terms of retained austenite compared to for instance 100Cr6 or Ovako 832. Due to the low level of carbide formers like chromium or molybdenum, the thermal stability of cementite or carbides is assumed to be comparably low.

Ovako 677 is not known as a commonly used steel for bearings. It contains a similar carbon level as 67SiCr5 and 70Mn4 and relatively high levels of silicon, manganese and molybdenum as well as a moderate amount of chromium. The hardenability is expected to be highest among all steel grades whereas the large amount of alloying elements might lead to slow transformation kinetics.

Temperatures for the onset of martensitic transformation (M_S) for the case of full alloying element dissolution were calculated using the average of 7 different formulas compiled by Besserdich and Krauss [Bes93, Kra05], see Table 4.

The steels were investigated in different prior conditions, see Table 5. Besides the as delivered conditions, the steels were heat-treated to quenched and tough tempered states (QT). To set the QT conditions, the steels were austenitised at 860 °C (30 min), quenched in 60 °C oil and subsequent tempered (2 h) at various temperatures (see Table 5), aiming for a hardness of 300 HV. The tough tempered state is a compromise between response to induction hardening and machinability or formability. Due to the presence of coarse lamellar carbides in the as delivered microstructure of 67SiCr5 (SA1), a second soft annealed state (SA2) was investigated. For grade 50CrMo4 a second quench and tempered state QT2 was investigated. The intention was to avoid the phases which appeared as lighter etched areas on the micrograph of the QT1 structure (possibly tempered bainite fractions) and examine their effect on the heating and quenching response.

*Table 5: Microstructures of prior condition variants; Nital 1.5 %, 20 s; * = as delivered condition; T_T = tempering temperature*

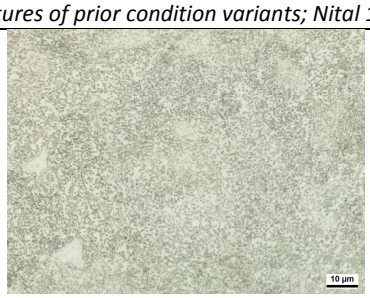 195 ± 9 HV1 SA*	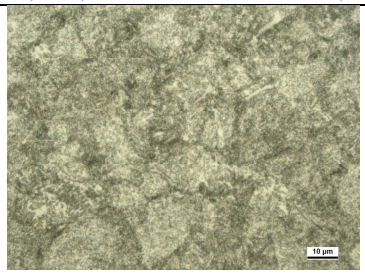 295 ± 2 HV1 T_T = 660 °C QT	100Cr6
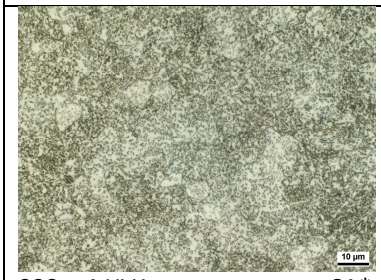 223 ± 4 HV1 SA*	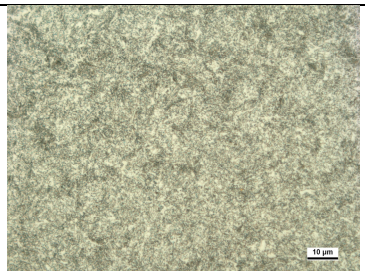 296 ± 2 HV1 T_T = 685 °C QT	Ovako 832
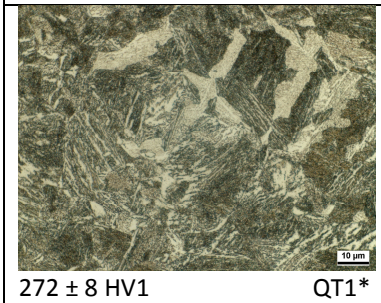 272 ± 8 HV1 QT1*	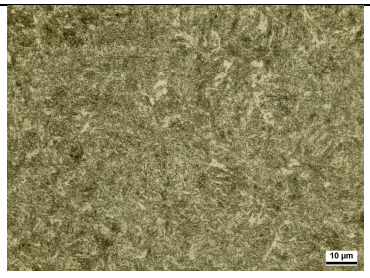 287 ± 7 HV1 T_T = 660 °C QT2	50CrMo4

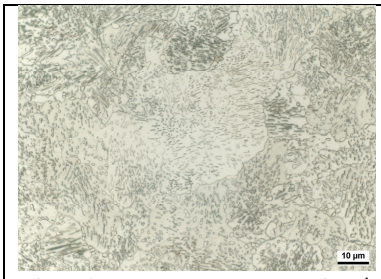 197 ± 2 HV1 SA1*	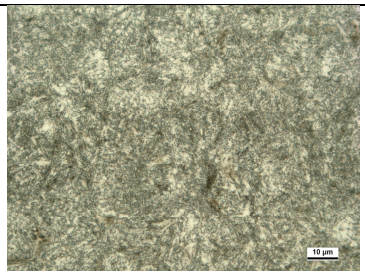 290 ± 2 HV1 T_T = 650 °C QT	67SiCr5
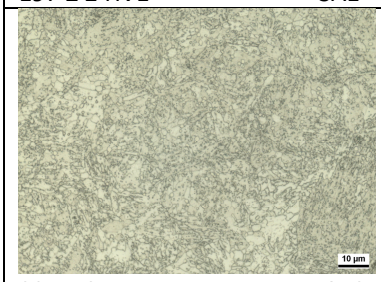 221 ± 2 HV1 SA2		
 284 ± 11 HV1 N*	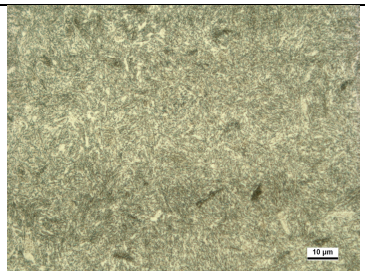 286 ± 7 HV1 T_T = 640 °C QT	70Mn4
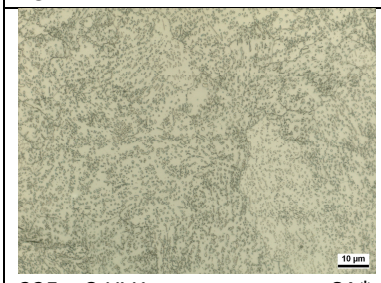 225 ± 8 HV1 SA*	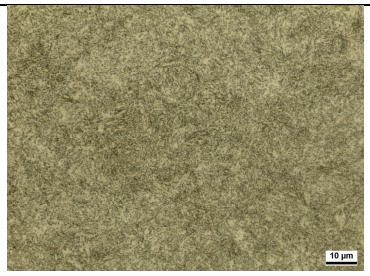 306 ± 7 HV1 T_T = 700 °C QT	Ovako 677

Experimental

The steels micro-cleanliness levels were examined according to ISO 4967:2013, method A (worst field), see Figure 42. Six samples from bar material were used for each material.

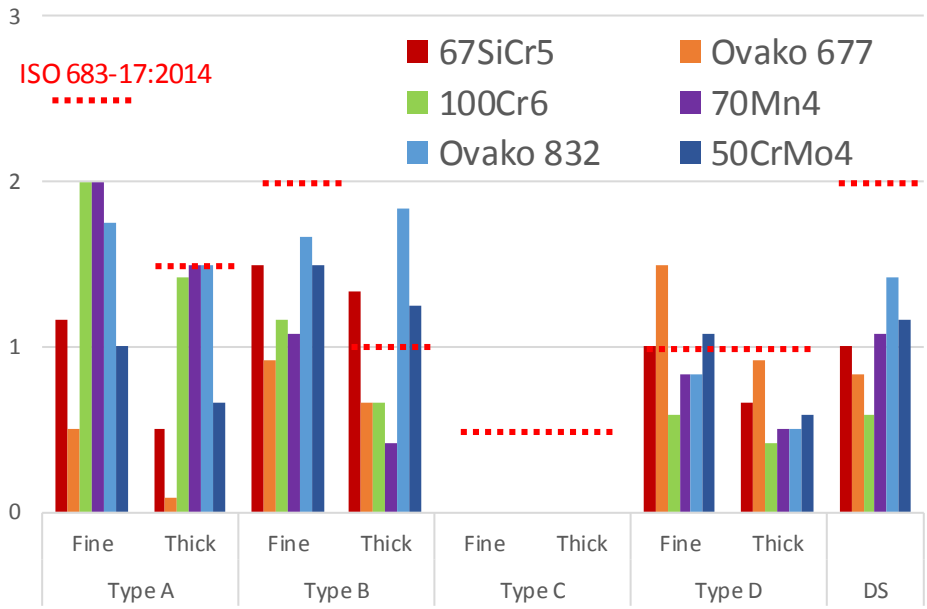

Figure 42: Micro-cleanliness rating according to ISO 4967:2013 and limits from ISO 683-17:2014

The definitions of the rated inclusion types according to ISO 4967 are listed in Table 6 below. The attributes "fine" and "thick" refer to the inclusion thickness (Types A, B, C) and diameter (Types D, DS). The individual ratings (index ranging from 0 to 3) refer to the inclusions frequency, length and diameter, where larger numbers mean increased lengths (types A, B, C), increased frequency (type D), and increased diameter (type DS).

Table 6: Definitions of inclusion types according to ISO 4967

Type A	**Sulfide type**: highly malleable, individual grey particles with a wide range of aspect ratios (length/width) and generally rounded ends; e.g. MnS
Type B	**Aluminate type:** numerous non deformable, angular, low aspect ratio (generally < 3), black or bluish particles (at least three) aligned in the deformation direction; e.g. Al_2O_3, MgO, SiO_2, CaO
Type C	**Silicate type:** highly malleable, individual black or dark grey particles with a wide range of aspect ratios (generally > 3) and generally sharp ends; e.g. CaO- Al_2O_3- $(SiO_2)_2$
Type D	**Globular oxide type**: non deformable, angular or circular, low aspect ratio (generally < 3), black or bluish, randomly distributed particles; e.g. Al_2O_3, MgO, CaO
Type DS	**Single globular type:** circular, or nearly circular, single particle with a diameter > 13 µm; e.g. e.g. Al_2O_3, MgO, CaO

3.2 Dilatometer testing

In order to understand the induction hardening response of the different steels and prior structures, a dilatometer study was carried out. The induction heat treatment of hollow cylinders ($Ø_O$ 4 mm, length 10 mm, wall thickness 0.5 mm) was done with a dilatometer (type Bähr 805 A). The cylinders were heated with a frequency of 2 MHz and a power of maximum 1.75 kW inside a coil ($Ø_I$ 17 mm, length 24 mm, 6 turns). The temperature was measured with a thermocouple (type S) spot welded on the outer cylinder surface (see Figure 43). After heating with a certain heating rate to the final temperature T_A and soaking for a certain time t_S, all cylinders were quenched with gaseous nitrogen (t_{8-5} = 5 s). The heating parameters are shown in Table 7. For the used dilatometer arrangement and sample geometry, a programmed heating rate of 300 K/s could not be maintained between the onset and completion of austenite transformation (A_{c1}/A_{c1b} and A_{c3}/A_{c1e}) although using full generator power. Possible reasons are the loss of magnetic properties from Curie temperature T_C (lower efficiency), increase of currents penetration depth, heat losses due to crystallization (latent heat) and reaction speed of the control loop. The measured heating rates between A_{c1}/ A_{c1b} and A_{c3}/ A_{c1e} as well as the measured transformation temperatures are given in Table 8.

Table 7: Heating parameters

heating rate/ K/s	T_A/ °C	t_S/ s
30	950	1
300	1000	10

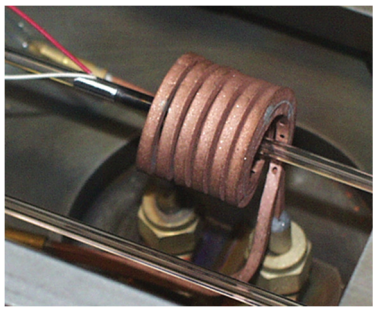

Figure 43: Dilatometer sample with welded thermocouple and heating coil with integrated quenching channels

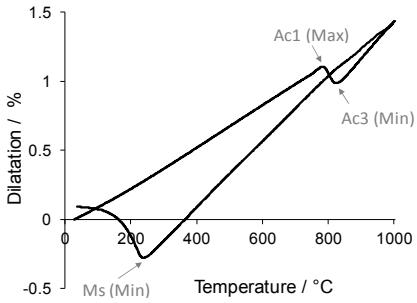

Figure 44: Phase transformation temperatures derived from dilatometer curve

The dilatometer curves were evaluated regarding beginning and end of the ferrite to austenite transformation (heating) and the beginning of transformation from austenite to martensite (quenching) using the local minima and maxima of the dilatation curves, see Figure 44. The heat-treated steel samples were characterized regarding hardness (8 indents HV1) and prior austenite grain size (geometric method, interception of grain boundaries with lines, 3 pictures evaluated), one sample per parameter setting. The calculated average length of interception line segments is referred to as prior austenite grain size in the following. For the prior austenite grain size determination, the heat-treated samples were etched in a mixture of picric acid, hydrochloride acid, and a wetting agent heated to approximately 60 °C.

Table 8: Programmed and measured heating rates and transformation temperatures during dilatometer heating; temperatures in grey indicate insufficient heating rates

Steel	Prior structure	Measured heating rate Ac_1/ Ac_{1b}-Ac_3/ Ac_{1e} (programmed) / K/s	A_{c1}/ A_{c1b}-A_{c3}/ A_{c1e} / °C ± 3 °C	A_{c1}/ A_{c1b}-A_{c3}/ A_{c1e} / °C ± 3 °C	Prior structure	Measured heating rate Ac_1/ Ac_{1b}-Ac_3/ Ac_{1e} (programmed) / K/s	A_{c1}/ A_{c1b}-A_{c3}/ A_{c1e} / °C ± 3 °C	A_{c1}/ A_{c1b}-A_{c3}/ A_{c1e} / °C ± 3 °C
100Cr6	SA	30 (30), 133 (300)	795-846	825-859	QT	30 (30), 115 (300)	774-811	794-822
Ovako 832	SA	30 (30), 144 (300)	797-844	823-858	QT	30 (30), 141 (300)	779-825	798-837
50CrMo4	QT1	30 (30), 91 (300)	785-816	810-831	QT2	30 (30), 104 (300)	778-817	799-828
67SiCr5	SA1 SA2	30 (30), 156 (300) 30 (30), 146 (300)	812-861 795-846	838-874 822-859	QT	30 (30), 113 (300)	783-819	801-830
70Mn4	N	30 (30), 13 (300)	759-779	785-789	QT	30 (30), 60 (300)	755-782	777-790
Ovako 677	SA	30 (30), 185 (300)	820-871	851-887	QT	30 (30), 166 (300)	797-848	821-862

3.3 Surface Induction hardening of rod samples

For the transfer of the gained information from the dilatometer study on surface hardened components, rods (diameter 9.53 mm, length 100 mm) were scan hardened with a single turn coil, see Figure 45. The investigation should answer the question whether characteristics of the dilatometer curves would be found in surface induction hardened components in terms of surface hardening depth, radial hardness change with the temperature profile and the transition between case and core.

The used coil was not customized for the used sample geometry and the inductor was run eccentric, leading to comparably high electrical losses. The scan speed was set comparably fast to avoid through heating and through hardening of the thin samples. The pyrometer showed a surface temperature of around 920 °C, measured at middle position of the inductor turn.

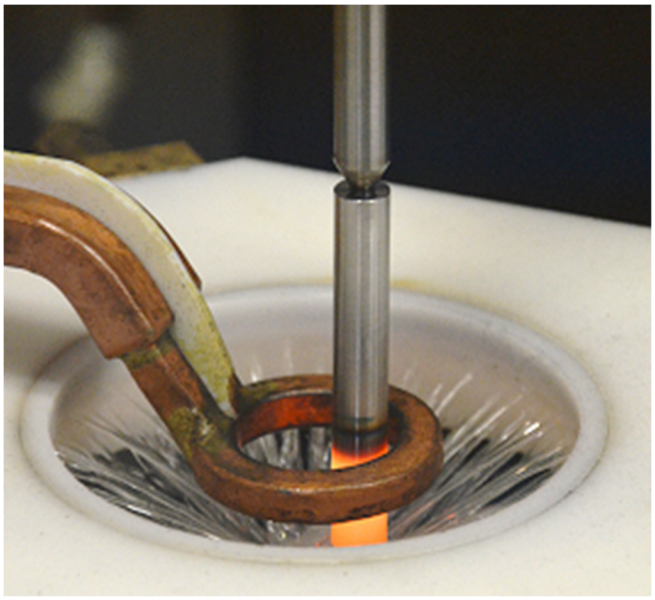

Figure 45: Scan hardening of rod samples

The following hardening parameters were used for all steel grades:

- Scanning speed: 16 mm/s
- Frequency: 100 kHz
- Power: 175 kW
- Quenchant flow: 20 litre/min
- Quenchant: Water based polymer solution (10 %)
- Part rotation: 180 rpm.

After induction hardening the sample were cooled in water (~ 10 °C, 10 minutes) and tempered at 160 °C for 2 hours. Residual stresses were measured beneath the surface (30 µm) in tangential direction using a mobile X-ray diffraction device from Stresstech, type G2. A position sensitive detector was used. More details are given in the below table. Stresses were evaluated according to the $\sin^2\psi$ method (E modulus: 210 GPa, Poisson`s ratio 0.3).

Table 9: *Residual stress measurement settings*

Radiation	CrKα
Diffraction angle 2θ	147°-165°
Lattice plane {hkl}	{211}
Chi angles	9 scans (from +45° until -45°)
X-ray beam diameter	1 mm
Exposure time	20 seconds
Measuring direction	Tangential
Tube voltage/ current	30 kV/ 6.7 mA

After residual stress measurements, the rod samples were cut at half axial height for metallographic investigation, including microstructure examination and radial hardness profile (HV0.5).

3.4 Induction through hardening of RCF rod samples

The samples for rolling contact fatigue testing (rods, diameter 9.53 mm, lengths 100 mm) were induction through hardened, see Figure 46. Through hardening was chosen to exclude the influence of the surface hardening depth on the rolling contact fatigue performance. The pyrometer showed a surface temperature of around 980 °C, measured at half axial inductor lengths.

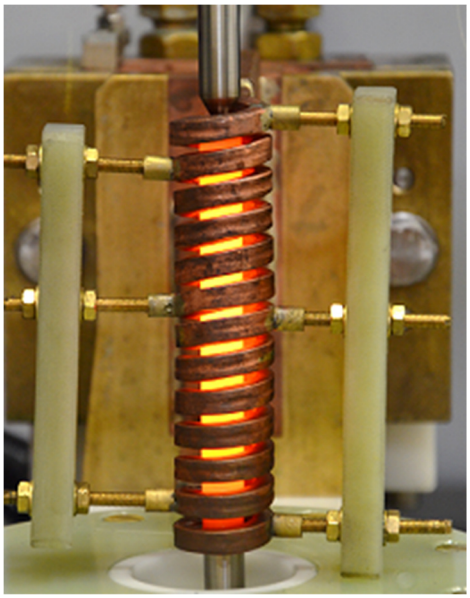

Figure 46: *Through hardening of rolling contact fatigue samples, single shot heating prior to quenching*

The following hardening parameters were used for all samples:

- Frequency: 20 kHz
- Power: 5 kW
- Heating time: 17 seconds
- Quenchant flow: 65 litre/min
- Quenchant: Water based polymer solution (10 %)
- Part rotation: 120 rpm
- Quench delay: 3 seconds.

After induction hardening the sample were cooled in water (~ 10 °C, 10 minutes) and tempered at 160 °C for 2 hours. After heat treatment, the samples were ground and polished prior to rolling contact fatigue testing.

Since 70Mn4 showed a comparably pronounced prior austenite grain growth among the investigated steels (see chapter 4.1), it was decided to include three 70Mn4 rod samples in the investigation. Those samples (70Mn4 LT, 70Mn4 MT, 70Mn4 HT) were quenched from different austenitisation temperatures (910 °C, 975 °C, 1060 °C) to set different degrees of microstructural coarseness.

3.5 RCF testing

In order to carry out RCF testing in a time and cost-efficient way and avoid full scale bearing testing, different RCF testing rigs have been developed. The use of high contact pressures, fast rotation and elevated temperatures shall lead to accelerated fatigue response.

A ball-on-rod rolling contact fatigue tester manufactured by Delta Research Corporation (model BR-4) was used to compare the rolling contact fatigue performance of the investigated steels. The tested sample, a rod, is loaded with three rotating steel balls, guided in between tapered bearing rings. A system with individual adjustable springs applies axial forces on the beforementioned two tapered bearing rings, translating the forces via the rotating balls on the rod in radial direction, see Figure 47. A detailed description of the test rig can be found in [Glo82, Kan13].

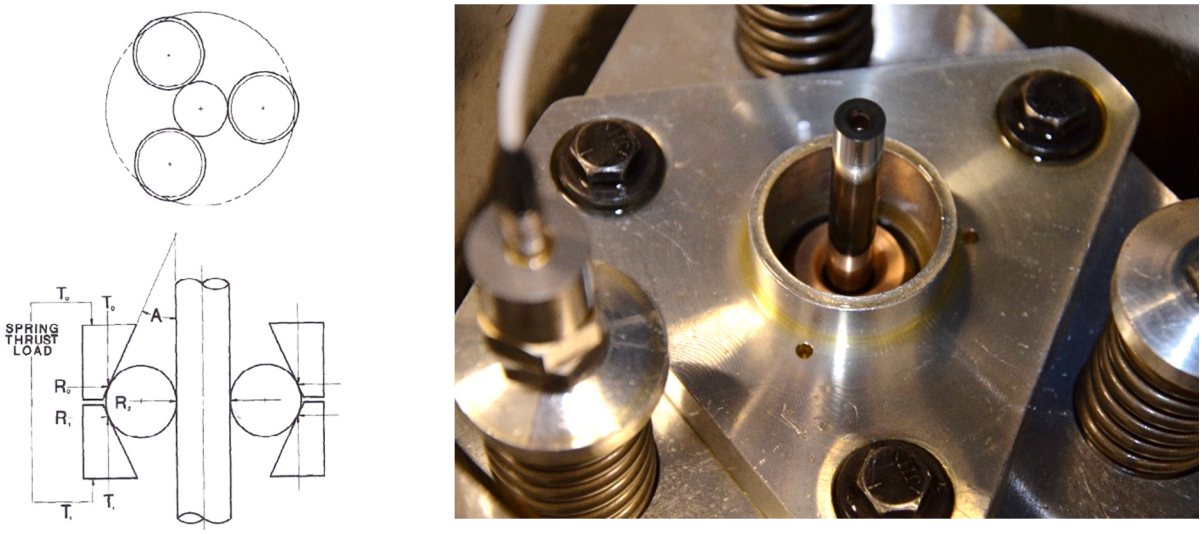

Figure 47: Three balls on the rod test rig; principal sketch (left [Glo82]) and test setup (right)

The main testing conditions and material properties for the load case calculation can be found in Table 10:

Table 10: Main testing conditions and material properties

Sample rotation	3600 rpm
Loading frequency	143.34 Hz or 2.389 cycles per rotation
Lubrication	Oil, BP TO 2380, 10 drops/ minute
Temperature samples during testing	35 °C
Balls	Diameter=12.7 mm, 100Cr6, Ra=0.02 µm
Rods/ samples	Diameter=9.53 mm, Ra=0.05 µm
Calibrated force on 3 springs	760.7 N
Elastic modulus rods and balls	210 GPa
Poisson ratio rods and balls	0.3

The contact pressure p_0, maximal shear stress τ_{max} and depth of maximal shear stress was calculated according to Hertz theory, see Table 11. For the calculation according to Johnson in [Joh03], please see appendix A. The lambda value was calculated according to equation 14, see above.

Table 11: Shear stresses, depth of maximal shear stress, contact pressure and lambda value for Hertz contact and testing conditions according to [Joh03]

Contact pressure p_0	5.57 GPa
Maximal unidirectional shear stress	1.8 GPa
Depth of maximal shear stress	138 µm
Lambda	1.5

In addition, with the help of SKFs simulation tool for general bearing calculation and contact mechanics, the maximal orthogonal shear stress and its depth were calculated. The contact pressure, maximal shear stress and its depth were of the same magnitude, see Table 12.

Table 12: Shear stresses, depth of maximal shear stress, contact pressure for Hertz contact and testing conditions according to SKF BEAST bearing calculation software

Contact pressure p_0	5.45 GPa
Maximal shear stress	1.8 GPa
Depth of maximal shear stress	138 µm
Maximal orthogonal shear stress	1.2 GPa
Depth of maximal orthogonal shear stress	97 µm

On each sample a minimum of seven runs were conducted. Each run was stopped after a defined time or number of load cycles N: 10^3, 10^5, $3x10^5$, 10^6, $3x10^6$, 10^7, $3x10^7$, see also Figure 48 and Figure 49.

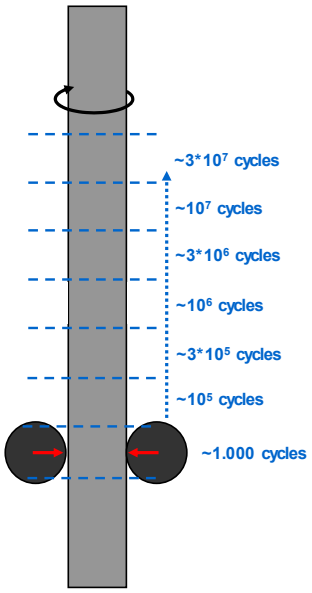

Figure 48: Runs with different load cycles on each sample

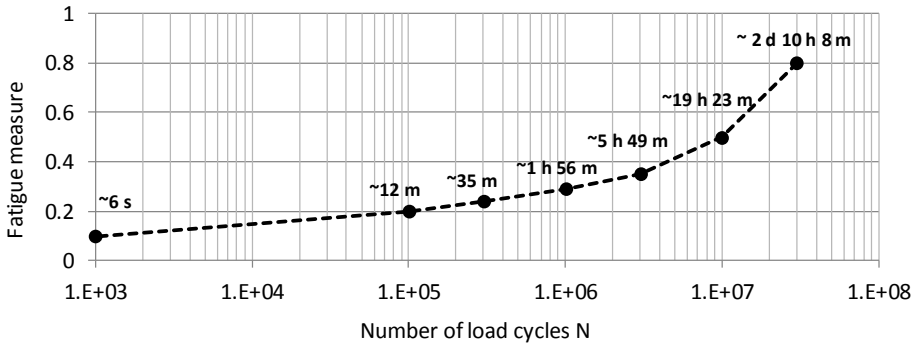

Figure 49: Load cycles and testing times for each sample and hypothetical fatigue development

3.5.1 Groove measurement

In order to quantify the developed fatigue damage, the grooving for each run was measured using a profilometer in axial direction of the sample, see Figure 50 and Figure 51. Each run was measured three times at different circumferential positions.

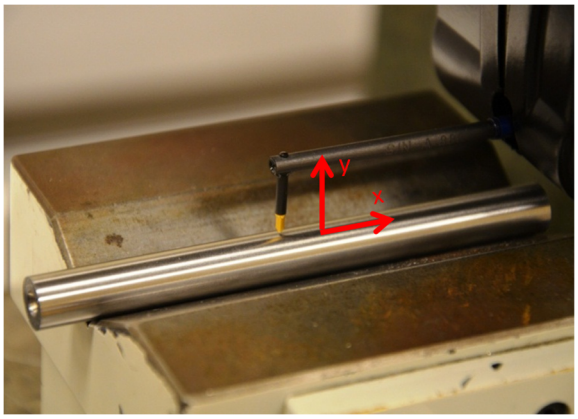

Figure 50: Groove measurement with Talysurf profilometer

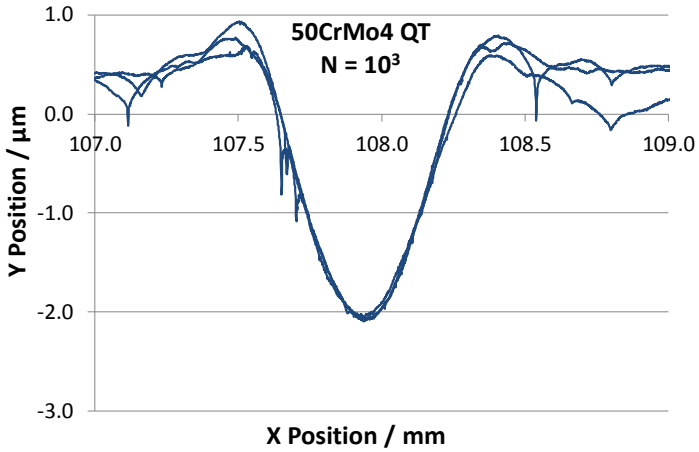

Figure 51: Example of groove measurements for 50CrMo4 QT after N = 10^3 load cycles

The peak-valley measurements were used as a measure for the groove development, see Figure 52.

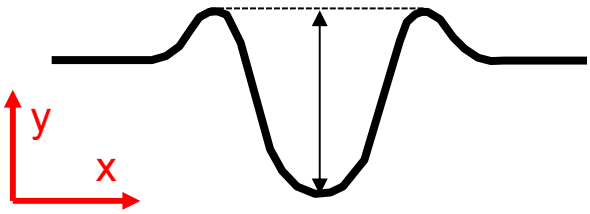

Figure 52: Peak-valley measure for grooving determination

3.5.2 XRD measurement

Residual stresses and retained austenite contents were measured for the fatigued and unaffected material volume. A stationary X-ray device from GE, type X-ray MZ VI E, was used, equipped with an Scinti counter detector. Stresses were evaluated according to the $\sin^2\psi$ method (E modulus: 220 GPa, Poisson`s ratio 0.28) retained austenite determination was done with the help of Topas software. The settings for residual stress and retained austenite content determination are shown in Table 13 and Table 14.

Table 13: Residual stress measurement settings

Radiation	CrKα
Diffraction angle 2θ	147°-165°
Lattice plane {hkl}	{211}
Step width	0.1 °
Chi angles	15 scans (from +45° until -45°)
X-ray beam diameter	~ 300 µm
Exposure time	10 seconds
Measuring direction	Tangential
Tube voltage/ current	33 kV/ 40 mA

Table 14: Retained austenite measurement settings

Radiation	CrKα
Diffraction angle 2θ	63°-165°
Step width	0.05 °
X-ray beam diameter	~ 300 µm
Exposure time	12 seconds
Tube voltage/ current	33 kV/ 40 mA

The measurements were made for the fatigued and the unaffected volume, see Figure 53 and Figure 54.

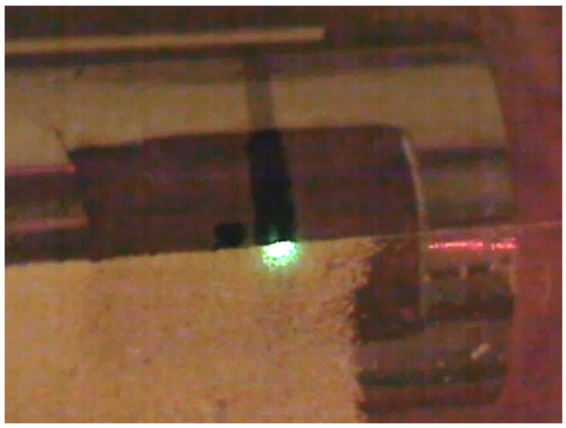

Figure 53: X-ray beam positioning on fatigued volume at 140 µm depth

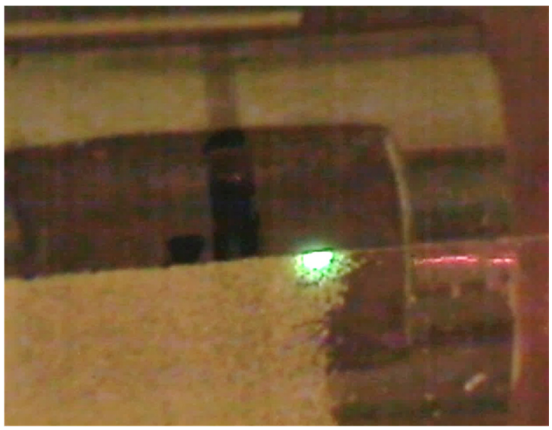

Figure 54: X-ray beam positioning on unaffected/ reference volume at 140 µm depth

For the determination of the measuring depth, one residual stress profile was measured on sample Ovako 832 QT, see Figure 55 and Figure 56. The depth of maximum compressive stress coincides with the depth of maximal shear stress (~ 140 µm), whereas the minimum in FWHM was measured at around 100 µm and 140 µm. For the retained austenite measurement, no clear difference between the depth of 100 µm and 140 µm was observed keeping in mind a standard deviation of ~ 2 % (see Figure 57). It was decided to measure stresses and retained austenite at a depth of 140 µm (depth of maximal unidirectional shear stress).

The material removal was done with electrochemical etching using a mixture of phosphoric acid and sulphuric acid.

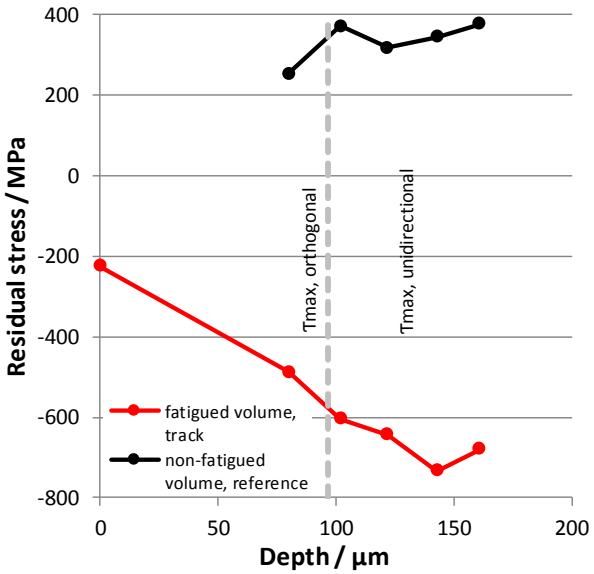

Figure 55: Residual stress profile for fatigued and reference volume of Ovako 832 QT

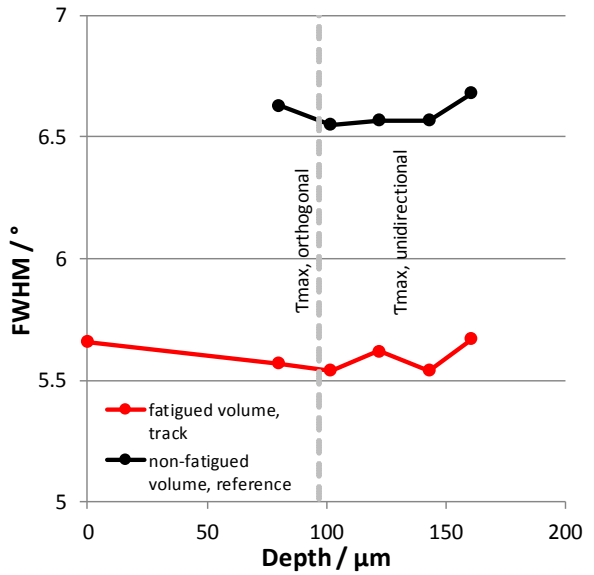

Figure 56: FWHM profile for fatigued and reference volume of Ovako 832 QT

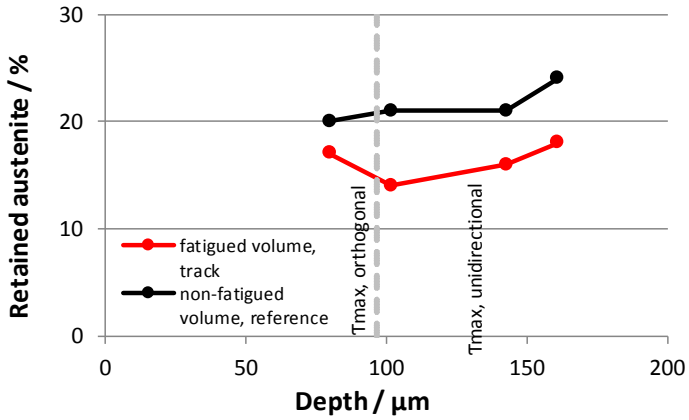

Figure 57: Retained austenite profile for fatigued and reference volume of Ovako 832 QT

3.5.3 Metallography

After rolling contact fatigue testing and X-ray diffraction measurements, the rods were cut as shown below (Figure 58, cutting disc 0.5 mm thick, coolant). For the metallographic examinations, the longest fatigue runs were used (N = $3x10^7$). The tracks were cut of the rod in radial direction, halved in axial direction, the circumferential sections were embedded, ground and polished. For each sample, several circumferential sections were examined. Around 50 µm were removed by fine grinding in axial direction for each section until the middle position of the track was reached. In average 14 sections were examined per sample.

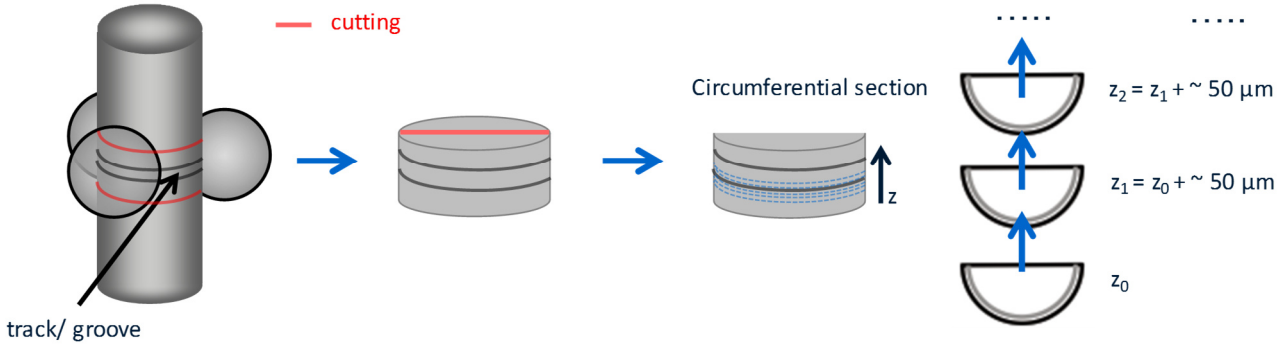

Figure 58: Sampling for metallographic investigations of fatigue tested rods

The sections were examined in etched and unetched condition. For the hardness development along the track Vickers hardness (HV 0.5) was measured in 100 µm and 200 µm radial depth, 3 measurements each. Microstructural alterations as described in chapter 2.4.3 and the occurrence of cracks were documented in un-etched and etched condition. Nital (1.5 % HNO_3 in Ethanol, etching time ~ 25 seconds) was used as a matrix etchant. The documentation was done with a microscope type Zeiss Axio Imager in 200x, 500x and 1000x magnification. In order to minimise the thermal effect of sample embedding on potential microstructural alterations or work hardening or softening effects, the embedding temperature was reduced to 140 °C (for 7 minutes).

4 Results

4.1 Dilatometer testing

Figure 59 until Figure 64 show the as quenched hardness and measured M_S temperatures of 100Cr6. As an example, prior austenite grain sizes (PAGSs) and dilatation curves in the temperature regime of martensite transformation during quenching are also shown for 100Cr6.

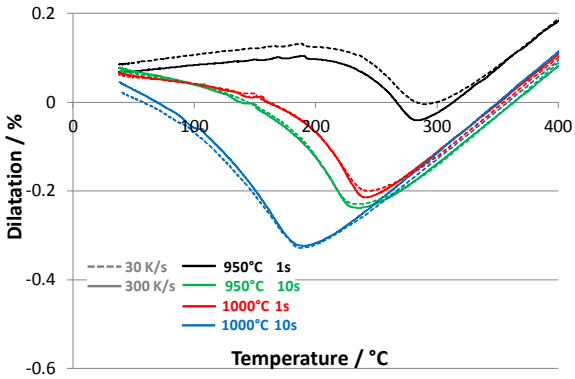

Figure 59: Dilatometer curves for quenching from different austenitisation conditions – 100Cr6 SA

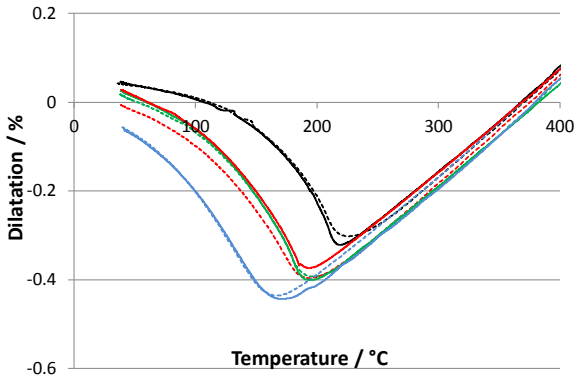

Figure 60: Dilatometer curves for quenching from different austenitisation conditions – 100Cr6 QT

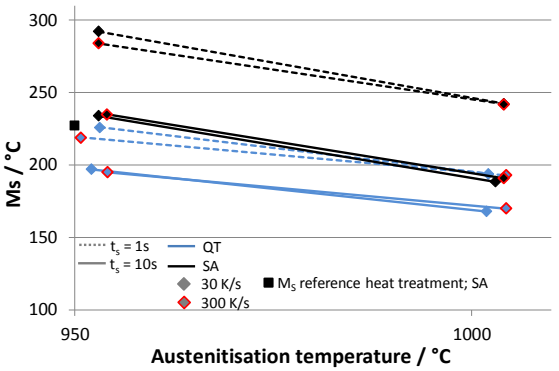

Figure 61: M_s temperatures determined from dilatometer curves (local minima) for different austenitisation degrees – 100Cr6

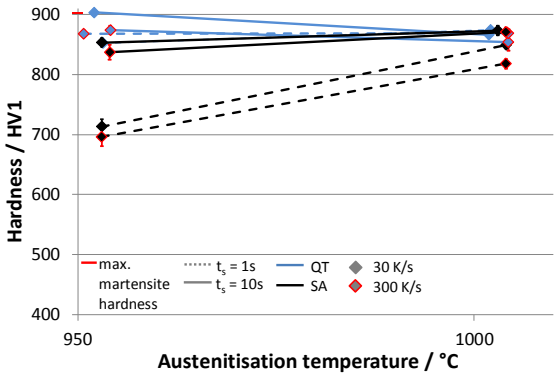

Figure 62: Hardness depending on austenitisation conditions; maximum, carbon depending martensite hardness according to [Lie03] - 100Cr6

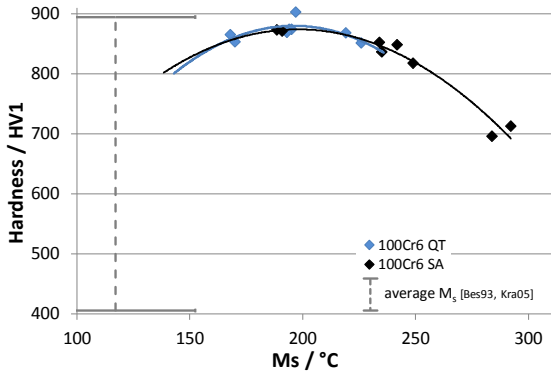

Figure 63: Hardness - M_s values and theoretical M_s for full dissolution of all alloying elements [Bes93, Kra05]; error bars show standard deviation – 100Cr6

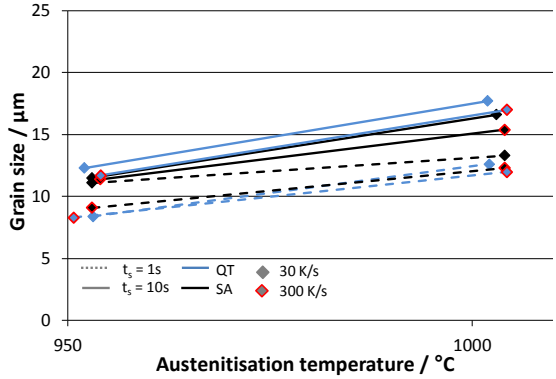

Figure 64: Prior austenite grain size depending on austenitisation conditions – 100Cr6

Figure 65 until Figure 70 show the results for Ovako 832 (left) and 50CrMo4 (right).

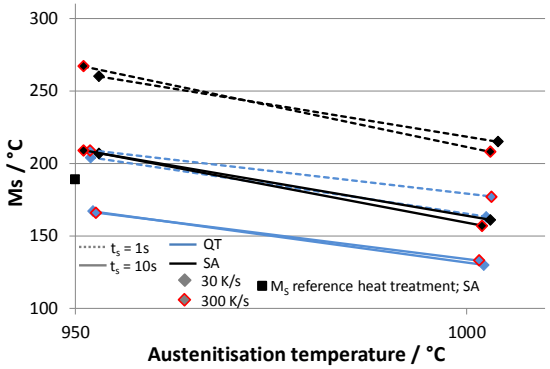

Figure 65: M_s temperatures determined from dilatometer curves (local minima) for different austenitisation degrees – Ovako 832

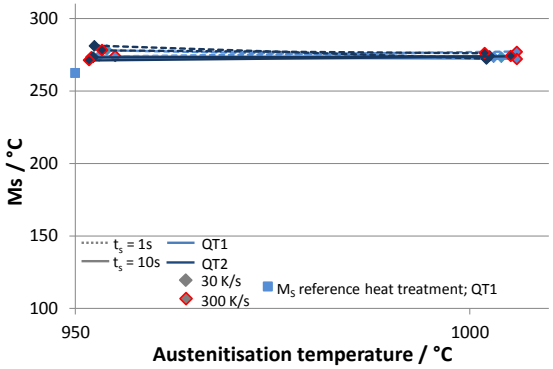

Figure 66: M_s temperatures determined from dilatometer curves (local minima) for different austenitisation degrees – 50CrMo4

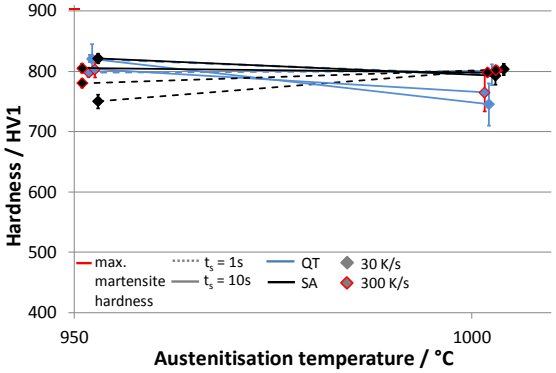

Figure 67: Hardness depending on austenitisation conditions; maximum, carbon depending martensite hardness according to [Lie03] – Ovako 832

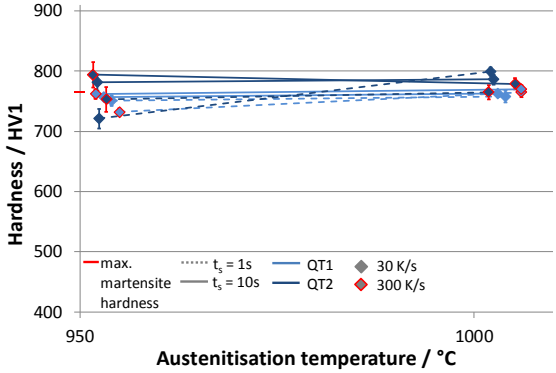

Figure 68: Hardness depending on austenitisation conditions; maximum, carbon depending martensite hardness according to [Lie03] – 50CrMo4

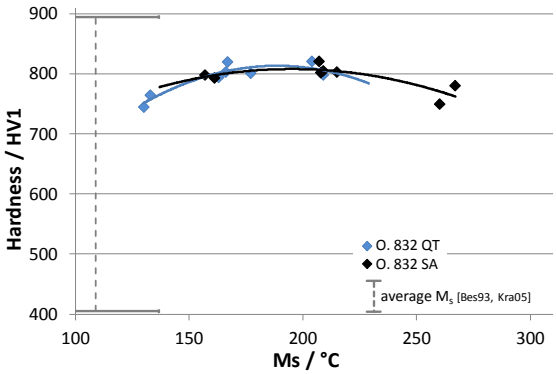

Figure 69: Hardness - M_s values and theoretical M_s for full dissolution of all alloying elements [Bes93, Kra05]; error bars show standard deviation – Ovako 832

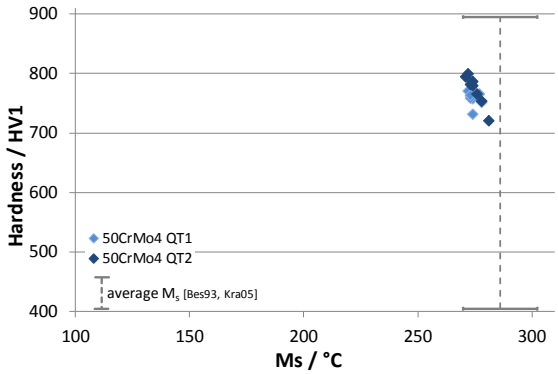

Figure 70: Hardness - M_s values and theoretical M_s for full dissolution of all alloying elements [Bes93, Kra05]; error bars show standard deviation – 50CrMo4

Figure 71 until Figure 76 show the results for 67SiCr5 (left) and 70Mn4 (right).

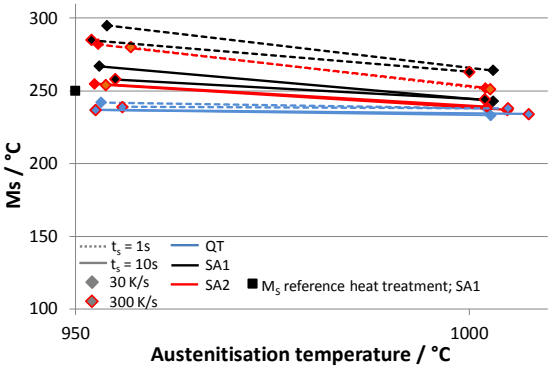

Figure 71: M_s temperatures determined from dilatometer curves (local minima) for different austenitisation degrees – 67SiCr5

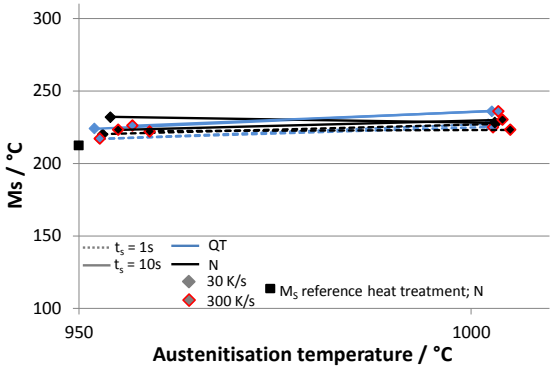

Figure 72: M_s temperatures determined from dilatometer curves (local minima) for different austenitisation degrees – 70Mn4

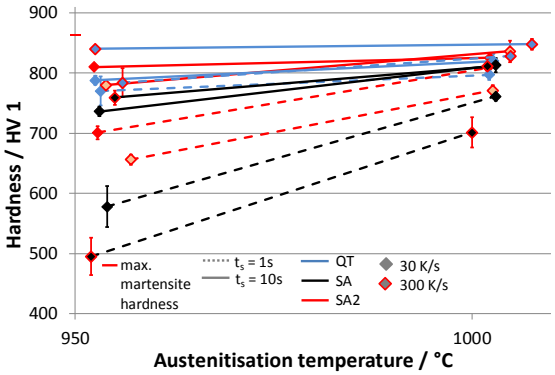

Figure 73: Hardness depending on austenitisation conditions; maximum, carbon depending martensite hardness according to [Lie03] – 67SiCr5

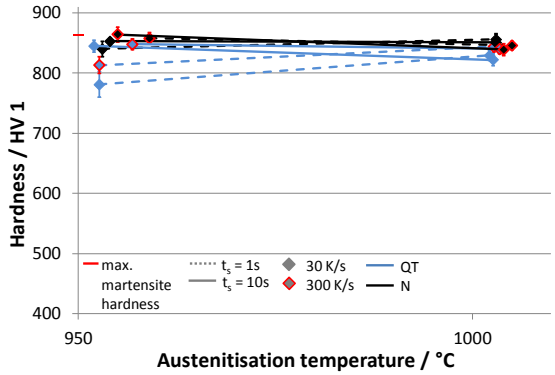

Figure 74: Hardness depending on austenitisation conditions; maximum, carbon depending martensite hardness according to [Lie03] – 70Mn4

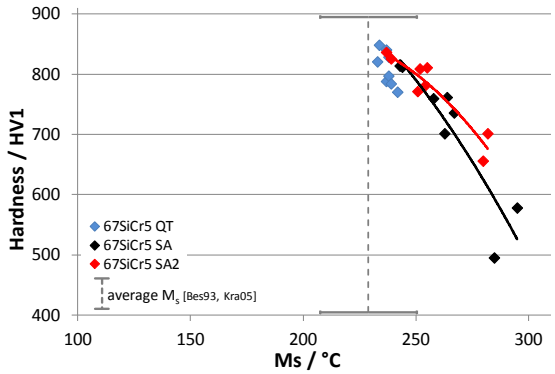

Figure 75: Hardness - M_s values and theoretical M_s for full dissolution of all alloying elements [Bes93, Kra05]; error bars show standard deviation – 67SiCr5

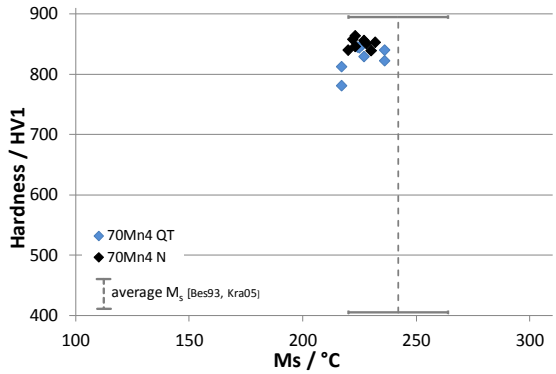

Figure 76: Hardness - M_s values and theoretical M_s for full dissolution of all alloying elements [Bes93, Kra05]; error bars show standard deviation – 70Mn4

Figure 77 until Figure 79 show the results for Ovako 677.

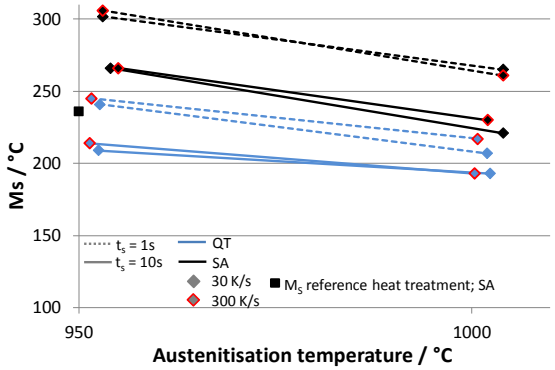

Figure 77: M_s temperatures determined from dilatometer curves (local minima) for different austenitisation degrees – Ovako 677

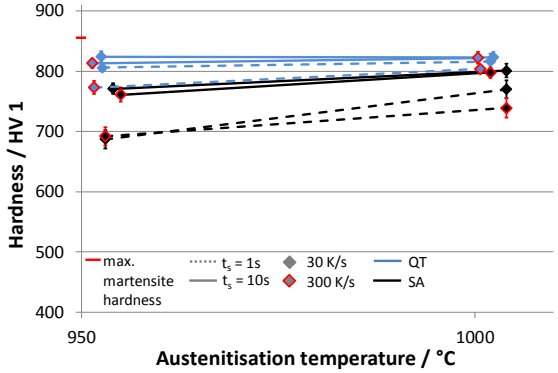

Figure 78: Hardness depending on austenitisation conditions; maximum, carbon depending martensite hardness according to [Lie03] – Ovako 677

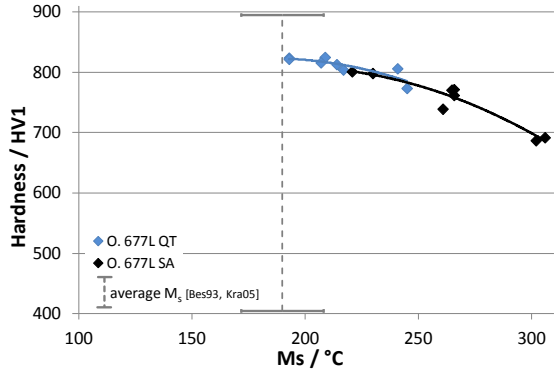

Figure 79: Hardness - M_s values and theoretical M_s for full dissolution of all alloying elements [Bes93, Kra05]; error bars show standard deviation – Ovako 677

Table 15 shows micrographs of the dilatometer samples in SA or N condition, heat-treated with the lowest and highest austenitisation degree. For 100Cr6 NMTPs (non-martensitic transformation products) are visible. The dilatation curves for the lowest austenitisation degree (300 K/s, 950 °C, 1 s) of 100Cr6 SA showed a deflection during quenching at temperatures of around 550 °C – 650 °C, typically indicating a diffusion controlled transformation of austenite (NMTPs). The amount of NMTPs on the micrographs of 100Cr6 SA was

clearly decreased for higher austenitisation degrees, however, NMTPs could not be fully avoided. NMTPs also appear for 67SiCr5 SA1 and, to a smaller extent, for SA2 as well as for 70Mn4 N. The dilatation curves for the lowest austenitisation degree (300 K/s, 950 °C, 1 s) of 67SiCr5 SA1 showed a deflection during quenching at temperatures around 550 °C – 650 °C, typically indicating a diffusion controlled transformation of austenite (NMTPs). The amount of NMTPs on the micrographs was clearly decreased from 67SiCr5 SA1 to 67SiCr5 SA2 prior condition. Increasing austenitisation degree clearly reduces the amount of NMTPs in case of 67SiCr5 SA1 and SA2. Ovako677 SA did not reveal NMTPs.

Table 15: Micrographs of dilatometer samples in SA or N condition, heat-treated with the lowest and highest austenitisation degree

100Cr6 SA	Ovako 832 SA	67SiCr5 SA1	
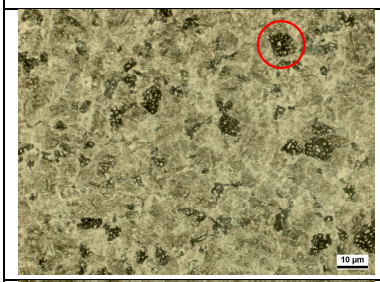	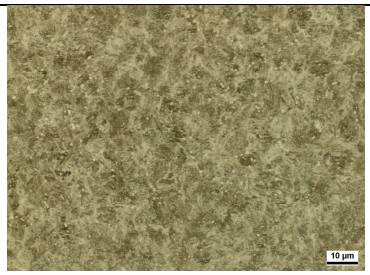	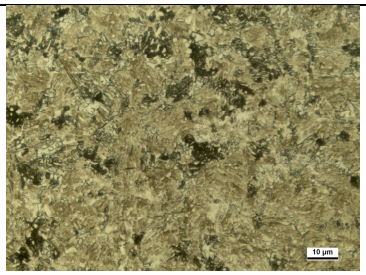	heating rate 300 K/s T_A 950 °C t_s 1 s
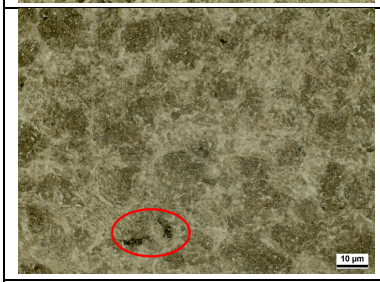	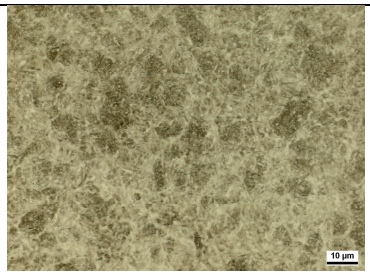	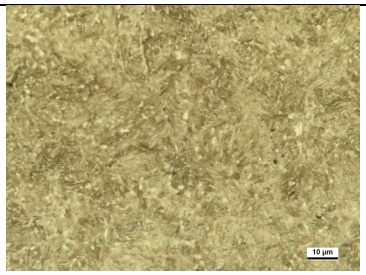	heating rate 30 K/s T_A 1000 °C t_s 10 s
67SiCr5 SA2	**70Mn4 N**	**Ovako 677 SA**	
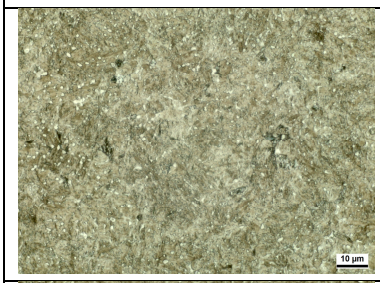	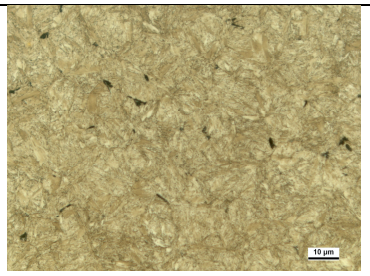	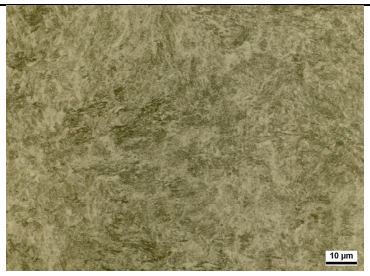	heating rate 300 K/s T_A 950 °C t_s 1 s
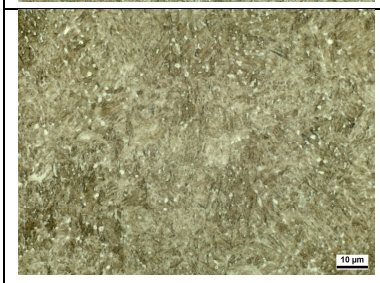	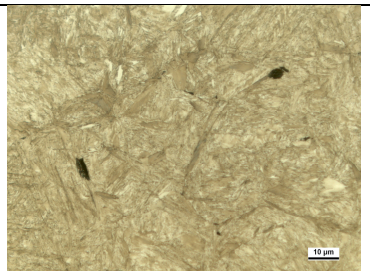	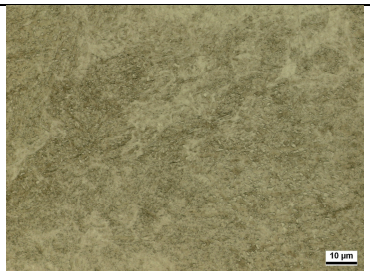	heating rate 30 K/s T_A 1000 °C t_s 10 s

Table 16 shows micrographs of dilatometer samples in QT condition, heat-treated with the lowest and highest austenitisation degree. 100Cr6 shows very few and small spots of NMTPs, which disappear for higher austenitisation degrees. Ovako 832 QT and 50CrMo4 QT did not reveal any NMTPs. 50CrMo4 QT2 micrographs were similar to the ones of 50CrMo4 QT1 and are therefore not shown.

Table 16: Micrographs of dilatometer samples in QT condition, heat-treated with the lowest and highest austenitisation degree

100Cr6 QT	Ovako 832 QT	50CrMo4 QT1	
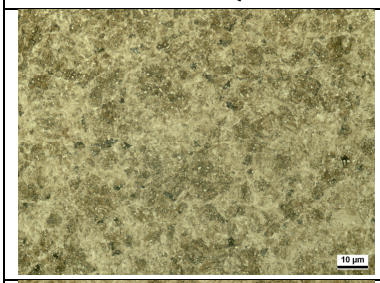	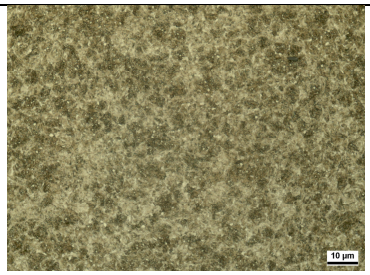	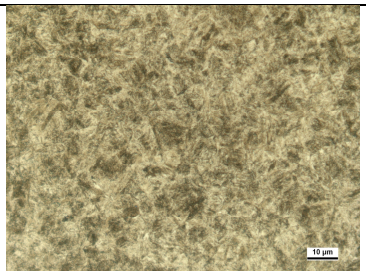	heating rate 300 K/s T_A 950 °C t_s 1 s
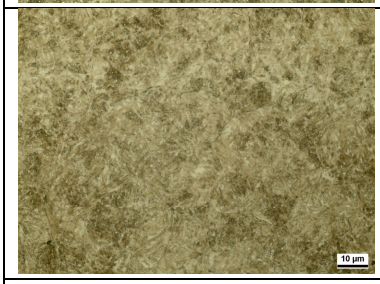	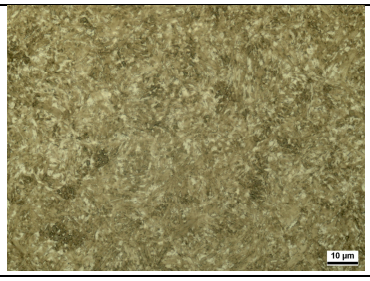	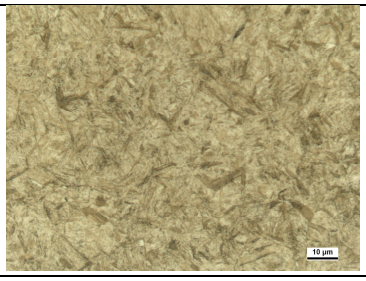	heating rate 30 K/s T_A 1000 °C t_s 10 s
67SiCr5 QT	**70Mn4 QT**	**Ovako 677 QT**	
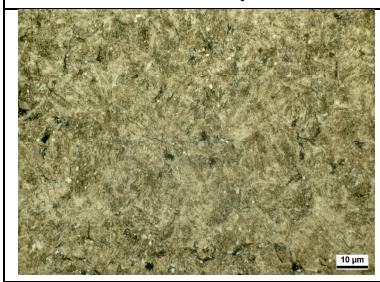	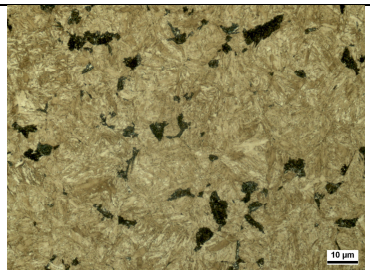	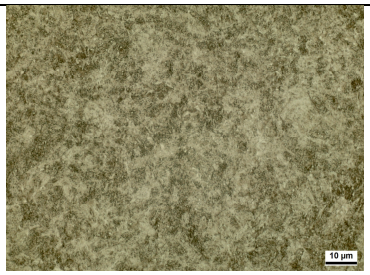	heating rate 300 K/s T_A 950 °C t_s 1 s
	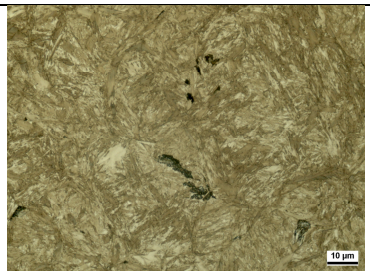		heating rate 30 K/s T_A 1000 °C t_s 10 s

Due to the similar behaviour of 70Mn4 in normalised and quench and tempered condition, it was decided to continue without 70Mn4 QT from hereon. For steel 67SiCr5 the starting structure SA was dropped and replaced by SA2.

4.2 Transfer of dilatometer study on surface induction hardened rod samples

The results from metallography and X-ray diffraction measurements are shown below. A clear difference in terms of surface hardening depth, maximum surface hardness, hardness decrease towards the rod centre, hardness gradient within the transition zone and residual stress level is evident.

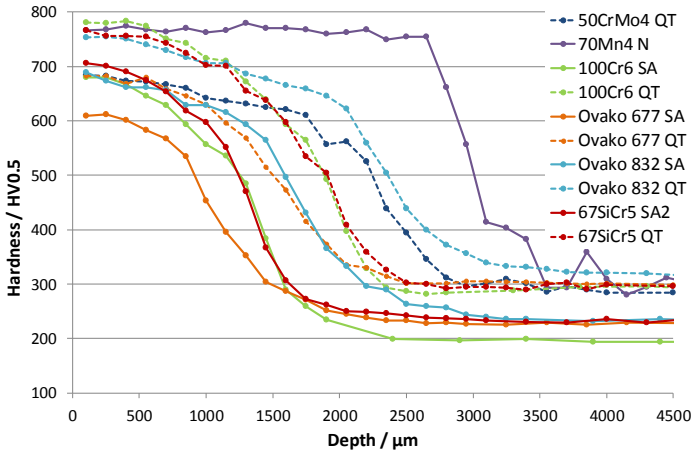

Figure 80: Hardness profiles (average profile of 3 profiles) for surface induction hardened samples

Table 17: Residual stress measurement on surface induction hardened rod samples

Steel	Tangential residual stress / MPa	Standard deviation / MPa
70Mn4 N	75.7	20.3
50CrMo4 QT	-174.8	9.5
67SiCr5 QT	-109.4	18.2
67SiCr5 SA2	-268.5	20.8
Ovako 832 QT	-29.4	29.5
Ovako 832 SA	-264.1	26.3
100Cr6 QT	-91.8	10.4
100Cr6 SA	-391.4	14.6
Ovako 677 QT	-315.2	20.8
Ovako 677 SA	-604.4	19.1

The **surface hardening depth** ranges from 0.8 mm until 3.0 mm. QT starting structures show generally larger hardening depths.

For the definition and characterization of the **transition zone** between hardened surface and soft core, the hardness gradient within the transition zone was determined. The hardness gradient was determined for the depths where the A_{c1}/ A_{c1b} and A_{c3}/ A_{c1e} temperatures were assumed. Hardness profiles and micrographs were used to define the depth where the A_{c1}/ A_{c1b} and A_{c3}/ A_{c1e} temperatures were reached. A_{c1}/ A_{c1b} temperatures were determined at the first hardness increase from core hardness towards the surface. A_{c3}/ A_{c1e} temperatures were determined at a depth where the core structure disappeared and no untransformed core material was present (see also Figure 81, Figure 83, Figure 84). The sharpest drop from hardened case to soft core was measured for sample 70Mn4 N, followed by 50CrMo4 QT. Samples with QT starting structures showed generally larger hardness gradients than SA starting structures (see Figure 82).

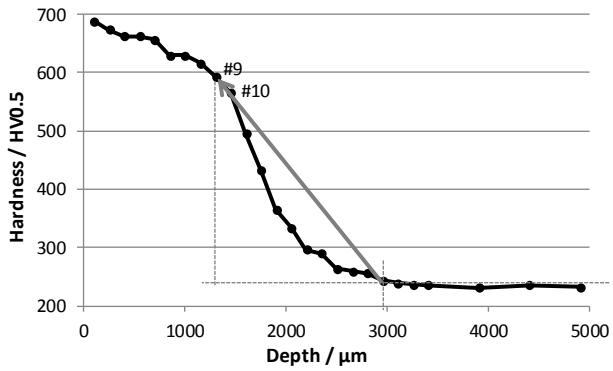

Figure 81: Hardness profile of Ovako 832 SA and characterization of transition zone

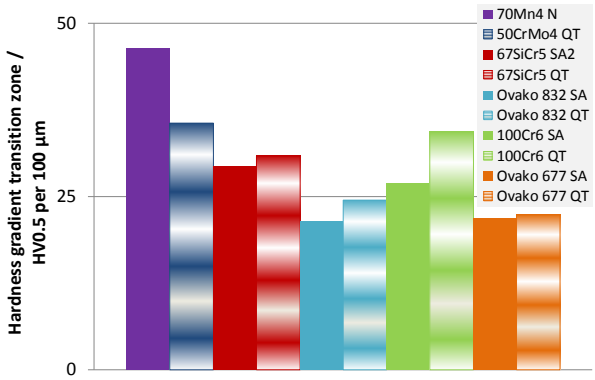

Figure 82: Hardness gradients in transition zone for surface induction hardened rod samples

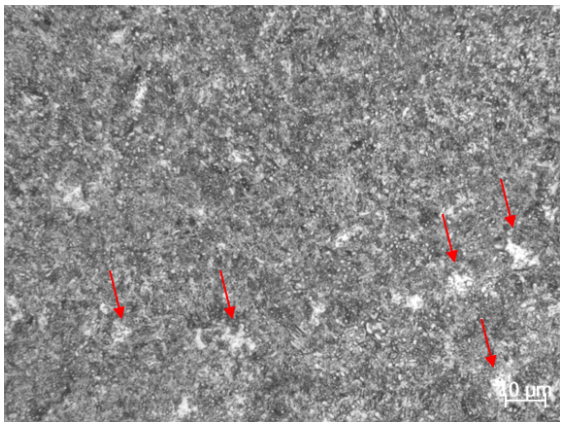

Figure 83: Micrograph at hardness indent #10 with not transformed starting structure (red arrows)

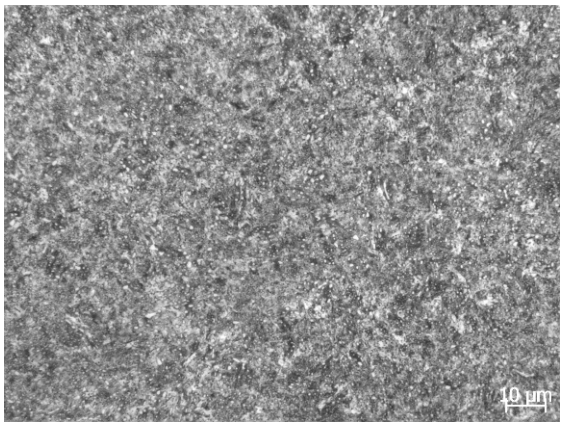

Figure 84: Micrograph at hardness indent #9, no untransformed starting structure

The **hardness gradient or hardness decrease in radial direction** was determined between the first hardness indent at 100 µm and the 6th indent at a depth of 850 µm. The results are shown in Figure 85. 70Mn4 N and 50CrMo4 QT show the smallest gradients or the flattest hardness profiles. QT starting structures resulted in smaller gradients than SA starting structures.

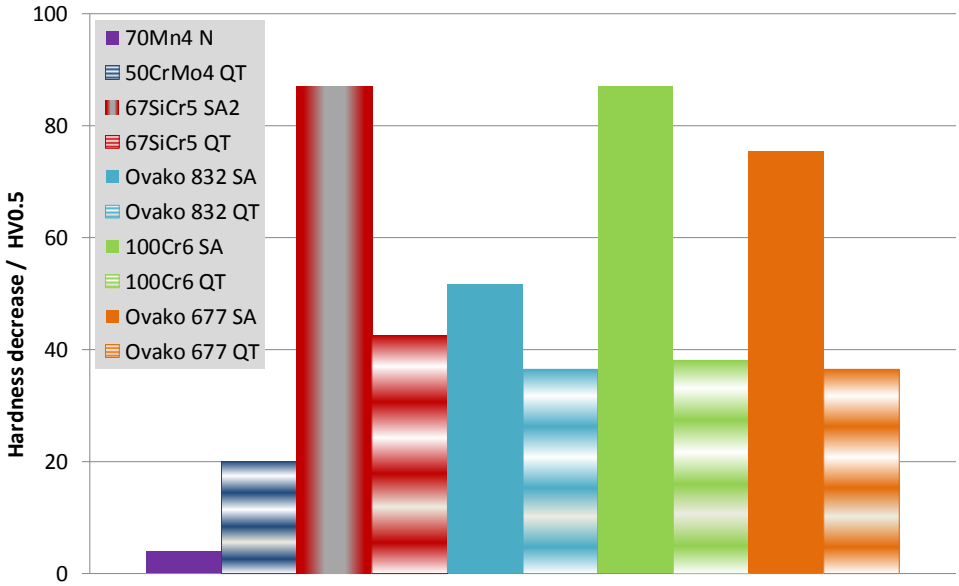

Figure 85: Hardness decrease between hardness indents at 100 µm and 850 µm depth in the hardened layer of the surface hardened rod samples

4.3 RCF testing

In the following chapters, the quantification of rolling contact fatigue damage in terms of

- Grooving
- XRD characterization (RS, RA, FWHM)
- Metallography (examples, hardness, observations/ WEA/ cracks)

will be shown.

4.3.1 Grooving

The grooving or plasticity after fatigue testing is shown in Figure 86. The steels show a slight increase in grooving over time or number of load cycles. A higher initial grooving leads generally to a more pronounced increase in groove depths with increased number of load cycles. Increased hardness before testing resulted in smaller grooving and smaller increase in grooving with an increased number of load cycles. The comparison of SA and QT starting microstructures does not reveal a clear difference.
As for 70Mn4, a higher austenitisation temperature leads to a more pronounced grooving.

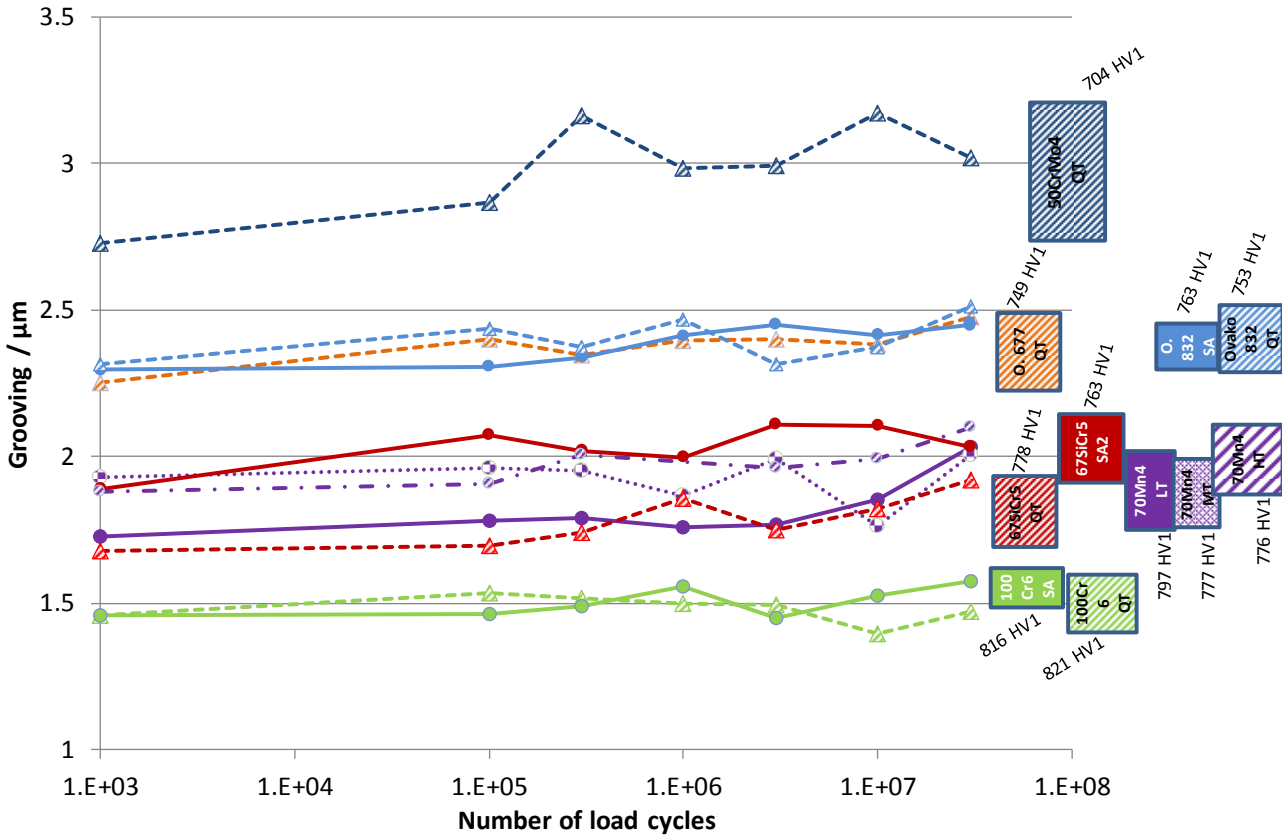

Figure 86: Measured grooving (peak-valley) for different numbers of load cycles after fatigue testing

4.3.2 XRD measurement

Figure 87 and Figure 88 show the measured **residual stresses** in the reference and fatigued volume, as well as the difference in stresses.

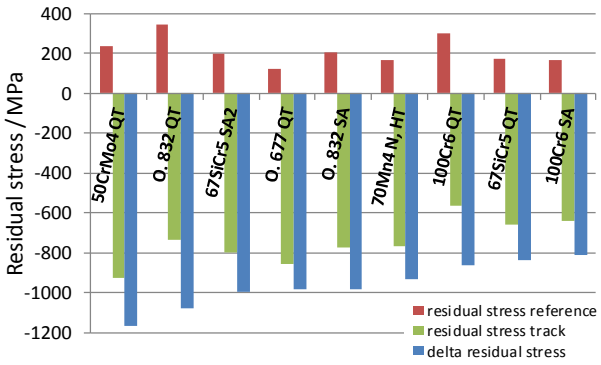

Figure 87: Residual stresses of the unloaded reference volume, loaded track and the difference in stress in a depth of 140 µm; values sorted from large to small delta in residual stress

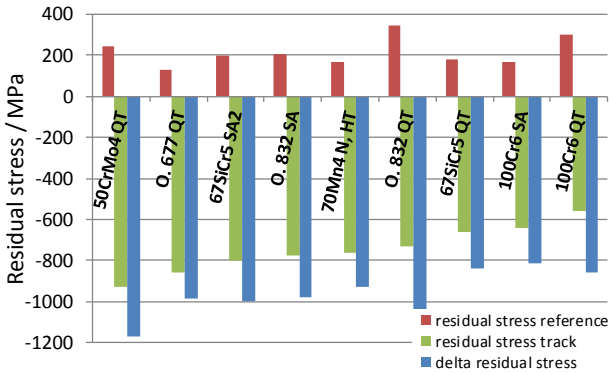

Figure 88: Residual stresses of the unloaded reference volume, loaded track and the difference in stress in a depth of 140 µm; values sorted from large to small residual stress in track volume

Considerable tensile stresses were measured for the unloaded material volume, which are partly higher than what would be expected for martensitic through hardening (~ 50 MPa). The reasons could be different ones, ranging from the used austenitisation conditions to the used quenching conditions.

After N = $3x10^7$ load cycles, a maximum of -900 MPa developed in the fatigued volume of 50CrMo4. It is 50CrMo4 which also exhibits the largest change in residual stress of 1170 MPa. Steel grades Ovako 832, 100Cr6 and 67SiCr5 build up less compressive stresses in the fatigued material volume for the QT starting structures than for the SA microstructures.

The **full width half maximum** values for the fatigued and non-fatigued material volumes are shown in Figure 89 and Figure 90.

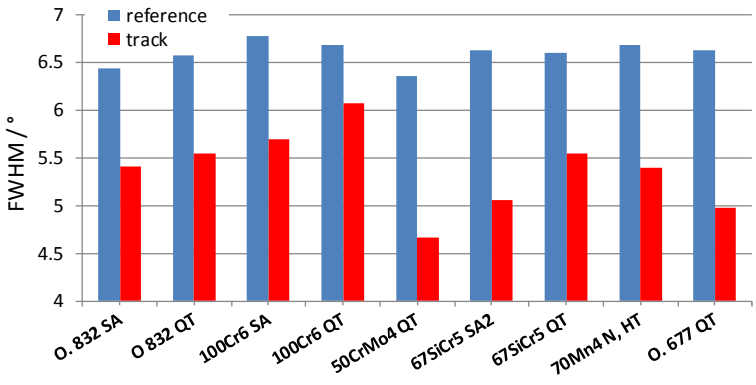

Figure 89: Full width half maximum (FWHM) of the unloaded reference volume and the loaded track in a depth of 140 µm

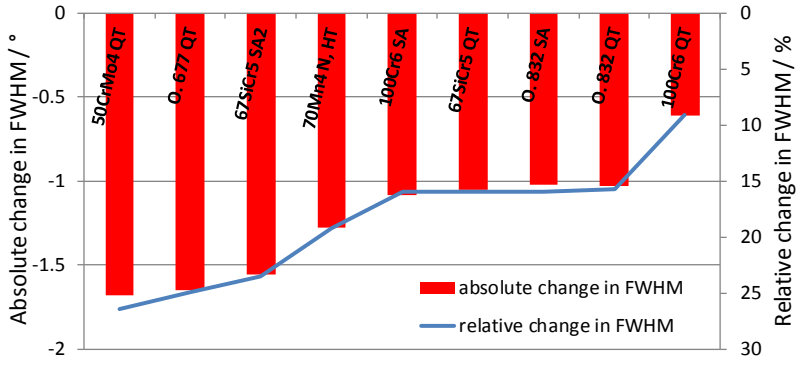

Figure 90: Absolute and relative change in full width half maximum (FWHM) of the unloaded reference volume and the loaded track in a depth of 140 µm; values sorted from large to small change in FWHM

The FWHM values decrease during rolling contact fatigue between 9 % and 26 % of its reference values. The decrease is most pronounced for 50CrMo4, Ovako 677 and 67SiCr5 SA, while 100Cr6 QT shows least reduction in FWHM.

Retained austenite contents of the fatigued and non-fatigued material volumes are shown in Figure 91 and Figure 92.

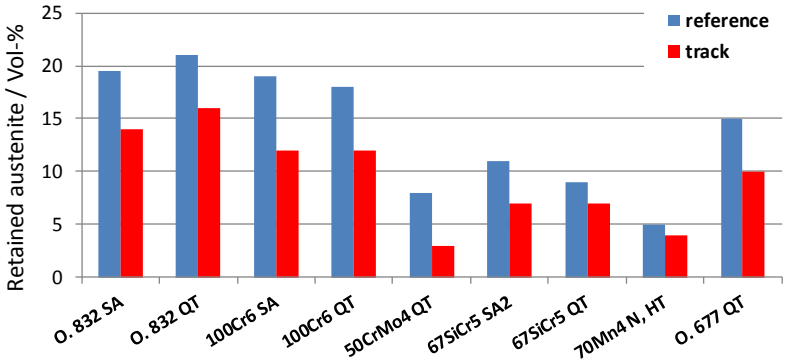

Figure 91: Retained austenite of the unloaded reference volume and the loaded track in a depth of 140 µm

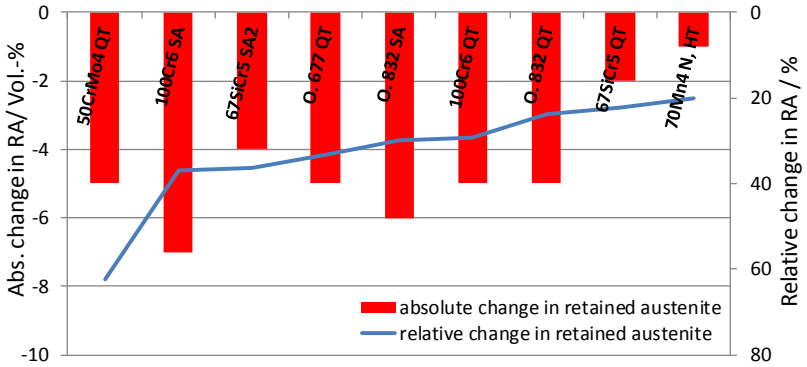

Figure 92: Absolute and relative change in retained austenite (RA) of the unloaded reference volume and the loaded track in a depth of 140 µm; values sorted from large to small change in relative RA

The content in retained austenite decreases after rolling contact fatigue whereas steel grade 50CrMo4 experienced the largest relative decrease of 63 %. Steel grades 67SiCr5 QT and 70Mn4 N, HT showed the smallest absolute and relative reduction in retained austenite. Generally, QT starting microstructures experience less reduction in retained austenite than SA starting microstructures.

4.3.3 Metallography

The fatigued samples contained many different microstructural alterations. A few examples are given in Table 18. Butterflies around non-metallic inclusions, cracks around non-metallic inclusions, longer cracks with white etching features were among the most frequent.

Table 18: Typical examples of microstructural alterations after rolling contact fatigue

<table>
<tr>
<td> 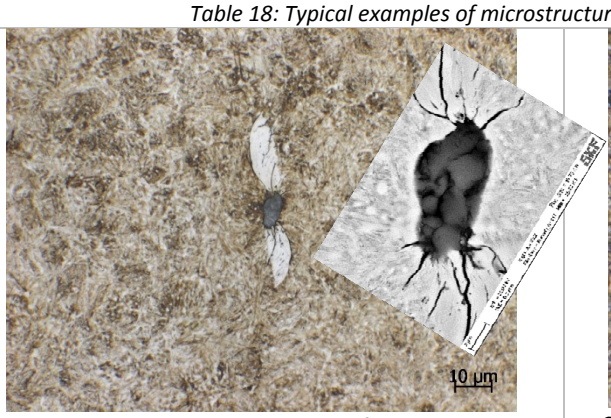

Butterfly in 100Cr6 steel after 1.5x10^6 load cycles in a depth of 303 µm below the contact surface, starting at an oxide inclusion</td>
<td> 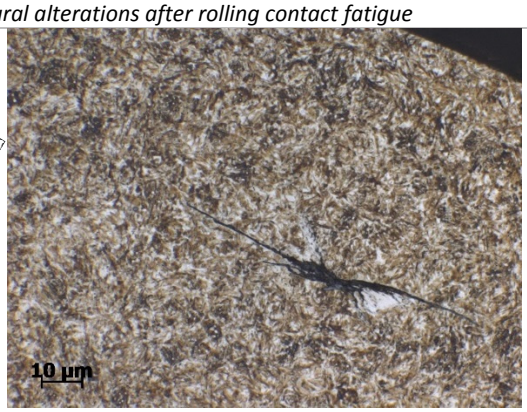

Crack with white etching features in grade 2 steel after 3x10^7 load cycles in a depth of 65 µm below the contact surface, starting at a MnS inclusion</td>
</tr>
<tr>
<td> 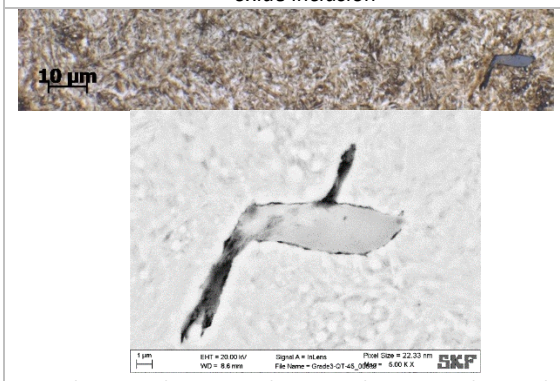

Cracks around a MnS inclusion without any white etching features in grade 2 steel after 3x10^7 load cycles</td>
<td> 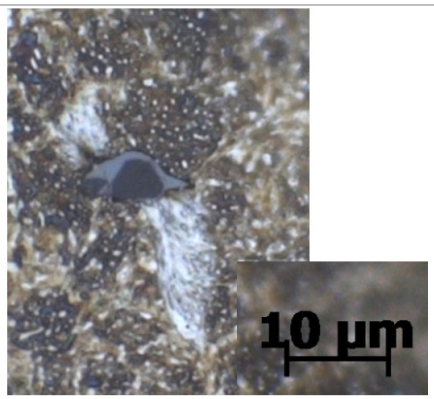

Butterfly at an inclusion type Manganesesulfide (+ Oxide)</td>
</tr>
</table>

Examples of hardness development and development of microstructural observations along the axial track direction are shown in Figure 93 and Figure 94. For all steels, a hardness increase or work hardening towards the track center was measured. The number of observations generally increase towards the track center, where the highest contact pressure can be expected.

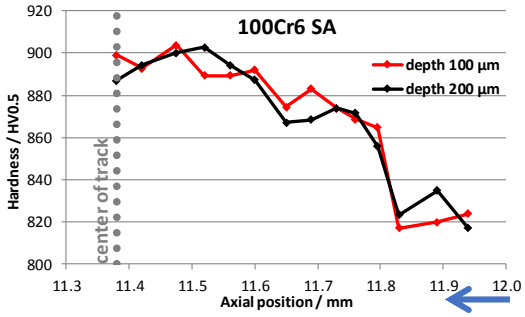

Figure 93: Example of hardness evolution along the track in axial rod direction; 100Cr6 SA after 3x10^7 load cycles

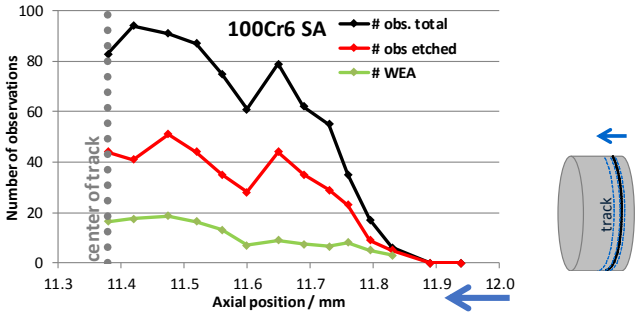

Figure 94: Example of observations (total number, observations in etched condition, number of white etching features) along the track in axial rod direction; 100Cr6 SA after 3x10^7 load cycles

The most pronounced work hardening behavior was measured for steel grade Ovako 832, see Figure 95. The smallest hardness increase was measured for 70Mn4 N and 67SiCr5 SA2. Due to a wrong mounting procedure (repeated mounting at elevated temperature 160 °C) for 67SiCr5 QT and a potential hardness decrease due to an additional tempering effect, the sample should be disregarded.

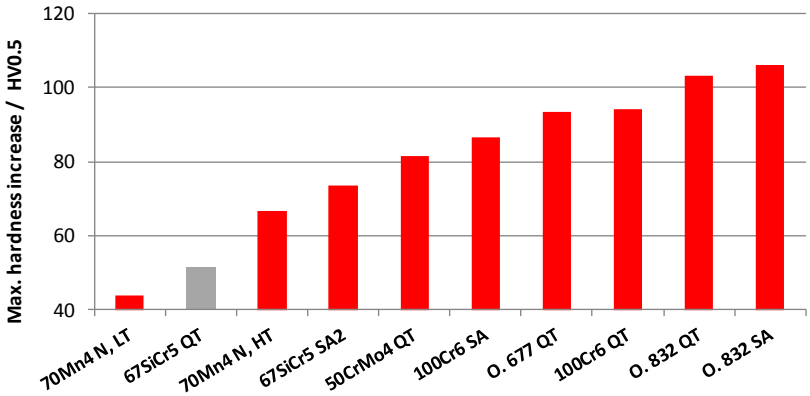

Figure 95: Maximum hardness increase/ work hardening after RCF testing (3x10^7 load cycles); note that 67SiCr5 QT was reduced in hardness due to wrong mounting procedure

Figure 96 until Figure 98 show the quantification of the observed microstructural alterations in terms of total number of observations (including all observations in un-etched and etched sample condition), number of observations in etched sample condition and number of observation with accompanied white etching area. A larger number of observations were documented for steel grade 70Mn4 N, HT, while Ovako 677 QT showed only a small number of observations. The number of observations with accompanied white etching area appeared smallest for Ovako 677 QT, while 50CrMo4 QT, 100Cr6 and 70Mn4 revealed a comparably large share.

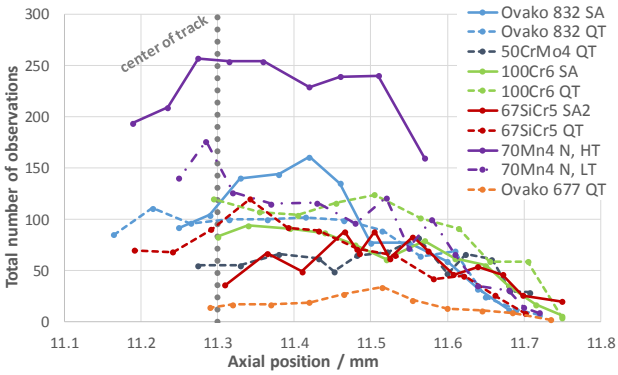

Figure 96: Total number of observation (# obs. total) after fatigue testing for N = 3x10^7 load cycles; sum of observations in etched and unetched condition

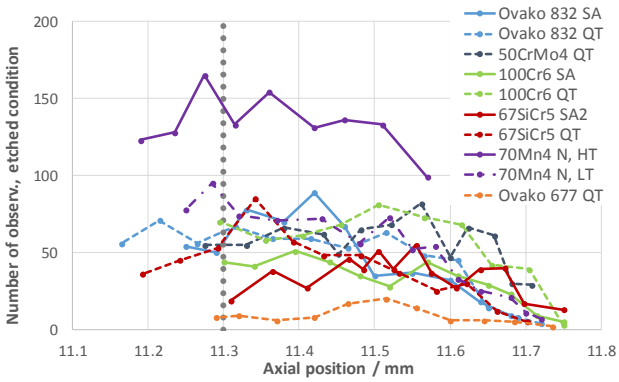

Figure 97: Number of observation (# obs. etched) in etched condition after fatigue testing for N = 3x10^7 load cycles

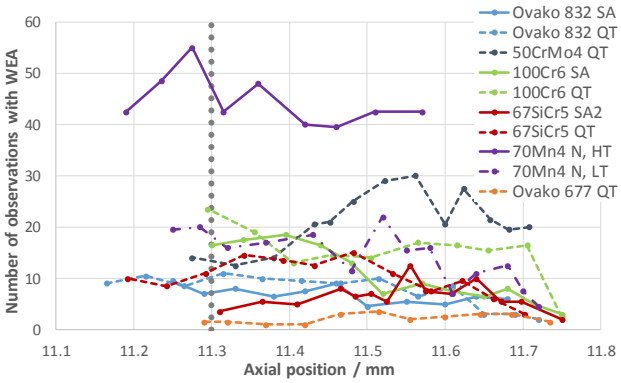

Figure 98: Number of observations with white etching areas (# WEA) after fatigue testing for N = 3x10^7 load cycles

The evaluation of cracks longer than 40 µm is shown in Figure 99 and Figure 100. A large number and comparably long cracks were found in sample 70Mn4 N HT. Steel grade 100Cr6 revealed numerous and longer cracks as well. Only a few or no cracks and short cracks were found in steel grades 50CrMo4, 67SiCr5 and Ovako 677.

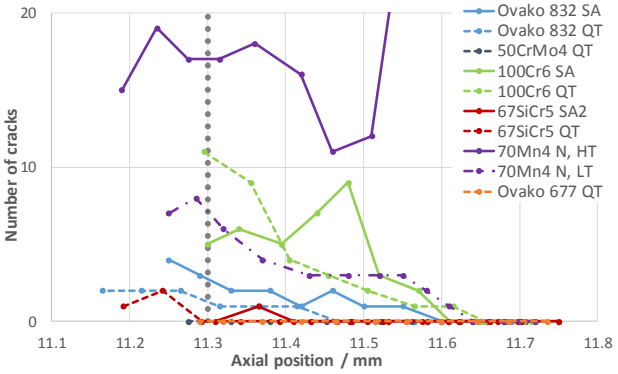

Figure 99: Number of cracks (cracks lengths > 40 µm) after fatigue testing for N = 3x10^7 load cycles

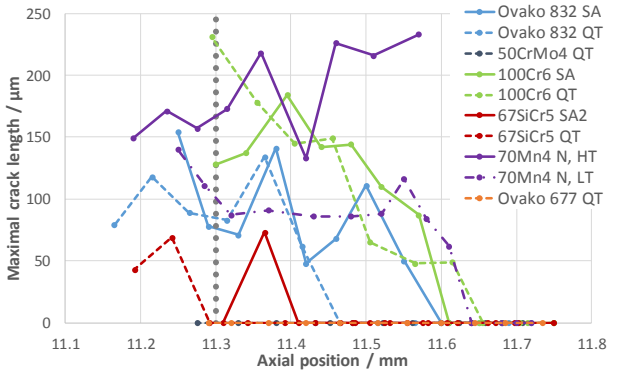

Figure 100: Maximal lengths of cracks (cracks lengths > 40 µm) after fatigue testing for N = 3x10^7 load cycles

Only 3 out of the total 104 runs were stopped due to spalling damage, so that the samples life could not be statistically evaluated.

5 Discussion

Chapter 5 contains the discussion of the previously shown results.

The dilatometer study and the individual steels are discussed in chapter 5.1. Chapter 5.1.7 summarises the dilatometer study with an overall benchmark of the investigated steel grades and a summary of the main findings. The chapter finishes with a recommended steel grade, which shows a comparably robust heat treatment result among the investigated steels.

The transfer of the dilatometer results on surface induction hardened rod-type samples is discussed in chapter 5.2. The derived conclusions from the through hardened dilatometer samples are compared with the surface hardening result of rod-type samples in terms of hardness gradients, surface hardening depths and residual stresses.

Chapter 5.3 discusses the outcomes of the rolling contact fatigue testing and finishes with the steels benchmark of rolling contact fatigue performance in chapter 5.3.4.

5.1 Dilatometer study

In order to assess the robustness of the selected steels and their prior microstructure regarding the induction heat treatment result, the arithmetic mean change in M_S, as quenched hardness and prior austenite grain size for changed austenitisation conditions are shown in Figure 101 until Figure 103. Figure 104 shows the prior austenite grain size mapping. Ovako 677 SA and all variants of 67SiCr5 showed a poor etching response and could not be included in the PAGS investigations.

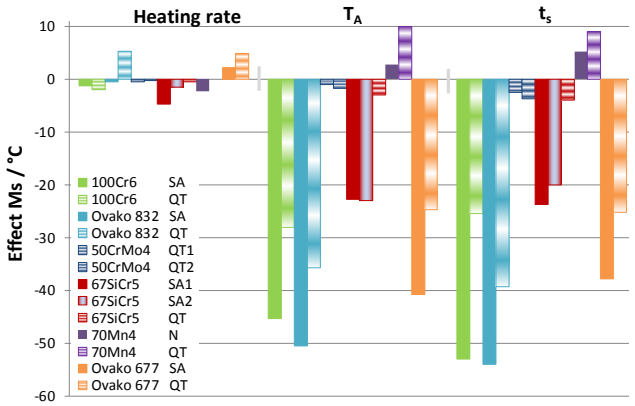

Figure 101: Effects of heating rate, austenitisation temperature T_A and soaking time t_S on M_S

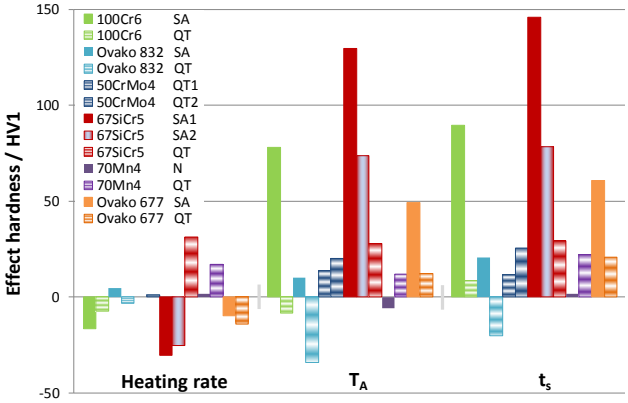

Figure 102: Effects of heating rate, austenitisation temperature T_A and soaking time t_S on hardness

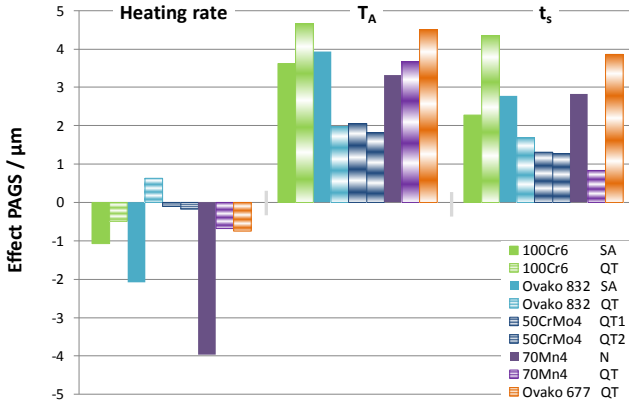

Figure 103: Effects of heating rate, austenitisation temperature T_A and soaking time t_S on prior austenite grain size

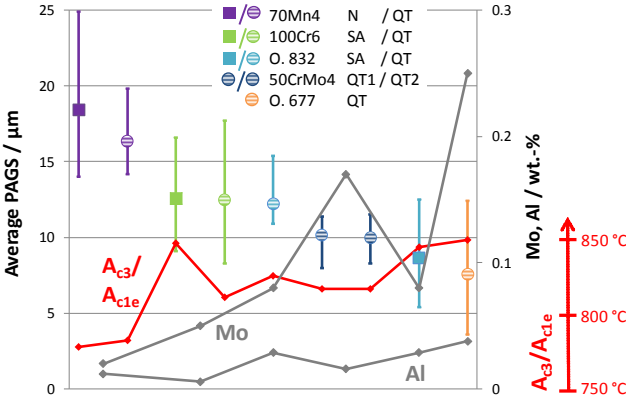

Figure 104: Prior austenite grain size mapping and steels molybdenum and aluminum content as well as A_{C3}/ A_{C1e} temperatures for 30 K/s heating rate; error bars show max. and min. measured grain size

5.1.1 100Cr6

100Cr6 - Martensite start temperature M_S

Ongoing dissolution of carbides and alloying elements into the austenitic matrix leads to decreasing M_S temperatures for increased austenitisation. Carbide size and carbide number on micrographs of the relevant dilatometer samples are decreasing with increased austenitisation degree. The QT structures show lower M_S temperatures due to faster austenitisation kinetics. Lower, measured transformation temperatures A_{c1}/A_{c1b} and A_{c3}/A_{c1e} for the QT prior structure, as well as microstructural features as carbide size, shape, spacing, density, individual phase chemistry or grain size are likely causes.

Generally, the magnitudes of T_A and t_S effects on M_S (arithmetic mean change in M_S when increasing or prolonging T_A and t_S) can be correlated to the steels theoretical M_S for full dissolution of all alloying elements, see Table 4. The more negative the effects on M_S, the lower the calculated theoretical M_S temperatures. This seems reasonable on the one hand since steels with higher amounts of M_S lowering alloying elements might be able to diffuse and dissolve more elements into the austenitic matrix at the same time or temperature. On the other hand, other features like carbides thermal stability, austenitisation kinetics or other microstructural features like carbide size, shape, spacing, density, individual phase chemistry or grain size might influence the dissolution kinetics as well.

Steels with fast changing M_S temperatures, containing higher amounts of M_S lowering alloying elements, are more difficult to control in terms of a desired M_S in the given austenitisation range. Too low M_S temperatures bear the risk of excessive retained austenite contents after quenching which might cause severe problems in terms of surface finishing (e. g. grinding), dimensional stability during operation or hardness loss. Retained austenite content as well as thermal and mechanical stability of retained austenite are important and might be very different for the investigated steel grades. Contrarily, higher retained austenite contents might be desirable for the performance of certain bearing applications [Bha12].

The effect of t_S on M_S appears larger for most steels than of T_A on M_S. The change in M_S is connected to the dissolution of carbides and alloying elements into the austenitic matrix. Whether the diffusion rate of carbon or other alloying elements is the controlling mechanism for carbide dissolution is discussed controversial in literature, as summarized in [Bro92]. An estimation for volume diffusion under simplified circumstances is given by Shewmon in [She89], see Figure 105. It shows a greater effect of an increased soaking time (1 s → 10 s) on the diffusion distance of carbon or chromium as compared to an increased temperature (950 °C → 1000 °C). Hence from a diffusion distance point of view, a larger effect of t_S could have been expected. 100Cr6 QT is an exception from the mentioned observation. Other mechanisms apart from diffusion rate or distance might be controlling mechanisms, like for example the thermal stability of alloyed carbides.

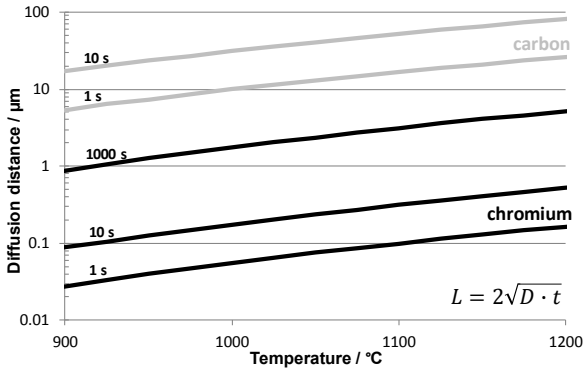

Figure 105: Volume diffusion distances of chromium and carbon in austenite for different temperatures and times

The change in M_S when changing T_A and t_S is smaller for the QT prior condition compared to the SA condition (smaller effect of T_A and t_S on M_S). A decrease in M_S for higher austenitisation degrees is connected to dissolution of carbides and dissolution of alloying elements in the austenitic matrix. Beswick, Grosch and Molinder show experimentally a decrease in carbide dissolution rate for long soaking times at constant austenitisation temperatures [Bes87, Gro84, Mol56]. The authors demonstrate that the decrease of carbide fraction over soaking time of a bearing steel and low alloyed high carbon steels (100Cr6, C85, 1.27 % C steel) follows a sigmoid function (”S function”), see Figure 106. Slowed down carbide dissolution kinetics for lower carbide fractions may have two possible reasons. Due to the faster austenitisation kinetics for the QT prior structure, higher amounts of alloying elements are dissolved in austenite for the same austenitisation condition compared to the SA prior structures. The driving force for diffusion, the difference in elements potential between the alloying element sources (e.g. carbides) and the alloying element sink (austenitic matrix), decreases with ongoing element dissolution in austenite. Since the QT structures` austenitic matrix contents a higher amount of alloying elements at the same austenitisation condition and hence exhibits a higher matrix potential and smaller potential difference, a further increase in temperature or time leads to slower alloying element uptake by the matrix.

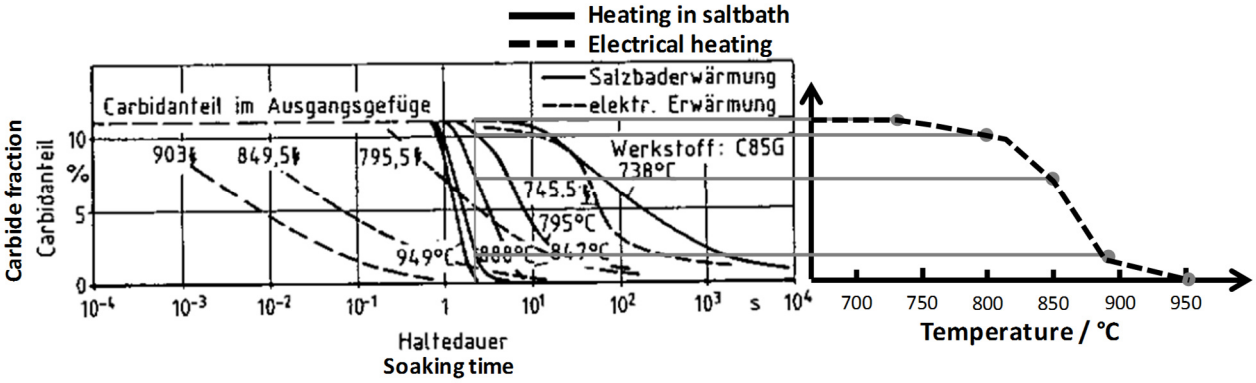

Figure 106: Isothermal carbide dissolution for different austenitisation temperatures of a C85 steel from Grosch [Gro84] (left) and derived dissolution for a constant soaking time and increasing austenitisation temperature (right)

Another approach takes different types of carbides into account. While Fe_3C carbides dissolve comparably fast at the beginning of the austenitisation process, more complex carbides alloyed with chromium, manganese or molybdenum are more stable and dissolve slower. A slowed down dissolution at higher

temperatures or longer times (higher austenitisation degrees) would be the result, hence a slower drop in M_S. Since the austenitisation degree in case of identical temperature and soaking time is higher for the QT structure compared to the SA structure, a slower dissolution and drop in M_S temperature would be expected.

An increased heating rate leads to very small effects on M_S in case of 100Cr6 as well as for all steel grades. Earlier measurements with a relatively high number of repetitions showed that M_S can differ in the range of ~ 5 °C for identical austenitisation conditions. Since the effects are in the range of –5 °C up to +5 °C for all steels, the significance is thought to be very low. Nevertheless, tendencies are tried to be elaborated.

The negative effects of heating rate on M_S of 100Cr6 might partly be caused by the increased appearance of NMTPs on the micrographs for higher heating rates. The dilatation curves for the lowest austenitisation degree (950 °C, 1 s) of 100Cr6 SA (see Figure 59), shifted to higher dilatation, show a diffusion controlled transformation at higher temperatures resulting in a certain amount of NMTPs. The diffusion controlled transformation during quenching at higher temperatures can lead to an enrichment of the adjacent austenite matrix with alloying elements, lowering M_S.

100Cr6 - Hardness

The effects of heating rate on hardness of 100Cr6 SA and QT are slightly negative. The negative effect of 100Cr6 SA appears larger and might partly be caused by an increased amount of NMTPs, as observed on the micrographs and as derived from the negative effect on M_S. Other indications are the increased standard deviations for the hardness of the fast heated samples. The shorter time available for dissolution of carbon and other alloying elements in case of higher heating rates might also contribute to the lower measured hardness. Both approaches will lower hardness whereas M_S would be shifted in negative (appearance of NMTPs) and positive (less time for dissolution) direction. The decrease of NMTPs and the ongoing dissolution of carbon for the case of 100Cr6 SA result in comparably high effects of T_A and t_S on the measured hardness.

NMTPs were observed to a much smaller extend in the case of 100Cr6 QT which might be one reason for a smaller negative effect on hardness for faster heating. The effects of T_A and t_S on hardness are small. An increased austenitisation degree and connected ongoing alloying element dissolution (see effects on M_S) lowers hardness from a M_S temperature of ~ 195–200 °C, most probably due to an increase in retained austenite content, see also Figure 62 and Figure 63. Hence 100Cr6 is easily overheatable in terms of retained austenite in the given austenitisation range, whereas 100Cr6 QT overheats at lower austenitisation degrees. The highest hardness among all steel grades was measured for 100Cr6 QT with 903 HV1 (theoretical carbon related martensite hardness 902 HV).

The appearance of NMTPs for low austenitisation degrees on the one hand and the risk of overheating for higher austenitisation degrees on the other hand, narrow the optimal process window.

100Cr6 - Prior austenite grain size

The increase in PAGSs is comparably large and the absolute PAGS level the second largest for 100Cr6. The highest carbon content would suggest a high carbide share and grain boundary pinning effects. At the same time, the A_{c3}/A_{c1e} temperatures are comparably high for 100Cr6 SA and might also suggest being beneficial

for smaller PAGSs. Arguments which might underline the relatively large PAGSs are the low amounts of aluminium and the low amount of molybdenum which can reduce PAGSs as shown by Hayashi et al. [Hay10] and stated by Rudnev [Rud03]. From the results obtained, 100Cr6 is thought to be less beneficial regarding PAGSs among the other steel grades.

Increasing temperature T_A has a larger impact on the PAGS than prolonging soaking time t_S in the examined range.

5.1.2 Ovako 832

Ovako 832 - Martensite start temperature M_S

Ongoing dissolution of carbides and alloying elements into the austenitic matrix leads to decreasing M_S temperatures for increased austenitisation. Carbide size and number on micrographs of the relevant dilatometer samples are decreasing with increased austenitisation degree. The QT structures show lower M_S temperatures due to faster austenitisation kinetics. Lower transformation temperatures, as well as microstructural features as carbide size, shape, spacing, density, individual phase chemistry or grain size are likely causes.

The change in M_S when changing T_A and t_S is smaller for the QT prior condition compared to SA (smaller effect of T_A and t_S on M_S). The same scenarios as for 100Cr6 seem reasonable for the described observation.

An increased heating rate leads to very small effects on M_S. The negative or smaller effect on M_S of Ovako 832 SA compared to Ovako 832 QT could be caused by a refinement of the prior austenite grains. Ovako 832 SA shows the second largest, negative effect of heating rate on grain size (~ –2 µm), see Figure 103. However, since the effects are in the range of –5 °C up to +5 °C, the significance is seen as very low.

Ovako 832 – Hardness

The effects on hardness for changed austenitisation degrees are small in the case of Ovako 832 SA, although increased T_A and prolonged t_S let to the largest decrease in M_S among all steel grades, see Figure 101. Looking at the hardness values in Figure 67, a small increase can be seen when increasing T_A for the short soaked samples and when prolonging t_S at low T_A. The reason for the small or missing increase is most likely the increasing level of retained austenite after hardening, which exhibits low hardness. Figure 67 and Figure 69 show that the overall hardness approaches relatively fast a stagnating or decreasing tendency for increasing austenitisation degrees or decreasing M_S temperatures.

As suspected from the lower absolute M_S values of Ovako 832 QT, the tendency of losing hardness due to higher retained austenite levels for increasing austenitisation is more pronounced. This leads to negative effects for increased T_A and prolonged t_S. The standard deviations of hardness measurements are increasing with T_A and t_S as well, indicating larger shares of phase fractions with different hardness levels (martensite and retained austenite).

The maximum measured hardness of 821 HV1 is lower than the theoretical, carbon related martensite hardness of 902 HV. This is another indication for higher shares of retained austenite which lowers the overall hardness.

The large share of M_S lowering alloying elements makes Ovako 832 easily overheatable in terms of hardness loss and higher retained austenite levels in the given austenitisation range, especially for the QT prior structure. Whether it is possible to exceed the maximal measured hardness of ~ 820 HV1 with changed austenitisation conditions remains unclear, but it seems unlikely that hardness levels of 100Cr6 can be reached.

Excessive retained austenite contents after hardening can be desirable for certain applications or unwanted with respect to phase changes and dimensional changes during operation. The thermal stability of retained austenite during tempering or tempering resistance in general influences the remaining amount of retained austenite for certain tempering conditions. Elements as silicon, chromium, molybdenum or manganese are known to enhance tempering resistance [Hou56, Bai39, Fur08, Miy07]. Comparing the chemistry of 100Cr6 and Ovako 832, one could expect a higher tempering resistance for Ovako 832 due to increased silicon and manganese contents.

Ovako 832 - Prior austenite grain size

The average PAGS is smaller for Ovako 832 SA while the change in PAGS is larger compared to Ovako 832 QT. The reasons might be various and cannot be given in the frame of this work. Among others, the lower, measured A_{c3}/A_{c1e} temperatures for the QT prior structure might contribute to larger PAGSs.

The increasing effect of heating rate on PAGS of the QT version is small and might be a result of the poor statistical coverage (only one sample per factor setting) and the subjective evaluation of the PAGS using the respective micrographs.

The average PAGSs of Ovako 832 appear to be smaller than those of 70Mn4 and 100Cr6 and partly larger than those of 50CrMo4 and Ovako 677. The same order is valid for the molybdenum and aluminium content of the steels, whereas the aluminium content of Ovako 832 is second largest after Ovako 677 (Figure 104). This is a hint that those elements partly play a role and can affect the PAGS, as shown in [Bha12, Hay10].

Increasing temperature T_A has a larger impact on the PAGS than prolonging soaking time t_S in the examined range.

5.1.3 50CrMo4

50CrMo4 - Martensite start temperature M_S

The transformation behaviour of 50CrMo4 shows little changes in M_S for the different austenitisation degrees. A relatively small, negative effect of T_A and t_S on M_S (see Figure 101) suggests that dissolution is ongoing but close to completion. Carbides are not visible on the micrographs (magnification 1000x) of the hardened dilatometer samples. The results of QT1 and QT2 are identical.

An increased heating rate leads to very small, negative effects on M_S. Assuming that no NMTPs are occurring during quenching and full dissolution of carbides and alloying elements is not completed for the lowest austenitisation degree, an increase in M_S would be expected for faster heating. This is connected to a decreased time spent in the austenitic regime for higher heating rates, which is caused by higher transformation temperatures and less time spent to reach the final temperature T_A. Shorter times spent in the austenitic regime shorten the time for carbide and alloying element dissolution and hence increases the M_S temperature.

Negative effects of heating rate on M_S could be caused by an austenite grain refinement. Different authors like Yang or Garcia-Junceda show in [Yan09, Gar08] that M_S can be lowered by a decrease in prior austenite grain size. The drop in M_S becomes steeper for smaller grain sizes. Garcia-Junceda shows a more or less linear drop in M_S of ~ 30 °C between grain sizes of ~ 3–10 µm, Yang a drop of ~ 30 °C between ~ 3–20 µm.

In the case of 50CrMo4, no NMTPs were observed and neither the prior austenite grain size (see Figure 103) nor the hardness (see Figure 102) was significantly changed by the heating rate. Since the mentioned changes in M_S, hardness, and PAGS are small, no significant conclusion can be drawn.

50CrMo4 – Hardness

The low change in hardness or effects of the heating rate, T_A, and t_S on hardness correspond well with the low effects on M_S. Generally, a decreasing M_S for increased T_A and t_S leads to an increased hardness. The increase in hardness and decrease in M_S is likely caused by ongoing dissolution of carbon and other elements into the austenitic matrix. The hardness of 50CrMo4 is not increasing with higher T_A for long t_S and not increasing with longer t_S for higher T_A. Furthermore, the theoretical martensite hardness is reached and no residual carbides are visible on the micrographs. Both points indicate that carbide dissolution is close to completion or completed. The low amount of visible NMTPs displays the steels' comparably high hardenability for the given austenitisation conditions. At the same time, 50CrMo4 shows the highest M_S for a hardness of ~ 800 HV1 among all steel grades. This makes the steel grade interesting, if low retained austenite levels are required after hardening or tempering effects during quenching (auto-tempering) are of interest. Due to the given carbon content, 50CrMo4 is limited to lower hardness levels compared to the other investigated steel grades. 50CrMo4 shows the lowest measured maximum hardness (799 HV1) as well as the lowest theoretical martensite hardness (765 HV).

50CrMo4 - Prior austenite grain size

Steel grade 50CrMo4 shows little sensitivity to austenite grain growth when changing austenitisation conditions on a comparably small absolute grain size level. The results are considered being beneficial from a process stability and mechanical property point of view. The lower carbon content and resulting low amount of remaining, on the micrographs visible, carbides after austenitisation as well as the relatively low A_{c3}/ A_{c1e} temperatures (only 70Mn4 N/ QT, 100Cr6 QT lower) would not suggest 50CrMo4 to show an advantageous behaviour regarding PAGS among the investigated steels. The aluminium alloying connected to a possible grain boundary pinning network of AlN precipitations is comparable to the other steel grades and somewhat lower compared to Ovako 832 and Ovako 677. Hayashi et al. show in [Hay10] that molybdenum additions have a large impact on refining prior austenite grains up to approximately 0.5 wt.-% molybdenum. The study was done on 0.5 wt.-% carbon steels, with a maximum addition of 1.2 wt.-%

molybdenum, and austenitisation temperatures of 900 °C and 1000 °C. The comparison of different alloying strategies showed, that the impact of molybdenum (0.4 wt.-%) on the grain refinement was larger as compared to vanadium (0.11 wt.-%), niobium (0.18 wt.-%), chromium (0.39 wt.-%), titanium (0.096 wt.-%) or zirconium (0.18 wt.-%). The author suggests that grain growth is hampered by the suppression of carbon diffusion by molybdenum in solid solution. The described effect might be one reason for the stable and small PAGSs of 50CrMo4, which contents the second highest amount of molybdenum (0.17 wt.-%).

Generally, the prior austenite grain size is influenced by many parameters. From the material site, micro alloying (e. g. Al, Nb, Ti) and the whole steels prior processing play major roles.

Increasing temperature T_A has a larger impact on the PAGS than prolonging soaking time t_S in the examined range.

5.1.4 67SiCr5

67SiCr5 - Martensite start temperature M_S

Ongoing dissolution of carbides and alloying elements into the austenitic matrix leads to decreasing M_S temperatures for increased austenitisation for 67SiCr5 in SA1 and SA2 prior condition. Carbide size and carbide number on micrographs of the relevant dilatometer samples are decreasing with increased austenitisation degree. The negative effect of an increased heating rate on M_S is comparably small, however, probably caused by a somewhat larger amount of NMTPs for faster heating, as observed on the micrographs. The diffusion controlled transformation during quenching at higher temperatures can lead to an enrichment of the adjacent austenite matrix with alloying elements, lowering M_S.

The QT prior structures main effects on M_S are small in comparison to the SA1 and SA2 structures. It is likely that the dissolution is close to being completed already for the lowest degree of austenitisation and the M_S temperature remains unchanged for the given austenitisation conditions.

It is obvious that the dissolution and austenitisation advances faster for the QT structure in comparison to SA1 and SA2. Likewise, prior structure SA2 showed lower M_S temperatures than SA1. Possible reasons are the lower, measured transformation temperatures A_{c1}/ A_{c1b} and A_{c3}/ A_{c1e} during heating as well as microstructural features as carbide size, shape, spacing, density, individual phase chemistry or grain size.

67SiCr5 – Hardness

The hardness for 67SiCr5 is increasing for increasing austenitisation degrees in case of all prior microstructures. The increase in hardness is connected to progressive dissolution of carbon and other alloying elements into the austenitic matrix as well as a decrease of NMTPs.

The hardness level is increasing from SA1 to SA2 to QT prior condition. The QT prior structure shows highest maximum hardness (848 HV1) among the 67SiCr5 prior structures as well as the lowest M_S temperatures. As mentioned before, lower measured ferrite to austenite transformation temperatures during heating as well

as microstructural features may play a role. The smaller effects of T_A and t_S on hardness are likely caused by the same reasons as for the smaller effects on M_S.

An increase in heating rate leads to a lower hardness for 67SiCr5 SA1 and SA2 as well as a higher standard deviation in hardness. The decrease in hardness corresponds well with the increased amount of NMTPs on the referring micrographs. A less negative effect of the heating rate on hardness and a less negative effect of the heating rate on M_S were measured for the SA2 prior structure as compared to SA1. This correlates well with the smaller amount of NMTPs on the micrograph for the SA2 prior condition, see Table 15.

The relatively large effects of T_A and t_S on hardness in case of prior structure SA1 are very likely caused by the large amount of NMTPs for the low austenitisation degrees, lowering hardness. Due to less NMTPs and hence an increased hardness for the lowest austenitisation degree of SA2, the effects appear smaller. The appearance of NMTPs for the lowest austenitisation degrees (950 °C, 1 s) of SA1 and SA2 could also be derived from the corresponding dilatation cooling curves, which showed a transformation related deflection at higher temperatures (550-650 °C). Again, the deflection appears to be more pronounced for the SA1 prior condition connected to a larger amount of NMTPs.

The reason for lower M_S temperatures, a higher hardness level, less NMTPs and connected lower effects of T_A and t_S on hardness of SA2 compared to SA1 can be various. One obvious reason is the decrease in the measured ferrite to austenite transformation temperatures upon heating for prior structure SA2, which prolongs the time spend in austenitic condition. Other microstructural features which are connected to the transformation temperatures upon heating might also influence the austenitisation process, as are carbide size, shape, spacing, density, individual phase chemistry or grain size. Looking at the effects of T_A and t_S on M_S, 67SiCr5 SA1 and SA2 show comparable values. This may indicate that the carbide dissolution itself takes place at the same speed.

67SiCr5 QT shows a positive effect of an increased heating rate on hardness. The individual hardness values in Figure 73 show, that the hardness values for higher heating rates are higher for each of the different combinations of t_S and T_A. A possible reason might be a difference in homogenization level for fast and slow heating. According to Roth in [Rot63], hardness can decrease for higher austenitisation levels due to an increased level of retained austenite caused by lower degrees of alloying element homogenization. Further dissolution accumulates alloying elements in the austenitic matrix around dissolved or remaining carbides, stabilizing austenite. For the given case, an increased austenitisation level, as for the slow heating of 67SiCr5 QT, might have caused a further accumulation of alloying elements in certain volumes, increasing the retained austenite content. Lower standard deviations for the hardness measurements of all fast heated samples (24, 4, 5, 9 HV1) compared to the slow heated samples (24, 7, 8, 12 HV1) underline the mentioned. However, a decrease in M_S temperatures, as should be expected for further dissolution and accumulation of alloying elements of the slow heated samples, was not measured. A clear grain refinement in case of fast heating and the connected decrease in M_S temperatures could have compensated the before mentioned expected difference in M_S temperatures (etching for PAGBs was not successful for 67SiCr5).

67SiCr5 - Prior austenite grain size

All variants of 67SiCr5 showed a poor etching response and could not be included in the PAGS investigations.

5.1.5 70Mn4

70Mn4 - Martensite start temperature M_S

70Mn4 shows small changes in the M_S temperature. A slight increase in M_S temperature was measured for increasing austenitisation degrees, while heating rate has a minor effect. Hence, the effects of T_A and t_S on M_S appear positive (Figure 101). As shown by Yang or Garcia-Junceda in [Yan09, Gar08], M_S temperatures can be increased with an increase in PAGS, at which the increase in M_S becomes less pronounced for bigger grain sizes. Like for all other steel grades, the PAGS of 70Mn4 increases with an increased austenitisation degree, see Figure 103. In case of 70Mn4 in prior condition N, a decrease in M_S due to progressing alloying element dissolution in austenite with increased austenitisation degree seems unlikely. Additionally, no differences in the amount of NMTPs were observed which could otherwise impact the M_S temperature. The before mentioned makes a correlation between PAGS and M_S temperature likely, keeping in mind that the measured effects are small. For the remaining steel grades, a potential increase in M_S due to austenite grain growth is probably compensated by the decrease in M_S due to progressive alloying element dissolution.

The effects of increased T_A and prolonged t_S on M_S were shown to be larger for 70Mn4 in QT prior condition as compared to prior condition N. The reduction in amounts of NMTPs for increased T_A and prolonged t_S in case of 70Mn4 QT might be one possible reason for a larger increase in M_S temperature, see Table 16.

70Mn4 – Hardness

The effects on hardness for 70Mn4 N are small. Most probably complete dissolution of all alloying elements into the austenitic matrix is already finished for the lowest austenitisation degree and an increased austenitisation does not affect the amount of dissolved carbon or other elements and hence hardness.

The positive effects of T_A and t_S on hardness of 70Mn4 QT show that, unlike for the normalized version, element dissolution or homogenization is still ongoing. An indication for the slower dissolution of 70Mn4 QT carbides might also be derived from the dilatometer heating curves in Figure 107. Looking at the slope of the dilatation curves after completion of the transformation ferrite to austenite, a steeper slope was measured for the QT prior conditions. Steeper slopes may indicate that the austenite carbon uptake connected to the dissolution of carbides is higher in those temperature ranges. Taking into account the lower hardness and the presence of NMTPs for the hardened 70Mn4 QT samples in case of lower austenitisation degrees, as compared to the hardened 70Mn4 N samples (Figure 74, Table 15, Table 16), this may indicate that dissolution of the spherical carbides in the QT state takes longer times or higher temperatures. The lower drop in dilatation from A_{c1}/ A_{c1b} to A_{c3}/ A_{c1e} for the 70Mn4 N samples might be another indication that the lamellar cementite dissolves fast and a larger amount of carbon is dissolved in the austenitic matrix comparably early, increasing the austenite specific volume. Hunkel shows however, that dilatation differences during phase transformations can be caused by segregations as well and shows a dependency of direction and position of the machined dilatometer samples in relation to the starting bar material [Hun11]. Since the direction and relative radial position in the bar material for the machined dilatometer samples were kept constant for all steel grades used and 70Mn4 is not known as a typically highly segregated steel grade, this effect is thought to be small.

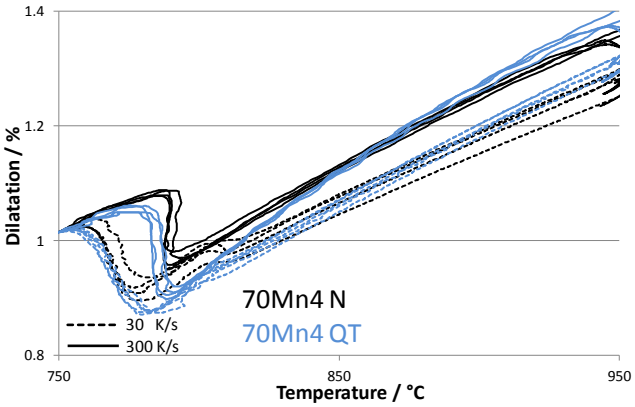

Figure 107: Dilatometer curves for heating of 70Mn4 in normalised (N) and tough tempered (QT) prior conditions

An increased heating rate for 70Mn4 QT let to a positive effect on hardness (+17 HV1) which was strongly affected by the measurements for the low austenitisation degree (30 K/s and 300 K/s, 950 °C, 1 s). Those samples showed larger standard deviations for the measured hardness and higher amounts of NMTPs, arranged in axial direction of the used bar material, probably connected to axial aligned segregation bands. Since only one sample was measured per austenitisation setting and the single hardness values strongly depended on the indent location, the positive effect of heating rate on hardness is thought to be caused by statistical reasons.

The second highest hardness (864 HV1) was measured for 70Mn4 among all steels although alloyed with the second lowest carbon content of 0.67 wt.-%. Likely reasons are fast austenitisation kinetics combined with sufficient hardenability and connected small amounts of NMTPs after hardening as well as an adequate M_S temperature to limit retained austenite contents after hardening.

Although the amount of NMTPs is small for the lowest austenitisation degree in the case of 70Mn4 N, higher austenitisation degrees did not reduce the amount of NMTPs and thus did not increase hardenability. This again shows the fast austenitisation kinetics of 70Mn4 on the one hand and the limited but rapidly available hardenability on the other hand. A reduced amount of NMTPs due to further element homogenization or austenite grain growth for higher austenitisation degrees might be possible.

70Mn4 - Prior austenite grain size

The largest measured PAGSs for 70Mn4 among all steels might be caused by the lowest measured transformation temperatures A_{c1}/ A_{c1b} and A_{c3}/ A_{c1e} upon heating and hence more time spent in the austenitic condition. Additionally, fast dissolution of low alloyed carbides results in the absence of carbides during a later stage of austenitisation, which could otherwise pin the austenite grain boundaries. As stated earlier, the dissolution of spherical carbides for 70Mn4 QT is indicated to be slower as for the lamellar condition of 70Mn4 N. The prolonged carbide existence might be one reason for the lower absolute grain size of 70Mn4 QT. The additional heat treatment of the 70Mn4 bar material in order to set the QT prior condition and a possible grain refinement might be another reason. Differences in austenite nucleation densities between the two prior structures might also be influencing.

Increasing temperature T_A has a larger impact on the PAGS than prolonging soaking time t_S in the examined range.

5.1.6 Ovako 677

Ovako 677 - Martensite start temperature M_S

Ongoing dissolution of carbides and alloying elements in the austenitic matrix leads to decreasing M_S temperatures for increased austenitisation. Carbide size and number on micrographs of the relevant dilatometer samples are decreasing with increased austenitisation degree. The QT prior structures show lower M_S temperatures due to faster austenitisation kinetics. Lower measured transformation temperatures A_{c1}/ A_{c1b} and A_{c3}/ A_{c1e} for the QT prior structure, as well as microstructural features as carbide size, shape, spacing, density, individual phase chemistry or grain size are likely causes.

The change in M_S when increasing T_A and prolonging t_S is smaller for prior condition QT compared to SA. The same explanation approach as for 100Cr6 and Ovako 832 might cause the described outcome. The lower alloying element potential difference between matrix and carbides for a certain austenitisation degree in the case of the prior structure QT is caused by its faster austenitisation kinetics. This decreases the driving force for ongoing element dissolution and a smaller change in M_S for changed soaking times or temperatures will take place. The second potential cause is the different thermal stability of carbides due to a different chemistry and as a result different dissolution rates. The faster austenitisation kinetics for the QT prior structures lead to a faster dissolution of the less stable (e. g. Fe_3C) carbides, possibly already for a low austenitisation degree. A further increase in temperature or time might lead to the dissolution of the more stable carbides, which dissolve slower and lead to slower change in M_S.

Ovako 677 – Hardness

The effects on hardness for Ovako 677 are in good accordance with the effects on M_S temperature, in opposite direction. Small changes in M_S temperature are caused by a lower dissolution rate of alloying elements (carbon) into the austenitic matrix, resulting in smaller hardness changes. The 677 QT variant does not change hardness in case of long soaking time when increasing T_A. The corresponding samples however show a decrease in M_S (see Figure 77 and Figure 78) due to ongoing dissolution of alloying elements. It is likely that the martensite hardness increase for increasing austenitisation and carbon dissolution is compensated by an increased amount of retained austenite, resulting in unchanged overall hardness. Ovako 677 is running into a hardness plateau for increased austenitisation degrees, see Figure 79. Since only small amounts of remaining carbides were seen on the micrographs for the highest austenitisation degree of Ovako 677 QT, it can be concluded that there might be no or only little hardness drop for higher austenitisation degrees until complete carbide dissolution.

Ovako 677 - Prior austenite grain size

The Ovako 677 QT variant provides the smallest average PAGS as well as the smallest measured PAGS among all steel grades. Generally, the prior austenite grain size is influenced by many parameters. From the material site, micro alloying (e. g. Al, Nb, Ti) and the whole steels prior processing play major roles. The highest measured A_{c3}/ A_{c1e} temperatures as well as the highest molybdenum (see Hayashi [Hay10]) and aluminium

content of Ovako 677 are possible reasons for the small measured PAGSs among others. Its low PAGS level makes Ovako 677 QT an interesting steel grade if small PAGSs are in focus.

5.1.7 Benchmark

Table 19 summarises the individual assessment of the investigated steels and their different prior microstructures. The assessment includes the control of M_S temperature, hardness, retained austenite level and the possibility to achieve different retained austenite levels with similar overall hardness (+: good, 0: worse, −: worst). Additionally, the amount of remaining carbides after hardening (micrographs, ×1000, +: high, 0: smaller, −: smallest/no carbides) and amount of NMTPs (+: none, 0: small, −: larger) are assessed.

Furthermore, the absolute PAGSs (+: small, 0: larger, −: largest) and achievable hardness levels (+: high, 0: lower, −: lowest) are included. The benchmark is only valid inside the investigated austenitisation and quenching conditions as well as for the used steel grades.

Table 19 Benchmark of dilatometer study

		Control of M_S[1]	Control of hardness[2]	Control of RA level[3]	Possibility to tailor RA level[4]	Remaining carbides (highest aust. degree)	NMTPs[5]	PAGS[6]	Hardness level
100Cr6	*SA*	-	-	0	+	+	-	0	+
	QT	0	+	-	+	+	0	0	+
Ovako 832	*SA*	-	+	-	+	+	+	0	0
	QT	-	+	-	+	+	+	+	0
50CrMo4	*QT1*	+	+	+	-	-	+	+	-
	QT2	+	+	+	-	-	+	+	-
67SiCr5	*SA1*	0	-	+	-	-	-	n.a.	0
	SA2	0	-	+	-	-	0	n.a.	+
	QT	+	+	+	-	-	+	n.a.	+
70Mn4	*N*	+	+	+	-	-	0	-	+
	QT	+	+	+	-	-	-	0	+
Ovako 677	*SA*	-	0	+	-	+	+	n.a.	0
	QT	0	+	0	0	0	+	+	0

1 According to effect chart: – for effect > 35 °C, + for effect ≤ 10 °C
2 According to effect chart: – for effect > 70 HV1, + for effect < 50 HV1
3 M_S ≥ 200 °C as a limit for acceptable amounts of RA
4 Possibility to adjust different RA levels with similar overall hardness
5 Share of NMTPs on micrographs of hardened samples, indicating local hardenability
6 With focus on absolute PAGS rather than change in PAGS with varied austenitisation
n.a. not available

The main findings are summarised below.

Control of M_S:

Smaller variations in the M_S temperature can be of importance for the induction heat treatment of bearing components due to the following reasons. The M_S temperature has an impact on the final microstructure and components properties, like hardness, hardenability and matrix alloy content or retained austenite content after quenching and tempering. A small variation in the M_S temperature and variation in the derived properties within one production batch is generally preferred. The mentioned is especially important for the process of induction hardening, in which the final temperature and temperature distribution at the end of the heating process is generally not directly controlled.

In addition, smaller variations in the M_S temperature will likely result in smaller variations in the derived component properties within one component, considering the typical temperature gradient (skin effect) when applying induction heating. The same applies for cases, where induction heating results in uneven heating along a components surface, like a bearing raceway surface.

For certain induction hardening machine configurations numerous quenching stations or arrangements are used, in which the component is successively quenched. Here, a stable and repeatable M_S temperature is of importance and needs to be aligned with the components temperature in between the different quenching stations.

The findings are:

- Linear regression analysis (Appendix B.4) revealed that the prior microstructure hardness as well as M_S temperature lowering elements (Cr, Ni, Mn, C, Si) affect the mean change in M_S temperature (effect on M_S). Increased alloying contents and decreased hardness leads to increased effects on the M_S temperature.

  The presence of M_S temperature lowering alloying elements, initially dissolved inside the ferritic matrix and carbides, leads to the ability to dissolve those elements to a larger share into the austenitic matrix for changed austenitisation conditions. In addition, other features like carbides thermal stability, austenitisation kinetics or other microstructural features like carbide size, shape, spacing, density, individual phase chemistry or grain size might influence the dissolution kinetics as well.

  The prior microstructure hardness is affected by the carbide size, shape, spacing or density, as well as the tempered martensite alloy content. The larger mean changes of M_s temperature for lower prior microstructure hardness was discussed above. Two possible explanations were mentioned, considering the characteristics of carbide dissolution rate, as well as the dissolution rate of different carbide types.

- QT starting microstructures show generally faster austenitisation kinetics but can lead to overheating in terms of low M_S and hardness drop due to increased retained austenite levels for the given austenitisation range.

Lower, measured transformation temperatures A_{c1}/A_{c1b} and A_{c3}/A_{c1e} for the QT prior structure, and connected microstructural features as carbide size, shape, spacing, density, individual phase chemistry or grain size are likely causes for the faster austenitisation kinetics. Generally, small and numerous carbides with a high surface to volume ratio can be expected for the QT starting microstructures, enhancing their dissolution.

- Small effects on M_S temperature as for 70Mn4, 50CrMo4 or 67SiCr5 QT make a process control inside the given austenitisation conditions easier.

  The limited alloying with M_S temperature lowering elements, especially with carbon, leads to the small changes in M_S temperature with changed austenitisation conditions. In addition, the starting microstructures (QT and N) and the connected austenitisation and carbide dissolution kinetics are probable causes. It is likely that carbide dissolution is close to completion or completed already for low austenitisation degrees and the matrix enrichment is close to its maximum (see also Figure 111).

- Steels containing larger amounts of M_S temperature lowering alloying elements are more difficult to control in terms of a desired M_S temperature and hence retained austenite content in the given austenitisation range.

- Comparing Ovako 832 with 100Cr6, the alloying with manganese and silicon lead to a more sensitive M_S towards increased austenitisation.

Control of hardness:

Small changes in hardness with changed austenitisation conditions are favoured due to the same reasons mentioned for the change in M_S temperature. Hardness variation within one production batch, hardness variation along a components surface (e.g. raceway surface) and steep radial hardness gradients shall be avoided.

The findings are:

- 50CrMo4 QT, 67SiCr5 QT, Ovako 677 QT and 70Mn4 show comparably small effects on hardness without hardness losses due to increased retained austenite contents and show therefore a better process stability regarding hardness.

  Small changes in hardness of the mentioned steels correspond well with low effects on the M_S temperature. It is likely that carbide dissolution is close to completion or completed already for low austenitisation degrees and the matrix enrichment is close to its maximum. The limited amount of M_S temperature lowering alloying elements within the steels avoid too low M_S temperatures and excessive amounts of retained austenite and thereby an overall hardness loss. The comparable small

shares of NMTPs for all austenitisation conditions is a result of the alloying strategy and austenitisation kinetics, which facilitates smaller changes in the as quenched hardness.

- Linear regression analysis (Appendix B.5) showed that increased prior structure hardness and manganese contents lower the effects on hardness while increased silicon contents increase the effects on hardness.

  It is known that manganese as well as a refined prior microstructure (as for the QT prior condition) accelerates austenitisation and leads to faster dissolution of carbon and other alloying elements, while silicon acts with opposite effect due to an increase in carbon activity in austenite [Kim12, Cha11]. It is likely that carbide dissolution is close to completion or completed already for low austenitisation degrees in case of fast austenitisation kinetics and a further increase in austenitisation degree does not lead to further matrix enrichment or hardness increase.

- A decrease in hardness was measured for 100Cr6 and Ovako 832 from M_S temperatures of approximately 200 °C and below and make the steel grades sensitive to overheating in terms of excessive retained austenite levels and hardness loss.

  The comparable large amount of M_S temperature lowering alloying elements within the steels forebodes larger amounts of retained austenite after hardening due to their austenite stabilization effect.

- Although 100Cr6 QT and Ovako 832 SA revealed small changes in hardness, changes in the microstructure in terms of increasing retained austenite contents are to be expected.

  The comparable large amount of M_S temperature lowering alloying elements within the steels forebodes larger amounts of retained austenite after hardening due to their austenite stabilization effect. The theoretical increase in martensite hardness due to on-going carbon dissolution is compensated by increased amounts of retained austenite after hardening.

- The alloying with manganese and silicon led in the comparison of Ovako 832 with 100Cr6 to a lower achievable hardness.

  The main differences in the chemistry of the steel grades are the increased silicon (+ 0.48 wt.-%) and manganese (+ 1.13 wt.-%) contents for Ovako 832. Especially manganese, with its pronounced stabilization impact on austenite, leads to lower achievable overall hardness levels after hardening due to increased amounts of retained austenite.

Discussion

Possibility to tailor retained austenite level:

The possibility to tailor the retained austenite level towards the bearing application and related bearing requirements can be of interest. Not only small shares, but also larger shares of retained austenite are shown to be beneficial for certain bearing applications [Bha12, Tsu92]. The possibility to adjust different microstructures with different shares of retained austenite and maintain a decent overall hardness level is seen as an advantage.

The finding is:

- 100Cr6, Ovako 832 and, to a smaller extend, Ovako 677 provide the possibility to adjust different microstructures on the same, individual hardness levels (e.g. low/ high retained austenite content). The change in hardness at a M_S temperature of ~ 200 °C appears to be small.

  Increased austenitisation degrees and connected ongoing alloying element dissolution lower the overall hardness from a M_S temperature of ~ 195–200 °C, most probably due to an increase in retained austenite content. The small changes in overall hardness at the M_S temperature region of 200 °C is likely caused by the balance of martensite hardness change (connected to the dissolved carbon content) and the different shares of retained austenite and martensite (connected to the dissolved alloy content).

Remaining carbides:

The role of remaining, undissolved carbides after hardening in bearing steels is controversially discussed. Carbides can be seen as stress raisers in the microstructure during over-rolling, but are also discussed to be beneficial under contaminated lubrication conditions if the contaminant particle sizes and carbide sizes are similar. From a heat treatment perspective, the presence of remaining, stable carbides helps to control and adapt the matrix enrichment by varying the austenitisation condition. The presence of carbides and precipitates during austenitisation are also facilitating small austenite grain sizes due to grain boundary pinning effects.

The findings are:

- Ovako 832, 100Cr6 and Ovako 677 show, on micrographs (magnification x1000) visible, remaining carbides for the highest austenitisation degree of QT prior structures, whereas Ovako 677 shows only a small amount.

  The amount of remaining carbides is connected to the carbide stability, the carbide chemistry and the previous number of present carbides. Alloying elements like chromium and molybdenum (carbide formers) increase carbide stability and are alloyed to a comparable large extent in the mentioned steel grades. In addition, higher amounts of carbon, as for steels Ovako 833 and 100Cr6, lead to larger shares of carbides.

- 50CrMo4, 67SiCr5 QT and 70Mn4 show a complete dissolution or are close to complete dissolution already for the lowest degree of austenitisation.

  Complete carbide dissolution is likely caused by the low contents of carbide formers and carbon in the mentioned steels. Additionally, austenitisation kinetics in general and microstructural features like carbide size, shape, spacing, density, individual phase chemistry or grain size might influence the dissolution kinetics and number of remaining carbides as well.

Non martensitic transformation products:

Non martensitic transformation products within the induction hardened material volume shall be avoided. They are of lower strengths, lower hardness, lower wear resistance, and can alter the residual stress profile in an disadvantageous way. Within the material volumes of NMTPs even tensile residual stresses can develop.

The findings are:

- Larger amounts of NMTPs were present for the samples of 100Cr6 SA, 67SiCr5 SA1 and 70Mn4 QT; smaller amounts for 100Cr6 QT, 67SiCr5 SA2 and 67SiCr5 QT, as well as for 70Mn4 N; Ovako 832, Ovako 677 and 50CrMo4 showed no or very little amounts of NMTPs and provide therefore a larger local hardenability for the given austenitisation range.

  The hardenability is influenced by different factors, such as the amount of dissolved alloying elements within the matrix prior to quenching, the austenite grain size or the presence of carbides and precipitates. The prior microstructure and hence the distribution of the alloying elements prior to hardening plays an important role. Generally, small and numerous carbides with a high surface to volume ratio, as for the QT starting microstructures, enhance their dissolution and a faster gain in hardenability. The use of silicon and manganese, which dissolve fully (silicon) or to a large extent (manganese) in ferrite, are most likely providing instant hardenability. Hence, steel grades Ovako 677 and Ovako 832 provide comparable large hardenability. The reasons for larger hardenability of steel 50CrMo4 are probably the alloying with molybdenum and chromium in connection with the limited amount of carbon and hence smaller amount of carbides. The smaller amount of carbides might lead to a larger extent of carbide formers dissolved in the ferritic matrix prior to hardening, where they can instantly contribute to the hardenability.

- The alloying with manganese and silicon led in the comparison of Ovako 832 with 100Cr6 to a clear decrease in NMTPs or increase in hardenability.

  The use of silicon and manganese, which dissolve fully (silicon) or to a large extent (manganese) in the ferritic matrix, are most likely providing instant hardenability.

Discussion

Prior austenite grain size:

The role of prior austenite grain size is generally well understood. Smaller prior austenite grain sizes are leading to larger material strength and toughness, and are therefore seen as advantageous in bearing steels. Large prior austenite grain sizes bear the risk of martensite plate cracking and microcracking. However, hardenability can be decreased for small prior austenite grain sizes.

The findings are:

- Among other factors, molybdenum and aluminium contents as well as austenitic transformation temperatures upon heating might affect the PAGS.

  Generally, the prior austenite grain size is influenced by many parameters and the prior processing during steel making and forming. From the information available for the given steels, it seems likely that larger amounts of molybdenum (molybdenum slows down the diffusion in solid solution [Hay10]), higher transformation temperatures upon heating (results in less time spent in the austenitic state), and large amounts of aluminium (grain boundary pinning by aluminium nitride precipitations) are important factors.

- 50CrMo4 shows advantageous behaviour due to the smallest change of PAGSs on a low absolute PAGS level.

  Likely reasons are the larger amount of molybdenum, the comparably high transformation temperatures upon heating, and the comparably large amount of aluminium.

- Ovako 832 SA, Ovako 677 QT and 50CrMo4 reveal the smallest measured PAGSs.

  Likely reasons are the larger amount of molybdenum, the comparably high transformation temperatures upon heating, and the comparably large amount of aluminium.

- 70Mn4 shows the highest PAGSs among the investigated steels, whereas the QT prior conditions show lower PAGSs and effects on PAGS.

  Likely reasons are the low amount of molybdenum, the comparably low transformation temperatures upon heating, and the comparably low amount of aluminium. The slower carbide dissolution for the QT prior microstructure of 70Mn4 as compared to the normalised prior microstructure most likely leads to grain boundary pinning effects and smaller prior austenite grain sizes.

- The effect of increased temperature T_A on the change in PAGSs appears to be larger than for a prolonged soaking time t_S, vice versa for the change in M_S and hardness for the chosen variations.

- Indications for a shift of M_S to lower temperatures for smaller PAGSs are shown.

  The effect is explained by different potential effects including individual grain strengths and an increased resistance towards martensite formation and the accompanied plasticity. Other approaches take into account an impact of grain size on the nucleation density for martensite transformation or the elimination of lattice imperfections for larger austenitisation temperatures (larger grains) and less shear energy needed during martensitic transformation [Yan09, Gar08].

- Linear Regression analysis reveals that larger contents of Cr and Mo and larger A_{c1} or A_{c3} temperatures having a decreasing effect on the absolute prior austenite grain size (see Appendix B.3).

  Chromium might act in a similar way as molybdenum. It slows the diffusion in solid solution and forms stable and numerous carbides which pin the grain boundaries.

Overall, steel grade 50CrMo4 offers a very good process stability in terms of hardness, M_S temperature, non-martensitic transformation products and prior austenite grains sizes among the investigated steels. The steel is therefore recommended as a comparably robust steel grade for induction hardening.

The absolute hardness level of 50CrMo4, however, is limited due to its carbon content and is low compared to the investigated steels. If higher levels of hardness are required, steel grades 67SiCr5 QT and 70Mn4 can be considered as robust alternatives. Their behaviour in terms of the prior austenite grain size and the change in prior austenite grain size is however worse (70Mn4) than for 50CrMo4 or not known (67SiCr5).

5.2 Transfer of dilatometer study on surface induction hardened samples

The **surface hardening depth** of the surface hardened rod samples can be clearly correlated to the dilatometric data, see Figure 108. The temperature at which the ferrite to austenite transformation was completed during heating, A_{c3}/ A_{c1e}, correlates well with the surface hardening depth (determined at 550HV). A larger surface hardening depth for lower A_{c3}/ A_{c1e} temperatures is reasonable, assuming a similar temperature profile after induction heating for all samples.

Minitab statistical software and linear regression analysis was used for further evaluation of dependencies. Chemical composition, phase transformation temperatures, pyrometer readings from induction hardening, materials electrical resistivity and magnetic permeability from JMatPro material database and hardness of the prior microstructure were used as potential predictors. The strong correlation for A_{c3}/ A_{c1e} was confirmed, see Table 20. Furthermore, manganese promotes an increase in hardening depth. Note that the coefficients "A_{c3}" and "Mn" are not independent, since manganese is known to lower A_{c3} temperature (see Appendix B.2, formula 4 and Figure 19).

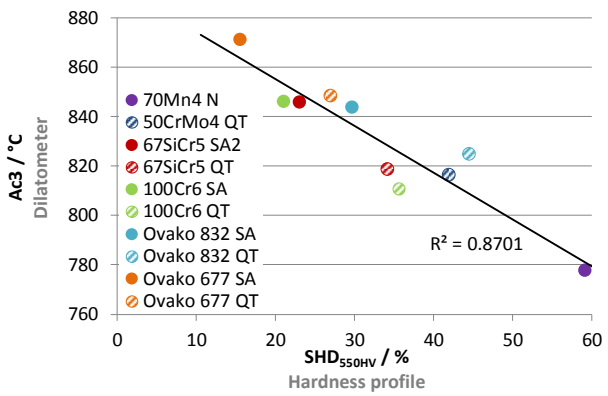

Figure 108: Surface hardening depth and measured A_{c3} temperatures from dilatometer curves

Table 20: Linear regression for response "surface hardening depth"

Model Summary			
S	R-sq	R-sq(adj)	R-sq(pred)
124.965	97.08%	96.25%	94.69%

Coefficients					
Term	Coef	SE Coef	T-Value	P-Value	VIF
Constant	22330	1360	16.42	0.000	
Mn	454.5	92.5	4.91	0.002	1.10
Ac3	-25.42	1.67	-15.25	0.000	1.10

Regression Equation		
SHD	=	22330 + 454.5 Mn – 25.42 Ac3

The hardness gradient as a characteristic of the **transition zone** correlates well with the measured transformation temperatures from the dilatometer study. The larger the difference between A_{c3} and A_{c1}, the smaller the hardness slope in the transition zone of the surface hardened sample (see Figure 109). The described correlation seems reasonable. Assuming a similar temperature profile for all samples upon heating, a small temperature interval for beginning and completion of ferrite to austenite transformation will lead to a narrow transition zone with a steeper decrease in hardness between hardened layer and soft core.

The statistical evaluation with the help of Minitab software resulted in the below result, see Table 21. A combination of increased manganese and larger differences in the transformation temperatures A_{c3}-A_{c1} leads to lower hardness gradients in the transition zone. The difference between A_{c3}-A_{c1} can be correlated to the contents of silicon, chromium and the prior-microstructure hardness (see appendix B.2). It follows that increasing amounts of silicon, chromium as well as lower prior-microstructure hardness leads to lower hardness gradients.

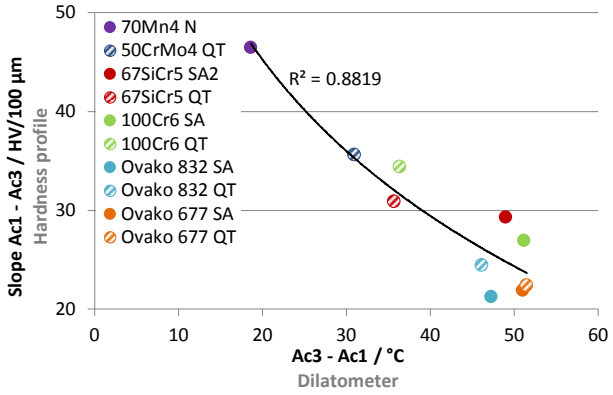

Figure 109: Hardness gradient in transition zone and difference in A_{c1}-A_{c3} from the dilatometer study

Table 21: Linear regression for response "hardness slope transition zone"

Model Summary			
S	R-sq	R-sq(adj)	R-sq(pred)
2.38565	92.84%	90.79%	77.26%

Coefficients					
Term	Coef	SE Coef	T-Value	P-Value	VIF
Constant	59.04	3.20	18.42	0.000	
Mn	-4.35	1.77	-2.46	0.043	1.10
Ac3-Ac1	-0.6096	0.0760	-8.02	0.000	1.10

Regression Equation		
slope HV/µm	=	59.04 – 4.35 Mn – 0.6096 Ac3-Ac1

The **hardness gradient or hardness decrease** in the surface near area (over 750 µm) correlates with the dilatometer data. The effects on hardness with changed austenitisation conditions derived from the dilatometer data show in most cases a good correlation with the hardness gradient derived from the hardness profile of the surface induction hardened rod samples, see Figure 110.

The deviations might be caused by different reasons. While the change in hardness with temperature is well defined for the dilatometer trials, the radial temperature gradient for the surface hardened samples is not known. Additionally, the tempering treatment of the surface hardened samples and their individual decrease

in hardness according to the steels dissolved alloying content and connected tempering resistance makes the comparison difficult (dilatometer samples were not tempered after hardening).
The linear regression model proposes the samples surface hardening depth as an additional predictor next to the arithmetic mean change in hardness (see Table 22). According to the equation, a larger hardening depth would facilitate a smaller hardness decrease in the hardened case. This is in accordance with the observation that steels in QT prior conditions as well as 70Mn4 resulted in larger hardening depth and additionally showed smaller arithmetic mean changes in hardness for the dilatometer samples (see Figure 102).

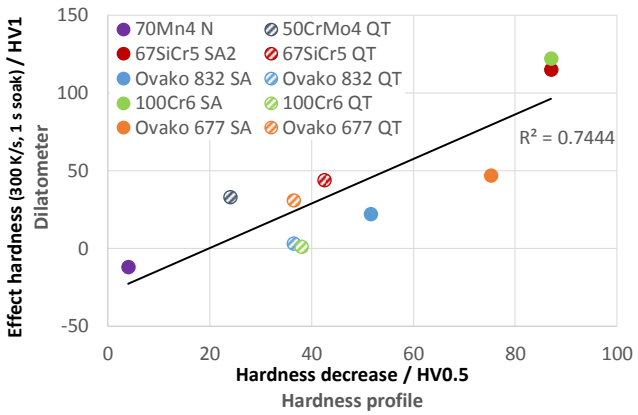

Figure 110: Correlation of hardness mean change (dilatometer data for 300K/s and 1 s soaking) and hardness decrease of surface induction hardened rod samples (hardness change between indents at a depth of 100 µm and 850 µm)

Table 22: Linear regression for response "hardness decrease"

Model Summary

S	R-sq	R-sq(adj)	R-sq(pred)
9.82629	89.92%	87.04%	83.40%

Coefficients

Term	Coef	SE Coef	T-Value	P-Value	VIF
Constant	75.3	15.3	4.92	0.002	
SHD	-0.02333	0.00712	-3.28	0.014	1.96
Effect on hardness	0.287	0.101	2.84	0.025	1.96

Regression Equation

Hardness decr. = 75.3 - 0.02333 SHD + 0.287 Effect on hardness

As shown in appendix B.5 the effects on hardness (dilatometer study) depend on contents of silicon, manganese and hardness of the prior microstructure. Smaller effects on hardness were measured for high contents of manganese, low contents of silicon and larger prior structure hardness. It is reported in literature that manganese as well as a refined prior microstructure (as for QT) accelerates austenitisation and leads to faster dissolution of carbon and other alloying elements, while silicon acts with opposite effect due to an increase in carbon activity in austenite [Kim12, Cha11].

Figure 111 shows a hypothetical carbide fraction evolution and hardness evolution, assuming the above described dissolution characteristics derived from Grosch [Gro84] (see Figure 106). A lower carbide fraction or higher hardness for the QT prior microstructure in case of identical austenitisation conditions was set. This is based on the related micrographs, the measured, lower M_S temperatures and the higher measured hardness. When increasing austenitisation temperature or prolonging soaking time (1→2), the QT prior microstructure (or Mn alloyed / low silicon / steel with fast austenitisation characteristic) shows a smaller decrease in carbide fraction and connected most likely a smaller decrease in M_S temperature and smaller increase in hardness. It shall be mentioned that the data from Grosch [Gro84] shows a tendency for slower carbide dissolution also at the beginning of the dissolution process, for short soaking times or low temperatures. Since the lowest used austenitisation temperature (950 °C) was well above Ac_3/ Ac_{1e} temperatures and the corresponding samples showed a comparably high hardness level, it is believed that the point of a possible slow carbide dissolution at the beginning of austenitisation was passed.

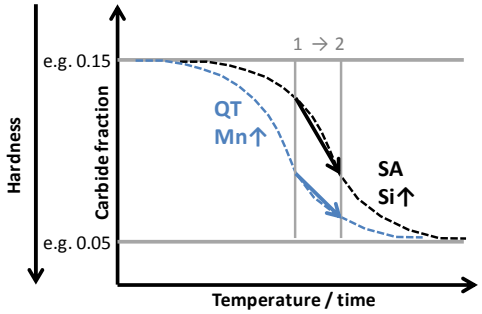

Figure 111: Hypothetical carbide fraction and hardness level for increasing austenitisation temperature or soaking time

The **residual stress measurements** at the very surface of the samples can be related to the surface hardening depth, see Figure 112. It was shown above that the surface hardening depth is a function of transformation temperature A_{c3}, which itself is affected by alloying elements (Si, Mn, Cr, C) and hardness of the prior microstructure (see Appendix B.2).

The tendency of increased residual compressive stresses with decreased surface hardening depth is known in literature [Mar09, Klo89]. The effect is often explained by the ability of the core to restrain the volume expansion of the surface during martensitic transformation. A bigger restraining potential by having a larger core (small surface hardening depth) will promote compressive stresses in the hardened layer. The strong effect of surface hardening depth across the different steels however is surprising. Other factors which are known to affect the residual stress level, such as for example dissolved carbon content, M_s temperature or austenite strengths, seem to play only minor roles.

Linear regression analysis revealed a dependency between the measured residual stresses and the A_{c1} temperature derived from dilatometer testing (see Table 23). Similar to the A_{c3} temperature, the A_{c1} temperature correlates well with the surface hardening depth and is affected by similar alloying elements (Si, Ni, Mo, Cr) and hardness of the prior microstructure (see Appendix B.2).

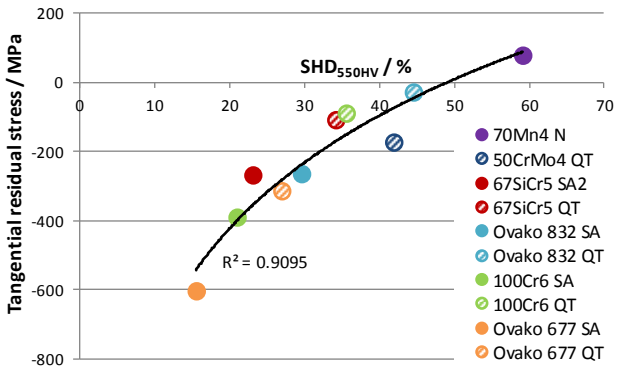

Figure 112: Tangential residual stress below the surface (depth: 30 µm) connected to surface hardening depth (SHD)

Table 23: Linear regression for response "residual stress"

Model Summary					
S	R-sq	R-sq(adj)	R-sq(pred)		
54.5914	93.09%	92.22%	89.50%		
Coefficients					
Term	Coef	SE Coef	T-Value	P-Value	VIF
Constant	8837	872	10.13	0.000	
Ac1	-11.49	1.11	-10.38	0.000	1.00
Regression Equation					
Res. stress = 8837 – 11.49 Ac1					

5.3 RCF testing

5.3.1 Grooving

The average grooving is affected by the samples hardness before testing, as shown in Figure 113. Increased hardness leads to less grooving or microplasticity. It follows that steels with higher hardness levels are more stable in terms of microplasticity for the given testing conditions. Following authors like Vegter or Andersson [Veg12, And12] it may be concluded that the resistance against microstructural alterations (for example dislocation glide or climb, creep, softening, diffusion processes) and fatigue damage during the repetitive over-rolling is increased by increased material strengths or hardness.

Minitab statistical software and linear regression analysis was used for further evaluation of dependencies. Chemical composition, hardness of the prior microstructure, cleanliness rating, prior austenite grain size derived from the dilatometer study, as well as the results from grooving measurement, XRD investigation and metallographic investigation were used as potential predictors.

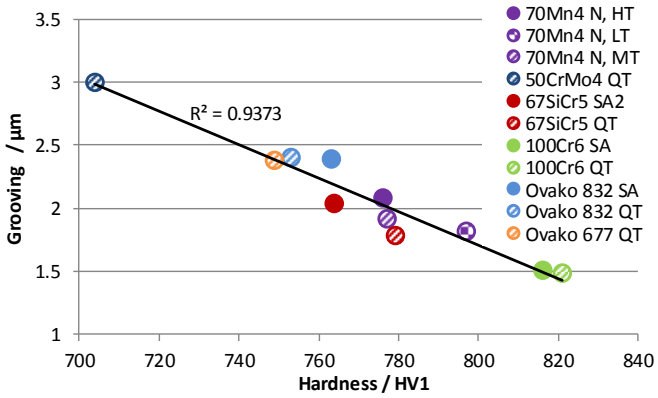

Figure 113: Average measured groove depth (grooving) and hardness prior to fatigue testing

Table 24: Linear regression for response "grooving"

Model Summary

S	R-sq	R-sq(adj)	R-sq(pred)
0.122863	93.93%	93.17%	92.24%

Coefficients

Term	Coef	SE Coef	T-Value	P-Value	VIF
Constant	12.286	0.917	13.39	0.000	
pr. hardness HV1	-0.01321	0.00119	-11.13	0.000	1.00

Regression Equation

grooving = 12.286 – 0.01321 prior hardness HV1

All Minitab models included the prior hardness a predictor which already results in a good prediction as a single predictor (see Table 24 until Table 26) and proves its` significance. Alternative models with a somewhat better prediction (R^2) include in addition the hardness increase after fatigue testing as a predictor. It follows that grooving facilitates work hardening of the fatigued microstructure. In the further discussion below, it will be demonstrated that the hardness increase or work hardening strongly correlates with the content in retained austenite before fatigue testing. This fits well with the third proposed regression model, which attributes a positive effect to manganese and nickel on the groove depth, while silicon acts in opposite way. Nickel and manganese are known to increase the retained austenite content, while silicon increases its stability [Kim12, Sid15].

Including the retained austenite content before fatigue testing into the model results in a fairly good fit (R^2 = 95 %), however does not attribute the coefficient "retained austenite" a significance (p = 0.194). A similar result was obtained when including the change in retained austenite into the model (see Appendix B.6)

Table 25: Linear regression for response "grooving"; "delta HV, work hard." with positive algebraic sign

Model Summary

S	R-sq	R-sq(adj)	R-sq(pred)
0.0875577	97.59%	96.79%	95.55%

Coefficients

Term	Coef	SE Coef	T-Value	P-Value	VIF
Constant	11.874	0.695	17.09	0.000	
delta HV, work hard.	0.00531	0.00174	3.05	0.023	1.00
hardness HV1	-0.013261	0.000875	-15.16	0.000	1.00

Regression Equation

grooving = 1.874 + 0.00531 delta HV, work hard. – 0.013261 prior hardness HV1

Table 26: Linear regression for response "grooving"

Model Summary

S	R-sq	R-sq(adj)	R-sq(pred)
0.0461775	99.46%	99.04%	97.56%

Coefficients

Term	Coef	SE Coef	T-Value	P-Value	VIF
Constant	12.172	0.423	28.79	0.000	
Si	-0.2073	0.0412	-5.03	0.004	1.30
Mn	0.1467	0.0545	2.69	0.043	2.53
Ni	1.890	0.738	2.56	0.050	2.03
hardness HV1	-0.013323	0.000542	-24.57	0.000	1.48

Regression Equation

grooving = 12.172 - 0.2073 Si + 0.1467 Mn + 1.890 Ni - 0.013323 prior hardness HV1

If the groove depth is seen as a measure of fatigue damage, steel grade 100Cr6 experienced least fatigue damage, followed by 70Mn4 and 67SiCr5. Generally, the steels hardness before fatigue testing was demonstrated to be most affecting and shall be maximized in terms of grooving.

5.3.2 XRD measurement

5.3.2.1 Residual stresses

The change in residual stress in a depth of 140 µm is correlating well with the measured groove depth. No other possible coefficient was proposed by Minitab software (see Figure 114 and Table 27).

This corresponds to different authors ideas of compressive residual stress generation like Voskamp in [Vos97], Schlicht in [Sch70] or Swahn in [Swa75]. Schlicht claims that the accumulation of plastic deformation leads to the generation of compressive residual stresses due to an increase in specific volume. The increase in volume is caused by an increased density of dislocation and free vacancies. Voskamp argues with expansion constraint of the plasticised volumes and resulting compressive stresses.

The transformation of retained austenite and the accompanied increase in specific volume was also reported to contribute to the residual stress generation [Vos70]. The measured retained austenite contents and change in retained austenite content could not be correlated to the generated compressive stresses or the change in residual stress.

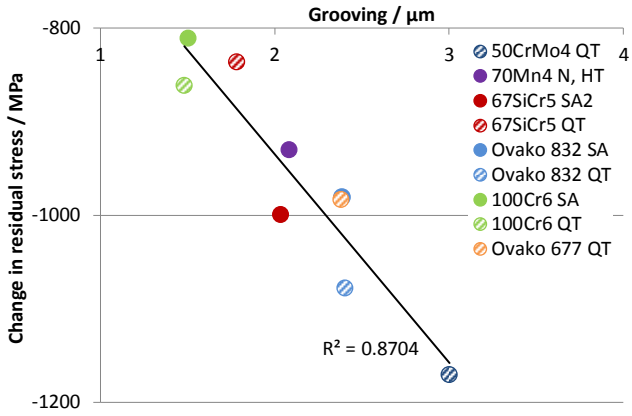

Figure 114: Change in residual stress at a depth of 140 µm and grooving of fatigued samples

Table 27: Linear regression for response "change in residual stress fatigued volume"; "delta RS 140 µm" with negative algebraic sign

Model Summary					
S	R-sq	R-sq(adj)	R-sq(pred)		
44.8706	87.04%	85.19%	80.52%		
Coefficients					
Term	Coef	SE Coef	T-Value	P-Value	VIF
Constant	-489.6	70.3	-6.96	0.000	
grooving	-222.7	32.5	-6.86	0.000	1.00
Regression Equation					
delta RS 140 µm = -489.6 – 222.7 grooving					

It was shown before that the developed groove depth can be correlated to the prior samples hardness. Since the change in residual stress correlates with the groove depth, it follows that also the change in residual stress correlates with the prior samples hardness, see Figure 115, Figure 116, Table 28 and Table 29.

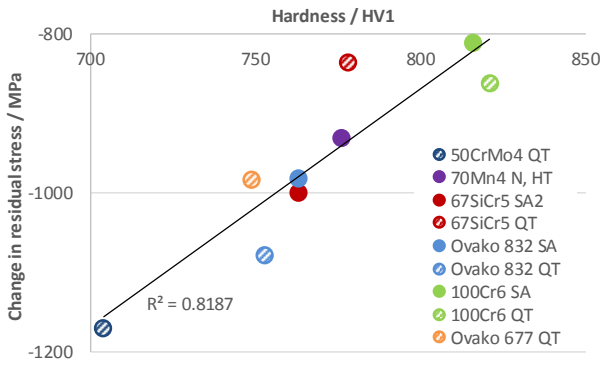

Figure 115: Change in residual stresses and prior hardness of fatigue samples

Table 28: Linear regression for response "change in residual stress fatigued volume"; "delta RS 140 µm" with negative algebraic sign

Model Summary					
S	R-sq	R-sq(adj)	R-sq(pred)		
52.8950	82.00%	79.42%	72.18%		
Coefficients					
Term	Coef	SE Coef	T-Value	P-Value	VIF
Constant	-3255	407	-8.00	0.000	
hardness HV1	2.981	0.528	5.65	0.001	1.00
Regression Equation					
delta RS 140 µm = -3255 + 2.981 prior hardness HV1					

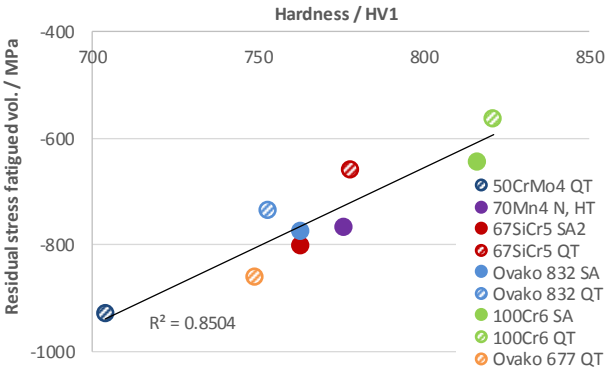

Figure 116: Residual stresses in fatigued material volume and prior hardness of fatigue samples

Table 29: Linear regression for response "residual stress fatigued volume"

Model Summary					
S	R-sq	R-sq(adj)	R-sq(pred)		
46.7245	85.16%	83.04%	77.65%		
Coefficients					
Term	Coef	SE Coef	T-Value	P-Value	VIF
Constant	-3021	359	-8.41	0.000	
hardness HV1	2.956	0.466	6.34	0.000	1.00
Regression Equation					
abs. RS track 140µm = -3021 + 2.956 prior hardness HV1					

If the change in residual stress is seen as a measure of fatigue damage, steel grade 100Cr6 experienced least fatigue damage, followed by 67SiCr5 QT and 70Mn4. Generally, the steels developed groove depth was demonstrated to be most affecting and shall be minimized. As shown before, a small groove depth can be

achieved for steels with high hardness levels. It can be concluded that the steels hardness should be maximized for a lower residual stress change or lower absolute compressive stress level.

5.3.2.2 Full width half maximum

A direct correlation of the measured full width half maximum (FWHM) values or the change in FWHM with the prior hardness or grooving was not possible. The most significant correlation was found with the magnitude of compressive stress of the fatigued volume, see Figure 117, Figure 118, Table 30 and Table 31. Larger compressive stresses lead to a lower magnitude of FWHM and a larger change in FWHM. The lack of correlation with the change in residual stress might be a hint that the magnitude of compressive stress in the fatigued material volume is a measure for microstructural changes, rather than the change in stresses.

An alternative regression model adds a negative effect of manganese on the relative change in FWHM (or vice versa on the absolute value of FWHM). Manganese is known to stabilize retained austenite and increase its content after hardening. Following that, more and stable retained austenite (+ Mn) would promote fewer changes in FWHM. Including the retained austenite content before fatigue testing into the model results in a negative effect of retained austenite on the change of FWHM and a fairly good fit (R^2 = 88 %), however does not attribute the coefficient "retained austenite" a significance (p = 0,279) (see appendix B.7). Including additionally the change in retained austenite (difference before and after fatigue testing), the model attributes the change in retained austenite a positive effect on the change in FWHM. The significance however turned out to be low (p = 0,589) (see appendix B.7). This can be interpreted as a hint that the retained austenite content as well as its stability plays a role for the change in FWHM. It must be noted, that the FWHM value is a characteristic of the alpha iron peak and does not describe the lattice characteristics of the retained austenite phase. A potential explanation might be that the present retained austenite phase, next to martensite or alpha iron in the loaded volume, takes a larger share of the cyclic loading, microplasticity, and hence fatigue damage. This seems reasonable, since austenite is known as a phase being able to undergo a larger amount of plastic strain as compared to martensite. In that way, an increased share of retained austenite leads to a larger ability to accumulate energy from cyclic loading and thereby expand the second stage of material behaviour during rolling contact fatigue, see also Figure 25.

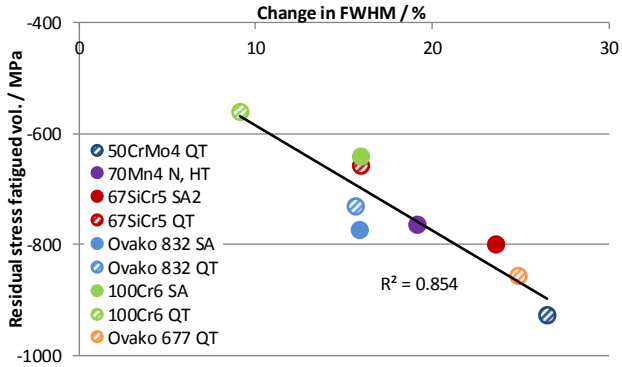

Figure 117: Relative change in FWHM of fatigued material volume and residual stress of fatigue material volume

Table 30: Linear regression for response "change in FWHM"

Model Summary					
S	R-sq	R-sq(adj)	R-sq(pred)		
2.26494	85.40%	83.31%	79.08%		
Coefficients					
Term	Coef	SE Coef	T-Value	P-Value	VIF
Constant	-15.21	5.33	-2.86	0.024	
abs. RS track 140µ	-0.04515	0.00706	-6.40	0.000	1.00
Regression Equation					
Delta FWHM % =	-15.21 – 0.04515 abs. RS track 140µ				

Table 31: Linear regression for response "change in FWHM"

Model Summary					
S	R-sq	R-sq(adj)	R-sq(pred)		
1.75060	92.52%	90.03%	75.39%		
Coefficients					
Term	Coef	SE Coef	T-Value	P-Value	VIF
Constant	-16.36	4.14	-3.95	0.008	
abs. RS track 140µ	-0.05085	0.00595	-8.54	0.000	1.19
Mn	-3.40	1.42	-2.39	0.054	1.19
Regression Equation					
Delta FWHM % =	-16.36 – 0.05085 abs. RS track 140µ - 3.40 Mn				

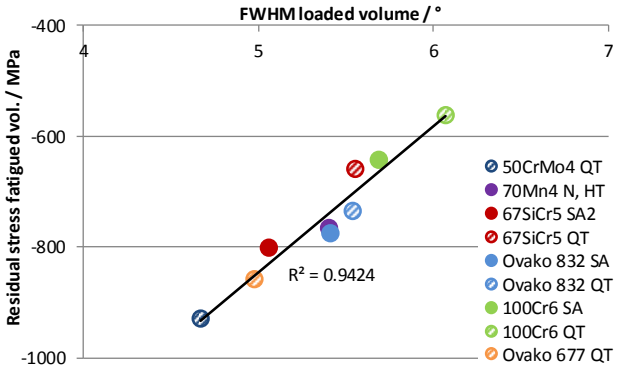

Figure 118: Absolute FWHM of fatigued material volume and residual stress of fatigue material volume

Table 32: Linear regression for response "absolute FWHM on track"

Model Summary

S	R-sq	R-sq(adj)	R-sq(pred)
0.107139	94.24%	93.41%	91.62%

Coefficients

Term	Coef	SE Coef	T-Value	P-Value	VIF
Constant	8.042	0.252	31.93	0.000	
abs. RS track 140µ	0.003572	0.000334	10.70	0.000	1.00

Regression Equation

abs FWHM track 140µm = 8.042 + 0.003572 abs. RS track 140µ

Table 33: Linear regression for response "absolute FWHM on track"

Model Summary

S	R-sq	R-sq(adj)	R-sq(pred)
0.0690207	97.95%	97.27%	95.60%

Coefficients

Term	Coef	SE Coef	T-Value	P-Value	VIF
Constant	8.105	0.163	49.61	0.000	
abs. RS track 140µ	0.003882	0.000235	16.54	0.000	1.19
Mn	0.1846	0.0560	3.30	0.016	1.19

Regression Equation

abs FWHM track 140µm = 8.105 + 0.003882 abs. RS track 140µ + 0.1846 Mn

If the change in FWHM is seen as a measure of fatigue damage, steel grade 100Cr6 QT experienced least fatigue damage, followed by 100Cr6 SA and 67SiCr5 QT. Generally, the steels developed compressive stress magnitude was demonstrated to be most affecting and shall be minimized. As shown before, an increased hardness level facilitates lower magnitudes of compressive residual stress in the fatigued material volume. Hence, the hardness level should be maximized for a smaller change in FWHM.

5.3.2.3 Retained austenite

In general QT starting microstructures experience less absolute and relative reduction in retained austenite than SA starting microstructures, see Figure 92 (100Cr6, Ovako 832 and 67SiCr5). One possible explanation is connected to the stability of retained austenite. The dilatometer study showed lower M_S temperatures and hence more alloying elements dissolved in the matrix in case of the QT starting microstructures. Increased amounts of dissolved alloying elements might have led to increased retained austenite stability (especially Si, Mn, Cr, Ni, Mo [Sid15]).

Minitab statistical software proposed different regression models for the relative change in retained austenite, see Table 34 until Table 36. All models include the alloying element manganese with a negative effect, most likely due to its stabilizing effect on retained austenite. The prior hardness is included in two models, where an increased hardness promotes smaller changes in retained austenite. The third model includes "grooving" with the opposite effect as compared to prior hardness. A combination of large grooving and large retained austenite level prior to fatigue testing promotes retained austenite transformation. It was shown earlier that increased prior hardness leads to less grooving. Smaller groove depths and hence less plasticity leads to less straining of retained austenite, which will most likely lead to less retained austenite transformation.

The second model includes the hardness increase or work hardening after fatigue testing and attributes a positive effect on the change in retained austenite. This seems reasonable if the hardness increase or work hardening resulted partly from the transformation of retained austenite to a phase with higher hardness (see discussion of work hardening below).

Table 34: Linear regression for response "relative change in retained austenite"

Model Summary

S	R-sq	R-sq(adj)	R-sq(pred)
6.00306	86.00%	77.60%	46.31%

Coefficients

Term	Coef	SE Coef	T-Value	P-Value	VIF
Constant	312.3	54.9	5.68	0.002	
Mn	-20.80	5.17	-4.02	0.010	1.34
hardness HV1	-0.3573	0.0700	-5.11	0.004	1.36
Cr	13.76	4.57	3.01	0.030	1.14

Regression Equation

Delta RA % = 312.3 – 20.80 Mn – 0.3573 prior hardness HV1 + 13.76 Cr

Table 35: Linear regression for response "relative change in retained austenite"

Model Summary

S	R-sq	R-sq(adj)	R-sq(pred)
4.45476	92.29%	87.67%	71.36%

Coefficients

Term	Coef	SE Coef	T-Value	P-Value	VIF
Constant	293.5	39.8	7.37	0.001	
Mn	-29.73	4.72	-6.30	0.001	2.03
hardness HV1	-0.3599	0.0516	-6.98	0.001	1.35
delta HV, work hardening	0.516	0.114	4.53	0.006	1.65

Regression Equation

Delta RA % = 293.5 – 29.73 Mn – 0.3599 prior hardness HV1 + 0.516 delta HV, work hardening

Table 36: Linear regression for response "relative change in retained austenite"

Model Summary

S	R-sq	R-sq(adj)	R-sq(pred)
4.64001	91.64%	86.62%	77.89%

Coefficients

Term	Coef	SE Coef	T-Value	P-Value	VIF
Constant	-26.7	10.5	-2.53	0.052	
Mn	-31.33	5.11	-6.13	0.002	2.19
abs. RA reference	1.180	0.355	3.33	0.021	1.59
grooving	33.84	4.76	7.11	0.001	2.01

Regression Equation

Delta RA % = -26.7 – 31.33 Mn + 1.180 abs. RA reference + 33.84 grooving

If the relative change in retained austenite is seen as a measure of fatigue damage, steel grades 70Mn4, 67SiCr5 QT and Ovako 832 QT experienced least fatigue damage, followed by 100Cr6 SA and Ovako 832 SA. The largest relative change or fatigue damage was measured for steel 50CrMo4.

Generally, the steels manganese content as well as its prior hardness were demonstrated to be most affecting and shall be maximized.

5.3.3 Metallography

5.3.3.1 Work hardening

The work hardening or hardness increase due to the cyclic loading shows a correlation towards the steels retained austenite content after heat treatment, see Figure 119. The presence of retained austenite promotes work hardening of the material and leads to a hardness increase due to cyclic loading. This is in accordance to the observation made by Sugino in [Sug70]. Two mechanisms most likely lead to a hardness increase in connection with the presence of retained austenite. Retained austenite might partly transform under load or deformation into a phase with higher hardness, such as martensite or bainite. It was shown above that the change in retained austenite content is facilitated by a combination of larger retained

austenite contents and larger grooving or amount of plasticity. In addition, plastically deformed retained austenite will work harden without transforming [Sid15]. Both mechanisms will contribute to an increase in overall hardness. The fact that the hardness increase correlates better with the absolute retained austenite content before testing (compare Figure 119 and Figure 120) might indicate that work hardening of retained austenite without any metallurgical phase transformation contributes to a larger extent. If martensitic phase fractions contribute to the overall hardness change by work hardening or softening cannot be answered here, but shall be taken into account.

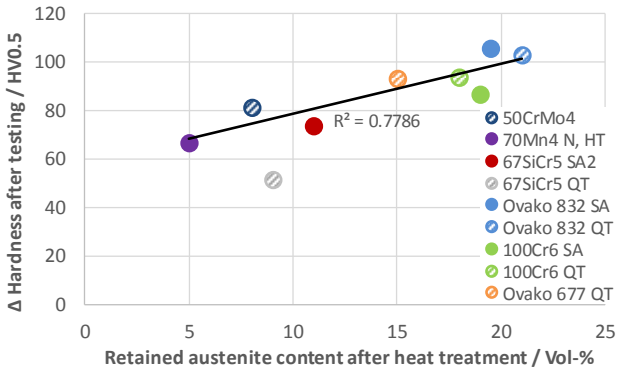

Figure 119: Work hardening or hardness increase after fatigue testing and retained austenite content after heat treatment

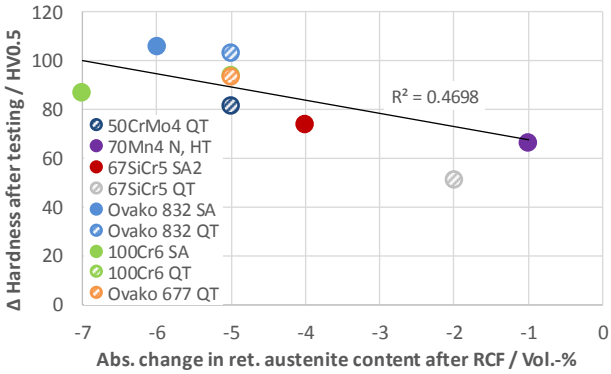

Figure 120: Work hardening or hardness increase after fatigue testing and absolute change in retained austenite content after fatigue testing

The proposed Minitab linear regression model contains the initial retained austenite content as well as the developed groove depth and aligns with the above assumptions (see Table 37). A combination of large retained austenite content as well as large grooving or plasticity promotes work hardening.

Table 37: Linear regression for response "work hardening"

Model Summary

S	R-sq	R-sq(adj)	R-sq(pred)
4.48172	92.43%	89.41%	81.64%

Coefficients

Term	Coef	SE Coef	T-Value	P-Value	VIF
Constant	29.9	10.1	2.95	0.032	
abs. RA reference	2.361	0.303	7.79	0.001	1.12
grooving	11.02	3.55	3.10	0.027	1.12

Regression Equation

delta HV, work hardening = 29.9 + 2.361 abs. RA reference + 11.02 grooving

If the increase in hardness can be interpreted as a measure of fatigue damage is not clear. Most studies in literature correlate fatigue with the observed decrease in hardness and accompanied dark etching regions or white etching bands. An increase in hardness was observed by Swahn in [Swa75] until approximately $6{,}5x10^5$ and 10^7 load cycles. Muro shows that higher contact pressures can lead to work hardening in early stages of fatigue [Mur70]. Voskamp describes three stages of fatigue and attributes work hardening to the first "shakedown" stage [Vos69] (see Figure 25), while other features of fatigue like retained austenite decay and material softening will occur in the later "instability" phase. In the present investigation, work hardening and retained austenite decay occur simultaneously and do not appear separated.

The ability to work harden is seen as a positive material attribute in some studies, such as [Hip10]. Damage tolerant material concepts were developed with increased ability to work harden. The work hardening

process is believed to reduced peak stresses in service due to plastic deformation. Steel grades Ovako 832, 100Cr6 and Ovako 677 exhibit the largest hardness increases and can be attributed the positive feature of increased ability to work harden.

5.3.3.2 Total number of observations

The total number of observations made during metallographic investigations correlate well with the cleanliness rating of the investigated steels. Due to the increasing number of observations from the beginning towards the centre position of the track, the numbers of observations were averaged over the last 200 µm towards the centre (axial position 11.3 – 11.5 mm) where the gradient becomes small. The A-type inclusions turned out to correlate well, see Figure 121. This is in line with the observation during microscopy that most cracks or white etching features were accompanied with sulphide based non-metallic inclusions, typically greyish in colour and having round edges.

The large number of observations for steel grade 70Mn4 N, HT is most likely caused by the chosen heat treatment and the high austenitisation temperature, which probably lead to larger prior austenite grains and a brittle material behaviour. The existence of microcracking after heat treatment was not observed for 70Mn4 N, HT.

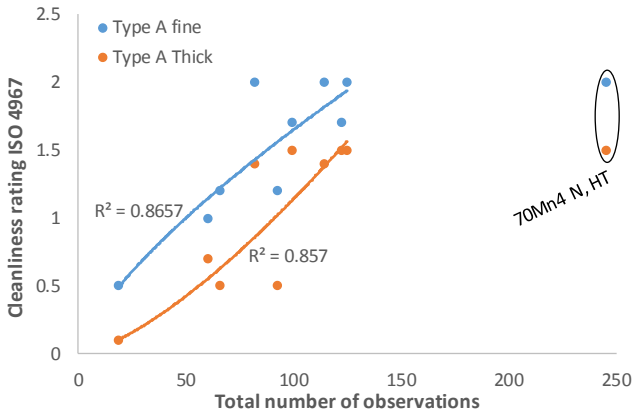

Figure 121: Cleanliness rating ISO 4967:2013 Method A (Type A inclusions) and total number of observed alterations in fatigued samples

The proposed linear regression model by Minitab (Table 38 and Table 39) confirms the beforementioned. Increased values for A-type inclusions as well as increased prior austenite grain sizes promote the occurrence of microstructural observations.

Non-metallic inclusions act as stress raisers and are known to be initiation locations for cracks, white etching features and similar. Why the rating for A-type inclusions, which are typically manganese or calcium sulphides, is the most affecting one is not known. One possible reason might be the comparably large size of sulphide type inclusions, which are deformable and generally stretched in the direction of rolling. The large dimensions can lead to large discontinuities and act as stress raiser, especially for the case of bad bonding to the surrounding matrix. The two-dimensional documentation of inclusions generally cannot easily detect mixed sulphide-oxide inclusions. In such cases, the combination of sulphides and oxides can lead to a combination of large inclusion size (sulphide) and bad or no bonding to the matrix (oxide). Such inclusions

were shown to be most detrimental for butterfly and crack formation in the work of Lund and Sugino [Lun10, Sug70].

Table 38: Linear regression for response "total number of observations"

Model Summary

S	R-sq	R-sq(adj)	R-sq(pred)
27.0141	84.13%	79.59%	49.70%

Coefficients

Term	Coef	SE Coef	T-Value	P-Value	VIF
Constant	-65.3	29.2	-2.24	0.060	
PAGS	7.57	1.84	4.11	0.005	1.09
A, thick	53.6	17.2	3.11	0.017	1.09

Regression Equation

obs. 11,3-11,5 = -65.3 + 7.57 PAGS + 53.6 A, thick

Table 39: Linear regression for response "total number of observations"

Model Summary

S	R-sq	R-sq(adj)	R-sq(pred)
19.5264	93.97%	90.35%	67.96%

Coefficients

Term	Coef	SE Coef	T-Value	P-Value	VIF
Constant	-250.4	78.3	-3.20	0.024	
PAGS	8.78	1.40	6.29	0.001	1.12
D, fine	123.6	52.5	2.36	0.065	4.54
A, thick	111.4	25.8	4.31	0.008	4.33

Regression Equation

obs. 11,3-11,5 = -250.4 + 8.78 PAGS + 123.6 D, fine + 111.4 A, thick

An alternative regression model includes oxide type inclusions (D-type), see Table 39. The significance for the D-type inclusion type was given as comparably low (p=0,065).

The conducted cleanliness rating according to ISO 4967:2014 Method A and its worst field approach does not give any information about the population of the different inclusions types, which will also affect the likelihood of crack or butterfly formation and similar.

5.3.3.3 Number of observations with white etching features

The total number of observation with accompanied white etching features turned out to decrease with increasing silicon content and increased compressive stress level after rolling contact, see Figure 122 and Figure 123. Two different linear regression models were proposed by Minitab, which include the mentioned silicon content and compressive stress level, see Table 40 and Table 41.

The first Minitab model attributes a decreasing effect for silicon and an increasing effect for chromium and molybdenum on the number of observation with white etching features. Different mechanisms are proposed in literature for white etching area formation. The connection of white etching matter formation and redistribution of carbon and silicon within white etching matter was shown by Kang et al. in [Kan13]. Silicon and carbon segregate at cell boundaries and avoid each other. This seems reasonable since silicon is known to increase carbon activity [Pet60, Kim12, She89]. The interaction between carbon and silicon is argued to have an important effect on carbon diffusion and therefore on the formation of nanocrystalline structures and carbide dissolution in white etching matter [Kan12]. The proposed model by Minitab supports the mentioned effect of silicon.

White etching areas were reported to be carbide depleted or free [Gra10b, Bri66, Swa76, Sug70, Öst82, Bri88, Sco66]. Neither primary nor temper carbides could be observed, which suggest that carbides have been dissolved in the white etching material volume either during, after or before white etching area formation. The dissolution of carbon into the ferrite matrix is strongly depended on the matrix carbon activity. Here, the difference in carbon activity between carbides and matrix is known to be the driving force for carbon diffusion [Por92]. It follows that larger carbon activities of the steel matrix leads to reduced carbon flux from cementite towards the matrix. While silicon is known to increase the carbon activity, chromium and molybdenum is

known to have a decreasing effect on carbon activity [Pet60, Kim12, She89]. The mentioned effects could explain the reduced number of white etching features for increased silicon and decreased chromium and molybdenum content.

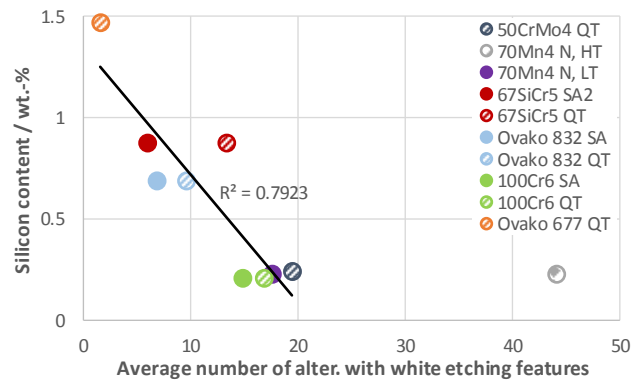

Figure 122: Average number of alterations with white etching feature for investigated axial positions (axial position 11.3-11.5) and steels silicon content

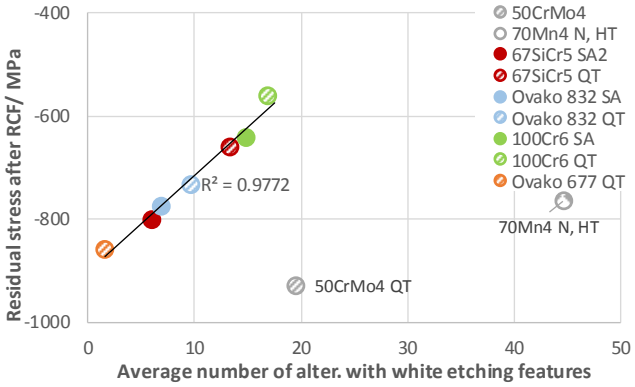

Figure 123: Average number of alterations with white etching feature for investigated axial positions (axial position 11.3-11.5) and steels residual stress after rolling contact fatigue (z = 140 µm)

Table 40: Linear regression for response "average number of alterations with white etching feature"

Model Summary

S	R-sq	R-sq(adj)	R-sq(pred)
2.90130	96.67%	94.01%	86.99%

Coefficients

Term	Coef	SE Coef	T-Value	P-Value	VIF
Constant	-58.3	14.1	-4.14	0.009	
Si	-17.18	2.61	-6.58	0.001	1.32
Cr	12.52	3.92	3.19	0.024	4.99
Mo	168.0	26.8	6.26	0.002	4.21
PAGS	3.942	0.589	6.70	0.001	9.67

Regression Equation

av. # alt. with WEA = -58.3 – 17.18 Si + 12.52 Cr + 168.0 Mo + 3.942 PAGS

Table 41: Linear regression for response "average number of alterations with white etching feature"

Model Summary

S	R-sq	R-sq(adj)	R-sq(pred)
1.90851	98.84%	97.68%	75.23%

Coefficients

Term	Coef	SE Coef	T-Value	P-Value	VIF
Constant	-4.57	5.39	-0.85	0.445	
Si	-19.98	1.75	-11.44	0.000	1.26
Mo	156.9	18.7	8.40	0.001	4.54
PAGS	2.739	0.208	13.18	0.000	2.60
abs. RS track 140µ	0.02774	0.00890	3.11	0.036	2.24

Regression Equation

av. # alt. with WEA = -4.57 – 19.98 Si + 156.9 Mo + 2.739 PAGS + 0.02774 abs. RS track 140µm

For both Minitab models, a larger prior austenite grain sizes leads to an increased number of white etching features. Larger grain sizes lead in general to a more brittle material behavior and enhances microcracking which might facilitate white etching feature generation [Bha12]. In addition, crack development and crack growth is enhanced by a brittle material behavior or larger grain sizes. Paladugu et al. show in [Pal17] that brittle microstructures with large grains promotes white etching matter formation in a carburized bearing steel. Bhadeshia et al. suggest in [Bha15] increased bearing steel toughness to avoid cracking and connected white etching matter formation. If the accompanied cracks next to white etching features are existing before white etching area formation or develop afterwards is discussed controversially in literature [Gou17, Kad17, Sol14]. Assuming that larger grains facilitate crack development and white etching area formation (see Minitab model), the pre-existence of cracks prior to white etching area formation appears reasonable.

The number of white etching features can be reduced by increased compressive residual stress levels after fatigue testing, as proposed in the second Minitab model. Subsurface compressive stresses are reported to increase the fatigue life of bearings. Fatigue crack initiation and propagation are believed to be decreased due to a decrease of the effective stresses by superimposed residual compressive stresses [Hyd96]. Assuming the necessity of pre-existing cracks for white etching matter formation, compressive residual stresses and

connected a decreased crack initiation rate [Hyd96, Tot02] would explain its decreasing effect on the number of white etching features.

The white etching matter formation is believed to be connected to small scale rubbing movement, sliding and material transfer between the two opponent crack faces [Kad17, Gra10b, Gra10a]. Kadin describes for a surface parallel crack the combination of normal compressive stresses (radial direction) and shear stresses acting on the crack (x/y -direction), see Figure 124. While the normal stress components press the crack faces onto each other, the shear stresses will lead to the sliding and rubbing movement leading to white matter formation. Taking the theory into account, it seems reasonable that the measured tangential compressive residual stresses might help to reduce the effect of both, the normal stresses and the shear stresses and thereby reduce the likelihood of white etching matter formation.

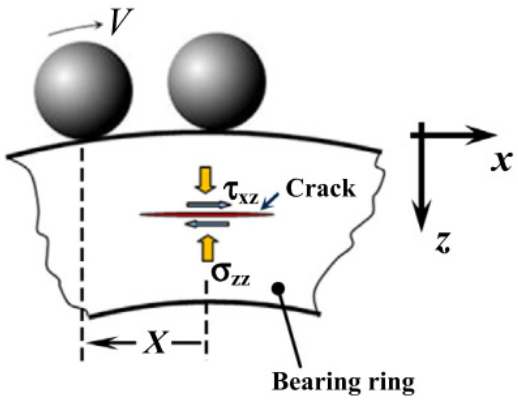

Figure 124: Schematic illustration of a sub-surface crack (parallel to the rolling surface) subjected to rolling contact [Kad17]

Contrary to the above described effect of chromium it was reported in literature that chromium enhances "white structure flaking life" [Uya11]. The increase in chromium content led to a decrease in hydrogen diffusion rate, where the diffusion of hydrogen towards defects was believed to cause the flaking phenomenon. Since it is not clear whether hydrogen plays a role for the white etching feature generation in the present investigation, the two findings do not contradict.

It is generally accepted that white etching matter and butterfly formation is often connected to stress raisers in the microstructures, such as non-metallic inclusions. Inclusions types DS, B-thick and B-fine (mainly oxide type inclusions) were possible to integrate into the second Minitab model (see Appendix B.8). However, the coefficient of determination (R^2) and the significance of the coefficients were not further improved.

5.3.3.4 Average number of cracks

Figure 125 and Figure 126 show the decrease in average number of cracks (cracks longer than 40 µm) with decreasing hardness (hardness prior to RCF testing) as well as increasing silicon content.

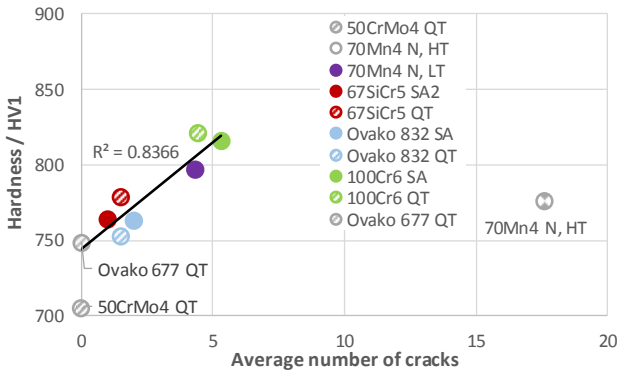

Figure 125: Average number of cracks after fatigue testing and steels hardness prior to fatigue testing

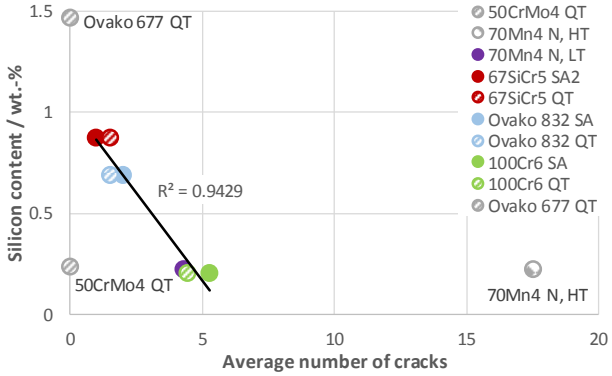

Figure 126: Average number of cracks after fatigue testing and steels silicon content

Minitab proposes two different models including the silicon content and hardness (see Table 42) and steels carbon content, A-thick inclusion type and prior austenite grain size (see Table 43).

Table 42: Linear regression for response "average number of cracks" excluding 70Mn4 N, HT

Model Summary

S	R-sq	R-sq(adj)	R-sq(pred)
0.469773	95.73%	94.31%	87.12%

Coefficients

Term	Coef	SE Coef	T-Value	P-Value	VIF
Constant	-28.21	3.84	-7.34	0.000	
Si	-1.844	0.410	-4.50	0.004	1.14
hardness HV1	0.04090	0.00485	8.43	0.000	1.14

Regression Equation

Av. number cracks = -28.21 – 1.844 Si + 0.04090 prior hardness HV1

Table 43: Linear regression for response "average number of cracks" including 70Mn4 N, HT

Model Summary

S	R-sq	R-sq(adj)	R-sq(pred)
0.569645	99.37%	98.90%	92.63%

Coefficients

Term	Coef	SE Coef	T-Value	P-Value	VIF
Constant	-62.25	4.05	-15.39	0.000	
C	39.20	3.57	10.97	0.000	4.89
A, thick	4.035	0.558	7.23	0.002	1.36
PAGS	1.8897	0.0963	19.63	0.000	4.21

Regression Equation

Av. number cracks = -62.25 + 39.20 C + 4.035 A, thick + 1.8897 PAGS

The hardness prior to fatigue testing (Table 42) and steels carbon content (Table 43) turned out to be affecting the number of appeared cracks. Increased hardness or increased carbon contents are known to decrease the steels toughness and lead to a brittle material behaviour facilitating crack formation and growths [Kra99].

The steels carbon content cannot always be related to the overall hardness, especially in case of different microstructural constituents like martensite and a larger fraction of retained austenite (e.g. Ovako832). Therefore, the total hardness was expressed as a linear mixture of martensite hardness and retained austenite hardness (assumed to be 450 HV), weighted according to their volume fractions. The result is shown in Figure 127 and displays the increasing carbon content in martensite for increased steels carbon contents. Brittle material behaviour with reduced toughness can be assumed for the martensitic phase fractions, which are most likely responsible for crack initiation and crack growth.

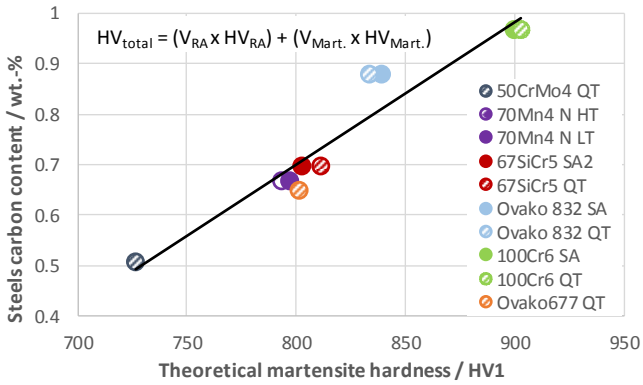

Figure 127: Steels carbon content and theoretical martensite hardness, derived from the measured overall hardness (HV1) and retained austenite content (volume fraction of austenite V_{RA} from XRD, $V_{Mart.} + V_{RA} = 1$), assuming a retained austenite hardness of 450 HV1

The decreasing effect of silicon on the number of cracks might have different reasons. Silicon is known to increase matrix strengths due to solid solution strengthening, where a higher matrix strength might increase the necessary stress for crack initiation. On the other hand, too large silicon contents might lead to a brittle material behaviour of the steel matrix.

It was shown before that silicon decreases the appearance of observations accompanied with white etching features. Almost all observed cracks in the range of 40 µm and longer showed white etching features or butterflies in their centre position (see Appendix B.9), implying that butterflies and similar are prerequisites of the observed cracks. The positive effect of silicon makes sense in this context.

The second Minitab model includes non-metallic inclusion type “A, thick” as well as the prior austenite grain size. Non-metallic inclusions of grey colour with round edges were frequently observed close to the white etching features in the centre position of longer cracks. Larger numbers for the A-type inclusion rating can therefore be connected to a larger number of longer cracks. If pure manganese or calcium sulphide or mixed inclusions are initiating points cannot be clarified using either the cleanliness rating according to ISO 683-17:2014 in worst field mode nor the documentation made with the light optical microscope.

The connection of larger prior austenite grains and more cracks can be explained by the reduced material toughness with increased grain size.

5.3.3.5 Average crack length

The first Minitab model (Table 44) suggest longer cracks for higher ratings of A and D type inclusions as well as larger changes for the FWHM. Higher ratings for A and D type inclusions are connected to more inclusions as well as increased size of inclusions. Assuming that cracks are initiated at internal defects such as non-metallic inclusions, more defects would lead to more cracks (see above). Bigger defects and potentially higher stress concentration at bigger defects could lead to earlier crack formation and more time for crack growths, leading to longer cracks.

If the change in FWHM is reflecting the microstructural damage and material weakening due to fatigue, a more developed material weakening can explain longer cracks in the material. Although a weakening in terms

of hardness reduction was not measured after fatigue testing, local effects might play a role. This could be local strength reduction, material embrittlement due to local plasticity or material embrittlement due to carbon supersaturation in white etching matter.

Table 44: Linear regression for response "average crack length"

Model Summary

S	R-sq	R-sq(adj)	R-sq(pred)
8.01389	98.91%	98.26%	94.88%

Coefficients

Term	Coef	SE Coef	T-Value	P-Value	VIF
Constant	-549.4	58.3	-9.43	0.000	
A, fine	240.7	17.2	14.02	0.000	10.36
D, thick	400.1	50.2	7.97	0.001	8.46
Delta HWB %	2.510	0.784	3.20	0.024	2.36

Regression Equation

average crack lengths = -549.4 + 240.7 A, fine + 400.1 D, thick + 2.510 Delta HWB %

Table 45: Linear regression for response "average crack length"

Model Summary

S	R-sq	R-sq(adj)	R-sq(pred)
7.19766	98.19%	96.83%	90.70%

Coefficients

Term	Coef	SE Coef	T-Value	P-Value	VIF
Constant	-445.5	51.1	-8.72	0.001	
C	359.9	45.2	7.97	0.001	4.89
A, thick	41.26	7.05	5.85	0.004	1.36
PAGS	13.20	1.22	10.86	0.000	4.21

Regression Equation

average crack lengths = -445.5 + 359.9 C + 41.26 A, thick + 13.20 PAGS

The second model includes the steels carbon content, A type inclusions and prior austenite grain size (Table 45). The role of non-metallic inclusion was mentioned above. The steels carbon content and prior austenite grain size can be connected to the steels toughness and leads to less resistance for crack growth. This point was discussed in the previous chapter.

The models for the average number of cracks (Table 43) and the average crack lengths (Table 45) contain the same coefficients. An alternative model (Table 46) could therefore include the average number of cracks into the model.

Table 46: Linear regression for response "average crack length"

Model Summary

S	R-sq	R-sq(adj)	R-sq(pred)
6.88983	99.20%	98.72%	96.83%

Coefficients

Term	Coef	SE Coef	T-Value	P-Value	VIF
Constant	-329.7	54.8	-6.02	0.002	
average Nr. cracks	2.664	0.674	3.95	0.011	2.32
A, fine	166.9	18.3	9.10	0.000	15.99
D, thick	272.2	51.8	5.26	0.003	12.17

Regression Equation

average crack lengths = -329.7 + 2.664 average Nr. cracks + 166.9 A, fine + 272.2 D, thick

An increased number of cracks, next to increased ratings for A and D type inclusions, leads to increased average crack lengths. The correlation seems reasonable, assuming that an increased number of cracks is connected to earlier crack formation and hence more load cycles for crack growth. In addition, in case of more cracks, there is an increased likelihood that the crack location is in the vicinity of the maximal crack growth driving stress component. The above-mentioned connection demonstrates the importance of material toughness, in terms of carbon content and prior austenite grain size, and the formation and growth of cracks.

5.3.3.6 Maximum cracks length

For each examined variant, the longest observed crack was determined. The linear regression models (Table 47 until Table 50) show a clear correlation between the maximum crack lengths and A type inclusions, which was discussed above. Other reoccurring coefficients are the materials hardness, steels carbon content and prior austenite grain size, which again demonstrates the importance of the materials toughness in terms of quantity and lengths of cracks.

Two models (Table 48, Table 50) attribute a negative effect of larger absolute retained austenite contents on the maximum crack lengths as well as a positive effect of larger absolute changes in retained austenite (note that absolute RA changes are negative in algebraic sign). Retained austenite is a comparable soft and tough phase which might lead to a reduced crack growth rate once the crack tip faces or stops at a retained austenite volume. In addition, the ability of austenite to easily plasticize can lead to a reduction of the acting stresses. The mechanical stresses and yielding of austenite can lead to a transformation to phases such as martensite or bainite. Due to the larger specific volume of martensite or bainite as compared to austenite, local compressive stresses can build up which in turn can slow down or stop crack growth.

Table 47: Linear regression for response "maximum crack length"

Model Summary

S	R-sq	R-sq(adj)	R-sq(pred)
29.1647	90.99%	88.41%	85.03%

Coefficients

Term	Coef	SE Coef	T-Value	P-Value	VIF
Constant	-863	238	-3.63	0.008	
A, thick	101.5	20.2	5.02	0.002	1.29
hardness HV1	1.139	0.320	3.56	0.009	1.29

Regression Equation

max. crack lengths = -863 + 101.5 A, thick + 1.139 prior hardness HV1

Table 48: Linear regression for response "maximum crack length"; delta RA 140 µm values with negative algebraic sign

Model Summary

S	R-sq	R-sq(adj)	R-sq(pred)
19.4259	97.06%	95.29%	87.62%

Coefficients

Term	Coef	SE Coef	T-Value	P-Value	VIF
Constant	-866	161	-5.39	0.003	
A, thick	111.8	13.9	8.06	0.000	1.26
delta RA 140 µm	10.22	3.71	2.76	0.040	1.03
hardness HV1	1.194	0.215	5.55	0.003	1.23

Regression Equation

max. crack lengths = -866 + 111.8 A, thick + 10.22 delta RA 140 µm + 1.194 prior hardness HV1

Table 49: Linear regression for response "maximum crack length"

Model Summary

S	R-sq	R-sq(adj)	R-sq(pred)
24.5523	91.19%	84.59%	24.57%

Coefficients

Term	Coef	SE Coef	T-Value	P-Value	VIF
Constant	-560	174	-3.21	0.033	
C	475	154	3.08	0.037	4.89
A, thick	83.7	24.0	3.48	0.025	1.36
PAGS	14.31	4.15	3.45	0.026	4.21

Regression Equation

max. crack lengths = -560 + 475 C + 83.7 A, thick + 14.31 PAGS

Table 50: Linear regression for response "maximum crack length"

Model Summary

S	R-sq	R-sq(adj)	R-sq(pred)
21.1312	96.52%	94.43%	83.56%

Coefficients

Term	Coef	SE Coef	T-Value	P-Value	VIF
Constant	-961	176	-5.47	0.003	
A, thick	117.0	15.6	7.50	0.001	1.34
abs. RA reference	-3.39	1.43	-2.38	0.063	1.24
hardness HV1	1.313	0.239	5.48	0.003	1.29

Regression Equation

max. crack lengths = -961 + 117.0 A, thick - 3,39 abs. RA reference + 1.313 prior hardness HV1

5.3.4 Benchmark RCF performance

For each of the investigated characteristics, a score was derived ranging from 1 (worst rating) to 10 (best rating). Linear interpolation between the best and worst rated characteristic was used to determine the intermediate ratings (see Table 51).

Table 51: Benchmark of RCF performance

		Grooving[1]	Abs. residual stress track[2]	Δ Residual stress[3]	Δ FWHM[4]	Δ RA[5]	Work hardening[6]	Microstructural observations[7]		Cracks[8]			Average Score
								7a	7b	8a	8b	8c	
100Cr6	*SA*	10	8	10	7	6	7	8	7	7	4	3	**7.0**
	QT	10	10	9	10	8	8	6	7	8	4	1	**7.4**
Ovako 832	*SA*	5	5	6	7	8	10	6	9	9	6	4	**6.8**
	QT	5	6	3	7	9	10	7	8	9	5	5	**6.7**
50CrMo4	*QT1*	1	1	1	1	1	6	8	6	10	10	10	**5.0**
67SiCr5	*SA2*	7	4	5	3	7	5	8	9	9	6	7	**6.4**
	QT	8	8	9	7	10	n.a.	7	8	9	7	7	**8.0**
70Mn4	*N, HT*	6	5	7	5	10	4	1	1	1	1	1	**3.8**
	N, LT	8	n.a.	n.a.	n.a.	n.a.	1	6	7	8	5	4	**5.6**
Ovako 677	*QT*	5	3	6	2	7	8	10	10	10	10	10	**7.4**

1 Score: 10 for smallest grooving, 1 for largest grooving

2 Score: 10 for smallest compressive stress, 1 for largest compressive stress at 140 µm depth on track

3 Score: 10 for smallest change in stress, 1 for largest change in stress between unfatigued and fatigue volume at 140 µm depth

4 Score: 10 for smallest relative change in FWHM, 1 for largest relative change in FWHM between unfatigued and fatigue volume at 140 µm depth

5 Score: 10 for smallest relative change in RA, 1 for largest relative change in RA between unfatigued and fatigue volume at 140 µm depth

6 Score: 10 for largest change in hardness, 1 for smallest change in hardness after fatigue testing

7 Score: 10 for smallest number of alterations, 1 for largest number of observations; 7a = rating for number of observations in etched sample condition; 7b = number of observations with accompanied WEA after fatigue testing

8 Score: 10 for smallest number/ shortest length of crack, 1 for largest number/ shortest length of crack; 8a = average number of cracks; 8b = average crack length; 8c = maximal crack length

n.a. Not available

The average score of the individual ratings attributes 67SiCr5 QT the best performance, followed by Ovako 677, 100Cr6 and Ovako 832. The worst overall performance was achieved by 70Mn4 and 50CrMo4.

The classical measures of fatigue damage development, others than microstructural observations and cracks, were mainly affected by the materials hardness. The regression models showed a clear reduction in grooving, change in residual stresses, change in FWHM and change in retained austenite with increased, as heat-treated hardness. It was followed at first that steels with larger carbon contents shall be favoured according to the mentioned measures. As an exception, the ability to work harden in terms of hardness increase after RCF testing was promoted by lower hardness levels or larger grooving and higher contents of retained austenite.

The observed larger scale microstructural material fatigue damage such as cracks (number and length) might cause flaking and failure at a later stage of life. Here, lower carbon contents and lower as heat-treated hardness levels were shown to be favourable. Since some of the observed cracks were comparably long (up to 250 µm) and reaching out to the raceway surface, it is believed that the crack number and crack length

are the life determining features of the conducted fatigue testing. Hence, steels with larger carbon contents or higher levels of hardness cannot be recommended for the conducted RCF test and RCF performance. Apart from a lower hardness, a better cleanliness level (mostly rating of A-type inclusion) and smaller prior austenite grain sizes promoted fewer and shorter cracks.

The presented outcome shows a discrepancy between the classical fatigue measures (see Figure 25 [Vos69]) and the microstructural observations (cracks). In addition, some characteristics of fatigue damage, like material softening, were absent while others were comparably developed. One example is the outcome for 50CrMo4, which experienced approximately a 60 % retained austenite decay, corresponding to the last stage of fatigue life according to Voskamp [Vos69]. In addition, microstructural alterations shown in Figure 128 were solely observed in 50CrMo4 material. Assuming that these alterations are the known fatigue connected high angle (~ 90°) bands, this indicates that fatigue damage is well developed. On the other hand, comparably small amount of cracks and comparably short cracks were found for 50CrMo4.

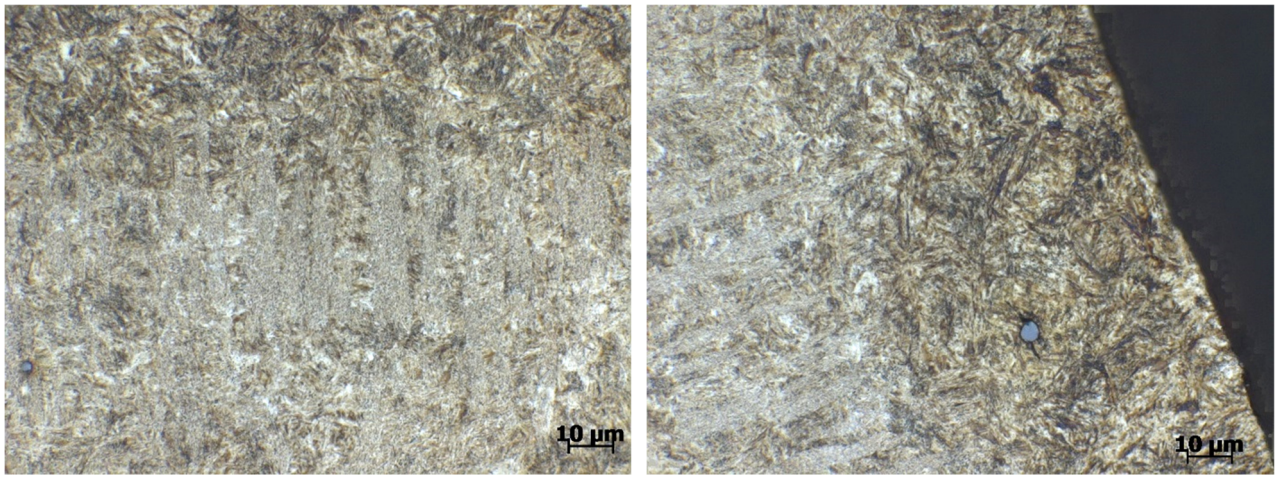

Figure 128: Microstructural alterations (possibly high angle bands) in 50CrMo4 steel after $3x10^7$ load cycles beneath the raceway (raceway on right micrograph, top right surface)

The mentioned discrepancy might be connected to the testing conditions and in particular to the relatively high contact pressure of p_0 = 5.56 GPa and following larger Hertzian stresses. The role of stress raisers such as non-metallic inclusions might be more pronounced leading to the formation and growth of cracks, especially for brittle material characteristics before the classical fatigue damage leads to failure.

As for the observations and cracks accompanied with white etching features, a positive impact of higher compressive residual stress levels, smaller prior austenite grains sizes as well increased silicon and decreased chromium and molybdenum was shown and previously discussed.

6 Summary and future work

The aim of the **dilatometer study** was to identify robust and suitable steels for induction hardening. The investigated steels were ranked accordingly. It was demonstrated that moderate alloyed steels, such as 50CrMo4, 70Mn4 or 67SiCr5 and partly Ovako 677 showed a comparable good stability in terms of changed M_S temperature and as quenched hardness with changed austenitisation conditions.

The change of the M_S temperature was increased by a decreased prior microstructure hardness (soft annealed prior microstructures) and increased amounts of alloying elements lowering M_S, such as carbon, manganese, nickel, chromium and silicon.

Smaller changes in hardness were shown for increased prior microstructures` hardness (quench and tempered prior microstructures) and increased amounts of manganese, most likely due to the acceleration of austenitisation kinetics. Silicon, which is known to slow down the dissolution of carbon in austenite by increasing the carbon activity, lead to increased changes in hardness with changed austenitisation conditions.

For cases where hardenability comes into focus (NMTPs in hardened surface or transition zone) increased prior microstructure hardness (quench and tempered prior microstructures) as well as increased alloying can be recommended. Silicon is seen as effective due to its instant availability, as it dissolves completely in the ferritic and austenitic matrix, and its comparably small impact on M_S temperature.

For cases where small prior austenite grain size is of interest, larger contents of chromium, molybdenum, aluminium and larger A_{c1} or A_{c3} temperatures were shown to be effective.

Increased alloying must be seen critical for a robust induction hardening steel grade. As for the change in M_S temperature and the absolute M_S temperature, it shall be limited. As for the change in hardness, manganese and generally faster austenitisation kinetics help. The absolute hardness however was shown to be lowered with increased alloying contents, such as manganese, due to increasing amounts of retained austenite. If hardenability and small prior austenite grain sizes are in focus, alloying with moderate amounts of molybdenum, chromium or silicon was shown to be effective.

Overall, steel grade 50CrMo4 offers a comparable good process stability in terms of hardness, Ms temperature, NMTPs and prior austenite grains sizes. The steel is recommended as a comparably robust steel grade for induction hardening.

The **transfer of the dilatometer study on surface induction hardened samples** was shown to be possible. The **surface hardening depth** was related to the steels transformation temperature A_{c3}. Larger surface hardening depths were achieved for lower A_{c3} temperatures. Increased prior microstructures` hardness (quench and tempered prior microstructures), increased manganese and carbon contents as well as decreased silicon and chromium contents were shown to decrease the A_{c3} temperature. In some cases, larger or shallower case depth is required or large variation in case depth is an issue. If machine or process limitations are present, prior microstructure and alloying bands shall be considered and tolerance bands narrowed if needed.

Furthermore, the **hardness gradient within the transition zone** of surface hardened samples correlates well with the measured transformation temperatures from the dilatometer study. For larger differences between

the temperatures A_{c1} and A_{c3}, smaller hardness slopes in the transition zone of the surface hardened sample were measured. The observation was explained, assuming a similar temperature profile for all samples upon heating. The statistical evaluation with the help of Minitab showed that a combination of increased manganese and larger differences between the transformation temperatures A_{c3} and A_{c1} leads to lower hardness gradients in the transition zone. Larger differences between the transformation temperatures A_{c3} and A_{c1} were correlated to increased silicon and chromium contents as well as decreased prior hardness. The hardness gradient within the transition zone is a controversially discussed. However, there are indications that a larger transition zone hardness gradient can lead to larger residual stress gradients and larger tensile stress peaks in a depth where the core structure begins or the transition zone ends [FVA660].

The **hardness gradient or hardness decrease** in the surface near area (over 750 µm) of the surface induction hardened samples correlate with the dilatometer data. The effects on hardness with changed austenitisation conditions derived from the dilatometer data were identified as significant coefficients. Furthermore, the surface hardening depth is an affecting coefficient, which itself is depending on the steels chemistry as well as prior hardness. A small near surface hardness gradient is preferred due to process stability reasons. In addition, a smaller hardness gradient facilitates a constant surface hardness in the components circumferential direction in case of different stock removal caused by distortion.

The **near surface residual stress level** of the surface induction hardened rods were mainly affected by the surface hardening depth. The regression model proposed a dependency of the A_{c1} temperature. The tendency of larger compressive residual stresses with shallower hardening is known in literature. The tendency is often explained by the ability of the core to restrain the volume expansion of the surface during martensitic transformation and the connected volume increase. A bigger restraining potential by having a larger core (small surface hardening depth) will promote compressive stresses in the hardened layer. As for bearing components, larger compressive residual stresses are of interest, since they can be superimposed to tensile stresses from mounting or operation and are generally conceived as advantageous.

It has been shown that the classical measures of **rolling contact fatigue** development were mainly affected by the materials hardness after hardening and tempering. The regression models showed a clear reduction in grooving, change in residual stresses, change in FWHM and change in retained austenite with increased as heat-treated hardness. It was followed at first that steels with larger carbon contents shall be favoured according to the mentioned measures. As an exception, the ability to work harden in terms of hardness increase after RCF testing was promoted by lower hardness level or larger grooving and higher contents of retained austenite.

However, looking into larger scale material damage such as developed cracks (number and length), which might be causing flaking and failure at a later stage of life, lower carbon contents and lower as heat-treated hardness levels were shown to be favourable. Since some of the observed cracks were comparably long (up to 250 µm) and reaching out to the raceway surface, it is believed that the crack number and crack length are the life determining features of the conducted fatigue testing. Under these circumstances, the evaluation of developed cracks must be the measure to rate the fatigue performance. Hence, steels with larger carbon contents or higher levels of hardness cannot be recommended for the conducted RCF test and RCF performance. Apart from a lower hardness, a better cleanliness level (mostly rating for A-type inclusion) and smaller prior austenite grain sizes promoted fewer and shorter cracks.

As for the appearance of observations and cracks accompanied with white etching features, a positive impact of higher compressive residual stress levels, smaller prior austenite grains sizes as well increased silicon and decreased chromium and molybdenum was shown and discussed.

It was shown that medium carbon silicon alloyed steel, such as 67SiCr5, seems to be a good compromise concerning the measured fatigue damage (RS, FWHM, RA, grooving) and metallographic investigations (cracks, WEA formation). The use of higher silicon contents for bearing steels in terms of soft machinability, formability and decarburization during forming must be critically reviewed. The example of the bearing steel Ovako 832, containing 0.7 wt.-% silicon, shows that higher silicon contents can be handled in the manufacturing chain of bearing components. Care must be taken, since silicon promotes ferrite stability and bears the risk of undissolved, carbon free ferrite within the hardened case.

The role of prior austenite grain size shall be highlighted since small grains were shown to be positive in terms of observed cracks and crack lengths, number of observations with accompanied white etching area and number of observations. The molybdenum, chromium, aluminum content and A_{c1}/ A_{c3} transformation temperatures affected the PAGS. A dedicated alloying with those elements and alloying with nitrogen balanced to aluminum is recommended.

The as heat-treated hardness has been an important factor for the classical measure of fatigue in terms of grooving or residual stresses build up. Under different testing conditions with lower contact pressures, the sensitivity of higher hardness levels to crack initiation and crack growth might be reduced.

Overall, taking into account the dilatometer study as well as the rolling contact fatigue testing, steel grade 67SiCr5 QT can be recommended as a steel with decent induction heat treatment robustness derived from the dilatometers study in combination with a comparable good rolling contact fatigue performance for the given testing conditions.

For future work, the following is suggested:

- The effect of silicon (reduction of WEA, stability of retained austenite, tempering resistance) and manganese (stability of retained austenite) contents on fatigue shall be investigated with defined silicon and manganese contents, defined cleanliness levels and identical steel routes and reduction ratios
- Since the starting microstructure was shown to be significant, it is recommended to conduct a more extensive characterisation, such as precipitation size and spacing, phase composition, grain size and segregation degree
- The measurement of material toughness (blunt notch testing, tensile testing) to underline the above-mentioned importance of material toughness
- Conduct rolling contact fatigue testing under elevated temperatures to reflect the trend of component downsizing and increase in energy density; the influence of alloying elements providing tempering resistance (Si, Cr, Mo) and the austenitisation conditions (Cr, Mo in solid solution) might alter the above results
- Conduct rolling contact fatigue testing with more moderate contact pressures, according to conditions in bearing applications, and larger loaded sample volumes to increase the probability of sample failure

- The positive impact of silicon, compressive residual stresses and small prior austenite grain size on the appearance of WEAs shall be further investigated
- The role of the transition zone on the development of residual stresses and rolling contact fatigue performance shall be investigated
- A modified steel grade 50CrMo4 with a larger carbon content (e.g. “60CrMo4”) and a larger achievable hardness level might combine the good robustness derived from the dilatometer study with a better resistance towards classical fatigue damage and shall be investigated.

7 Literature

[Ahm02] R. Ahmed, Rolling Contact Fatigue, Failure Analysis and Prevention, Vol 11, ASM Handbook, ASM International, 2002, p. 941–956.

[Alv16] W. Solano-Alvarez, E. J. Pickering, M. J. Peet, K. L. Moore, J. Jaiswal, A. Bevan, H. K. D. H. Bhadeshia. Soft novel form of white.etching matter and ductile failure of carbide-free bainitic steels under rolling contact stresses. Acta Materialia 121, p. 215-226. 2016.

[And12] J.-E. Andersson, G. Wicks, P. L. J. Olund. Raceway Grooving: A Tool for Monitoring Microstructural Changes. STP 1548 on bearing steel. Bearing Steel: Advances in Rolling Contact Fatigue Strength Testing and Related Substitute Technologies. p. 291 – 302. 2012.

[And65] K.W. Andrews, Empirical Formulae for the Calculation of Some Transformation Temperatures, JISI, Vol 203, 1965, p 721–727.

[And93] I.-M. Andersson-Drugge, T. Lund. A ferritic-pearlitic steel with eutectoid composition. Creative use of bearing steels. ASTM. Philadelphia, 1993.

[ASM96] ASM Handbook Volume 19, Fatigue and Fracture. ASM International. Ohio, 1996.

[Baa10] E. Baake, B. Nacke. Efficient heating by electromagnetic sources in metallurgical processes: recent applications and development trends. Proceedings Heating by electromagnetic sources 2010, pp. XXIII-XXX. Padua, 2010.

[Bai39] E. C. Bain. Functions of the alloying elements in steel. U.S. Steel Corporation. Pittsburgh, 1939.

[Bar06] H.-J. Bargel, G. Schulze. Werkstoffkunde. Springer Verlag, Berlin. 2006.

[Bea57] H. R. Bear, R. H. Butler. Preliminary metallographic studies of ball fatigue under rolling-contact conditions. National advisory committee for aeronautics. Washington, 1957.

[Bec81] P. C. Becker. Microstructural changes around non-metallic inclusions caused by rolling-contact fatigue of ball-bearing steels. Metals Technology Vol June 1981, p. 234-243. 1981.

[Bes75] J. M. Beswick. Measurement of carbon levels in structurally transformed SAE 52100 ball bearing steel by microprobe analysis. Practical Metallography, Vol. 12, p. 200-207. 1975.

[Bes87] J. M. Beswick. The Effect of Chromium in High Carbon Bearing Steels. Metallurgical Transactions A. Volume 18A, pp. 1897-1906. Boston, 1987.

[Bes93] G. Besserdich. Untersuchung zur Eigenspannungs- und Verzugsausbildung beim Abschrecken von Zylindern aus den Stählen 42CrMo4 und Ck45 unter Berücksichtigung der Umwandlungsplastizität. Dissertation University Karlsruhe. 1993.

[Bha12] H. K. D. H. Bhadeshia. Steels for bearings. Progress in Material Science 57, pp. 268-435. Elsevier. 2012.

[Bha15] H.K.D.H. Bhadeshia, W. Solano-Alvarez. Critical Assessment 13: Elimination of white etching matter in bearing steels. Material Science and Technology, Vol 31, No 9, p. 1011-1015. 2015.

[Bha15] H. K. D. H. Bhadeshia, W. Solano-Alvarez. Critical Assessment 13: Elimination of white etching matter in bearing steels. Materials Science and Technology, Vol. 31, No. 9, p. 1011-1015. 2015.

[bmu18] Bundesministerium für Umwelt, Naturschutz und nukleare Sicherheit. Broschüre Nr. 10010, Klimaschutz in Zahlen (2018). https://www.bmu.de/publikation/klimaschutz-in-zahlen-2018/

[Boz93] R. M. Bozorth. Ferromagnetism. IEEE Press. Piscataway, 1993.

[Bri66] J. L. O`Brien, A. H. King. Electron Microscopy of Stress-Induced Structural Alterations Near Inclusions in Bearing Steels. Transactions of the ASME, Vol. 59, p. 568-572. 1966.

[Bro92] C. R. Brooks. Principles of the austenitization of steels. Elsevier science publishers ltd. London, 1992.

[Buc68] J. Buchwald, R. W. Heckel. An analysis of microstructural changes in 52100 steel bearings during cyclic stressing. Transactions of the ASM, Vol. 61, p. 750-756. 1968.

[Bus62] J. J. Bush, W. L. Grube, G. H. Robinson. Microstructural and Residual Stress Changes in Hardened Steel due to Rolling Contact. Rolling contact phenomena, p. 365-399. Elsevier Publ., New York, 1962.

Literature

[bwe18] Bundesministerium für Wirtschaft und Energie. Struktur des Energieverbrauchs, Tabelle 5 der Gesamtausgabe Energiedaten. 2018. https://www.bmwi.de/Redaktion/DE/Binaer/Energiedaten/Energiegewinnung-und-Energieverbrauch/energiedaten-energiegewinnung-verbrauch-3-xls.xlsx?__blob=publicationFile&v=19

[Cha11] J.-Y. Chae, J.-H. Jang, G. Zhang, K.-H. Kim, J. S. Lee, H.K.D.H. Bhadeshia, D.-W. Suh. Dilatometric analysis of cementite dissolution in hypereutectoid steels containing Cr. Scripta Materialia 65. P. 245-248. 2011.

[Cla08] K. Clarke. The effect of heating rate and microstructural scale on austenite formation, austenite homogenization and as-quenched microstructure in three induction hardenable steels. Dissertation Colorado School of Mines. Colorado, 2008.

[Cla14] B. Clausen, C. Stöberl, W. Trojahn, H.-W. Zoch. Imrpoved Chemical Composition of Low Alloyed High Carbon Martensitic Bearing Steels for Higher Fatigue Strengths. Bearing steel technologies, Vol 10, p. 1-21. 2014.

[Czi08] H. Czichos, M. Hennecke. Hütte, Das Ingenieurwissen. Springer Verlag. Berlin, 2008.

[Die09] A. M. Diederen. Metal minerals scarcity: A call for managed austerity and the elements of hope. TNO Defence, Security and Safety. Netherland. Rijswijk, 2009.

[Dow95] D. Dowson. Elastohydrodynamic and micro-elastohydrodynamic lubrication. Wear 190, p. 125-138. 1995.

[Eck69] H.-J. Eckstein. Wärmebehandlung von Stahl. VEB Deutscher Verlag für Grundstoffindustrie, Leipzig.1969.

[Eva12] M.-H. Evans. Literature Review – White structure flaking in wind turbine gearbox bearings: effects of butterflies and white etching cracks. Material Science and Technology, Vol. 28, No. 1, p. 3-22. 2012.

[Fur08] T. Furuharal, G. Miyamoto, T. Maki. Refinement of cementite in tempered lath martensite. Proceedings of 17th IFHTSE congress, 27.-30.10.2008, pp. 423 – 429.

[Fur96] K. Furumura, Y. Murakami, T. Abe. Development of Long Life Bearing Steel for Full Film Lubrication and for Poor and Contaminated Lubrication. NSK Motion & Control No. 1, p. 30-36. 1996.

[FVA660] D. Nadolski, F. Dobler. FVA Bericht Nr. 660 I “Induktionshärtung“, Tragfähigkeit und Festigkeitseigenschaften induktionsgehärteter Zahnräder. Forschungsvereinigung Antriebstechnik e.V.

[Gar08] A. Garcia-Junceda, C. Capdevila, F.G. Caballero, C. Garcia de Andres. Dependence of martensite start temperature on fine austenite grain size. Scripta Materialia 58, pp. 134-137, Elsevier. 2008.

[Gar81] C. I. Garcia, A. J. Deardo. Formation of austenite in 1.5 pct Mn steels. Metallurgical transactions A, Vol. 12A, pp. 521-530. 1981.

[Geg11] Jürgen Gegner (2011). Tribological Aspects of Rolling Bearing Failures, Tribology - Lubricants and Lubrication, Dr. Chang-Hung Kuo (Ed.), ISBN: 978-953-307-371-2, InTech, Available from: http://www.intechopen.com/books/tribology-lubricants-and-lubrication/tribological-aspects-of-rolling-bearing-failures

[Gen65] A. J. Gentile, E. F. Jordan, A. D. Martin. Phase Transformations in High-Carbon, High-Hardness Steels under Contact Loads. Trans. Metall. Soc. of AIME, Vol. 233, p. 1085-1093. 1965.

[Glo82] D. Glover. A Ball-Rod Rolling Contact Fatigue Tester. ASTM STP 771. p. 107-124. 1982.

[Gou17] B. Gould, A. Greco, K. Stadler, E. Vegter, X. Xiao. Using advanced tomography techniques to investigate the development of White Etching Cracks in a prematurely failed field bearing. Tribology International 116, p. 362-370. 2017.

[Gra07] A. Grabulov, U. Ziese, H. W. Zandbergen. TEM/SEM investigation of microstructural changes within the white etching area under rolling contact fatigue and 3-D crack reconstruction by focused ion beam. Scripta Materialia 57, p. 635-638. 2007.

[Gra10a] A. Grabulov. Fundamentals of Rolling Contact Fatigue. PhD thesis, Technical University of Delft. 2010.

[Gra10b] A. Grabulov, R. Petrov and H. W. Zandbergen. EBSD investigation of the crack initiation and TEM/FIB analyses of the microstructural changes around the cracks formed under rolling contact fatigue (RCF). Int. J. Fatigue, Vol. 32, p. 576–583. 2010.

[Gro84] J. Grosch, B. Kocjancic, G. Reichelt. Geschwindigkeitsbestimmende Vorgänge bei der Kurzzeitaustenitisierung. Härterei-Technische-Mitteilungen. Vol. 39. München, 1984.

[Ham76] B. J. Hamrock, D. Dowson. Isothermal Elastohydrodynamic Lubrication of Point Contacts. Part 3 – Fully Flooded Results. Nasa technical note D-8317. Lewis Research Center. Cleveland, Ohio. 1976.

[Hay10] T. Hayashi, N. Kurosawa, K. Yamada. Method of Prior Austenite Grain Refining Using Induction Hardening. JFE technical report No. 15. 2010.

[Hay75] T. Hayama. Effect of Residual Stress on Fatigue Strength of Induction – Hardened Steel. JSME, Vol. 18, No. 125, p. 1194-1200. 1975.

[Hen02] F. Hengerer. Wälzlagerstahl 100Cr6 – ein Jahrhundert Werkstoffentwicklung. Carl Hanser Verlag, München. 2002.

[Her81] Hertz, Über die Berührung fester elastischer Körper, Journal für die reine und angewandte Mathematik 92, p. 156-171. 1881

[Hip10] Gemeinschaftsprojekt DFG - AiF “Hipercomp”.

[Hou56] E. Houdremont. Handbuch der Sonderstahlkunde. Zweiter Band. Verlag Stahleisen. Düsseldorf, 1956.

[Hun11] M. Hunkel. Modelling of phase transformations and transformation plasticity of a continous casted steel 20MnCr5 incorporating segregations. Proceedings 3rd International Conference on Distortion Engineering. Bremen, 2011.

[Hwg09] HWG Inductoheat. http://www.hwg-inductoheat.de/fileadmin/pdf/wii.pdf

[Hyd96] R. S. Hyde. Contact Fatigue of Hardened Steels. Factors Influencing Contact Fatigue Life. ASM Handbook Vol. 19 – Fatigue and Fracture. p. 691–703. 1996.

[ISO15243] International standard ISO 15243:2004, Rolling bearings – Damage and failures – Terms, characteristics and causes. Geneva, 2004.

[Joh03] K. L. Johnson. Contact mechanics. Cambridge University Press. Cambridge, 2003.

[Joh82] G. B. Johnston, T. Andersson, E. v. Amerongen, A. Voskamp. Experience of Element and Full-Bearing Testing of Materials over Several Years. Proc. Rolling Contact Fatigue Testing of Bearing Steels. ASTM STP 771, p. 190-205. 1982.

[Jon46] Jones, A. B.: Metallographic observations of ball bearing fatigue phenomena. Proc. ASTM Symposium on Testing of Bearings. 1946, p. 1-26.

[Kad17] Y. Kadin, M. Y. Sherif. Energy dissipation at rubbing crack faces in rolling contact fatigue as the mechanism of white etching area formation. International Journal of Fatigue, No. 96, p. 114-126. 2017.

[Kan12] J.-H. Kang, B. Hosseinkhani, P. E. J. Rivera-Diaz-del-Castillo. Rolling contact fatigue in bearings: multiscale overview. Materials Science and Technology, Vol. 28, No. 1, p. 44-49. 2012.

[Kan13] J.-H. Kang, B. Hosseinkhani, C.A. Williams, M.P. Moody, P.A.J. Bagot, P.E.J. Rivera-Diaz-del-Castillo. Solute redistribution in the nanocrystalline structure formed in bearing steels. Scripta Materialia, Vol 69, p. 630-633. 2013.

[Kan13] J. Kang. Mechanisms of Microstructural Damage during Rolling Contact Fatigue of Bearing Steels. Dissertation at the University of Cambridge, 2013.

[Kel01] G. Kell, D. Liedtke, D. Roempler, W. Vogel, K.-H. Weissohn, U. Wyss. Stand der Erkenntnisse über die mathematische Voraussage des Härteprofils einsatzgehärteter Bauteile. HTM Härterei-Techn. Mitt. 56, Heft 3, p. 166-178. 2001.

[Kim12] K.-H. Kim, J.-S. Lee. On microstructure and properties of Si modified 100Cr6 bearing steels. Materials Science and Technology. Vol 28, No 1, p. 50-54. 2012.

Literature

[Kin66] A. H. King, J. L. O`Brien. Microstructural Alterations in Rolling Contact Fatigue. Proc. ASTM 66, p. 74-88, 1966.

[Klo89] K. H. Kloos. Festigkeits- und Verschleißeigenschaften induktiv randschichtgehärteter Proben und Bauteile. HTM Härterei-Techn. Mitt. 44, Heft 3, p. 157-165. 1989.

[Kra05] G. Krauss. Steels: Processing, Structure and Performance. ASM International. Ohio, 2005.

[Kra96] G. Krauss. Bending Fatigue of Carburized Steels. Residual Stresses and Shot Peening. ASM Handbook Vol. 19 – Fatigue and Fracture. 1996.

[Kra99] G. Krauss. Martensite in steel: strength and structure. Material science and Engineering A273-275, p. 40-57. 1999.

[Lan96] R. W. Landgraf. Fatigue Resistance and Microstructure of Ferrous Alloys. Selective Surface Processing. ASM Handbook Vol. 19 – Fatigue and Fracture. 1996.

[Lem59] B. S. Lement. Distortion in tool steels. ASM, Metals Park, Novelty, Ohio. 1959.

[Lie03] D. Liedtke. About the interrelation between carbon content in steels and the martensite hardness. Materialwissenschaft und Werkstofftechnik. Wiley-VCH Verlag. Weinheim, 2003.

[Lie09] D. Liedtke, H. Stiele. Wärmebehandlung von Stahl – Randschichthärten. Merkblatt 236. Stahl-Informations-Zentrum. Düsseldorf, 2009.

[Lun10] T. B. Lund. Sub-Surface Initiated Rolling Contact Fatigue – Influence of Non-Metallic Inclusions, Processing History, and Operating Conditions. Journal of ASTM International, Vol. 7, No. 5, p. 1-12. 2010.

[Lun69] T. Lund. Structural alterations in fatigue-tested ball bearing steel. Jernkont. Ann. 153, 1969.

[Man70] Mannot, J . ; Tricot, R.; Gueussier, A.: Resistance a la fatigue et endurance des aciers pour roulements. Rev. Metallurg. Vol. 5, p. 619-638. 1970.

[Mar09] L. Markegård, H. Kristoffersen. Residual Stress After Surface Hardening – An Explanation Of How Residual Stress Is Created. “New challenges in heat treatment and surface engineering” conference. Croatia, Dubrovnik, 09.-12. June 2009.

[Mar66] J. A. Martin, S. F. Borgese, A. D. Eberhardt. Microstructural Alterations of Rolling – Bearing Steel Undergoing Cyclic Stressing. J. Basic Eng., Vol. 88, Nr. 3, p. 555-567. 1966.

[Mer63] J. E. Merwin, K. L. Johnson. An analysis of plastic deformation in rolling contact. Proc Instn Mech Engrs, Vol 177, p. 676-690. 1963.

[Miy07] G. Miyamoto, J.C. Oh, K. Hono, T. Furuhara, T. Maki. Effect of partitioning of Mn and Si on the growth kinetics of cementite in tempered Fe-0.6 mass% C martensite. Acta Materialia 55. pp. 5027 – 5038. 2007.

[Mol56] G. Molinder. A quantitative study of the formation of austenite and the solution of cementite at different austenitizing temperatures for a 1.27% C steel. Acta Metallurgica, Vol. 4. 1956.

[Mon88] J. Monnot, B. Heritier and J.Y. Cogne: Relationship of Melting Practice, Inclusion Type, and Size with Fatigue Resistance of Bearing Steels, ASTM STP 987, American Society for Testing Materials, Philadelphia, PA, 1988, pp. 149–165

[Muh07] D. Muhs, H. Wittel, D. Jannasch, J. Voßiek. Roloff / Matek Maschinenelemente. Vieweg Verlag, Wiesbaden. 2007.

[Mur02] Y. Murakami. Metal Fatigue: Effects of Small Defects and Nonmetallic Inclusion. Elsevier Science Ltd. Oxford, 2002.

[Mur70] Muro, H.; Tsushima, N.: Microstructural, microhardness and residual stress changes due to rolling contact. Wear, Vol. 15, p. 309-330. 1970.

[Nak08] H. Nakashima. Trends in materials and heat treatments for rolling bearings. NTN technical review No. 76, 2008.

[Öst80] R. Österlund, O. Vingsbo. Phase changes in fatigued ball bearings. Metall. Mater. Trans. A, Vol. 11A, p. 701–707. 1980.

[Öst82] R. Österlund, O. Vingsbo, L. Vincent, P. Guiraldenq. Butterflies in Fatigued Ball Bearings – Formation Mechanisms and Structure. Scand. J. Metall., Vol. 11, p. 23-32. 1982.

[Pal17] M. Paladugu, R. S. Hyde. White etching matter promoted by intergranular embrittlement. Scripta Materialia, Vol. 130, p. 219-222. 2017.

[Pax67] H. W. Paxton. The Formation of Austenite. Transformation and Hardenability in Steels. Symposium. Climax

[Pet60] E. F. Petrova, M. I. Lapshina, L. A. SHV Artsman. Effect of alloying on the thermodynamic activity and solubility of carbon in alpha-iron. Metallovedenie I Term. Obrabotka, No. 4, p. 22-25. 1960.

[Por92] D. A. Porter, K. E. Easterling. Phase Transformations in Metals and Alloys. 2nd edition. Springer-Science and Business Media, B.V. 1992.

[Roll99] J. Rollmann. Wälzfestigkeit von induktiv randschichtgehärteten bauteilähnlichen Proben. Dissertation TU Darmstadt, 1999.

[Rot63] W. Roth. Untersuchungen über die Austenitbildung bei einigen unlegierten und niedriglegierten Stählen unter besonderer Berücksichtigung hoher Erhitzungsgeschwindigkeiten. PhD thesis. RWTH Aachen. 1963.

[Rud03] V. Rudnev, D. Loveless, R. Cook, M. Black. Handbook of Induction Heating. Marcel Dekker AG, Basel. 2003.

[Sch06] H. Scheerer, C. Berger. Untersuchungen zur Wälzermüdung nach induktivem Kurzzeitanlassen. Mat.-wiss. U. Werkstoftechn., Vol. 37, No.2, p. 183-190. 2006.

[Sch08] H. Schlicht. Über adiabatic shear bands und die Entstehung der “Steilen Weißen Bänder” in Wälzlagern. Mat.-wiss. u. Werkstofftech. Vol. 39, No. 3, p. 217 – 226. 2008.

[Sch59] E. Schmidtmann, H. Brandis. Beitrag zur Austenitbildung in unlegierten und niedrig legierten untereutektoidischen Stählen. Archiv für das Eisenhüttenwesen. Verlag Stahleisen M.B.H. Düsseldorf, 1959.

[Sch68] H. Schlicht, E. Schreiber, H. Fahry. Induktives Härten eines übereutektoiden Wälzlagerstahls. Härterei-Technische Mitteilungen. Rudolf Haufe Verlag. Freiburg, 1968.

[Sch68] Schlicht, H.: Strukturelle Änderungen in Wälzelementen. Wear, Vol. 12, p. 149-163, 1968.

[Sch70] Schlicht, H. Der Überrollungsvorgang in Wälzelementen. HTM Härterei-Techn. Mitt. 25, Heft 1, p. 47-55. 1970.

[Sch73] H. Schlicht. Über die Entstehung von White Etching Areas (WEA) in Wälzelementen. HTM Härterei-Techn. Mitt. 28, Heft 2, p. 112-123. 1973.

[Sch74] H. Schlicht. Beitrag zur Theorie des schnellen Erwärmens und schnellen Abkühlens von Stahl. Härterei Technische Mitteilungen, Vol. 29, pp. 184-192. 1974.

[Sch74] E. Schreiber. Untersuchungen zur plastischen Verformung gehärteten Stahls. HTM Härterei-Techn. Mitt. 29, Heft 4, p. 248-258. 1974.

[Sco66] D. Scott, B. Loy, G. H. Mills. Metallurgical aspects of rolling contact fatigue. Proc Instn Mech Engrs, Vol 181, p. 94-103. 1966.

[Sem86] S. L. Semiatin, D. E. Stutz. Induction Heat Treatment of Steel. American Society for Metals, Ohio. 1986.

[She89] P. Shewmon. Diffusion in Solids, 2nd edition. Wiley. Hoboken, 1989.

[Sid15] C. Sidoroff, M. Perez, P. Dierickx, D. Girodin. Advantages and Shortcomings of Retained Austenite in Bearing Steel: A Review. Bearing steel technologies, Vol 10. 2015.

[Smi00] K. C. Smith, J. P. Wise, G. Krauss. A microstructural analysis of rapid austenite formation in induction hardened steels. Proceedings of the 5th ASM Heat Treatment ans Surface Engineering Conference in Europe. ASM International. 2000.

[Sol14] W. Solano-Alvarez, H. K. D. H. Bhadeshia. White-Etching Matter in Bearing Steel. Part 1: Controlled Cracking of 52100 Steel. Metallurgical and Materials Transactions A, Vol. 45A, p. 4907-4915, 2014.

[Sty51] H. Styri. Fatigue Strength of Ball Bearing Races and Heat-Treated 52100 Steel Specimens. Proc. ASTM 51, p. 682-700, 1951.

[Sug70] K. Sugino, K. Miyamoto, M. Nagumo, K. Aoki. Structural Alterations of Bearing Steels under Rolling Contact Fatigue. Trans. ISIJ, Vol. 10, p. 98-111. 1970.

[Swa75] H. Swahn, L. Hellner, C. G. Andersson, B. Zetterlund, O. Vingsbo. Phase Transformations and Residual Stress Changes in Steel Rolls during Contact Fatigue. Scandinavian Journal of Metallurgy Vol. 4, p. 263-266. 1975.

Literature

[Swa76] H. Swahn. P. C. Becker, O. Vingsbo. Martensite Decay During Rolling Contact Fatigue in Ball Bearings. Metallurgical Transactions A, Vol. 7A, August, p. 1099-1110. 1976.

[Swa76b] H. Swahn, P. C. Becker, O. Vingsbo. Electron-microscope studies of carbide decay during contact fatigue in ball bearings. Met. Sci., Vol. 10, p. 35–39. 1976.

[Tal67] T. E. Tallian. On Competing Faiure Modes in Rolling Contact. ASLE Transactions, of the American Society of Lubrication Engineers, Vol. 10, p. 418-439. 1967.

[Tot02] G. Totten, M. Howes, T. Inoue. Handbook of Residual Stress and Deformation of Steel. ASM International. Ohio, 2002.

[Tsu92] N. Tsushima, K. Maeda. Influence of retained austenite on rolling contact fatigue strength and wear strength. Journal of the Japan Society for Heat Treatment, Vol. 32, p. 43-47. 1992.

[Tud60] C. A. Tudbury. Basics of induction heating. Vol. 1. John F. Rider, Inc., New York, 1960.

[uba18] Umweltbundesamt. https://www.umweltbundesamt.de/sites/default/files/medien/384/bilder/dateien/7_abb_energieverbrauch-industrie-waermezwecke_2018-02-14.pdf

[Uya11] H. Uyama. The mechanism of white structure flaking in rolling bearings. Wind turbine tribology seminar. Bloomfield, CO, USA, 2011.

[Vas72] GH. Vasilca, V. Raszillier. A study of dark etching area type structure modification of material and hertzian contact area induced by ball bearing type motion. Wear Vol. 19. P. 1 – 15. 1972.

[Veg10] R. H. Vegter, J. T. Slycke. The role of Hydrogen on Rolling Contact Fatigue Response of Rolling Element Bearings. Journal of ASTM International, Vol. 7, No. 2, p. 1-12. 2010.

[Veg12] R. H. Vegter, J. T. Slycke. Metal Physics and Rolling Contact Fatigue Testing. STP 1548 on bearing steel. Bearing Steel: Advances in Rolling Contact Fatigue Strength Testing and Related Substitute Technologies. p. 341 – 352. 2012.

[Vos80] A. P. Voskamp, R. Österlund, P. C. Becker, O. Vingsbo. Gradual changes in residual stress and microstructure during rolling contact fatigue in ball bearings. Metals Technology, 7 (1980) 14-21.

[Vos92] A. P. Voskamp. Ermüdungsvorgänge im Wälzkontakt an Wälzlager-Laufbahn. AWT-Tagung „Randschichtermüdung im Wälzkontakt“. AWT Arbeitsgemeinschaft Wärmebehandlung und Werkstofftechnik e.V., p. 19-33. 1992

[Vos96] A. P. Voskamp, E. J. Mittemeijer. Crystallographic Preferred Orientation Induced by Cyclic Rolling Contact Loading. Metallurgical and Materials Transactions A, Vol. 27A, p. 3445-3465. 1996.

[Vos97] A. P. Voskamp. Microstructural changes during rolling contact fatigue. Dissertation Technical University of Delft. 1997.

[Wou09] H. Wouters, D. Bol. Material Scarcity – an M2i study. Material innovation institute (M2i). Netherlands. Delft, 2009.

[Yan09] H.-S. Yang, H.K.D.H. Bhadeshia. Austenite grain size and the martensite-start temperature. Scripta Materialia 60, pp. 493-495. Elsevier. 2009.

[Zar69] E. V. Zaretsky, R. J. Parker, W. J. Anderson. A study of residual stress induced during rolling. Trans. ASME Vol. 91F, p. 314-319. 1969.

[Zin88] S. Zinn, S. L. Semiatin. Elements of Induction Heating. ASM International, Ohio. 1988.

[Zoc92] H.-W. Zoch. Wärmebehandlungsverfahren in der Wälzlagerfertigung.Carl Hanser Verlag, München. 1992.

[Zwi80] O. Zwirlein, H. Schlicht. Werkstoffanstrengung bei Wälzbeanspruchung – Einfluß von Reibung und Eigenspannungen. Z. Werkstofftechn. Volume 11. p. 1 – 14. 1980.

8 Appendix

A Calculation of shear stresses and depth of maximal shear stresses for general profiles

From [Joh03]:

p. 96, equation 4.32:

contact pressure p_0

$$p_0 = \frac{3P}{2\pi ab}$$

a=minor semi axis of contact ellipse, b=major semi axis of contact ellipse, P=total load

With equation 4.30, p. 96:

$$c = \sqrt{ab} = \left(\frac{3PR_e}{4E^*}\right)^{1/3} F_1(e)$$

and equation 4.33, p.96:

$$\frac{b}{a} = \left(\frac{B}{A}\right)^{-2/3}$$

It follows:

$$a = c\left(\frac{B}{A}\right)^{1/3}$$

and

$$b = c\left(\frac{B}{A}\right)^{-1/3}$$

p. 85, equations 4.4 and 4.5:

R_x^y= principal radii of curvature of bodies in contact

$R_1^I = R_1^{II} = R_1$= const. for balls

$$A = 0{,}25 * \left(\frac{2}{R_1} + \frac{1}{R_2^I} + \frac{1}{R_2^{II}}\right) - 0{,}25 * (\frac{1}{R_2^I} - \frac{1}{R_2^{II}})$$

$$B = 0{,}25 * \left(\frac{2}{R_1} + \frac{1}{R_2^I} + \frac{1}{R_2^{II}}\right) + 0{,}25 * (\frac{1}{R_2^I} - \frac{1}{R_2^{II}})$$

p. 97, Fig. 4.4:

With $\sqrt{\frac{B}{A}}$ read F1 from figure 4.4

➔ $F_1 \sim 0{,}99$

p. 92, equation for reduced elastic modulus E*:

$$E^* = \left(\frac{1 - \nu_1^2}{E_1} + \frac{1 - \nu_2^2}{E_2}\right)^{-1}$$

The maximum shear stress and its depth was taken from table 4.1 on page 99 in connection to the relation to the major and minor axis of the contact ellipse: b/a

B Dilatometer study and fatigue testing

B.1 Dilatometer curves heating

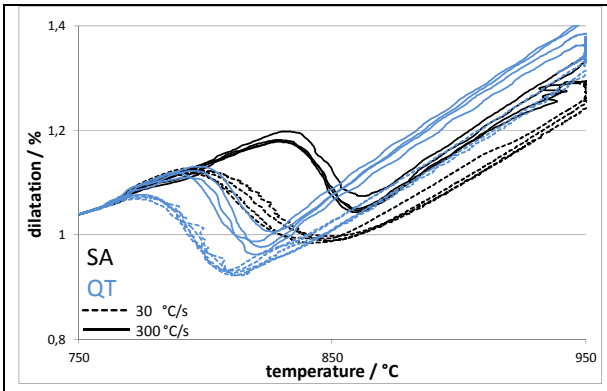

100Cr6

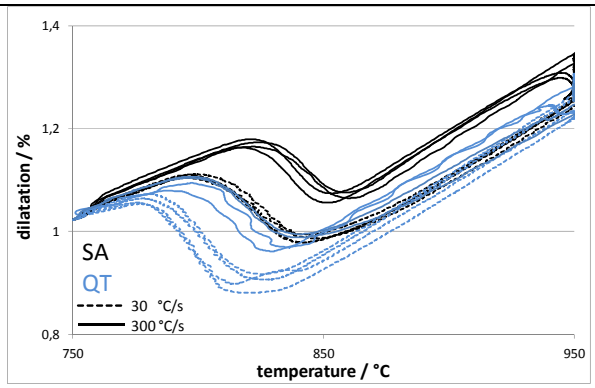

Ovako 832

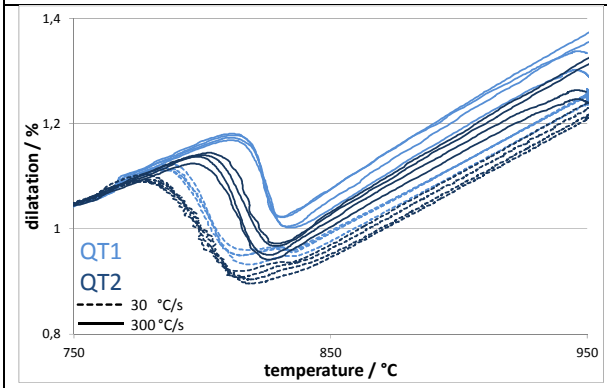

50CrMo4

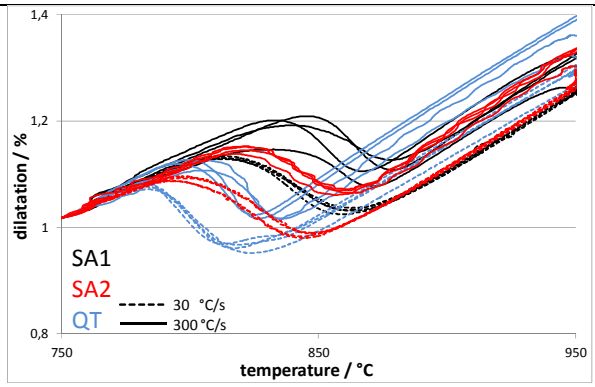

67SiCr5

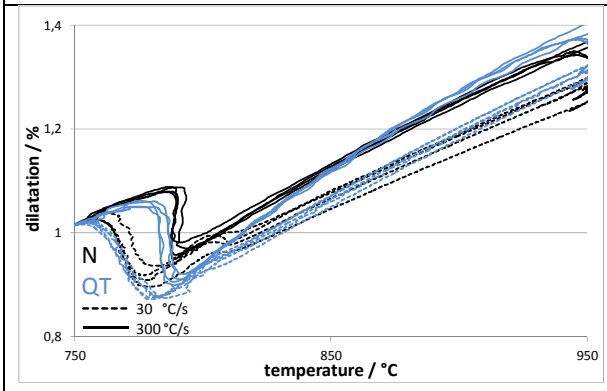

70Mn4

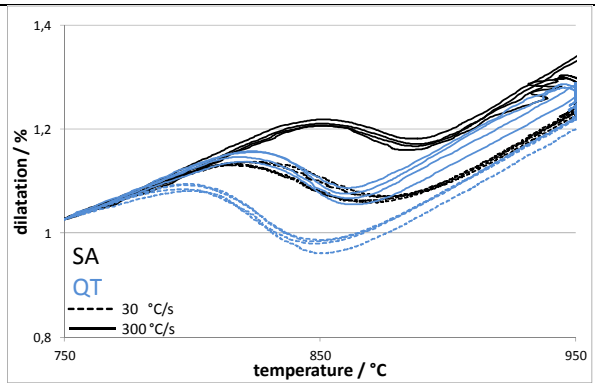

Ovako 677

B.2 Regression analysis for transformation temperatures ferrite -> austenite

A_{c1}

Best fit :

Model Summary

S	R-sq	R-sq(adj)	R-sq(pred)
2.62231	98.87%	97.46%	0.00%

Coefficients

Term	Coef	SE Coef	T-Value	P-Value	VIF
Constant	828.74	6.95	119.16	0.000	
Si	20.67	2.46	8.40	0.001	1.90
Cr	14.77	2.89	5.11	0.007	2.38
Mo	78.2	15.2	5.15	0,007	2.42
Ni	-173.9	51.3	-3.39	0.028	3.46
Hardness pre structure	-0.2306	0.0225	-10.24	0.001	1.08

Regression Equation

A_{c1} = 828.74 + 20.67 Si + 14.77 Cr + 78.2 Mo - 173.9 Ni - 0.2306 Hardness pre structure

Including elements from formula “Andrews” [And65] Si, Mn, Cr, Mo, Ni and hardness :

Model Summary

S	R-sq	R-sq(adj)	R-sq(pred)
2.82403	99.02%	97.05%	*

Coefficients

Term	Coef	SE Coef	T-Value	P-Value	VIF
Constant	827.69	7.65	108.18	0.000	
Si	21.19	2.76	7.67	0.005	2.07
Mn	-2.36	3.53	-0.67	0.551	3.14
Cr	13.78	3.44	4.01	0.028	2.91
Ni	-138.4	76.5	-1.81	0.168	6.64
Hardness pre structure	-0.2284	0.0245	-9.34	0.003	1.10
Mo	75.7	16.8	4.51	0.020	2.55

Regression Equation

A_{c1} = 827.69 + 21.19 Si - 2.36 Mn + 13.78 Cr - 138.4 Ni - 0.2284 Hardness pre structure + 75.7 Mo

A_{c3}

Best fit :

Model Summary

S	R-sq	R-sq(adj)	R-sq(pred)
2.85409	99.47%	98.82%	96.53%

Coefficients

Term	Coef	SE Coef	T-Value	P-Value	VIF
Constant	882.36	9.52	92.69	0.000	
Si	42.06	2.51	16.76	0.000	1.67
Mn	-8.86	2.52	-3.51	0.025	1.57
Cr	30.13	2.83	10.65	0.000	1.93
C	-25.76	8.81	-2.92	0.043	2.09
Hardness pre structure	-0.3252	0.0247	-13.18	0.000	1.09

Regression Equation

A_{c3} = 882.36 + 42.06 Si - 8.86 Mn + 30.13 Cr - 25.76 C - 0.3252 Hardness pre structure

Including elements from formula “Andrews” [And65] C, Ni , Si, Mo and hardness :

Model Summary

S	R-sq	R-sq(adj)	R-sq(pred)
9.50595	94.16%	86.87%	47.13%

Coefficients

Term	Coef	SE Coef	T-Value	P-Value	VIF
Constant	814.7	40.9	19.93	0.000	
Si	34.06	8.49	4.01	0.016	1.72
Ni	-528	335	-1.58	0.190	11.22
Hardness pre structure	-0.3380	0.0821	-4.12	0.015	1.09
C	140.2	61.8	2.27	0.086	9.25
Mo	284	126	2.25	0.088	12.71

Regression Equation

A_{c3} = 814.7 + 34.06 Si - 528 Ni - 0.3380 Hardness pre structure + 140.2 C + 284 Mo

Including Si, Ni, Mo, Cr, hardness

Model Summary

S	R-sq	R-sq(adj)	R-sq(pred)
3.61957	99.15%	98.10%	0.00%

Coefficients

Term	Coef	SE Coef	T-Value	P-Value	VIF
Constant	874.10	9.60	91.05	0.000	
Si	39.62	3.40	11.67	0.000	1.90
Ni	-219.5	70.8	-3.10	0.036	3.46
Hardness pre structure	-0.3306	0.0311	-10.63	0.000	1.08
Mo	55.5	21.0	2.65	0.057	2.42
Cr	30.64	3.99	7.69	0.002	2.38

Regression Equation

A_{c3} = 874.10 + 39.62 Si - 219.5 Ni - 0.3306 Hardness pre structure + 55.5 Mo + 30.64 Cr

Including Si, Mn, Ni, Mo, Cr, hardness

Model Summary

S	R-sq	R-sq(adj)	R-sq(pred)
3.27320	99.48%	98.44%	*

Coefficients

Term	Coef	SE Coef	T-Value	P-Value	VIF
Constant	871.61	8.87	98.29	0.000	
Si	40.86	3.20	12.77	0.001	2.07
Ni	-135.1	88.7	-1.52	0.225	6.64
Hardness pre structure	-0.3256	0.0284	-11.48	0.001	1.10
Cr	28.30	3.99	7.10	0.006	2.91
Mn	-5.62	4.09	-1.38	0.263	3.14
Mo	49.5	19.5	2.54	0.085	2.55

Regression Equation

A_{c3} = 871.61 + 40.86 Si - 135.1 Ni - 0.3256 Hardness pre structure + 28.30 Cr - 5.62 Mn + 49.5 Mo

Appendix

A_{c3}-A_{c1}

Model Summary

S	R-sq	R-sq(adj)	R-sq(pred)
4.50856	88.76%	83.14%	65.01%

Coefficients

Term	Coef	SE Coef	T-Value	P-Value	VIF
Constant	44.4	11.5	3.87	0.008	
Si	14.75	3.08	4.79	0.003	1.01
Hardness pre structure	-0.1026	0.0381	-2.69	0.036	1.04
Cr	13.32	3.30	4.04	0.007	1.05

Regression Equation

A_{c3}-A_{c1} = 44.4 + 14.75 Si - 0.1026 Hardness pre structure + 13.32 Cr

B.3 Linear regression analysis for prior austenite grain size

Model Summary

S	R-sq	R-sq(adj)	R-sq(pred)
1.13903	96.69%	95.03%	82.43%

Coefficients

Term	Coef	SE Coef	T-Value	P-Value	VIF
Constant	90.0	18.5	4.87	0.003	
Cr	-6.184	0.717	-8.63	0.000	1.08
Mo	-36.19	5.35	-6.76	0.001	1.09
Ac1	-0.0844	0.0234	-3.61	0.011	1.03

Regression Equation

PAGS = 90.0 - 6.184 Cr - 36.19 Mo - 0.0844 Ac1

Model Summary

S	R-sq	R-sq(adj)	R-sq(pred)
1.45649	94.58%	91.87%	67.38%

Coefficients

Term	Coef	SE Coef	T-Value	P-Value	VIF
Constant	62.8	16.7	3.77	0.009	
Cr	-5.532	0.921	-6.01	0.001	1.09
Mo	-32.65	7.27	-4.49	0.004	1.23
Ac3	-0.0485	0.0204	-2.37	0.055	1.22

Regression Equation

PAGS = 62.8 - 5.532 Cr - 32.65 Mo - 0.0485 Ac3

Appendix

B.4 Linear regression analysis – Effects on M_S

Model Summary

S	R-sq	R-sq(adj)	R-sq(pred)
6.91427	91.23%	87.94%	83.59%

Coefficients

Term	Coef	SE Coef	T-Value	P-Value	VIF
Constant	-40.1	14.3	-2.80	0.023	
Hardness pre structure	0.2378	0.0527	4.51	0.002	1.11
Cr	-17.87	5.67	-3.15	0.014	1.90
Ni	-268.2	89.8	-2.99	0.017	1.88

Regression Equation

effect Ms T_A = -40.1 + 0.2378 Hardness pre structure - 17.87 Cr - 268.2 Ni

Model Summary

S	R-sq	R-sq(adj)	R-sq(pred)
2.69395	99.12%	98.39%	75.37%

Coefficients

Term	Coef	SE Coef	T-Value	P-Value	VIF
Constant	-3.96	8.39	-0.47	0.654	
Hardness pre structure	0.2157	0.0211	10.22	0.000	1.18
Si	-9.28	2.19	-4.24	0.005	1.59
Mn	-11.67	2.22	-5.25	0.002	1.46
Cr	-20.62	2.24	-9.22	0.000	1.95
C	-50.73	8.21	-6.18	0.001	2.12

Regression Equation

effect Ms t_s = -3.96 + 0.2157 Hardness pre structure - 9.28 Si - 11.67 Mn - 20.62 Cr - 50.73 C

B.5 Linear regression analysis – Effects on hardness

Model Summary

S	R-sq	R-sq(adj)	R-sq(pred)
16.7174	90.09%	86.38%	77.42%

Coefficients

Term	Coef	SE Coef	T-Value	P-Value	VIF
Constant	240.0	33.1	7.26	0.000	
Hardness pre structure	-0.723	0.127	-5.70	0.000	1.10
Si	40.5	12.5	3.25	0.012	1.34
Mn	-54.8	13.5	-4.07	0.004	1.39

Regression Equation

effect hardness Ta = 240.0 - 0.723 Hardness pre structure + 40.5 Si - 54.8 Mn

Model Summary

S	R-sq	R-sq(adj)	R-sq(pred)
27.0187	68.75%	65.62%	50.59%

Coefficients

Term	Coef	SE Coef	T-Value	P-Value	VIF
Constant	275.3	50.9	5.41	0.000	
Hardness pre structure	-0.915	0.195	-4.69	0.001	1.00

Regression Equation

effect hardness ts = 275.3 - 0.915 Hardness pre structure

B.6 Linear regression analysis – grooving

Model Summary

S	R-sq	R-sq(adj)	R-sq(pred)
0.119997	95.47%	93.96%	89.34%

Coefficients

Term	Coef	SE Coef	T-Value	P-Value	VIF
Constant	12.736	0.951	13.39	0.000	
hardness HV1	-0.01401	0.00128	-10.97	0.000	1.14
abs. RA reference	0.01133	0.00775	1.46	0.194	1.14

Regression Equation

track depth = 12.736 - 0.01401 hardness HV1 + 0.01133 abs. RA reference

Model Summary

S	R-sq	R-sq(adj)	R-sq(pred)
0.126025	95.01%	93.34%	87.12%

Coefficients

Term	Coef	SE Coef	T-Value	P-Value	VIF
Constant	12.354	0.969	12.74	0.000	
hardness HV1	-0.01347	0.00126	-10.68	0.000	1.01
delta RA 140 µm	-0.0279	0.0238	-1.17	0.285	1.01

Regression Equation

track depth = 12.354 - 0.01347 hardness HV1 - 0.0279 delta RA 140 µm

B.7 Linear regression analysis – Change in FWHM

Model Summary

S	R-sq	R-sq(adj)	R-sq(pred)
2.20053	88.18%	84.24%	76.54%

Coefficients

Term	Coef	SE Coef	T-Value	P-Value	VIF
Constant	-10.19	6.67	-1.53	0.178	
abs. RS track 140µ	-0.04166	0.00746	-5.59	0.001	1.18
abs. RA reference	-0.173	0.145	-1.19	0.279	1.18

Regression Equation

Delta FWHM % = -10.19 - 0.04166 abs. RS track 140µ - 0.173 abs. RA reference

Model Summary

S	R-sq	R-sq(adj)	R-sq(pred)
2.33400	88.92%	82.28%	29.29%

Coefficients

Term	Coef	SE Coef	T-Value	P-Value	VIF
Constant	-9.25	7.27	-1.27	0.259	
abs. RS track 140µ	-0.03853	0.00959	-4.02	0.010	1.74
Delta RA %	0.0461	0.0798	0.58	0.589	1.51
abs. RA reference	-0.181	0.155	-1.17	0.294	1.19

Regression Equation

Delta FWHM % = -9.25 - 0.03853 abs. RS track 140µ + 0.0461 Delta RA % - 0.181 abs. RA reference

B.8 Linear regression analysis – average number of alterations with white etching feature

Model Summary

S	R-sq	R-sq(adj)	R-sq(pred)
1.55980	99.23%	98.45%	94.25%

Coefficients

Term	Coef	SE Coef	T-Value	P-Value	VIF
Constant	-15.49	2.91	-5.32	0.006	
Si	-19.24	1.45	-13.30	0.000	1.29
Mo	155.4	14.6	10.68	0.000	4.13
PAGS	2.788	0.173	16.08	0.000	2.71
Delta HWB %	-0.585	0.144	-4.06	0.015	2.09

Regression Equation

av. # alt. with WEA = -15.49 - 19.24 Si + 155.4 Mo + 2.788 PAGS - 0.585 Delta HWB %

Model Summary

S	R-sq	R-sq(adj)	R-sq(pred)
0.769796	99.86%	99.62%	98.51%

Coefficients

Term	Coef	SE Coef	T-Value	P-Value	VIF
Constant	-12.03	2.70	-4.45	0.021	
Si	-20.416	0.711	-28.72	0.000	1.28
Mo	211.4	13.9	15.16	0.001	15.57
PAGS	3.211	0.132	24.36	0.000	6.43
abs. RS track 140µ	0.04811	0.00567	8.49	0.003	5.58
B, fine	8.49	1.83	4.65	0.019	3.49

Regression Equation

av. # alt. with WEA = -12.03 - 20.416 Si + 211.4 Mo + 3.211 PAGS + 0.04811 abs. RS track 140µ + 8.49 B, fine

Model Summary

S	R-sq	R-sq(adj)	R-sq(pred)
0.809670	99.84%	99.58%	96.88%

Coefficients

Term	Coef	SE Coef	T-Value	P-Value	VIF
Constant	-6.07	2.31	-2.62	0.079	
Si	-21.837	0.854	-25.58	0.000	1.67
Mo	204.2	13.4	15.26	0.001	12.95
PAGS	3.217	0.140	22.93	0.000	6.58
abs. RS track 140µ	0.04520	0.00549	8.23	0.004	4.73
B,thick	4.43	1.01	4.38	0.022	3.17

Regression Equation

av. # alt. with WEA = -6.07 - 21.837 Si + 204.2 Mo + 3.217 PAGS + 0.04520 abs. RS track 140µ + 4.43 B, thick

Model Summary

S	R-sq	R-sq(adj)	R-sq(pred)
0.978771	99.77%	99.39%	91.24%

Coefficients

Term	Coef	SE Coef	T-Value	P-Value	VIF
Constant	-2.24	2.85	-0.79	0.489	
Si	-20.253	0.899	-22.52	0.000	1.27
Mo	174.3	10.8	16.15	0.001	5.77
PAGS	2.821	0.109	25.85	0.000	2.73
abs. RS track 140µ	0.04146	0.00602	6.88	0.006	3.90
DS	5.38	1.54	3.49	0.040	1.80

Regression Equation

N WEA 11.3-11.5 = -2.24 - 20.253 Si + 174.3 Mo + 2.821 PAGS + 0.04146 abs. RS track 140µ + 5.38 DS

B.9 Examples of longer cracks (> 40 µm) with white etching features in center position

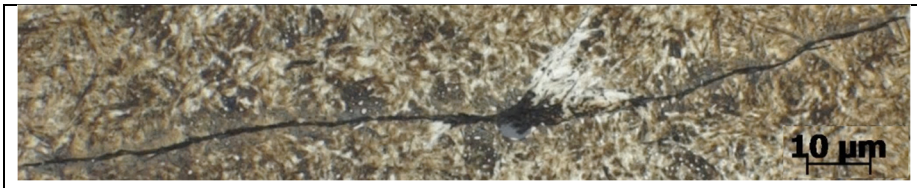	100Cr6 QT
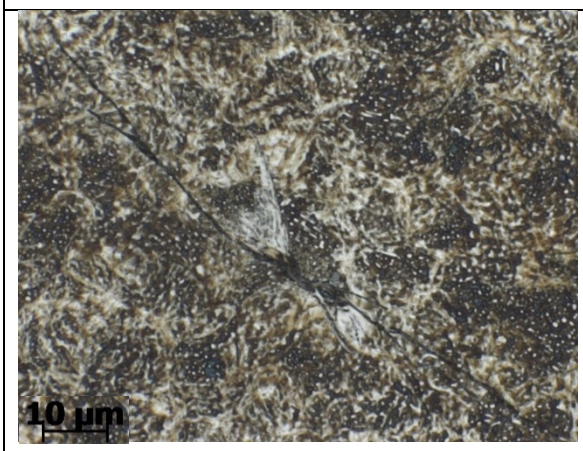	100Cr6 SA
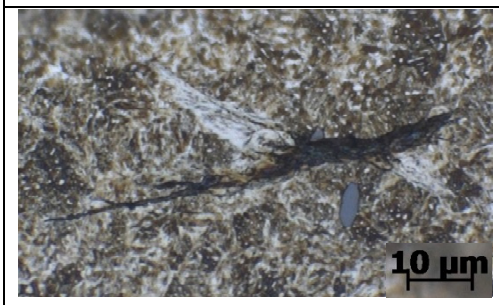	Ovako 832 SA
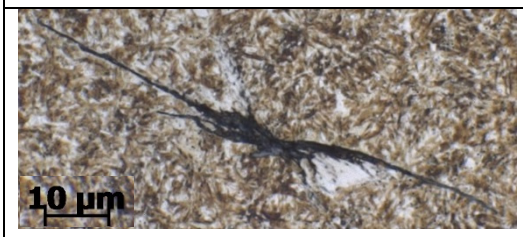	Ovako 832 QT
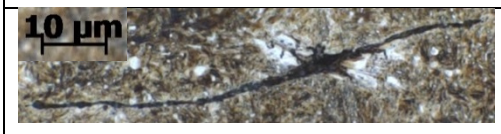	67SiCr5 SA2
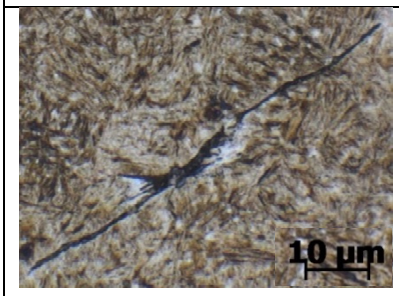	67SiCr5 QT